Robust estimation of dynamics behavior and driving diagnosis applied to an intelligent MAGV

Angel Gabriel Alatorre Vasquez

Université de Technologie Compiègne

Par **Angel Gabriel ALATORRE VAZQUEZ**

Robust estimation of dynamics behavior and driving diagnosis applied to an intelligent MAGV

Thèse présentée
pour l'obtention du grade
de Docteur de l'UTC

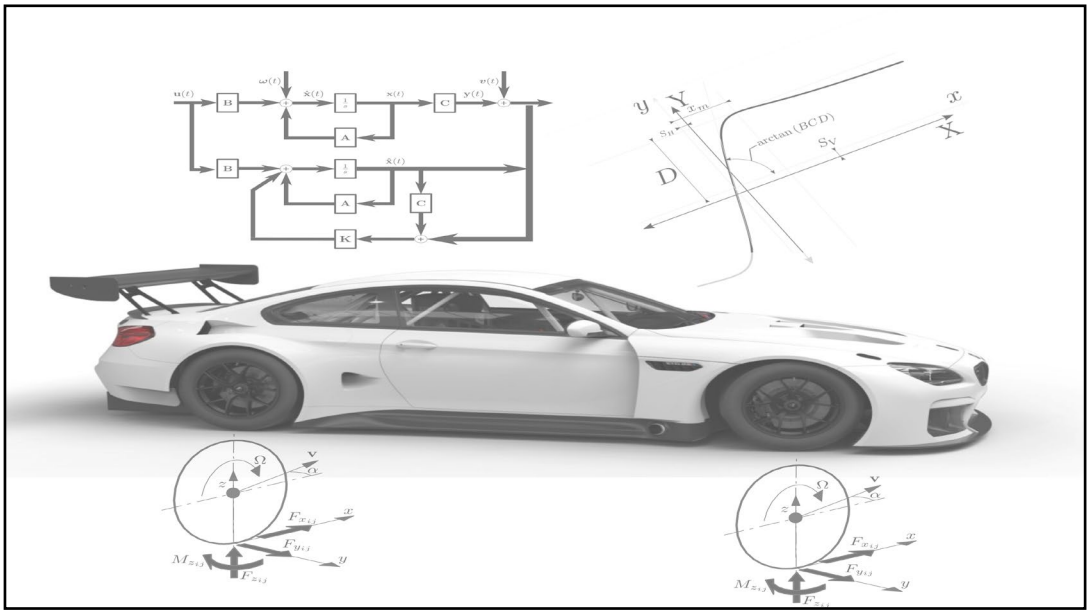

Soutenue le 13 juillet 2020
Spécialité : Automatique et Robotique : Unité de recherche Heudyasic (UMR-7253)

D2554

Robust estimation of dynamics behavior and driving diagnosis applied to an intelligent MAGV

Angel Gabriel ALATORRE VAZQUEZ

Spécialité : Automatique et Robotique

Thesis defended on 13th July 2020, before the jury composed of:

Jury president:

Michel BASSET
professeur des universités, Université de Haute-Alsace
IRIMAS UR7499

Jury members:

Valentin IVANOV
directeur de recherche, Techniche University Ilmeau

Mohammed CHADLI
professeur des universités, Université Paris-Saclay, IBISC laboratory

Reine TALJ
professeur des universités, Université de Technologie de Compiègne, Heudiasyc laboratory

Thesis advisors: Ali Charara

professeur des universités, Université de Technologie de Compiègne, Heudiasyc laboratory

Alessandro Correa-Victorino
professeur des universités, Université de Technologie de Compiègne, Heudiasyc laboratory

---

Université de Technologie de Compiègne
Heudiasyc UMR CNRS 7253
Labex MS2T

Droit devant soi, on ne peut pas aller bien loin.

Dedico este trabajo a mi hijo. Me haz hecho mas fuerte y feliz de lo que jamás podria haber imaginado. Te quiero de aqui a la luna.

Acknowledgements

I want to begin by extending heartfelt gratitude to each of my supervisors Ali Charara and Alessandro Victorino. For these three years of guidance, perseverance, and valuable time, the constant support and encouragement for this thesis work and other activities; the freedom and critiques made possible this work and shaped my character as a person.

I am grateful to the jury members for doing me the honors to evaluate my work. The reviewers for their valuable remarks and critiques of this manuscript. All the jury members for their valuable questions and comments.

I would like to thank the ITEAM project network, specially Prof. Ivanov and other early stage researchers of ITEAM, it has been great to live this adventure with all you by my side.

I would also like to thank European Commission and for LABEX MS2T, ROBOTEX financially supporting this project under the H2020 Grant agreement ITEAM No. 675999.

Finally, I would like to partially dedicate this work to my family, mother, and father, whose unconditional support kept me on track, and my little sisters always push me to be improve.

Abstract

The context of this thesis is the improvement of road safety through the development of active safety systems. One challenge in the development of active safety systems is obtaining accurate information about unmeasurable vehicle dynamic states. Specifically, the necessity to estimate the vertical load, frictional forces at each wheel (longitudinal and lateral), and also the sideslip angle at the center of gravity. These states are the critical parameters for optimizing the control of a vehicle's stability. If the vertical load on each tire can be estimated, then the risk of rollover can be evaluated. Estimating tire lateral forces can help to reduce lateral slip and prevent dangerous situations like spinning and drifting out the road. Tire longitudinal forces influence the performance of a vehicle. Sideslip angle is one of the essential parameters for controlling the lateral dynamics of a vehicle. However, the different technologies that the market offers, are no tbased on tire-ground forces due to the lack of cost-effective methods for obtaining the required information.

For the above mentioned reasons, we want to develop a system that monitors these dynamic vehicle states using only low-cost sensors. To accomplish our endeavor, we propose developing novel observers to estimate unmeasured states. Constructing an observer that met the reliability, robustness and accuracy requirements is not an easy task. It requires one the one hand, accurate and efficient models, and on the other hand, robust estimation algorithms that take into account variations in parameters and measurement errors. The present thesis has consequently been structured around the following two aspects: modeling of vehicle dynamics, and design of observers.

Under the heading of modeling, we propose new models to describe vehicle dynamics. Current models simplify the vehicle motion as a planar motion. In our proposal, our models describe vehicle motion as a 3D motion, including the effects of road inclination. Regarding vertical dynamics, we propose incorporating the suspension deflection to calculate the transfer of vertical load. Regarding lateral dynamics, we propose a model for the lateral forces transfer to describe the interaction between the left wheel and the right wheel. With this relationship, the lateral force on each tire is computed without using the sideslip angle. Similarly,

for longitudinal dynamics, we also propose a model for the transfer of longitudinal forces to calculate the longitudinal force at each tire.

Under the heading of observer design, we propose a novel observation system consisting of four individual observers connected in cascade. The four observers are developed for estimating vertical tire force, lateral tire force, longitudinal tire force, and sideslip angle, respectively. For the linear system, the Kalman filter is employed, while for the nonlinear system, the EKF applied to reduce estimation errors.

Finally, we implement our algorithm in an experimental vehicle to perform estimation in real-time, and we validate our proposed algorithm using experimental data.

Contents

List of figures

List of tables

Acronyms

ADAS: Advanced Driver Assistance Systems

CAN: Controller area Network

CNRS: Centre national de la recherche scientifique

COG: Center of Gravity

EKF: Extended Kalman Filter

EMBO: Euler Model Based Observer

ESC: Electronic Stability Control

GPS: Global positioning sysem

HIL: Hardware in the loop

IMU: Intertial measure Unit

ISO: Internation Standard organization

ITEAM: Interdisciplinary Training Network in Multi-Actuated Ground Vehicles

KF: Kalman filter

KU: Katholic University

LMI: Linear matrix inequality

LO: Luenberger Observer

LPV: Linear Parameter Varying

LQ: Linear Quadratic

LQR: Linear quadratic regulator

LS: Least squares

MF: Magic formula

MPC: model predictive control

MSE: Mean square error

NMSE: Normalized mean square error

NRMSE: Normalized root mean squared error

ONISR: Observatoire National Interministriel de la Sécurite Routière

PC: Personal computer

PSO: Particual swarm optimization

QMBO: Quaternion Model Based Observer

RLS: Recurseve least squares

RTK: Real-time kinematics

SMO: Sliding Modes Observer

TGF: Tire-ground force

TU: Technical University

UK: United Kingdom

UKF: Uncented Kalman filter

USA: United States of America

UTC: Universite de technologie de Compiegne

Introduction

1.1 Motivation

The early history of the automobile can be divided into few eras, based on the prevalent means of propulsion; later periods were defined by trends in exterior styling, size, and utility preferences. In 1769 the first steam-powered automobile capable of human transportation was built by Nicolas-Joseph Cugnot, see [Eckermann, 2001]. In 1885, Karl Benz developed a petrol/gasoline-powered automobile. This vehicle is the first "production" vehicle as Benz made several identical copies. In 1913, the Ford Model T became the first automobile to be mass-produced on a moving assembly line. By 1927, Ford had produced over 15 million model T automobiles; nowadays, the world vehicle population exceeded 1 billion units in 2010. One of the drawbacks of such success is vehicle collisions; today, standard automobiles can achieve high speeds, resulting in deadly crashes. Traffic crashes are the largest cause of injury-related deaths worldwide. In France, according to the latest statistic report of the ONISR (*Observatoire National Interministriel de la Sécurite Routière*) manifest that 58,352 accidents occurred in France in 2018, and a total of 3,488 deaths were the product of those accidents, see [ONI, 2018]. These fatalities and injuries are related to three principal types: single-vehicle crashes, multi-vehicle crashes, and rollovers. The report also states that human errors cause over 90% of all accidents.

The automotive industry has made significant improvements in the last decades, addressing passenger safety, driving quality, and energetic efficiency; recently, with the introduction of on-board automatic control systems, the leaps have increased exponentially. One example of this trend is the amount of first-event rollovers for single-vehicle crashes, which has decreased considerably. For instance, as reported in [Pai, 2017], in the USA, it went from 4.29% in 2004 to 2.61% in 2010. This decrease is the result of the introduction of the Electronic Stability Control (ESC) system. Also, vehicles equipped with Anti-lock Braking System and ESC, have 50% less probability of running off the road, see [Liu and Ye, 2011]. Within the scope

of active safety control systems and energy efficiency topics, the estimation of tire-ground contact forces has become an important research topic; knowledge of these forces can prevent over-steering or under-steering phenomena, leading to accidents.

1.2 Objective and contribution

Autonomous manufacturers are currently giving much interest to in-vehicle sensors and their intelligent system applications. The number of in-vehicle sensors is continuously increasing, given their proven benefits represented in avoided accidents, higher driving efficiencies, and ubiquitous sensing-based services. Each vehicle has from 60 to 100 sensors on board, and we can expect this number to grow as the car gets smarter. The industry projects 200 sensors installed on each vehicle, and the price range for a sensor installed on a mass-produced vehicle varies between 50 and 200 dollars.

Currently, sensors that measure tire-ground forces are available in the market. Nevertheless, their cost amounts to more than 100,000 euros; thus, their use for mass production automobile systems becomes prohibited. The introduction of observers to estimate these forces is an effective solution for this problem. However, providing accurate estimates of the tire-ground forces is considered a difficult task. The variation of vehicle mass, the center of gravity (COG), the load transfer effects, the road slope or bank angles, its irregularities, among others, increase the problem complexity considerably. Accurate knowledge of vehicle dynamics is essential to determine the wheel tire-ground forces with a level of accuracy suitable for the Advanced Driver Assistance Systems (ADAS). Motivated by this necessity of improving ADAS and safety controllers' performances, numerous research works have addressed the estimation of vehicle parameters and forces [Bae et al., 2001, Vahidi et al., 2005, Fathy et al., 2008, McIntyre et al., 2009, Han et al., 2009, Hong et al., 2015]. Conversely, on the side of energetic efficiency, recent vehicle controllers developed for fuel consumption reduction require an accurate estimation of the vehicle traction force [Hellström et al., 2009, Ganji et al., 2011, Khayyam et al., 2011, Shakouri and Ordys, 2014].

This dissertation's main contribution is the introduction of a tire-ground forces estimation scheme for vehicle states, tire-ground forces, and design parameters. The observers presented in this dissertation are based on vehicle models without requiring a tire-model and their respective parametric identification. Our proposal implements an observation scheme with sensors available for mass-produced vehicles.

1.3 Context of the research work

The entire work is completed at the HeuDiaSyc (“Heuristic et Diagnostic des Systèmes Complexes”) UMR 7253 CNRS Laboratory at the Computer Science Department of Université de Technologie de Compiègne (UTC) in France, under the supervision of Prof. Ali Charara and A.P. Alessandro Victorino.

Figure 1.1 – Experimental testbed: Dyna

This project has received funding from the European Commission under the H2020 Grant agreement ITEAM No. 675999. The ITEAM (Interdisciplinary Training Network in Multi-Actuated Ground Vehicles) program, see Figure 1.1, unites academic and industrial partners across Europe; the following organization form part of the ITEAM consortium:

- Academy: TU Ilmenau (Germany), Coventry University (UK), KU Leuven (Belgium), University of Pavia (Italy), Flanders Make (Belgium), UTC - The University of Technology of Compiègne (France), TU Delft (Netherlands), The University of Liverpool (UK), The Institute of Information Theory and Automation (Czech Republic), TU Graz (Austria), Chalmers University of Technology (Sweden), Tallinn University of Technology (Estonia).

- Industry: AVL List (Austria), Infineon (Germany), Škoda Auto (Czech Republic), Virtual Vehicle (Austria), Volvo Car Group (Sweden), IPG Automotive (Germany), Jaguar Land Rover (UK).

This work was also carried out in the framework of the Labex MS2T, (Reference ANR-11-IDEX-0004-02) and the Equipex ROBOTEX (Reference ANR-10-EQPX-44-01) which were funded by the French Government, through the program "Investments for the future” managed by the National Agency for Research.

1.4 Publications

A. Alatorre, A. Victorino, A. Charara; *Robust Multi-Model Tire-Ground Force Estimation Scheme*, in IEEE Transactions on Intelligent Vehicles, vol. 3, no. 4, pp. 486-500. 2018

E. Regolin and **A. Alatorre** and M. Zambelli and A. Victorino and A. Charara and A. Ferrara *A Sliding Mode Virtual Sensor for Wheel Forces Estimation with Accuracy Enhancement via EKF*, in IEEE Transactions on Vehicular Technology. 2019

Valentin Ivanov et al *Challenges of Integrated Vehicle Chassis Control: Some Findings of the European Project EVE*, in IEEJ Journal of Industry Applications, vol. 8, no. 2. 2019

A. Alatorre, A. Victorino, A. Charara *Estimation of Wheel-Ground Contact Normal Forces: Experimental Data Validation* 20th International Federation of Automatic Control World Congress (IFAC WC 2017), vol. 50, num. 1, pp. 14843-14848. Toulouse, France 2017

M. Acosta, **A. Alatorre**, S. Kanarachos, A. Victorino, A. Charara *Estimation of tire forces, road grade, and road bank angle using tire model-less approaches and Fuzzy Logic*. 20th International Federation of Automatic Control World Congress (IFAC WC 2017), vol. 50, num. 1, pp. 14836-14842. Toulouse, France 2017

A. Alatorre, A. Victorino, A. Charara *Robust Multi-Model Longitudinal Tire-force Estimation Scheme: Experimental Data Validation* 20th IEEE International Conference on Intelligent Transportation Systems (ITSC 2017). Yokohama, Japan 2017

A. Alatorre, A. Victorino, A. Charara *Sideslip estimation algorithm comparison between Euler angles and quaternion approaches with black box vehicle model*, IEEE 15th International Workshop on Advanced Motion Control (AMC 2018). Tokyo, Japan 2018

S. Mcbride, **A. Alatorre**, C. Sandu, A. Victorino *Estimation of Vehicle Tire-Road Contact Forces: A Comparison between Artificial Neural Network and Observed Theory Approaches*, Published by SAE International in United States. Detroit, U.S.A 2018

1.5 Experimental Vehicle-Infrastructure

1.5.1 Dyna308

Our experimental vehicle known as Dyna308 is instrumented by the laboratory heudiasyc UMR 7253 CNRS at Compiègne, France, see Figure 1.2. The baseline vehicle is a Peugeot 308sw. This car is additionally instrumented with transducers to

Figure 1.2 – Experimental testbed: Dyna

measure dynamic vehicle states. The sensors installed in our vehicle are validation sensors, input sensors, and exteroceptive sensors.

1.5.1.1 Validation sensors

- CORREVIT S-400: It is a non-contact optical sensor that measures the transversal dynamics at large operating ranges. The sensor is installed at the place of the spare wheel under the car it returns the measurement of transversal speed, $v_g = \sqrt{v_x^2 + v_y^2}$, and sideslip angle, β (see Figure 1.3(a)). The cost of this sensor is around 8,000 €.

- Kistler RoaDyn S625 wheel force transducers: four-wheel force sensors for passenger cars RoaDyn (Kistler) are fixed at each wheel, see Figure 1.3(b). They measure the forces and torques at the tire for its three axes (x, y, z), it also offers an accurate measurement of the wheel angular speed. The cost of a single Kysler sensor is around 120,000 €.

- GPS receiver operating in RTK mode locates the vehicle with a centimeters accuracy.

1.5.1.2 Input sensors

- Sensor CROSSBOW VG700AB: An inertial measurement unit designed specifically for automotive test applications. It combines MEMSIC's high-performance fiber optic gyros with silicon micro-machined accelerometer technology to provide a highly accurate Vertical Gyro. The location of this sensor is at the trunk.

(a) Correvit Sensor (b) Kysler Sensor

Figure 1.3 – Validation sensors

- CORRSYS-DATRON HT500: This transducer is an optical device that measures the distance between chassis and ground. They are installed respectively at each vehicle corner; see Figure 1.4(a).
- Sensor WAYCON SX50: These sensors are installed at the suspension, see Figure 1.4(b); these sensors can measure the deflection of the suspension, emulating the distance between the sprung and unsprung masses.
- Other sensors available through CAN bus are the wheel rotation velocity, the engine speed, the yaw rate, the brake pressure, the lateral and longitudinal acceleration, and the steering wheel angle.

1.5.1.3 Exteroceptive sensors

- A scenario record camera is used to register the vehicle trajectory.
- Mobileye system: It provides a list of detected obstacles (pedestrians, vehicles, etc.) and their position relative to the vehicle in real-time.
- Ibeo Standard (8L) Eight Layer/Multi-Echo Lux Sensor (Ibeo LUX 8L): the sensor is installed at the front bumper to track the object on the top 4 layers and raw data ground scanning/profiling (see Figure 1.4(c)).
- All the electronics systems and PC are located in the trunk, see Figure 1.4(d).

The complete vehicle architecture is presented in Appendix A.

1.5.2 Flanders Make evoque

This works has been made in collaboration with Flanders Make. They allow us to use data from its testing platform, see Figure 1.5. The main peculiarity of this

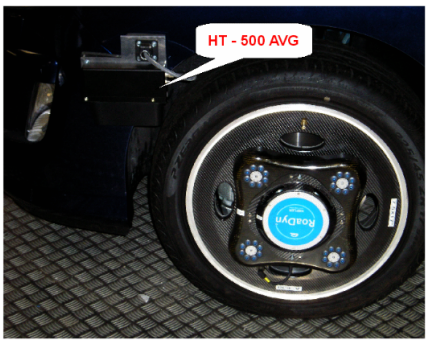

(a) Laser Sensor

(b) Deflection Sensor

(c) Front laser

(d) Computer

Figure 1.4 – Validation sensors

vehicle is that the combustion engine of a Range Rover evoque is replaced by an electrical drivetrain with four independent electrical motors.

Figure 1.5 – Land Rover Evoque experimental testbed at Flander Make

The technical specification of this vehicle is

- Fully electric vehicle.
- Four individual drivetrains and in-house developed battery pack.
- Individual wheel drive control: Four x switched reluctance motor.
- Individual wheel friction brake control: Slip Control Boost unit.
- Steer-by-Wire
- dSPACE rapid prototyping platform and Nvidia drive PX2 360° sensors for environment perception by:
  - 6 camera's
  - 6 Lidars
  - 6 radars
  - 12 ultrasound sensors
- V2X communication capabilities
- Throttle and brake by wire

1.6 Thesis structure

This dissertation has seven chapters: The organization is as follows:

- **Chapter 2: Modeling preliminaries.** This chapter presents the most common models used to estimate tire-ground forces and sideslip angle, and the models used as the base for our estimation schemes.
- **Chapter 3: Lateral speed estimation.** This chapter shows the use of a kinematic model to estimate the lateral speed; first, we discuss the reason for using a kinematic model; second, an adaptation of a kinematic model with gravity compensation with quaternions. The method selected to use the estimation is the Kalman filter.
- **Chapter 4: Normal tire-ground force estimation.** This chapter shows the challenges to estimate normal TGFs. We perform the tire-ground forces estimation using vehicle dynamics and the suspension model to enhance robustness and accuracy.
- **Chapter 5: Longitudinal and lateral tire-ground force estimation: Part 1.** This chapter shows one proposed methodology to estimate the longitudinal and lateral TGFs; based on two lumped models and a Kalman filter implementation to built a close loop observer.
- **Chapter 6: Longitudinal and lateral tire-ground force estimation: Part 2**. This chapter presents a second proposal to estimate the longitudinal and lateral TGFs; this model bases the tire-ground forces' computation on local accelerations and equivalent masses, thus, do not require any vehicle, neither a tire model.
- **Chapter 7: Application of TGFs estimation to enhance vehicle subsystem controllers.** In this chapter, the TGFs estimation application improves the performance of a road profile estimator and a closed-loop controller for an active suspension system.
- **Chapter 8: Conclusions.** This is the last chapter of this thesis, here we present the conclusions, perspectives, and future work for our research group.

Modeling preliminaries

Contents

2.1 Introduction

In recent years, an essential share of automotive research aims to improve active safety systems and energy efficiency. Vehicle dynamics research stands out since knowing the car behavior allows engineers to increase their grades in certain performance indexes, such as maneuverability, comfort, and road holding. The tire-ground interaction forces significantly influence the vehicle's longitudinal and lateral dynamics; these forces trigger the vehicle's movement from a physical perspective. Thus, an accurate estimation of such effects will improve several vehicle subsystems' effectiveness, like braking, steering, electronic stability, or comfort. The vehicle dynamics estimation methods associate a tire model, a vehicle model, and an observer technique. Then, the knowledge about the dynamics of the tires and vehicle body is essential. This chapter shows the background of tire-ground forces formulations, vehicle models, and suspension subsystem models as the advantages and drawbacks of each model.

2.2 Important parameters and variables

This section is an introduction to vehicle dynamics with an emphasis on the influence of tire properties. We discuss the steady-state cornering behavior of simple automobile models and the transient motion after small and large steering inputs and other disturbances. The effects of various shape factors of tire characteristics, see Figure 2.1, on vehicle handling properties, will be analyzed. The slope of the side force, F_y, versus sideslip angle, α, near the origin (the cornering stiffness) is the determining parameter for the basic linear handling and stability behavior automobiles.

Let us consider a free-rolling wheel over a flat road along a straight line without any sideslip angle, $\alpha = 0$, a small pulling force is needed to overcome the rolling resistance[1] present at the tire, also a side force, and an aligning torque could appear due to the asymmetrical structure of the tire when the zero-slip condition occurs other tire deformations accompanied by sliding section in the contact patch. Thus, this results in the generation of more tire ground forces.

Figure 2.1 shows a wheel turning with an angular speed Ω, with a linear velocity v with two components, a longitudinal $v_x = || \mathbf{v} ||_2 \cos\alpha$, and a lateral component $v_y = || \mathbf{v} ||_2 \sin\alpha$; where $|| \mathbf{v} ||_2$ is the 2-norm of the velocity vector $\mathbf{v}$. These velocity

[1] Rolling resistance is the force resisting the motion when the wheel rolls on a surface. Non-elastic effects mainly cause it. Several factors increase the magnitude of the rolling resistance: wheel radius, forward speed, surface adhesion, and relative micro-sliding.

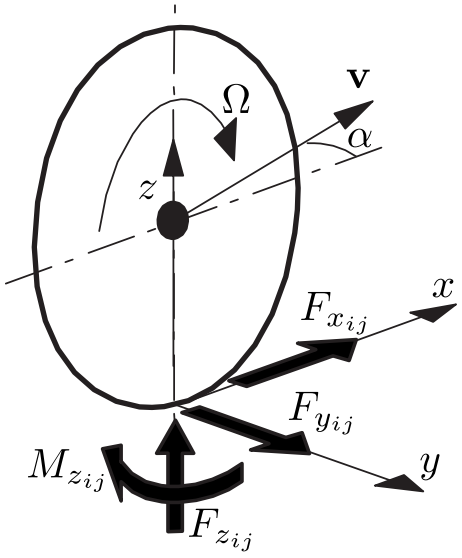

Figure 2.1 – Slip angle and force and moment positive directions

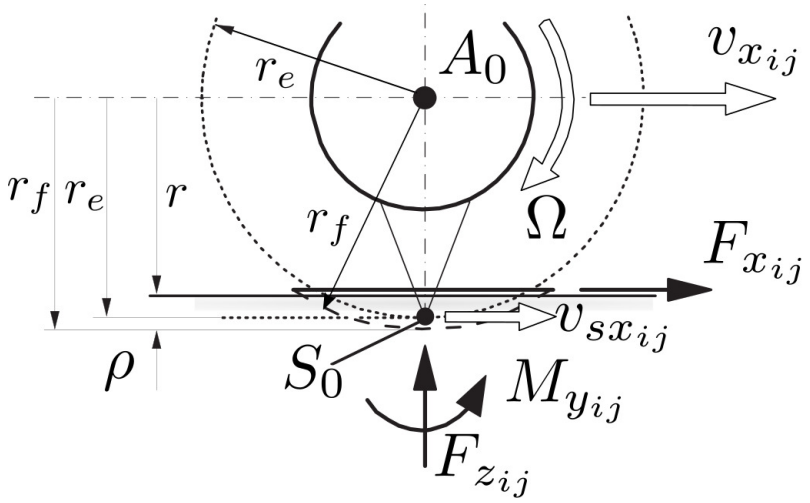

Figure 2.2 – Effective rolling radius and longitudinal slip velocity.

components are related by to the sideslip angle, α.

For the freely rolling wheel, we can measure the forward speed v_x (a component of the velocity vector **v** at the wheel center) and the tire's angular speed Ω_0 and compute the effective rolling radius, r_e, given by the ratio of both quantities:

$$r_e = \frac{v_x}{\Omega_0}$$

The radial deflection of the tire, ρ, is defined as the reduction of the radius from the unloaded situation, r_f, to the loaded scenario, r:

$$\rho = r_f - r$$

To properly define the longitudinal slip, the slip point S is introduced, see Figure 2.2. This point is attached to the rim or wheel body at a radius equal to the slip radius r_e and forms the center of rotation when the wheel rolls at a longitudinal slip equal to zero. Figure 2.3 shows several planes on a wheel to improve the reader's understanding; the figure shows the wheel, road, and normal-to-road planes; notice the camber, γ, and the sideslip angle, α. The velocity vector origin is the center of the wheel, A_0. Also, at the zero-slip condition, the longitudinal speed, v_x is:

$$v_x = r_e \Omega \tag{2.1}$$

Notice that $\Omega \neq \Omega_0$, Ω_0 is the free-rolling angular speed of the wheel, and Ω is the wheel speed produced by a torque input. Thus, when the longitudinal slip is no longer zero, and if $\gamma\dot{\psi} = 0$ holds, it is possible to define:

$$v_{sx} = v_x - r_e \Omega$$

since $\gamma\dot{\psi} = 0$; if a camber angle exists, the vehicle does not have a yaw rate, and backward, if there is a yaw rate different to zero, the camber angle is equal to zero. The longitudinal slip is denoted by κ and stands for the ratio between the longitudinal slip velocity, v_{sx} and the forward speed of the wheel center v_x:

$$\kappa = -\frac{v_{sx}}{v_x}$$

Remember this holds for a wheel on a flat road with $\gamma\dot{\psi} = 0$. The slip angle α, which for a wheel, not showing camber rate $\dot{\gamma} = 0$, nor radial deflection rate, $\dot{\rho} = 0$ and yaw rate $\dot{\psi}$ at nonzero camber angle γ; also when running on a flat road, is defined as the ratio of the lateral and forward speed at the wheel center A_0:

$$\tan \alpha = -\frac{v_y}{v_x} \tag{2.2}$$

2.3 Tire Models

Tire models are usually classified according to their formulation in two major groups: physical and empirical models. On the one hand, physics-based models characterize the tire-ground interactions deterministically, using equations based on physics laws. It is assumed that the tire-ground force generation follows physical principles such as adhesion, elastic deformation, and friction forces. On the other

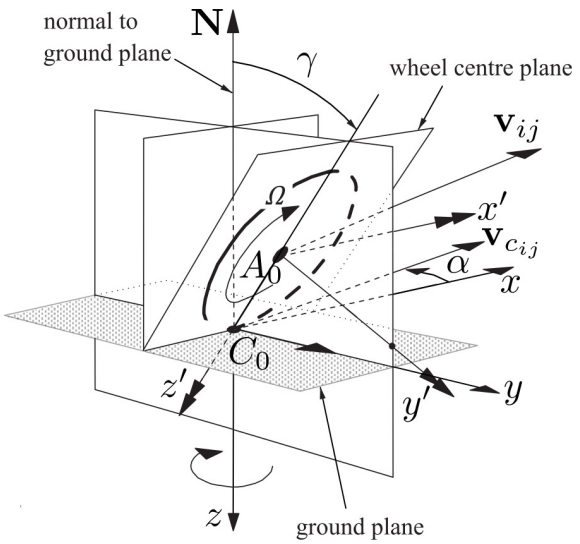

Figure 2.3 – Definition of position, attitude, and motion of the wheel and the forces and moments acting from the road on the wheel

hand, empirical models are based on experimental data; the most popular approach is the Magic Formula.

Finite element models belong to the physics-based group; they consider the tire's composite materials structure and its constitutive elements' nonlinear properties. The main backlash of finite element formulations is its computational cost that limits its use in real-time applications. Several companies have developed tire models, and such formulations take into account complex phenomena, such as the temperature, its compounding materials, to predict the tire-ground forces. Vehicle dynamics simulation software implements these models in emulation environments as Hardware in the loop (HIL); nevertheless, there is no evidence pointing towards the model convenience for embedded applications of vehicle state estimation. Researchers also have developed simpler physical models to compute tire-ground forces; they introduce simplifications regarding the force generation mechanism at the contact patch. The main differences between these approaches depend on the considerations taken during the model development process while maintaining a reduced computational burden. The most popular approaches that fall into this category are the brush, Dugoff, and linear tire models.

On the other hand, to avoid errors induced by physical models without considerably increasing the computational burden, empirical experimental-data based models have been developed. The Magic Formula is based on a complex nonlinear function's parameterization to fit bast amounts of experimental data. Several variants of this model have been proposed during the last years, and MF-Tire is a commercial model developed by Delft-Tire and is based on the standard Pacejka

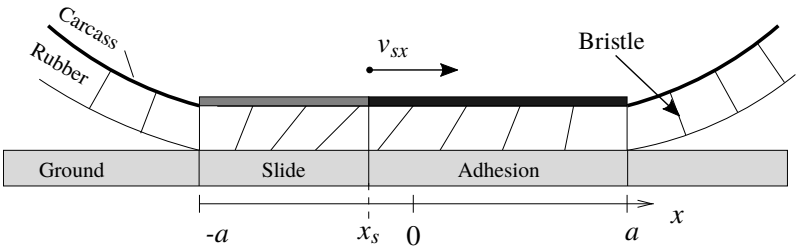

Figure 2.4 – Deformation of the rubber layer between the tire carcass and the road according to the brush model

formulation. MF-Swift is an extension of the standard Magic Formula that provides enhanced results when modeling the tire's behavior at high frequency, especially for comfort and vibrational analysis.

2.3.1 Brush Tire Model

The brush model assumes that the slip occurs due to the rubber material's deformation between the carcass and the ground. The technique proposes to model the material as small bristles attached to the carcass; see Figure 2.4. Every brush element can deform independently of the other. Three different phenomena at the contact patch may occur:

- Adhesion occurs in the entire contact area. The slip curves depend only on the rubber properties.
- Sliding and adhesion. Two sections divide the contact area, one with pure adhesion and the other with pure sliding, see Figure 2.4 the sections are divided at point x_s.
- The entire surface slides against the ground.

The development of the brush tire model is similar to the longitudinal and lateral tire-ground forces. In the following two subsections are created to deal with each one of these phenomena separately.

2.3.1.1 Longitudinal force-slip model

To develop the brush tire model, we divide the tire into its composing elements, the bristles, and study its particular behavior; thus, a brush element k comes in contact with the road at time $t = t_0$ and position $x = a$. The position can be defined either by the bristles' upper point or by its lower point, as illustrated in Figure 2.5. First,

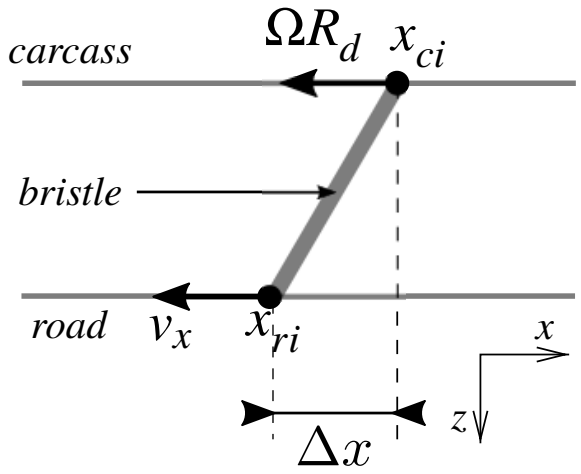

Figure 2.5 – The relative velocity and the position of upper and lower point of a brush element.

let us consider a bristle in the adhesion region; its position is defined by:

$$\begin{aligned} x_{ck} &= a - \int_{t_0}^{t} \Omega r_e dt \\ x_{rk} &= a - \int_{t_0}^{t} v_x dt \end{aligned} \tag{2.3}$$

where a is half of the length of the contact patch in the longitudinal direction, Ω, r_e and v_x have been already defined at equation (2.1). From Figure 2.5, the deformation of k^{th} element is defined as:

$$\Delta x_k = x_{ck} - x_{rk} = \int_{t_0}^{t} (v_x - \Omega r_e) dt = \int_{t_0}^{t} v_{sx} dt$$

If constant velocity is assumed, gives

$$\Delta x_k = \frac{v_{sx}}{\Omega r_e}(a - x_{ck}) = \frac{v_{sx}}{v_x}(a - x_{rk})$$

The force produced from such a deformation is

$$F_{xk} = m_x \Delta x_k$$

Is widely known that the longitudinal tire-ground force F_{xk} is constrained by the friction, μ, present at the tire-road and the tire-ground normal force, F_{zk}, acting on the i brush element, given by

$$F_{xk,max} = \mu F_{zk}$$

thus, the maximum deformation is:

$$\Delta x_{i,max} = \frac{\mu F_{zk}}{k}$$

The brush element starts to slide when the deformation reaches $\Delta x_{k,max}$. When both adhesion and sliding occurs at the contact patch, it is possible to compute the exact position where the sliding section begins

$$x_{cks} = \frac{\mu F_{zk} \Omega R_d}{v_{sx} k} - a = \frac{\mu F_{zk}}{k s_x} - a \tag{2.4}$$

Finally, if we sum-up the forces generated by all the bristles within the contact patch, gives:

$$F_x = \int_{x_s}^{a} c_{px} \frac{v_{sx}}{\Omega r_e}(a - x_c) dx_c + \int_{-a}^{x_s} q_z(x_c) \mu dx_c \tag{2.5}$$

with $m_x = c_{px} dx_c$ and $F_{zi} = q_z(x_c) dx_c$, where c_{px} denotes the stiffness per length unit and q_z means the vertical force per length unit between tire and road. The vertical pressure is assumed to have a parabolic distribution, then

$$q_z(x_c) = \frac{3\mu F_z}{4a}\left(1 - \left(\frac{x_c}{a}\right)^2\right) \tag{2.6}$$

To solve (2.5) is necessary to find the breakaway point, x_s, thus similarly as in eq. (2.4) we have

$$c_{px} \frac{v_{sx}}{\Omega r_e}(a - x_s) = \mu q_z(x_s)$$

and after some algebraic manipulation

$$x_s = \frac{4 a c_{px} s_x - 3 a \mu F_z}{3 \mu F_z} \tag{2.7}$$

Solving (2.5) for the pressure distribution given in (2.6), and evaluating the integral with the breaking point (2.7), gives

$$F_x = 2 c_{px} a^2 s_x - \frac{4}{3}\frac{(c_{px} a^2 s_x)^2}{\mu F_z} + \frac{8}{27}\frac{(c_{px} a^2 s_x)^3}{(\mu F_z)^2} \tag{2.8}$$

Thus, the longitudinal tire-ground force is computed with (2.5), and eq. (2.8) is valid for the following longitudinal slip range

$$0 \leq s_x \leq \frac{3\mu F_z}{2 c_{px}}$$

the slip that produces the maximum longitudinal tire-ground force is

$$s_x^* = \frac{3\mu F_z}{4c_{px}}$$

nonetheless, for $s_x > \frac{3\mu F_z}{2c_{px}}$ the longitudinal force is simply governed by $F_x = \mu F_z$.

2.3.1.2 Lateral force-slip model

For the lateral tire-ground force development, the strategy is similar that for the longitudinal force, the main differences rely on the k^{th} bristle deformation definition, thus:

$$\Delta y_k = (x_k - a)\tan(\alpha_k)$$

and the force produced for such deformation is

$$F_{yk} = m_y \Delta y_k$$

the lateral force of that bristle is constrained by the friction and normal force at the k^{th} bristle, as follows

$$F_{yk,max} = \mu F_{zk}$$

analogously to the longitudinal force, the lateral tire-ground force response from the brush model is:

$$F_y = \int_{-a}^{x_s} q_z(x_c)\mu dx_c + \int_{x_s}^{a} c_{py}\tan(\alpha)(a - x_c)dx_c \tag{2.9}$$

Solving (2.9) with the pressure distribution (2.6) and the breakaway point (2.7), gives

$$F_y = 2c_{py}a^2\tan(\alpha) - \frac{4}{3}\frac{(c_{py}a^2\tan(\alpha))^2}{\mu F_z} + \frac{8}{27}\frac{(c_{py}a^2\tan(\alpha))^3}{(\mu F_z)^2} \tag{2.10}$$

Thus, the longitudinal tire-ground force is computed with (2.9), nonetheless the solution eq. (2.10) gives a valid response withing the sideslip angle range:

$$0 \leq \tan(\alpha) \leq \frac{3\mu F_z}{2c_{py}}$$

for $\frac{3\mu F_z}{2c_{py}} < \tan(\alpha) \leq \frac{\pi}{2}$ the longitudinal tire-ground force is governed by $F_y = \mu F_z$.

2.3.2 Dugoff tire model

The Dugoff tire model provides a method to compute the longitudinal and lateral forces in different situations as pure cornering, pure longitudinal acceleration, or combined maneuvers. This approach considers uniform vertical pressure distribution at the tire contact patch. The advantages of this approach are:

- The Dugoff tire model represents the tire-ground forces nonlinear dynamics.
- The Dugoff tire model represents the tire-ground forces at combined slips (lateral and longitudinal).

Hence, it is widely used when the tire forces are intervened in the vehicle control or estimation system. In extensive literatures such as [Zhang et al., 1998, Dakhlallah et al., 2008, Boyden and Velinsky, 1994, Smith and Starkey, 1995] [Dakhlallah et al., 2008, Zhang et al., 1998], the Dugoff model is adopted for its simplicity and efficiency. The Dugoff tire model can also be used to calculate lateral and longitudinal forces, either for pure-slip or combined-slip conditions [Ding and Taheri, 2010]. The longitudinal force is:

$$F_{x_{ij}} = C_{s_{ij}} \frac{s_{ij}}{1 + s_{ij}} f(\lambda) \tag{2.11}$$

and the lateral forces is:

$$F_{y_{ij}} = C_{\alpha_{ij}} \frac{\alpha_{ij}}{1 + s_{ij}} f(\lambda) \tag{2.12}$$

with s_{ij} and α_{ij} represent the longitudinal slip ratio and the sideslip angle. Where

$$s_{ij} = \frac{v_{x_{ij}} - r_{e_{ij}}\Omega}{v_{x_{ij}}}$$

$$\alpha_{ij} = \arctan\left(\frac{v_{y_{ij}}}{v_{x_{ij}}}\right)$$

the suffixes $i, j \in \mathcal{A} := \{1, 2\}$ help to describe an effect in a particular tire, i.e. α_{11} stands for the front-left wheel slip angle. Notice that the equations presented in this section are defined in the ij^{th} wheel frame of reference. The function $f(\lambda)$ is defined as

$$f(\lambda) = \begin{cases} \lambda(2 - \lambda) & \lambda \leq 1 \\ 1 & \lambda > 1 \end{cases}$$

with

$$\lambda = \frac{\mu_{ij} F_{z_{ij}} (1 + s_{ij})}{2\sqrt{(C_{s_{ij}} s_{ij})^2 + \left(C_{\alpha_{ij}} \tan(\alpha_{ij})\right)^2}}$$

The function $f(\lambda)$ acts as a constraint to limit the longitudinal and lateral force responses for (2.11) and (2.12) and for this case μ_{ij} stands for the local friction and $F_{z_{ij}}$ means the normal tire-ground force at the ij^{th} tire.

2.3.3 Linear Tire Model

The most simple tire model description is the linear tire model. The tire's dynamic properties are derived from the longitudinal slip, sideslip angle, normal tire-ground force, and maximum road friction coefficient. On the one hand, the linear relationship to compute the longitudinal tire-ground force is:

$$F_{x_{ij}} = C_{s_{ij}} (s_{ij} + S_H) + S_V \tag{2.13}$$

with S_H and S_V are the horizontal and vertical shifts, $C_{s_{ij}}$ represents the longitudinal tire stiffness; $C_{s_{ij}}$ depends on the wheel load, $F_{z_{ij}}$, and the tire-road friction, $\mu_{x_{ij}}$. Also, the longitudinal tire stiffness is:

$$C_{s_{ij}} = \lim_{s_{ij} \to 0} \left(\frac{\partial F_{x_{ij}}}{\partial s_{ij}} \right)$$

On the other hand, the lateral tire-ground force linear representation is:

$$F_{y_{ij}} = C_{\alpha_{ij}} \alpha_{ij} + S_V \tag{2.14}$$

where

$$\begin{aligned} \alpha_{1,j} &= \delta_j - \beta_{1j} + S_H \\ \alpha_{2,j} &= -\beta_{2,j} + S_H \end{aligned} \tag{2.15}$$

with S_H and S_V are already defined, and $C_{\alpha_{ij}}$ means the tire cornering stiffness; analogously to (2.13), $C_{\alpha_{ij}}$ depends on the wheel load and the tire-road friction, $\mu_{y_{ij}}$, and the normal tire-ground force. Finally, δ_j stands for the steering angle for the left or right wheel respectively. Also,

$$\beta_{ij} = \arctan \left(\frac{v_{y_{cog}} + (-1)^i l_i \dot{\psi}}{v_{x_{cog}} + (-1)^j e_j \dot{\psi}} \right) \tag{2.16}$$

and

$$C_{\alpha_{ij}} = \lim_{\alpha_{ij} \to 0} \left(\frac{\partial F_{y_{ij}}}{\partial \alpha_{ij}} \right)$$

Notice that the definition for the sideslip angle, α_{1j}, is given from the vehicle body

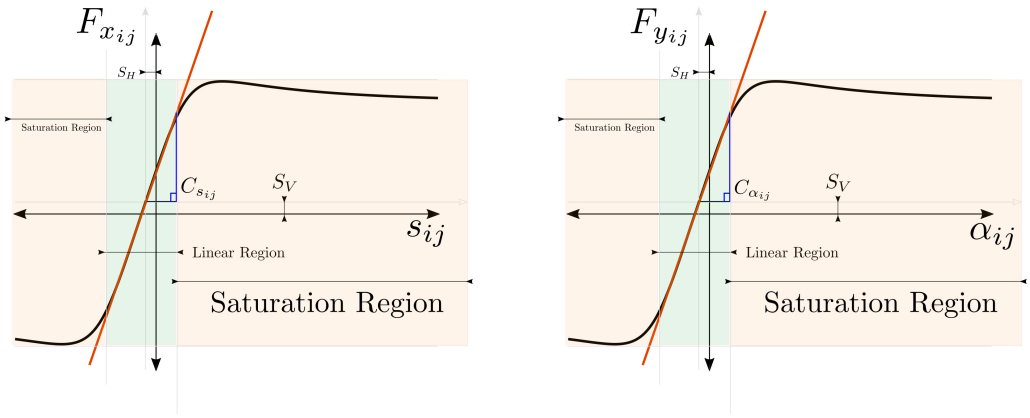

(a) Equation (2.13) response (b) Equation (2.14) response

Figure 2.6 – Operation Region of equations (2.13) and (2.14)

frame of reference placed at the center of gravity. Figure 2.6 shows the region in which eqs. (2.13) and (2.14) are valid. With a black-solid line, this figure shows the actual tire-ground force trough all the domain and, on the other hand, with a red-solid line depicts the response of eq. (2.14). Notice in green color, this figure portrays the actual linear region, while in pink color depicts the saturation region. An automobile's operation domain is mainly within the linear region; nevertheless, most of the lane departure accidents occur while performing on the non-linear region.

2.3.4 Magic Formula Tire Model

A widely used semi-empirical tire model to calculate tire-ground force and moment characteristics for vehicle dynamics studies is known as Magic Formula. The development of this model started as a joint venture between Volvo and TU-Delft in the mid-eighties. Several versions were developed through the years [Bakker et al., 1987, Bakker et al., 1989, Pacejka and Besselink, 1997a]. In these models, the combined slip situation is modeled from a physical viewpoint. In 1993, Michelin introduced a purely empirical method using Magic Formula-based functions to describe the tire horizontal force generation at a combined slip. This approach has been adopted in subsequent versions of the Magic Formula Tire Model.

The general form of the formula holds for given values of vertical load and camber angle is the set

$$\begin{aligned} Y(X) &= y(x) + S_V \\ y(x) &= D \sin\left[C \arctan\{Bx - E\left(Bx - \arctan Bx\right)\}\right] \\ x &= X + S_H \end{aligned} \tag{2.17}$$

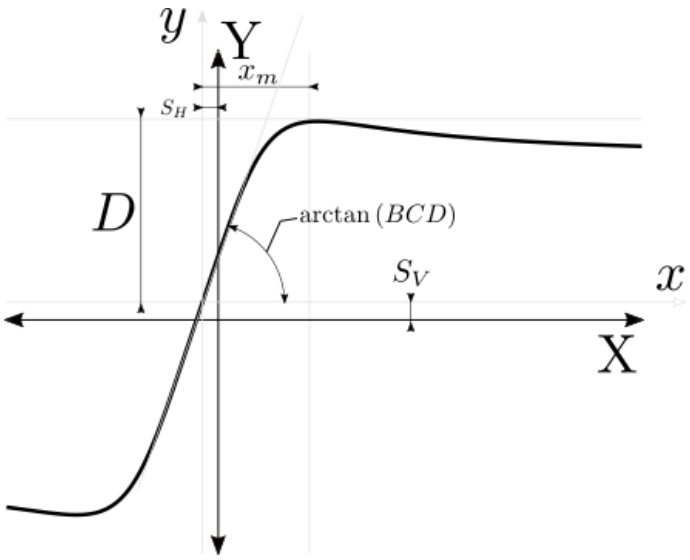

Figure 2.7 – Curve produced by the original sine version of the Magic Formula, Eqn (2.17). The meaning of curve parameters has been indicated.

where $Y(X)$ is the output variable $F_{x_{ij}}$, $F_{y_{ij}}$ or $M_{z_{ij}}$ and X stands for the input variable $\tan(\alpha_{ij})$ or κ_{ij}, and B is the stiffness factor, C the shape factor, D the peak value, E the curvature factor, S_H, and S_V are the horizontal and vertical shifts. The Magic Formula (2.17) typically produces a curve that passes through the origin $x = y = 0$, reaches a maximum, and subsequently tends to a horizontal asymptote. A new set of coordinates arises, see Figure 2.7. The formula is capable of producing characteristics that match measured curves for the lateral force $F_{y_{ij}}$ and for the longitudinal force $F_{x_{ij}}$ as functions of their respective slips: the sideslip angle, α, and the longitudinal slip, κ, with the effect of load, $F_{z_{ij}}$, and camber angle, γ, included in the parameters.

Figure 2.7 illustrates the meaning of some of the factors using a typical side force characteristic. The product BCD corresponds to the slope at the origin ($x = y = 0$). The shape factor C controls the range limits of the sine function appearing in formula (2.17) and thereby determines the shape of the resulting curve. The factor B is left to determine the slope at the origin and is called the stiffness factor. The factor E controls the curvature at the peak and, at the same time, the peak's horizontal position. The offsets S_H and S_V appear to occur when ply-steer[2], conicity[3] effects or possibly the rolling resistance cause the $F_{y_{ij}}$ and $F_{x_{ij}}$ curves not to pass through the origin. Wheel camber may give rise to a large offset of the $F_{y_{ij}}$ versus α_{ij} curves. Such a shift may be accompanied by a significant

[2]Ply steer describes the lateral force a tire generates due to asymmetries in its carcass as it rolls forward with zero slip angle and may be called pseudo side slip.

[3]Conicity is a parameter based on lateral force behavior. It is the characteristic that describes the tire's tendency to roll like a cone.

Table 2.1 – Main Components of the Magic formula for the longitudinal tire-ground force computation (2.18)

Coefficient	Name	Formula
C	Shape factor	$C = b_0$
D	Peak factor	$D = F_{z_{ij}} \left(b_1 F_{z_{ij}} + b_2\right)$
BCD	Stiffness	$BCD = (b_3 F_{z_{ij}}^2 + b_4 F_{z_{ij}}) e^{-b_5 F_{z_{ij}}}$
B	Stiffness factor	$B = BCD/(CD)$
E	Curvature factor	$E = \left(b_6 F_{z_{ij}}^2 + b_7 F_{z_{ij}} + b_8\right)(1 - b_1 3\text{sign}(s_{ij} + S_H))$
S_H	Horizontal Shift	$S_H = b_9 F_{z_{ij}} + b_{10}$
S_V	Vertical Shift	$S_V = b_{11} F_{z_{ij}}$
B_s		$B_s = B\,(s_{ij} + S_H)$

deviation from the original curve's pure anti-symmetric shape.

In the following two subsections, the magic formula parameters are defined for the longitudinal and lateral directions.

2.3.4.1 Longitudinal Tire-Ground Force

From (2.17) is easy to obtain the formula to compute the longitudinal tire-ground force, thus:

$$F_{x_{ij}} = D \sin\left[C \arctan\{B_s - E \arctan\left(B_s - \arctan\left(B_s\right)\right)\}\right] + S_V \tag{2.18}$$

with elements D, C, B_s, E, and S_v defined in Table 2.1. Table 2.2 presents the formulas to derive the main components from coefficients $b_0, b_1, ...b_{13}$, including its nominal values, and its ranges. The main components are b_0 known as shape factor, b_2 as the longitudinal friction coefficient, b_4 is the change of stiffness related to the slip, and b_8 the curvature factor. The inputs are the friction coefficient, the normal tire-ground force in kilo-Newtons, and the longitudinal slip (value between 0 and 100).

2.3.4.2 Lateral Tire-Ground Force

The formula to compute the longitudinal tire-ground force from (2.17) is:

$$F_{y_{ij}} = D \sin(C \arctan\left(B_\alpha - E \arctan\left(B_\alpha - \arctan\left(B_\alpha\right)\right)\right)) + S_V \tag{2.19}$$

Table 2.2 – Components require to form the (2.18)

Param.	Role	Typical range	Nom. Value
b_0	Shape factor	1.4 ... 1.8	1.5
b_1	Load influence on longitudinal friction coefficient	-80 ... +80	0
b_2	Longitudinal friction coefficient	900 ... 1700	1000
b_3	Curvature factor of stiffness/load	-20 ... +20	0
b_4	Change of stiffness with slip	100 ... 500	300
b_5	Change of progressiveness of stiffness/load	-1 ... +1	0
b_6	Curvature change with square load	-0.1 ... +0.1	0
b_7	Curvature change with load	-1 ... +1	0
b_8	Curvature factor	-20 ... +1	-2
b_9	Load influence on horizontal shift	-1 ... +1	0
b_{10}	Horizontal shift	-5 ... +5	0
b_{11}	Vertical shift	-100 ... +100	0
b_{12}	Vertical shift at load = 0	-10 ... +10	0
b_{13}	Curvature shift	-1 ... +1	0

Table 2.3 – Main Components of the Magic formula for the lateral tire-ground force computation (2.19)

Coefficient	Name	Formula
C	Shape factor	$C = a_0$
D	Peak factor	$D = F_{z_{ij}} \left(a_1 F_{z_{ij}} + a_2\right) (1 - a_{15}\gamma^2)$
BCD	Stiffness	$BCD = (a_3 \sin(\arctan(F_{z_{ij}})2)(1 - a_5 \mid \gamma \mid)$
B	Stiffness factor	$B = BCD/(CD)$
E	Curvature factor	$E = \left(a_6 F_{z_{ij}} + a_7\right) (1 - (a_{16}\gamma + a_{17})\text{sign}(\alpha_{ij} + S_H))$
S_H	Horizontal Shift	$S_H = a_8 F_{z_{ij}} + a_9 + a_{10}\gamma$
S_V	Vertical Shift	$S_V = a_{11} F_{z_{ij}} + a_{12} + (a_{13} F_{z_{ij}} + a_{14})\gamma_{ij} F_{z_{ij}}$
B_α		$B_\alpha = B\left(\alpha_{ij} + S_H\right)$

in this case Table 2.3 presents the main components of equation (2.19) and their dependence on coefficients $a_0, a_1, ..., a_{17}$. Table 2.4 presents the range of such coefficients with their nominal values. Notice here that even the camber angle γ is introduced to define some of the main components of (2.19). The main coefficients used are the shape factor a_0, the lateral friction coefficient, a_2, the change of stiffness with the sideslip angle, a_3, the change of progressiveness of stiffness against the load, a_4, and the Curvature factor, a_7.

Table 2.4 – Components require to form the (2.19)

Param.	Role	Typical range	Nom. Value
a_0	Shape factor	1.2 ... 1.8	1.4
a_1	Load influence on longitudinal friction coefficient	-80 ... +80	0
a_2	Lateral friction coefficient	900 ... 1700	1000
a_3	Change of stiffness with slip	500 ... 2000	1000
a_4	Change of progressiveness of stiffness / load	0 ... 50	10
a_5	Camber influence on stiffness	-0.1 ... +0.1	0
a_6	Curvature change with load	-2 ... +2	0
a_7	Curvature factor	-20 ... +1	-2
a_8	Load influence on horizontal shift	-1 ... +1	0
a_9	Horizontal shift at load = 0 and camber = 0	-1 ... +1	0
a_{10}	Camber influence on horizontal shift	-0.1 ... +0.1	0
a_{11}	Vertical shift	-200 ... +200	0
a_{12}	Vertical shift at load = 0	-10 ... +10	0
a_{13}	Camber influence on vertical shift, load dependent	-10 ... +10	0
a_{14}	Camber influence on vertical shift	-15 ... +15	0
a_{15}	Camber influence on lateral friction coefficient	-0.01 ... +0.01	0
a_{16}	Curvature change with camber	-0.1 ... +0.1	0
a_{17}	Curvature shift	-1 ... +1	0

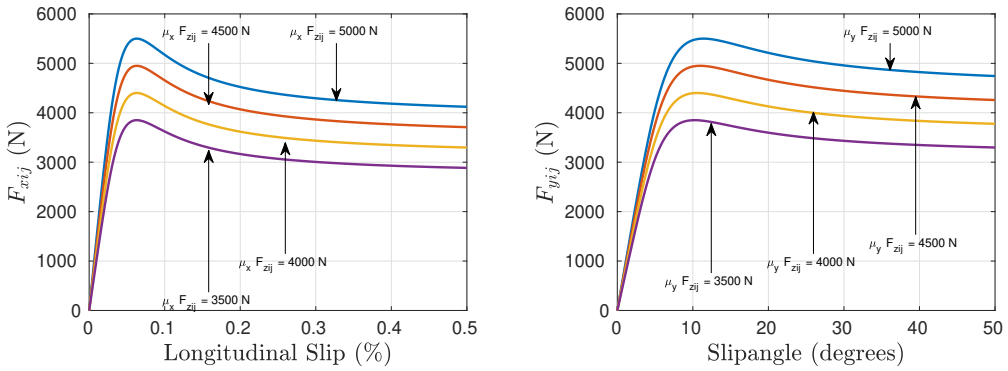

(a) $F_{x_{ij}}$ - κ (b) $F_{y_{ij}}$ - β

Figure 2.8 – Tire-ground force vs the longitudinal or lateral slip respectively

Figure 2.8 shows the magic formula (2.17) response with different input values of μF_{zij} from 3500 Newtons to 5000 Newtons, and assuming a camber angle equal to zero, $\gamma = 0$ and a friction coefficient equal to 1.0; this means that the magic formula is not constrained to a tire operation region as the linear tire model (2.13)-(2.14). Notice that the normal tire-ground force units are kilo-Newtons.

2.4 Vehicle Models

The tire models are useful and valid; nevertheless, they consider prior knowledge on the normal tire-ground force, the friction coefficient, and the camber angle,

among others, its implementation to an embedded unit within the car is not possible yet. Several authors had the idea to use both the tire and vehicle models to improve the estimation's robustness and accuracy by developing closed-loop observers. Therefore, three mathematical representations of a vehicle are introduced in this section: the double track, the bicycle, and the hoverboard model. These models help to develop the vehicle state observers and the control schemes proposed in the following chapters.

2.4.1 Double Track Model

The double-track model is a four-wheel vehicle representation widely used in the literature. This model assumes null rear steering angles, the direction or heading of the rear tires are considered the same as the vehicle, thus from Figure 2.9 and using Newton-Euler laws of motion:

$$\begin{aligned}
ma_x =& F_{x_{11}}\cos(\delta_{11}) - F_{y_{11}}\sin(\delta_{11}) + F_{x_{12}}\cos(\delta_{12}) - F_{y_{12}}\sin(\delta_{12}) + F_{x_{21}} + F_{x_{22}} \\
& - mg\sin(\theta_r) - \frac{1}{2}\rho C_{D_x} S_x \bar{v}_x^2 \\
ma_y =& F_{x_{11}}\sin(\delta_{11}) + F_{y_{11}}\cos(\delta_{11}) + F_{x_{12}}\sin(\delta_{12}) + F_{y_{12}}\cos(\delta_{12}) + F_{y_{21}} + F_{y_{22}} \\
& - mg\sin(\phi_R)\cos(\theta_R) - \frac{1}{2}\rho C_{D_y} S_y \bar{v}_y^2 \\
ma_z =& F_{z_{11}} + F_{z_{12}} + F_{z_{21}} + F_{z_{22}} - mg\cos(\theta_R)\cos(\phi_R) \\
I_x\ddot{\phi} =& e_1(F_{z_{11}} + F_{z_{21}}) - e_2(F_{z_{12}} + F_{z_{22}}) - hma_y \\
I_y\ddot{\theta} =& l_1(F_{z_{11}} + F_{z_{12}}) - l_2(F_{z_{21}} + F_{z_{22}}) + hma_x \\
I_z\ddot{\psi} =& l_1 ma_y - l(F_{y_{21}} + F_{y_{22}}) + e_2 ma_x - e(F_{x_{11}}\cos(\delta_{11}) - F_{y_{11}}\sin(\delta_{11}) + F_{x_{21}})
\end{aligned} \tag{2.20}$$

where m stands for the mass of the vehicle, a_p, $\forall p \in \mathcal{B} := \{x, y, z\}$ means an acceleration at the p-axis, $F_{p_{ij}}$ represents a force at the ij^{th}, $\forall i, j \in \mathcal{A} : +\{1, 2\}$ wheel directed towards its particular p-axis, δ_{ij} describes the steering wheel angle of the ij^{th} wheel, θ_r denotes the road slope angle, ρ*[4] is the air's density, C_{Dp} means the drag coefficient, S_p is the vehicle's surface in hitting the wind while vehicle's movement, ϕ_r describes the road bank angle, l_i means the distance between the COG and the front, ($i = 1$), and rear ($i = 2$) axles, also $L = \sum_{i\in\mathcal{A}} l_i$ holds, h is the minimum distance from the COG to the ground, e_i stands for the distance in the lateral direction from the COG to the left or right tires, also in this case E*[5] $= \sum_{j\in\mathcal{A}} e_j$ holds, g is the acceleration due to the gravity, I_p is the inertia for a given

[4] ρ is redefined in this section.
[5] E in this case is a distance and not the curvature factor used by the magic formula

p-axis; finally, ϕ, θ, and ψ define the attitude of the vehicle and $\ddot{\phi}$, $\ddot{\theta}$ and $\ddot{\psi}$ describe the angular acceleration for the roll, pitch and yaw angles respectively.

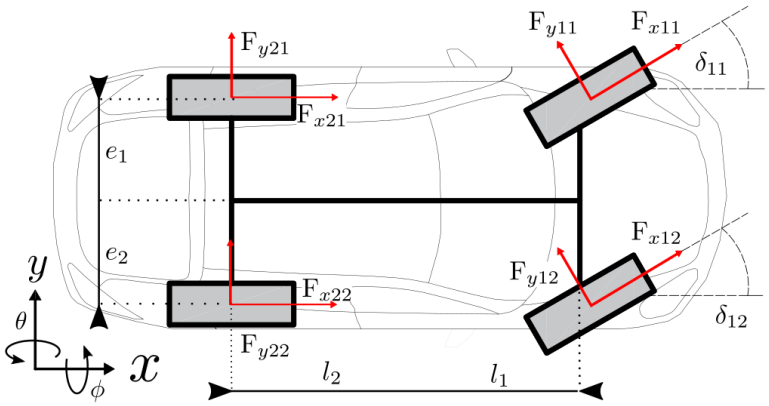

Figure 2.9 – Double track model

2.4.2 Single Track Model

The bicycle model is arguably the most used mathematical representation of a vehicle in the literature; see Figure 2.10. Its main characteristic is that it considers the left and right front wheels as a single central wheel with a steering angle δ defined as the average of left and right steering angles. Also, one central wheel without steering represents the rear left and right tires. In this case, only the front tire is controlled. Further, as an intrinsic property of this model, the roll dynamics are ignored. Then, from Figure 2.10 and using Newton-Euler laws of motion, the following set of equations are formulated:

$$
\begin{aligned}
ma_x &= \sum_{j\in\mathcal{A}} F_{x_{1j}}\cos(\delta) - \sum_{j\in\mathcal{A}} F_{y_{1j}}\sin(\delta) + \sum_{j\in\mathcal{A}} F_{x_{2j}} - \frac{1}{2}\rho C_{Dx} S_x \bar{v}_x^2 - mg\sin(\theta_r)\\
ma_y &= \sum_{j\in\mathcal{A}} F_{x_{1j}}\sin(\delta) + \sum_{j\in\mathcal{A}} F_{y_{1j}}\cos(\delta) + \sum_{j\in\mathcal{A}} F_{y_{2j}} - mg\sin(\phi_r)\cos(\theta_r)\\
ma_z &= \sum_{i\in\mathcal{A}}\sum_{j\in\mathcal{A}} F_{z_{ij}} - mg\cos(\theta_r)\cos(\phi_r)\\
I_x\ddot{\phi} &= 0\\
I_y\ddot{\theta} &= l_1\sum_{j\in\mathcal{A}} F_{z_{1j}} - l_2\sum_{j\in\mathcal{A}} F_{z_{2j}} + hma_x\\
I_z\ddot{\psi} &= l_1 ma_y - l\sum_{j\in\mathcal{A}} F_{y_{1j}}
\end{aligned}
\tag{2.21}
$$

where m, a_p, $F_{p_{ij}}$, ρ, C_{Dx}, S_x, $\bar{v}_x$, g, θ_r, ϕ_r, l_1, l_2, L, ϕ, θ and ψ are already defined

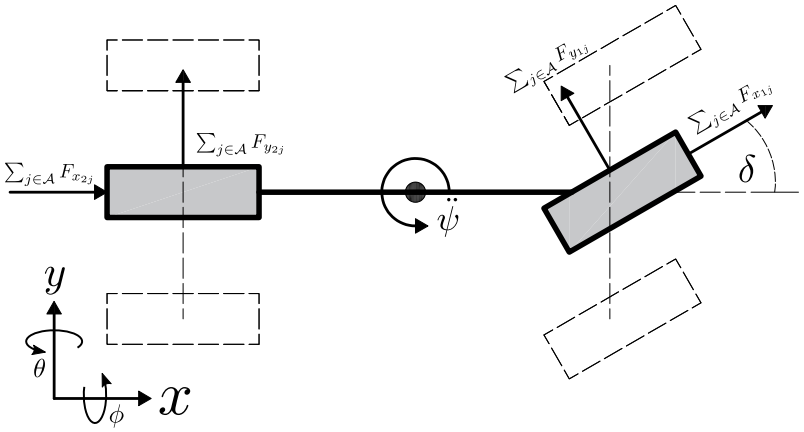

Figure 2.10 – Single Track Model

in last subsection. In this model δ describes the steering wheel which has been defined as the average of the front left and right tires, $\delta := (\delta_{11} + \delta_{12})/2$, and as the model is different the values for I_p even thought represents the same could be different.

2.4.3 Hoverboard Model

Figure 2.11 portrays the hoverboard model; this model represents the left tires (front/rear) as one left wheel and the right tires (front/rear) as a single right wheel. Here, the steering wheel system and the pitch vehicle dynamics are neglected. Therefore, from Figure 2.11 and using Newton-Euler laws of motion, gives:

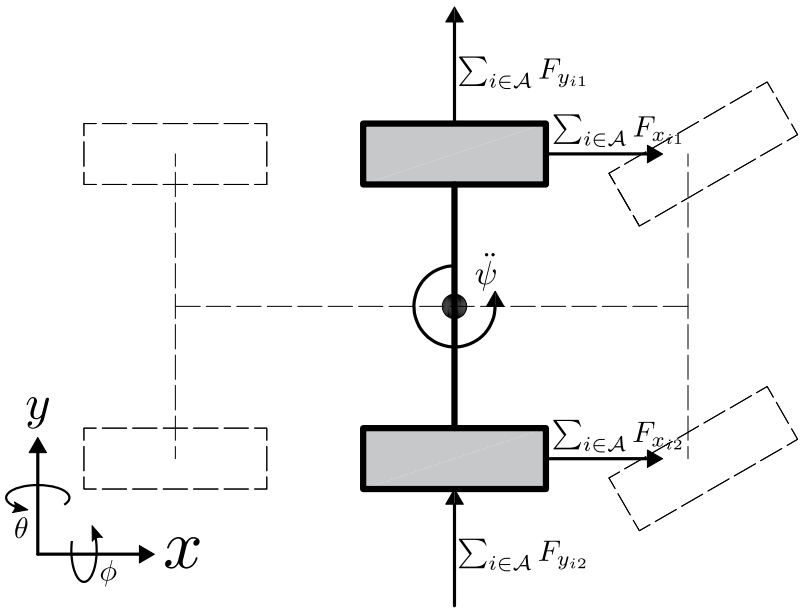

Figure 2.11 – Hoverboard car representation sketch - Superior view

$$
\begin{aligned}
ma_x &= \sum_{i\in\mathcal{A}} F_{x_{i1}} + \sum_{i\in\mathcal{A}} F_{x_{i2}} - \frac{1}{2}\rho C_{Dx} S_x \bar{v}_x^2 - mg\sin(\theta_r) \\
ma_y &= \sum_{i\in\mathcal{A}} F_{y_{i1}} + \sum_{i\in\mathcal{A}} F_{y_{i2}} \\
ma_z &= \sum_{i\in\mathcal{A}} F_{z_{i1}} + \sum_{i\in\mathcal{A}} F_{z_{i1}} - mg\cos(\theta_r)\cos(\phi_r) \\
I_x\ddot{\phi} &= e_2 \sum_{i\in\mathcal{A}} F_{z_{i2}} - e_1 \sum_{i\in\mathcal{A}} F_{z_{i1}} \\
I_y\ddot{\theta} &= 0 \\
I_z\ddot{\psi} &= e_2 \sum_{i\in\mathcal{A}} F_{x_{i2}} - e_1 \sum_{i\in\mathcal{A}} F_{x_{i1}}
\end{aligned}
\tag{2.22}
$$

where m, a_p, $F_{p_{ij}}$, ρ, C_{Dx}, S_x, $\bar{v}_x$, g, θ_r, ϕ_r, e_1, e_2, E, ϕ, θ and ψ are already defined in last subsection. Also here the values for I_p could be different even thought represent the same effects.

2.5 Torque-based models

In other cases, authors have taken advantage of using the torque τ coming from the powertrain subsystem. In some cases, linear models relating the brake pressure and some braking stiffness are used to provide more information and generate new and more accurate observation systems. In this section, the torque is available, and two models have been introduced: the single-corner model and the double-corner model.

2.5.1 Single-corner model

The single-corner model is a simple but effective model, typically used to design and test braking subsystems. Therefore, the model considers the four wheels as dynamically decoupled, neglecting the effects of the suspension dynamics and load transfer. This model is valid for straight-line maneuvers, where the camber angle γ and the tire slip angle α are near zero, and considers a constant wheel radius. The model is given by the following set of equations obtained after applying Newton laws of motion and Figure 2.12:

$$
\begin{aligned}
I_\Omega \dot{\Omega}_{ij} &= r_{ij} F_{x_{ij}} - \tau_{ij} \\
m_{ij}\dot{v}_{x_{ij}} &= -F_{x_{ij}}
\end{aligned}
\tag{2.23}
$$

where Ω is the angular speed of the wheel, $v_{x_{ij}}$ stands for the longitudinal speed of the it^{th} tire, τ_{ij} means the torque (drive or braking torque), $F_{x_{ij}}$ is the longitudinal

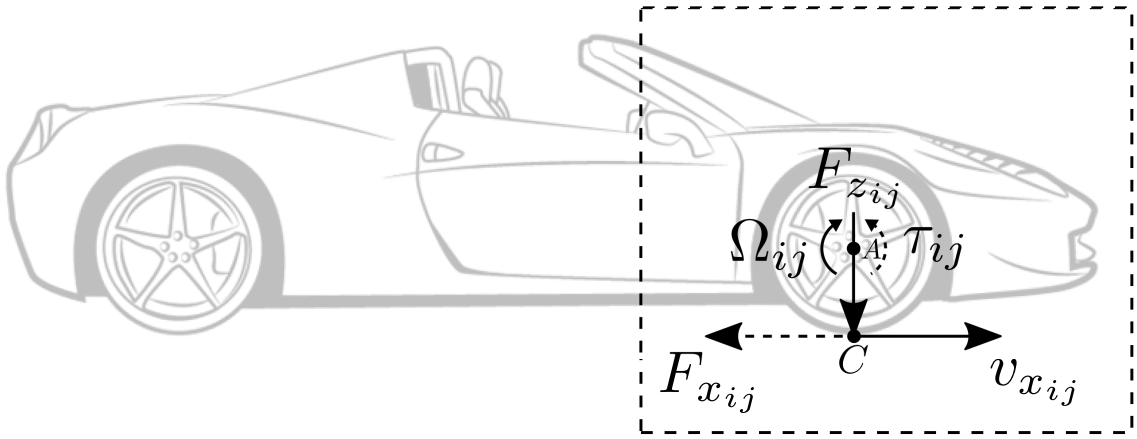

Figure 2.12 – Simple corner model

tire-road contact force and I_Ω, m_{ij} and r_{ij} are the moment of inertia of the wheel, the single-corner mass and the wheel radius, respectively.

2.5.2 Double-corner model

The double-corner model can be regarded as a side view of the vehicle, where one front and one rear wheel are modeled, (similar to the single-track model). Let us consider the double-corner model shown in Figure 2.13, the vehicle dynamics are described by the following set of equations:

$$\begin{aligned} I_\Omega \dot{\Omega}_f &= r_f \sum_{j\in\mathcal{A}} F_{x_{1,j}} - \sum_{j\in\mathcal{A}} \tau_{x_{1,j}} \\ I_\Omega \dot{\Omega}_r &= r_r \sum_{j\in\mathcal{A}} F_{x_{2,j}} - \sum_{j\in\mathcal{A}} \tau_{x_{2,j}} \\ m\dot{v}_x &= -\sum_{j\in\mathcal{A}} F_{x_{1,j}} - \sum_{j\in\mathcal{A}} F_{x_{2,j}} \end{aligned} \tag{2.24}$$

where $\Omega_f = 0.5\sum_{i\in\mathcal{A}} \Omega_{1i}$ is the mean speed of the two front wheels, $\Omega_r = 0.5\sum_{i\in\mathcal{A}} \Omega_{2i}$ represents the averages speed of the two rear wheels, $\sum_{i\in\mathcal{A}} \tau_{x_{1,i}}$ means the torque at the virtual-centered front wheel, $\sum_{i\in\mathcal{A}} \tau_{x_{2,i}}$ is the torque at the virtual-centered rear wheel, $\sum_{i\in\mathcal{A}} F_{x_{1,i}}$ and $\sum_{i\in\mathcal{A}} F_{x_{2,i}}$ are already defined. Finally, $r_f = 0.5\sum_{i\in\mathcal{A}} r_{1i}$, and $r_r = 0.5\sum_{i\in\mathcal{A}} r_{1i}$ are the mean radius of the front and rear wheels, respectively.

2.6 Suspension System Models

While driving, the vehicle is under the influence of the driver commands (acceleration, deceleration), external disturbances (road conditions, bumps, bank, and

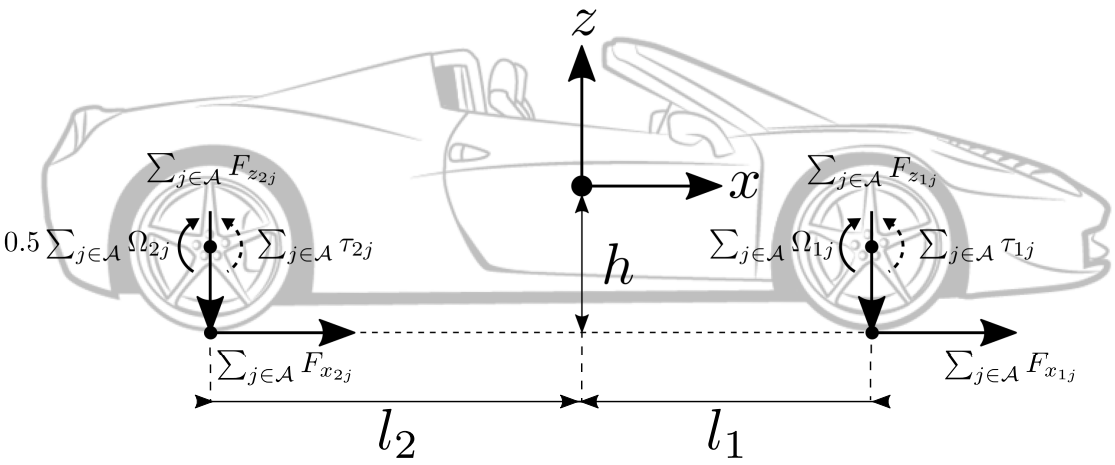

Figure 2.13 – Double-corner model

slope angles), environmental conditions, etc. Specifically, the suspension system experiments two primary disturbances:

- The load transfer is the change in tire-ground normal force produced due to longitudinal and lateral vehicle accelerations, i.e., when accelerating, the chassis experiments a force that pulls or pushes in the vertical axes at the front or rear axle. This force affects the driving experience by diminishing the driver's comfort.
- The road profile affects the driver's comfort and the vehicle's road holding.

2.6.1 Quarter Car Model

The most used vehicle suspension model is known as a quarter car model, see Figure 2.14. With this model, the vertical vibration of a vehicle could be represented by two solid masses m_s and m_{us} denoted as sprung and unsprung mass, respectively. The equivalent values for spring stiffness k_s, and the damping coefficient c_s, support the sprung mass while the unsprung mass is in contact with the ground. While using the quarter car model, equivalent coefficients also represent the tire for spring stiffness k_t and a shock absorber c_t; these values (k_t, c_t) emulate the compression and decompression of the tire's rubber. Thus, from Newton laws of motion and Figure 2.14 is obtained:

$$\begin{aligned} m_s\ddot{z}_s &= -k_s(z_s - z_{us}) - c_s(\dot{z}_s - \dot{z}_{us}) \\ m_{us}\ddot{z}_{us} &= k_s(z_s - z_{us}) + c_s(\dot{z}_s - \dot{z}_{us}) - k_t(z_{us} - z_r) - c_t(\dot{z}_{us} - \dot{z}_r) \end{aligned} \tag{2.25}$$

where z_n, $\dot{z}_n$ and $\ddot{z}_n$ stand for the mass' height, velocity and acceleration respectively, with $n \in \mathcal{C} := \{s, us\}$. The suffix n stands for an effect applied at the sprung or

unsprung mass correspondingly, and variables z_r, and $\dot{z}_r$ are unknown inputs representing the road profile and its time derivative.

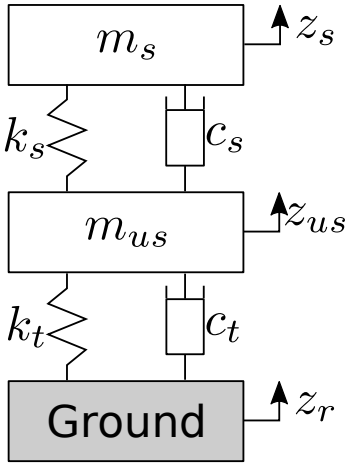

Figure 2.14 – Passive suspension system

Figure 2.15 shows in red-solid line the actual force produced at the suspension spring and dampers (left figures) and the actual force produced by the tire represented by a series of springs and dampers (right figures). Also, displays with black circles the linear approximation of such forces using the equivalent parameters (k_s, c_s , k_t and c_t). Notice that this linear approximation lacks accuracy at the edges of the graphs. Moreover, the presence of such uncertainties increases the estimation problem complexity.

2.6.2 7 degrees of freedom vehicle vertical model

This model includes the chassis' vertical dynamics, pitch and roll, and the vertical motions of the wheels. The dynamic equations are:

$$\begin{aligned} m_s\ddot{z}_s &= -\sum_{i\in\mathcal{A}}\sum_{j\in\mathcal{A}} F_{zs_{ij}} \\ I_x\ddot{\phi} &= e_1\sum_{j\in\mathcal{A}} F_{zs_{i1}} - e_2\sum_{j\in\mathcal{A}} F_{zs_{i2}} - hma_y \\ I_y\ddot{\theta} &= l_1\sum_{j\in\mathcal{A}} F_{zs_{1j}} - l_2\sum_{j\in\mathcal{A}} F_{zs_{2j}} - hma_x \\ m_{us_{ij}}\ddot{z}_{ij} &= F_{zs_{ij}} - F_{zt_{ij}} \end{aligned} \tag{2.26}$$

with m_s defined as the sprung mass of the whole vehicle, $\ddot{z}_s$ is the vertical acceleration of the vehicle's COG, $m_{us_{ij}}$ stands for the ij^{th} unsprung mass, $\ddot{z}_{us_{ij}}$ represent the acceleration of the ij^{th} unsprung mass, I_p, ϕ, θ, h, e_j, l_i and a_p are already

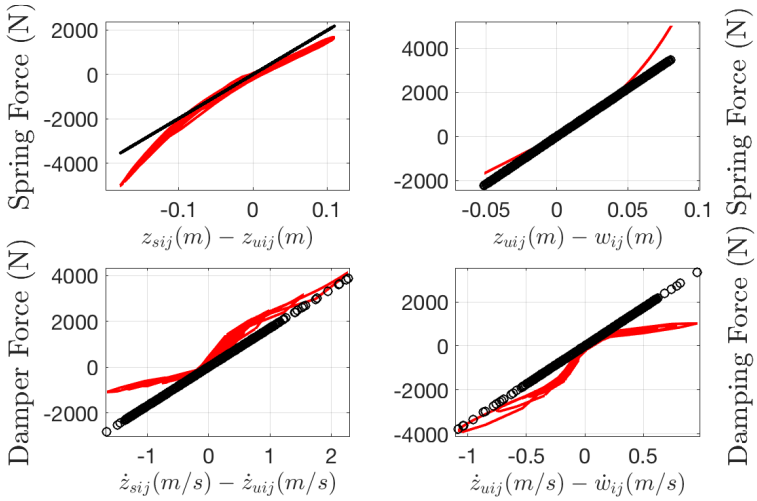

Figure 2.15 – Spring and Damping force response measured forces portrayed with red-solid line and linear model depicted with black-circled line. Up-left: Suspension deflection against spring force at the suspension. Up-right: Tire deflection against the spring force at the tire. Down-left: Suspension deflection speed against the damping force at the suspension. Down-right: Tire deflection speed against the damping force at the tire.

defined. The forces $F_{zs_{ij}}$ are modeled by a linear equation as in (2.25), thus,

$$F_{zs_{ij}} = k_{s_{ij}}(z_{s_{ij}} - z_{us_{ij}}) + c_{s_{ij}}(\dot{z}_{s_{ij}} - \dot{z}_{us_{ij}}),$$

and

$$F_{zus_{ij}} = k_{t_{ij}}(z_{us_{ij}} - z_{r_{ij}}) + c_{t_{ij}}(\dot{z}_{us_{ij}} - \dot{z}_{r_{ij}}),$$

where the coefficients $k_{s_{ij}}$, $c_{s_{ij}}$, $k_{t_{ij}}$, $c_{t_{ij}}$, are found as:

$$k_{s_{ij}} = \left(\frac{\partial F_{zs_{ij}}}{\partial z_{sd_{ij}}}\right)|_{\dot{z}_{sd_{ij}}=0}, \quad c_{s_{ij}} = \left(\frac{\partial F_{zs_{ij}}}{\partial \dot{z}_{sd_{ij}}}\right)|_{z_{sd_{ij}}=0},$$

$$c_{t_{ij}} = \left(\frac{\partial F_{zt_{ij}}}{\partial z_{td_{ij}}}\right)|_{\dot{z}_{td_{ij}}=0}, \quad k_{t_{ij}} = \left(\frac{\partial F_{zs_{ij}}}{\partial \dot{z}_{d_{ij}}}\right)|_{z_{td_{ij}}=0},$$

with $z_{sd_{ij}} = z_{s_{ij}} - z_{us_{ij}}$, $\dot{z}_{sd_{ij}} = \dot{z}_{s_{ij}} - \dot{z}_{us_{ij}}$, $z_{td_{ij}} = z_{us_{ij}} - z_{r_{ij}}$ and $\dot{z}_{td_{ij}} = \dot{z}_{us_{ij}} - \dot{z}_{r_{ij}}$.

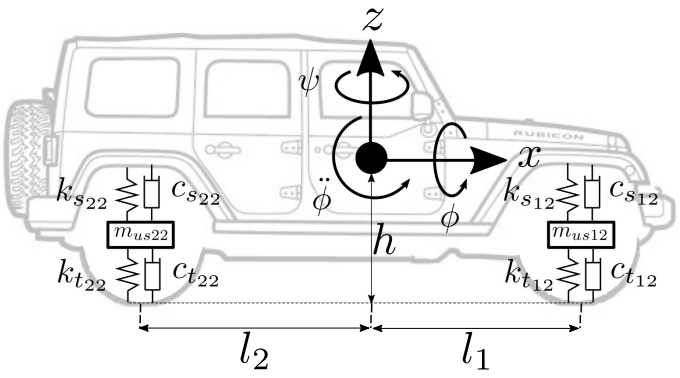

(a) 7 DoF model Lateral view

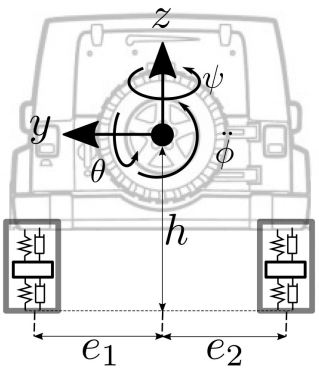

(b) 7 DoF model rear view

Figure 2.16 – 7 DoF model

2.7 Conclusions

This chapter provides a brief introduction to the vehicle dynamics modeling stated of the art. The vehicle dynamics study is mainly divided into two major topics: the dynamics of the road-tire interactions and vehicle motion dynamics. The road-tire interactions explain how the tire-ground forces are generated. The vehicle dynamics emphasize the relation between the tire forces and vehicle motion.

This chapter presents the brush model, the Dugoff model, the linear tire model, and the Magic tire formula. The brush model is a simplified physical model of a tire that considers the tire as a series of small bristles that model the tire rubber's compression and decompression. The reader can get a lot of intuition from it. The Dugoff model is even simpler than the brush model, and this is more suitable for embedded implementations. An extra simplification is introduced by the linear tire model, which captures the relation between the tire-ground forces and the tire slips; as the name implies, this representation does not consider the force saturation that a tire can experiment. The magic formula is the most complex of all, and also is the most accurate.

This chapter also presents the vehicle models that represents the vehicle motions. The double-track, single-track, and the hoverboard models represent the car in 6 degrees of freedom environment. On the other hand, the single-corner and double-corner models are presented; they consider the vehicle as the tire or couple of tires; these models consider the motor torque as the longitudinal force producer. Finally, the quarter-car model and the 7 degrees of freedom suspension model help us explain the vertical motion of the vehicle in more detail.

Longitudinal and lateral speed estimation

Contents

3.1 Introduction

This section proposes techniques to estimate the longitudinal and lateral speed, which is an important variable related to the sideslip angle. Most of the lateral stability controllers for vehicles define the sideslip angle as part of the vehicle state; thus, estimating both the longitudinal and lateral speed is crucial to increase the lateral stability controller's performance.

In Section 3.2, we present the preliminaries of state estimation; this section's scope is the Luenberger observer and Kalman filter techniques that are the basis of the developed observers in this thesis. Section 3.3 presents a review specifically on the most relevant works in the sideslip angle / lateral speed estimation topic. This thesis's contribution that addresses lateral speed estimation is seen in Section 3.4, while Section 3.5 analyses the results of the estimation technique. Finally, in Section 3.6, the conclusions and perspectives are discussed.

3.2 Preliminaries

In control theory, state-feedback controllers and most controllers assume that all the state variables are available for feedback. This assumption may not hold in practice because sensing devices are not available, or the cost is too high for mass-produced vehicles. In this case, we must design a device, called state estimator or state observer, so that the device's output will generate an estimate of the state.

3.2.1 Observability for Linear Systems

In this section, we explain the notion of state to provide the basis for the Luenberger Observer. This definition is crucial to formulate a state-space model, thus:

- System equation, which describes the evolution of the state through time.
- Measurement equation, which describes the dependence of the measurements on the state.

Definition 3.2.1. *In general, we can say that the state of a system at a given time instant $t_1 \geq t_0$ should include the minimal information that allows one to continue the dynamic for $t \geq t_1$.*

In this chapter we will consider the n-dimensional, p-input, q-output state-space equation:

$$\begin{aligned}\dot{\mathbf{x}}(t) =& \mathbf{A}\mathbf{x}(t) + \mathbf{B}\mathbf{u}(t)\\ \mathbf{y}(t) =& \mathbf{C}\mathbf{x}(t)\end{aligned} \tag{3.1}$$

where $\mathbf{A} \in \mathbb{R}^{n\times n}$, $\mathbf{B} \in \mathbb{R}^{n\times p}$ and $\mathbf{C} \in \mathbb{R}^{q\times n}$ with constant elements and usually known as the state, input and output matrices, the state $\mathbf{x}(t) \in \mathbb{R}^{n\times 1}$ and the output $\mathbf{y}(t) \in \mathbb{R}^{q\times 1}$.

The problem of interest is to estimate the state $\mathbf{x}(t)$ based on the measurements $\mathbf{y}(t)$. The general form of the estimate $\hat{\mathbf{x}}(t)$ is:

$$\hat{\mathbf{x}}(t) = \alpha\left(\hat{\mathbf{x}}(0), \mathbf{Y}(t)\right)$$

where $\hat{\mathbf{x}}(0)$ is a guess of the statistical mean[1],[2] and $\mathbf{Y}(t) = \int_0^t \mathbf{y}(t)dt$. Let us define observable state.

Definition 3.2.2. *The state-space equation (3.1) is said to be observable if for any unknown initial state $\mathbf{x}(0)$ there exists a finite $t_1 > 0$ such that the knowledge of the input, $\mathbf{u}$, and the output, $\mathbf{y}$, over $[0, t_1]$ suffices to determine uniquely the initial state $\mathbf{x}(0)$. Otherwise, the equation is said unobservable.*

The response of (3.1) is

$$\mathbf{y}(t) = \mathbf{C}e^{\mathbf{A}t}\mathbf{x}(0) + \mathbf{C}\int_0^t e^{\mathbf{A}(t-\tau)}\mathbf{B}\mathbf{u}(\tau)d\tau \tag{3.2}$$

Theorem 3.2.1. *The state-space equation (3.1) is observable if and only if the matrix*

$$\mathbf{W}_0(t) = \int_0^t e^{\mathbf{A}^T\tau}\mathbf{C}^T\mathbf{C}e^{\mathbf{A}\tau}d\tau$$

is non-singular for any $t > 0$

Proof. First, lets rewrite (3.2) as

$$\mathbf{C}e^{\mathbf{A}t}\mathbf{x}(0) = \bar{\mathbf{y}}(t) \tag{3.3}$$

[1]The statistical mean is also called the mathematical expectation, $m_x = E(x)$ and $E(x) = \int_S xp(x)dx$, where $p(x)$ is the probability density function and S the support on which the variable is defined

[2]In probability theory, a probability density function is a function whose value at any given sample in the sample space provides a relative likelihood that the variable's value would equal that sample.

with

$$\bar{\mathbf{y}}(t) := \mathbf{y}(t) - \mathbf{C}\int_0^t e^{\mathbf{A}(t-\tau)}\mathbf{B}\mathbf{u}(\tau)d\tau$$

if we premultiply (3.3) and then integrate it over $[0, t_1]$, yields

$$\int_0^{t_1} e^{\mathbf{A}^T\tau}\mathbf{C}^T\mathbf{C}e^{\mathbf{A}\tau}d\tau\mathbf{x}(0) = \int_0^{t_1} e^{\mathbf{A}^T\tau}\mathbf{C}^T\bar{\mathbf{y}}(\tau)d\tau$$

and finally

$$\mathbf{x}(0) = \mathbf{W}_0(t_1)^{-1}\int_0^{t_1}\mathbf{A}^{T\tau}\mathbf{C}^T\bar{\mathbf{y}}(\tau)d\tau$$

□

Theorem 3.2.2. *The state-space equation (3.1) is observable if and only if the observability matrix*

$$\mathbf{O} = \begin{bmatrix} \mathbf{C} \\ \mathbf{CA} \\ \vdots \\ \mathbf{CA^{n-1}} \end{bmatrix} \tag{3.4}$$

has rank n (full column rank).

Proof. Lets consider (3.3), differentiating it repeatedly $n-1$ times and set the time to zero, we obtain:

$$\begin{bmatrix} \mathbf{C} \\ \mathbf{CA} \\ \vdots \\ \mathbf{CA}^{n-1} \end{bmatrix}\mathbf{x}(0) = \begin{bmatrix} \bar{\mathbf{y}}(\mathbf{0}) \\ \dot{\bar{\mathbf{y}}}(0) \\ \vdots \\ \bar{\mathbf{y}}^{n-1}(0) \end{bmatrix}$$

if and only if $\mathbf{O}$ is a full column rank matrix could be an invertible matrix, and it follows that the initial state condition $\mathbf{x}(0)$ could be isolated as

$$\mathbf{x}(0) = \left(\begin{bmatrix} \mathbf{C} \\ \mathbf{CA} \\ \vdots \\ \mathbf{CA}^{n-1} \end{bmatrix}^T \begin{bmatrix} \mathbf{C} \\ \mathbf{CA} \\ \vdots \\ \mathbf{CA}^{n-1} \end{bmatrix}\right)^{-1} \begin{bmatrix} \mathbf{C} \\ \mathbf{CA} \\ \vdots \\ \mathbf{CA}^{n-1} \end{bmatrix}^T \begin{bmatrix} \bar{\mathbf{y}}(\mathbf{0}) \\ \dot{\bar{\mathbf{y}}}(0) \\ \vdots \\ \bar{\mathbf{y}}^{n-1}(0) \end{bmatrix} \tag{3.5}$$

□

The problem is to estimate the state, $\mathbf{x}$, from the input, $\mathbf{u}$, and the output $\mathbf{y}$ using the knowledge of matrices $\mathbf{A}$, $\mathbf{B}$, and $\mathbf{C}$; with this knowledge, we can duplicate the original system as:

$$\dot{\hat{\mathbf{x}}}(t) = \mathbf{A}\hat{\mathbf{x}}(t) + \mathbf{B}\mathbf{u}(t) \tag{3.6}$$

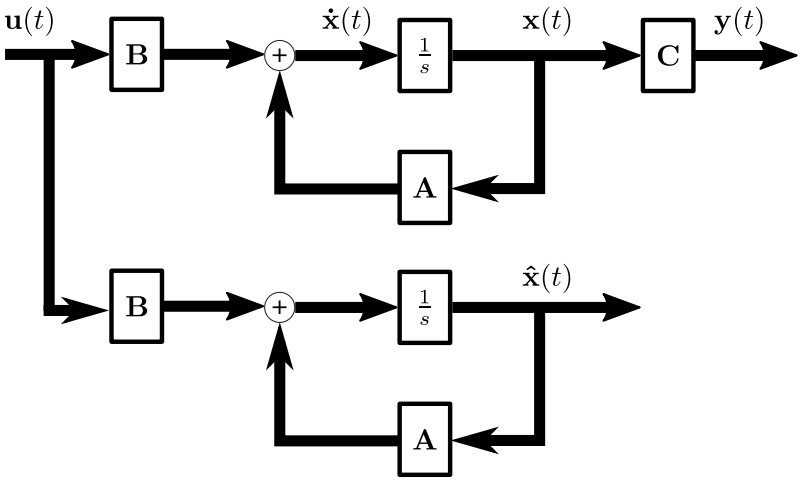

Figure 3.1 – Open Loop Observer

the system (3.6) is known as open-loop estimator, see Figure 3.1.

There are, however, two disadvantages of using an open-loop estimator. First, the initial state must be computed and set each time we use the estimator. Second, if the matrix $\mathbf{A}$ has eigenvalues with positive real parts, the estimation error will grow with time.

The open-loop estimator in (3.6) could be modified as:

$$\dot{\hat{\mathbf{x}}}(t) = (\mathbf{A} - \mathbf{LC})\hat{\mathbf{x}}(t) + \mathbf{Bu}(t) + \mathbf{Ly}(t) \tag{3.7}$$

where $\mathbf{L}$ is the gain matrix defined this way in honor of David Gilbert Luenberger, giving the diagram shown in Figure 3.2.

Now, let us define the estimation error as $\hat{\mathbf{x}}(0) = \mathbf{x}(0) + \tilde{\mathbf{x}}(0)$, and differentiating the estimation error yields

$$\begin{aligned} \dot{\tilde{\mathbf{x}}}(t) =& \mathbf{Ax}(t) + \mathbf{Bu}(t) - (\mathbf{A} - \mathbf{LC})\hat{\mathbf{x}}(t) - \mathbf{Bu}(t) - \mathbf{Ly}(t) \\ =& (\mathbf{A} - \mathbf{LC})\tilde{\mathbf{x}}(t) \end{aligned} \tag{3.8}$$

Suppose the system (3.1) is fully observable. In that case, it means that all eigenvalues of $\mathbf{A} - \mathbf{LC}$ can be arbitrarily assigned, then we can control the rate in which the estimation error, $\tilde{\mathbf{x}}(t)$, decays to zero.

3.2.2 Kalman Filter

In this section, we complete our study with a linear optimum filter by developing the Kalman filter's basic ideas. A distinctive feature of the Kalman filter is that its mathematical formulation describes the state-space. Another part of a Kalman filter is that it has a recursive solution; only the previous estimate requires storage. The

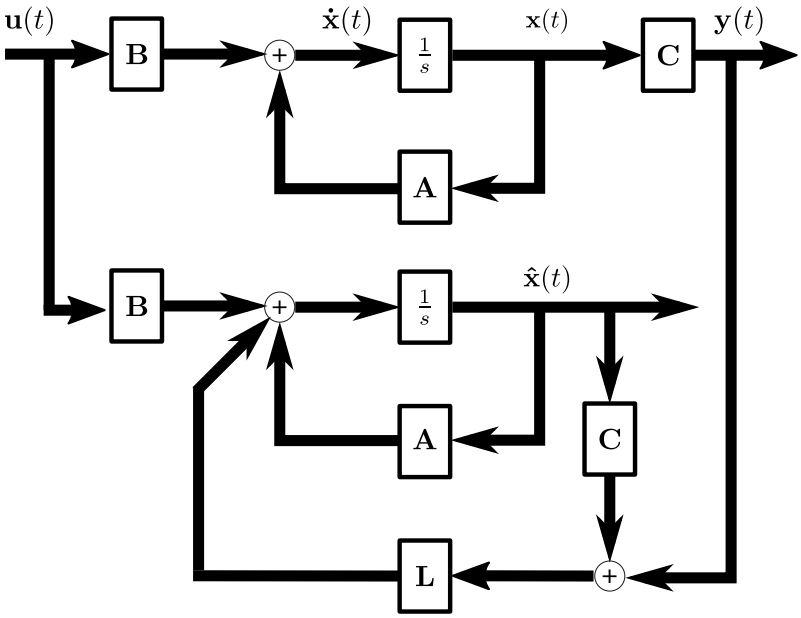

Figure 3.2 – Closed Loop Observer

Kalman filter is ideally suited for computer implementations. In a few words, the Kalman filter is an "estimator/predictor" observer whose gain $\mathbf{K}$ is calculated such that the estimate is optimal in the sense of the orthogonality principle.

The state-space system (3.1) is redefined in this section and discretized. We assume that the signal $\mathbf{y}_n$ can be described by a linear time-invariant state model and additive-noise model for the measurements $\mathbf{z}_n$. Then we have the state-space model:

$$\mathbf{x}_{n+1} = \mathbf{\Phi}\mathbf{x}_n + \mathbf{\Gamma}\boldsymbol{\omega}_n, \tag{3.9a}$$

$$\mathbf{y}_n = \mathbf{C}\mathbf{x}_n, \tag{3.9b}$$

and

$$\mathbf{z}_n = \mathbf{y}_n + \boldsymbol{v}_n \tag{3.10}$$

where $\mathbf{\Phi} \in \mathbb{R}^{n\times n}$, $\mathbf{\Gamma} \in \mathbb{R}^{n\times m}$, and $\mathbf{C} \in \mathbb{R}^{q\times n}$ are known deterministic matrices, $\mathbf{x}_n \in \mathbb{R}^{n\times 1}$ is the current state vector with $\mathbf{x}_0$ is the initial state, $\boldsymbol{\omega}_n \in \mathbb{R}^{m\times m}$ denotes the stationary process noise with covariance matrix, $\mathbf{Q} \in \mathbb{R}^{m\times m}$, $\boldsymbol{v}_n \in \mathbb{R}^q$ means the stationary measurement noise with zero-mean white-noise and covariance matrix $\mathbf{R} \in \mathbb{R}^{q\times q}$. Notice that $\boldsymbol{\omega}_n$ and $\boldsymbol{v}_n$ are considered uncorrelated, zero-mean, white noise processes, and system (3.9) has no input.

Once the system (3.9) is defined, we could develop the two main stages of the Kalman filter: The prediction and update stages.

3.2.2.1 Prediction Stage

In this stage the filter finds the *a priori* estimate, $\hat{\mathbf{x}}_{n|n-1}$, from the a posteriori estimate, $\hat{\mathbf{x}}_{n-1|n-1}$, and the error covariance matrix, $\mathbf{P}_{n|n-1}$. Thus, the *a priori* estimate, $\hat{\mathbf{x}}_{n|n-1}$, should be the optimum estimate and $\hat{\mathbf{x}}_{n|n-1}$ must satisfy the orthogonality condition. Then,

$$\mathbf{E}\left[\left(\mathbf{x}_{n|n} - \hat{\mathbf{x}}_{n|n-1}\right)\mathbf{Z}_{n-1}\right] = \mathbf{0} \tag{3.11}$$

with $\mathbf{Z}_{n-1} = [\mathbf{z}_1, \mathbf{z}_2, \ldots, \mathbf{z}_{n-1}]$ and $\mathbf{0}$ represents a matrix full of zeros with adequate dimensions.

Lets consider the error defined as $\mathbf{x}_{n-1} = \hat{\mathbf{x}}_{n-1|n-1} + \tilde{\mathbf{x}}_{n-1|n-1}$, and introducing the state-space equation (3.9a), to eq. (3.11) becomes:

$$\mathbf{E}\left[\left(\mathbf{\Phi}\hat{\mathbf{x}}_{n-1|n-1} - \hat{\mathbf{x}}_{n|n-1}\right)\mathbf{Z}_{n-1}\right] + \mathbf{\Phi}\mathbf{E}\left[\tilde{\mathbf{x}}_{n-1|n-1}\mathbf{Z}_{n-1}\right] + \mathbf{\Gamma}\mathbf{E}\left[\boldsymbol{\omega}_{n-1}\mathbf{Z}_{n-1}\right] = \mathbf{0}$$

Since $\hat{\mathbf{x}}_{n-1|n-1}$ is the optimal estimate of $\mathbf{x}_{n-1}$,

$$\mathbf{\Phi}\mathbf{E}\left[\tilde{\mathbf{x}}_{n-1|n-1}\mathbf{Z}_{n-1}\right] = \mathbf{0}$$

holds. Similarly, $\boldsymbol{\omega}_{n-1}$ is independent of all measurements in $\mathbf{Z}_{n-1}$,

$$\mathbf{\Gamma}\mathbf{E}\left[\boldsymbol{\omega}_{n-1}\mathbf{Z}_{n-1}\right] = \mathbf{0},$$

therefore,

$$\mathbf{E}\left[\left(\mathbf{\Phi}\hat{\mathbf{x}}_{n-1|n-1} - \hat{\mathbf{x}}_{n|n-1}\right)\mathbf{Z}_{n-1}\right] = \mathbf{0}$$

holds, if

$$\hat{\mathbf{x}}_{n|n-1} = \mathbf{\Phi}\hat{\mathbf{x}}_{n-1|n-1} \tag{3.12}$$

The covariance matrix $\mathbf{P}_n$ is defined as:

$$\mathbf{P}_{n|n} = \mathbf{E}\left[\tilde{\mathbf{x}}_{n|n}\tilde{\mathbf{x}}_{n|n}^T\right]$$

thus, the *a priori* covariance matrix $\mathbf{P}_{n|n-1}$ is:

$$\mathbf{P}_{n|n-1} = \mathbf{E}\left[\tilde{\mathbf{x}}_{n|n-1}\tilde{\mathbf{x}}_{n|n-1}^T\right] \tag{3.13}$$

where $\tilde{\mathbf{x}}_{n|n-1} = \mathbf{x}_n - \hat{\mathbf{x}}_{n|n-1}$. Then, considering that $\mathbf{E}\left[\tilde{\mathbf{x}}_{n-1}\boldsymbol{\omega}_{n-1}^T\right] = \mathbf{0}$, eq. (3.13) becomes:

$$\mathbf{P}_{n|n-1} = \mathbf{\Phi}\mathbf{P}_{n-1|n-1}\mathbf{\Phi}^T + \mathbf{\Gamma}\mathbf{Q}\mathbf{\Gamma}^T \tag{3.14}$$

The recursions (3.12) and (3.14) are called the time update. They describe the evolution of the estimate and error covariance across time $n-1$ to n before the measurement is available.

3.2.2.2 Update stage

When the measurement becomes available, the estimator shall produce the estimate of $\mathbf{x}$ given the observations $\mathbf{Z}_n$; to perform this action, we also need the *a posteriori* error covariance matrix.

On the one hand, we assume knowledge of $\mathbf{x}_{n-1|n-1}$, the optimal estimate of $\mathbf{x}_{n-1}$ given $\mathbf{Z}_{n-1}$. Then we write $\hat{\mathbf{x}}_{n-1}$ as a linear combination of the measurements $\mathbf{Z}_{n-1}$, then,

$$\hat{\mathbf{x}}_{n-1|n-1} = \mathbf{J}_{n-1}\mathbf{Z}_{n-1} \tag{3.15}$$

thus it follows that the actual estimate $\mathbf{x}_{n|n}$ is

$$\hat{\mathbf{x}}_{n|n} = \mathbf{J}_n\mathbf{Z}_n$$

last equation could be rewritten as

$$\hat{\mathbf{x}}_{n|n} = \mathbf{k}_n\mathbf{z}_n + \mathbf{G}_n\mathbf{Z}_{n-1} \tag{3.16}$$

where $\mathbf{k}_n \in \mathbb{R}^{q\times 1}$ and $\mathbf{G}_n \in \mathbb{R}^{q\times n-1}$. Now, let us consider (3.9) and substitute into (3.16), gives

$$\begin{aligned}\hat{\mathbf{x}}_{n|n} =& \mathbf{k}_n\left[\mathbf{C}\mathbf{x}_n + \boldsymbol{v}_n\right] + \mathbf{G}_n\mathbf{Z}_{n-1}\\ =& \mathbf{k}_n\mathbf{C}\boldsymbol{\Phi}\mathbf{x}_{n-1} + \mathbf{k}_n\mathbf{C}\boldsymbol{\Gamma}\boldsymbol{\omega}_{n-1} + \mathbf{k}_n\mathbf{v}_n + \mathbf{G}_n\mathbf{Z}_{n-1}\end{aligned}$$

Remember that $\hat{\mathbf{x}}_n$ has to be the optimal estimate of $\mathbf{x}_n$, then, the following holds

$$\mathbf{E}\left[\left(\mathbf{x}_n - \hat{\mathbf{x}}_{n|n}\right)\mathbf{Z}_n\right] = \mathbf{0} \tag{3.17a}$$

$$\mathbf{E}\left[\tilde{\mathbf{x}}_n\mathbf{Z}_{n-1}\right] = \mathbf{0} \tag{3.17b}$$

$$\mathbf{E}\left[\tilde{\mathbf{x}}_n\mathbf{z}_n\right] = \mathbf{0} \tag{3.17c}$$

Equations (3.17b) and (3.17c) are direct derivations from (3.17a), thus we have

$$\tilde{\mathbf{x}}_n = \left[\mathbf{I}-\mathbf{k}_n\mathbf{C}\right]\boldsymbol{\Phi}\hat{\mathbf{x}}_{n-1|n-1} + \left[\mathbf{I}-\mathbf{k}_n\mathbf{C}\right]\boldsymbol{\Phi}\tilde{\mathbf{x}}_{n-1|n-1} + \left[\mathbf{I}-\mathbf{k}_n\mathbf{C}\right]\boldsymbol{\Gamma}\boldsymbol{\omega}_{n-1} - \mathbf{k}_n\mathbf{v}_n - \mathbf{G}_n\mathbf{Z}_{n-1}$$

and considering $\mathbf{E}\left[\boldsymbol{\omega}_{n-1}\mathbf{Z}_{n-1}\right] = \mathbf{0}$ and $\mathbf{E}\left[\mathbf{v}_n\mathbf{Z}_{n-1}\right] = 0$ we get

$$\begin{aligned}\mathbf{E}\left[\tilde{\mathbf{x}}_n\mathbf{Z}_{n-1}\right] &= \left[\mathbf{I}-\mathbf{k}_n\mathbf{C}\right]\boldsymbol{\Phi}\mathbf{E}\left[\hat{\mathbf{x}}_{n-1|n-1}\mathbf{Z}_{n-1}\right] + \left[\mathbf{I}-\mathbf{k}_n\mathbf{C}\right]\boldsymbol{\Phi}\mathbf{E}\left[\tilde{\mathbf{x}}_{n-1|n-1}\mathbf{Z}_{n-1}\right] - \mathbf{G}_n\mathbf{E}\left[\mathbf{Z}_{n-1}\mathbf{Z}_{n-1}\right]\\ \mathbf{0} &= \left[\mathbf{I}-\mathbf{k}_n\mathbf{C}\right]\boldsymbol{\Phi}\mathbf{J}_{n-1}\mathbf{E}\left[\mathbf{Z}_{n-1}\mathbf{Z}_{n-1}\right] - \mathbf{G}_n\mathbf{E}\left[\mathbf{Z}_{n-1}\mathbf{Z}_{n-1}\right]\\ \mathbf{G}_n &= \left[\mathbf{I}-\mathbf{k}_n\mathbf{C}\right]\boldsymbol{\Phi}\mathbf{J}_{n-1}\end{aligned}$$

the above is accomplished by the fact that $\mathbf{R} > 0$ is positive definite, thus, it follows that $\mathbf{E}\left[\mathbf{Z}_{n-1}\mathbf{Z}_{n-1}^T\right]$ is also positive-definite and consequently invertible. Also, as $\hat{\mathbf{x}}_{n-1|n-1}$ is already the optimal estimate of $\mathbf{x}_{n-1}$ the expectancy $\mathbf{E}\left[\tilde{\mathbf{x}}_{n-1|n-1}\mathbf{Z}_{n-1}^T\right] = \mathbf{0}$. Substituting this result into (3.16), and taking into account equations (3.12)-(3.15), gives

$$\hat{\mathbf{x}}_{n|n} = \hat{\mathbf{x}}_{n|n-1} + \mathbf{k}_n\left[\mathbf{z}_n - \mathbf{C}\hat{\mathbf{x}}_{n|n-1}\right] \tag{3.18}$$

To define $\mathbf{k}_n$, it must be fulfilled the condition (3.17c), then from (3.9) and (3.18) is obtained:

$$\tilde{\mathbf{x}}_{n|n} = \mathbf{\Phi}\tilde{\mathbf{x}}_{n-1|n-1} + \left[\mathbf{I} - \mathbf{k}_n\mathbf{C}\right]\mathbf{\Gamma}\omega_{n-1} - \mathbf{k}_n\mathbf{v}_n$$

consequently,

$$\mathbf{E}\left[\tilde{\mathbf{x}}_{n|n}\right] = \mathbf{\Phi}\mathbf{P}_{n-1|n-1}\mathbf{\Phi}^T\mathbf{C}^T + \mathbf{\Gamma}\mathbf{Q}\mathbf{\Gamma}^T\mathbf{C}^T - \mathbf{k}_n\mathbf{C}\mathbf{\Phi}\mathbf{P}_{n-1|n-1}\mathbf{\Phi}^T\mathbf{C}^T - \mathbf{k}_n\mathbf{C}\mathbf{\Gamma}\mathbf{Q}\mathbf{\Gamma}^T\mathbf{C}^T - \mathbf{k}_n\mathbf{R}$$

using (3.14), it follows

$$\begin{aligned} \mathbf{0} &= \mathbf{P}_{n|n-1}\mathbf{C}^T - \mathbf{k}_n\left[\mathbf{C}\mathbf{P}_{n|n-1}\mathbf{C}^T + \mathbf{R}\right] \\ \mathbf{k}_n &= \mathbf{P}_{n|n-1}\mathbf{C}^T\left[\mathbf{C}\mathbf{P}_{n|n-1}\mathbf{C}^T + \mathbf{R}\right]^{-1} \end{aligned} \tag{3.19}$$

The matrix $\mathbf{k}_n$ is known as the Kalman gain. Finally, we need to compute the formulation for the *a posteriori* error covariance, therefore, from its definition

$$\begin{aligned} \mathbf{P}_{n|n} &= \mathbf{E}\left[\tilde{\mathbf{x}}_n\tilde{\mathbf{x}}_n^T\right] \\ &= \mathbf{P}_{n|n-1} - \mathbf{k}_n\mathbf{C}\mathbf{P}_{n|n-1} - \mathbf{P}_{n|n-1}\mathbf{C}^T\mathbf{k}_n^T + \mathbf{k}_n\left[\mathbf{C}\mathbf{P}_{n|n-1}\mathbf{C}^T + R\right]\mathbf{k}_n^T \end{aligned} \tag{3.20}$$

If we substitute the Kalman gain (3.19), $\mathbf{P}_{n|n}$ becomes:

$$\mathbf{P}_{n|n} = \mathbf{P}_{n|n-1} - \mathbf{k}_n\mathbf{C}\mathbf{P}_{n|n-1} \tag{3.21}$$

3.2.2.3 Algorithm

Algorithm 3.1 shos the Kalman filter, the initialization for $\mathbf{x}_{0|0}$ and $\mathbf{P}_{0|0}$ is zero and the identity matrix, respectively, $\mathbf{\Gamma}$ is the identity matrix and matrices $\mathbf{Q}$ and $\mathbf{R}$ are the tunning parameters of the filter, that should be coherent with the covariance in the model and the sensors respectively. The Kalman filter is similar to the Luenberger observer; notice the similarities by comparing Figures 3.2 and 3.3.

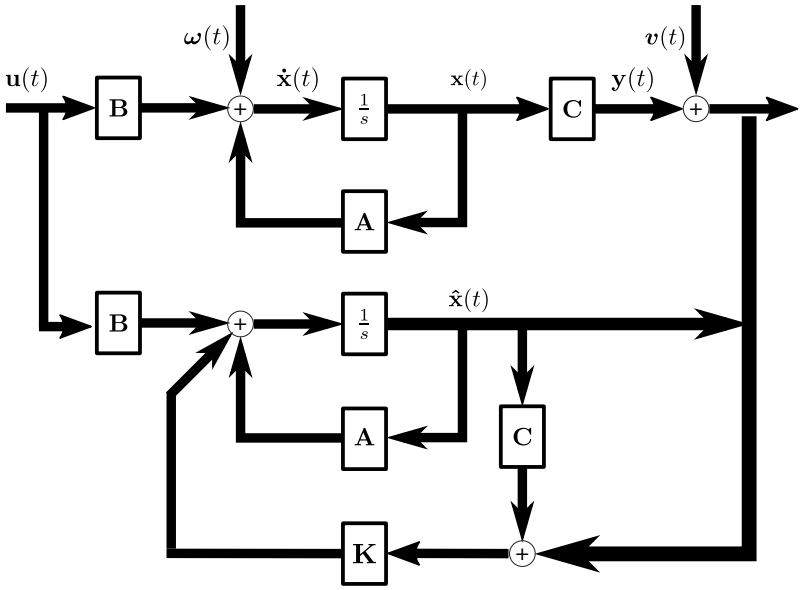

Figure 3.3 – Kalman Filter

Algorithm 3.1: Kalman filter

Initialization

$\mathbf{x}_{0|0}$, $\mathbf{P}_{0|0}$, $\mathbf{\Gamma}$, $\mathbf{Q}$, $\mathbf{R}$

for $(n = 1 : \infty)$

Time update stage (prediction stage)

$$\hat{\mathbf{x}}_{n|n-1} = \mathbf{\Phi}\hat{\mathbf{x}}_{n-1|n-1}$$

$$\mathbf{P}_{n|n-1} = \mathbf{\Phi}\mathbf{P}_{n-1|n-1}\mathbf{\Phi}^T + \mathbf{\Gamma}\mathbf{Q}\mathbf{\Gamma}^T$$

Measurement update stage (correction stage)

$$\mathbf{k}_n = \mathbf{P}_{n|n-1}\mathbf{C}^T\left[\mathbf{C}\mathbf{P}_{n|n-1}\mathbf{C}^T + \mathbf{R}\right]^{-1}$$

$$\hat{\mathbf{x}}_{n|n} = \hat{\mathbf{x}}_{n|n-1} + \mathbf{k}_n\left[\mathbf{z}_n - \mathbf{C}\hat{\mathbf{x}}_{n|n-1}\right]$$

$$\mathbf{P}_{n|n} = \mathbf{P}_{n|n-1} - \mathbf{k}_n\mathbf{C}\mathbf{P}_{n|n-1}$$

end

3.2.3 Observability for linear time varying systems

The estimation techniques presented so far are developed for linear time-invariant models. Nevertheless, nonlinear equations describe many systems in real-life. In this case, we will consider systems with the following form:

$$\begin{aligned} \dot{\mathbf{x}}(t) =& \mathbf{A}(t)\mathbf{x}(t) + \mathbf{B}(t)\mathbf{u}(t) \\ \mathbf{z}(t) =& \mathbf{C}(t)\mathbf{x}(t) \end{aligned} \tag{3.22}$$

where $\mathbf{x}(t)$ is the state of system, $\mathbf{u}(t)$ is the input control, $\mathbf{z}(t)$ is the measurement of the system and, $\mathbf{A}(t)$ and $\mathbf{C}(t)$ are some time-varying matrices.

Definition 3.2.3. *A system expressed with set of equations (3.22) is said to be completely observable if there exist some $t_f > t_0$ such that the initial state x_0 of the system can be determined from the knowledge of $\mathbf{z}(t)$ on the interval $[t_0, t_f]$.*

For the linear-time-invariant system, the Gramian matrix of observability is:

$$\mathbf{O}(t, t_0) = \int_{t_0}^{t_f} \boldsymbol{\phi}^T(t, t_0)\mathbf{C}^T(t)\mathbf{C}(t)\boldsymbol{\phi}(t, t_0)dt$$

where $\boldsymbol{\phi}(t, t_0)$ is the state transfer matrix that transfers the state at t_0 to the state at the moment t.

Theorem 3.2.3. *The system characterized by equations (3.22) is completely observable on the interval $[t_0, t_f]$ if and only if the matrix $\mathbf{O}(t_0, t_f)$ is nonsingular.*

Considering the discrete form of system, and then rewrite system (3.22) as:

$$\begin{aligned} \mathbf{x}_{k+1} =& \boldsymbol{\Phi}_k\mathbf{x}_k + \boldsymbol{\Gamma}\boldsymbol{u}(t) \\ \mathbf{z}_k =& \mathbf{C}_k\mathbf{x}_k \end{aligned} \tag{3.23}$$

Definition 3.2.4. *System (3.23) is said to be locally observable on the interval $[t_k, t_{k+l-1}]$, if for a state $\mathbf{x}_k$, there is a finite $[t_k, t_{k+l-1}]$, such that knowledge of the measurement $\mathbf{z}_k$ from t_k to t_{k+l-1} are sufficient to determine the state $\mathbf{x}_k$ which may be considered as the initial state of the interval, uniquely.*

Definition 3.2.5. *The local observability matrix is*

$$\mathbf{O}_k = \begin{bmatrix} \mathbf{C}_k \\ \mathbf{C}_{k+1}\boldsymbol{\Phi}_k \\ \vdots \\ \mathbf{C}_{k+j-1}\boldsymbol{\Phi}_{k+j-2}\boldsymbol{\Phi}_k \end{bmatrix}$$

3.2.4 Nonlinear estimation - Extended Kalman filter

In this section, the Kalman filter is modified to address nonlinear systems, and the resulting observer/estimator is known as the extended Kalman filter (EKF). Let us consider a nonlinear system of the form

$$\begin{aligned} \mathbf{x}_{n+1} =& \boldsymbol{\phi}\left(\mathbf{x}_{\boldsymbol{n}}\right) + \boldsymbol{\Gamma}\boldsymbol{\omega}_n \\ \mathbf{z}_n =& \boldsymbol{\gamma}(\mathbf{x}_n) + \mathbf{v}_n \end{aligned} \tag{3.24}$$

where $\boldsymbol{\omega}(n)$ and $\mathbf{v}(n)$ are uncorrelated, zero-mean, withe noise processes with covariance matrices $\mathbf{Q}_n$ and $\mathbf{R}_n$, respectively. The operators $\boldsymbol{\phi}(x)$ and $\boldsymbol{\gamma}(x)$ represent nonlinear vector-valued functions of the state, $\mathbf{x}$ and dimension n. Let $\mathbf{x}$ consist of m states, the $\boldsymbol{\phi} \in \mathbb{R}^{m\times 1}$, and as the measurement $\mathbf{z}_n$ are p-vectors, $\boldsymbol{\gamma} \in \mathbb{R}^{p\times 1}$.

The next step to develop the EKF requires linearization of system (3.24). Then, expanding $\boldsymbol{\phi}$ into a first order Taylor expansion series about $\hat{\mathbf{x}}_{n|n}$, gives:

$$\boldsymbol{\phi}(\mathbf{x}_n) = \boldsymbol{\phi}(\hat{\mathbf{x}}_{n|n}) + \mathbf{J}_{\phi}(\hat{\mathbf{x}}_{n|n})\left[\mathbf{x}_n - \hat{\mathbf{x}}_{n|n}\right]$$

where $\mathbf{J}_{\boldsymbol{\phi}}(\mathbf{x})$ is the Jacobian of $\boldsymbol{\phi}$ evaluated at $\mathbf{x}$. Then,

$$\mathbf{J}_{\boldsymbol{\phi}(\hat{\mathbf{x}}_{n|n})}(\hat{\mathbf{x}}_{n|n}) = \frac{\partial \boldsymbol{\phi}}{\partial \hat{\mathbf{x}}_{n|n}} = \begin{bmatrix} \frac{\partial \phi_1}{\partial \hat{x}^{(1)}_{n|n}} & \frac{\partial \phi_1}{\partial \hat{x}^{(2)}_{n|n}} & \cdots & \frac{\partial \phi_1}{\partial \hat{x}^{(m)}_{n|n}} \\ \frac{\partial \phi_2}{\partial \hat{x}^{(1)}_{n|n}} & \frac{\partial \phi_2}{\partial \hat{x}^{(2)}_{n|n}} & \cdots & \frac{\partial \phi_2}{\partial \hat{x}^{(m)}_{n|n}} \\ \vdots & \vdots & \ddots & \vdots \\ \frac{\partial \phi_m}{\partial \hat{x}^{(1)}_{n|n}} & \frac{\partial \phi_m}{\partial \hat{x}^{(2)}_{n|n}} & \cdots & \frac{\partial \phi_m}{\partial \hat{x}^{(m)}_{n|n}} \end{bmatrix}$$

Likewise, for $\boldsymbol{\gamma}(\mathbf{x}_n)$, we expand about $\hat{\mathbf{x}}_{n|n-1}$, gives:

$$\boldsymbol{\gamma}\left(\mathbf{x}_n\right) = \boldsymbol{\gamma}\left(\hat{\mathbf{x}}_{n|n-1}\right) + \mathbf{J}_{\boldsymbol{\gamma}}(\hat{\mathbf{x}}_{n|n-1})\left[\mathbf{x}_n - \hat{\mathbf{x}}_{n|n-1}\right]$$

with

$$\mathbf{J}_{\boldsymbol{\gamma}(\hat{\mathbf{x}}_{n|n-1})}(\hat{\mathbf{x}}_{n|n-1}) = \frac{\partial \boldsymbol{\gamma}}{\partial \hat{\mathbf{x}}_{n|n-1}} = \begin{bmatrix} \frac{\partial \gamma_1}{\partial \hat{\mathbf{x}}^{(1)}_{n|n-1}} & \frac{\partial \gamma_1}{\partial \hat{\mathbf{x}}^{(2)}_{n|n-1}} & \cdots & \frac{\partial \gamma_1}{\partial \hat{\mathbf{x}}^{(m)}_{n|n-1}} \\ \frac{\partial \gamma_2}{\partial \hat{\mathbf{x}}^{(1)}_{n|n-1}} & \frac{\partial \gamma_2}{\partial \hat{\mathbf{x}}^{(2)}_{n|n-1}} & \cdots & \frac{\partial \gamma_2}{\partial \hat{\mathbf{x}}^{(m)}_{n|n-1}} \\ \vdots & \vdots & \ddots & \vdots \\ \frac{\partial \gamma_p}{\partial \hat{\mathbf{x}}^{(1)}_{n|n-1}} & \frac{\partial \gamma_p}{\partial \hat{\mathbf{x}}^{(2)}_{n|n-1}} & \cdots & \frac{\partial \gamma_p}{\partial \hat{\mathbf{x}}^{(m)}_{n|n-1}} \end{bmatrix}$$

by now, we have a linearized state-space model given by

$$\begin{aligned} \mathbf{x}_{n+1} =& \boldsymbol{\phi}(\hat{\mathbf{x}}_{n|n}) + \mathbf{J}_{\phi}(\hat{\mathbf{x}}_{n|n}) \left[\mathbf{x}_n - \hat{\mathbf{x}}_{n|n}\right] + \boldsymbol{\Gamma}\boldsymbol{\omega}_n \\ \mathbf{z}_n =& \boldsymbol{\gamma}\left(\hat{\mathbf{x}}_{n|n-1}\right) + \mathbf{J}_{\boldsymbol{\gamma}}(\hat{\mathbf{x}}_{n|n-1}) \left[\mathbf{x}_n - \hat{\mathbf{x}}_{n|n-1}\right] + \mathbf{v}_n \end{aligned} \tag{3.25}$$

We have skipped some steps; if required, please follow the same pattern as the linear Kalman filter.

3.2.4.1 Prediction stage

The *a priori* estimate is given by

$$\begin{aligned} \hat{\mathbf{x}}_{n|n-1} =& \boldsymbol{\phi}\left(\hat{\mathbf{x}}_{n-1|n-1}\right) \\ \mathbf{P}_{n|n-1} =& \mathbf{J}_{\boldsymbol{\phi}(\hat{\mathbf{x}}_{n|n-1})} \mathbf{P}_{n-1|n-1} \mathbf{J}^T_{\boldsymbol{\phi}(\hat{\mathbf{x}}_{n|n-1})} + \boldsymbol{\Gamma}\mathbf{Q}_k\boldsymbol{\Gamma}^T \end{aligned}$$

3.2.4.2 Measurement Update stage

The *a posteriori* estimate is given by

$$\begin{aligned} \hat{\mathbf{x}}_{n|n} =& \hat{\mathbf{x}}_{n|n-1} + \mathbf{k}_n \left[\mathbf{z}_n - \mathbf{J}_{\boldsymbol{\gamma}(\hat{\mathbf{x}}_{n|n-1})} \hat{\mathbf{x}}_{n|n-1}\right] \\ \mathbf{P}_{n|n} =& \mathbf{P}_{n|n-1} - \mathbf{k}_n \mathbf{C} \mathbf{P}_{n|n-1} \\ \mathbf{k}_n =& \mathbf{P}_{n|n-1} \mathbf{J}^T_{\boldsymbol{\gamma}(\hat{\mathbf{x}}_{n|n-1})} \left[\mathbf{J}_{\boldsymbol{\gamma}(\hat{\mathbf{x}}_{n|n-1})} \mathbf{P}_{n|n-1} \mathbf{J}^T_{\boldsymbol{\gamma}(\hat{\mathbf{x}}_{n|n-1})} + \mathbf{R}_{\mathbf{k}}\right]^{-1} \end{aligned}$$

3.3 State of the art on sideslip angle estimation

Research on vehicle dynamics active control has been more diligent in recent years. Active safety systems improve vehicle stability during critical maneuvers by applying specific inputs from the braking, steering, or drive systems. The sideslip angle measures vehicle lateral drift; therefore, many vehicle dynamics control schemes use the sideslip angle to improve the stability of the vehicle, see [Abe et al., 2001, Zhu et al., 2013, Klomp et al., 2014, Reif, 2014, Tchamna and Youn, 2013]. Nowadays, three main categories of vehicle sideslip angle estimation exist:

- Kinematic-based Observer: This approach uses the kinematic model for an estimate of the object velocities; taking advantage of some non-holonomic constraints, the model is simplified. The most significant benefit of state estimation based on kinematic models is that they are immune to parameter variations and unknown disturbances. Since it suggests using a combination of low-cost sensors, these transducers' specific characteristics will have a significant effect on the performance of the state estimator.

- Dynamic-based Observer: This approach uses the vehicle dynamic model for state estimations. Besides using low-cost sensors, the method requires a model; this implies that its performance is also related to the model complexity and the prior knowledge of its parameters. Another degree of complexity is introduced with the description of the tires and their interaction with the road.

- Neural network-based: This method does not require the vehicle model either its parameters; nonetheless, the estimation results depend on how accurately the training dataset represents the actual vehicle behavior.

3.3.1 Kinematics Models

Kinematic models are simple and depend on the velocity of the vehicle. Including the non-holonomic constraints of a ground vehicle, we neglect the vertical speed

$$\mathbf{v}_g = v_x \boldsymbol{i} + v_y \boldsymbol{j} \tag{3.26}$$

where $\mathbf{v}_g$ stands for the velocity vector, v_x and v_y means the longitudinal and lateral velocity, respectively, $\boldsymbol{i}$ and $\boldsymbol{j}$ are unit vectors aligned with the body coordinate frame of reference. The time derivative of (3.26) is

$$\boldsymbol{a_g} = a_x \boldsymbol{i} + a_y \boldsymbol{j} = \frac{d\boldsymbol{v_g}}{dt} = \dot{v}_x \boldsymbol{i} + v_x \frac{d\boldsymbol{i}}{dt} + \dot{v}_y \boldsymbol{j} + v_y \frac{d\boldsymbol{j}}{dt} \tag{3.27}$$

where $\frac{d\boldsymbol{i}}{dt} = \omega_z \boldsymbol{j}$ and $\frac{d\boldsymbol{j}}{dt} = -\omega_z \boldsymbol{i}$, gives:

$$\begin{aligned} a_x &= \dot{v}_x - v_y \omega_z \\ a_y &= \dot{v}_y + v_x \omega_z \end{aligned} \tag{3.28}$$

The kinematic model observer-based approaches mainly use (3.28) to estimate lateral speed and the sideslip angle from its definition (**??**). Moreover, from (3.26), and considering small sideslip angles, $\beta << 1$, such that, $|| \mathbf{v}_g ||_2 \approx v_x$, and given the sideslip definition (2.2), is possible to consider $v_y \approx v_x \beta$, then the sideslip angle time derivative could be expressed as:

$$\dot{\beta} = \frac{a_y - a_x \beta - \omega_z v_x}{v_x} \tag{3.29}$$

Equation (3.29) have already introduced considerations that do not hold with sideslip angles higher than ten degrees; most sideslip estimation schemes based on dynamic models introduce this consideration. Therefore, in order to avoid such

assumptions, from (3.28) the velocity derivatives $\dot{v}_x$ and $\dot{v}_y$ are isolated as:

$$\begin{aligned} \dot{v}_x &= a_x + v_y\omega_z \\ \dot{v}_y &= a_y - v_x\omega_z \end{aligned} \tag{3.30}$$

Many approaches use the set of equations (3.30) and solve using an observation strategy. Nonetheless, they assume that the road surface is horizontal. This assumption is not accurate on regular driving maneuvers. Therefore including the slope and bank angle in (3.30), gives:

$$\begin{aligned} \dot{v}_x =& a_x + v_y\omega_z + g\sin(\theta_r) \\ \dot{v}_y =& a_y - v_x\omega_z - g\cos(\theta_r)\sin(\phi_r) \end{aligned} \tag{3.31}$$

where θ_r stands for the slope road angle, and ϕ_r means the bank road angle.

The main strategies to estimate the vehicle sideslip angle are known in the control research domain: Luenberger Observer (LO), Kalman Filter (and its variants), and lately, linear parameter varying (LPV) Observer.

There are many works on the literature referring to kinematic based-observers; in this section, we will describe three propositions made relatively recently.

In [Grip et al., 2009], the author proposes a pure kinematic model approach; the system (3.31) includes the slope and bank angles. The signals required to apply this strategy are the accelerations in the longitudinal and lateral direction, the yaw rate, and the vehicle tires' angular speed to emulate the longitudinal speed of the vehicle. The observer has a nonlinear Luenberger-structure, where the observer gain complies with the system stability on the Lyapunov sense.

In [Madhusudhanan et al., 2016], the authors used an extended Kalman filter build with system (3.30). The Kinematic model was modified to have a smooth transition between the maneuvers with and without lateral excitation. The modification is:

$$\begin{bmatrix} \hat{\dot{v}}_x \\ \hat{\dot{v}}_y \end{bmatrix} = \begin{bmatrix} 0 & \omega_z \\ -\omega_z & f_v \end{bmatrix} \begin{bmatrix} \hat{v}_x \\ \hat{v}_y \end{bmatrix} + \begin{bmatrix} \frac{1}{m} & 0 \\ 0 & \frac{1}{m} \end{bmatrix} \begin{bmatrix} F_x \\ F_y \end{bmatrix}$$

with

$$f_v = \begin{cases} -20\left(1 - \frac{\omega_z^2}{0.01\frac{\pi^2}{180^2}}\right), \text{if } \mid \omega_z \mid < 0.1\text{deg/s and } \mid F_y \mid < 100\text{Newtons} \\ 0 \end{cases}$$

This approach's particularity relies on the use of load-bearing sensors to compute

equivalent accelerations from its measurement of normal, longitudinal, and lateral forces; nonetheless, the equivalent accelerations resulting from the system do not overcome disturbances introduced by the road profile (bank and slope angle).

In [Selmanaj et al., 2017a], the authors use a pure kinematic model complemented with a smoothing function to prevent deviation due to accumulated integration errors. Instead of f_v, the use a value $F(t)$, choosing $F(t) > 0$ and sufficiently high when the vehicle is moving straight, the lateral velocity converge to zero. The value of $F(t)$ is scheduled by a heuristic algorithm that identifies straight driving. The sensor required is an inertial measurement unit, compensated for bias and the gravity components affecting the acceleration measurements and the longitudinal speed. The observation technique is a nonlinear observer with the same structure as the LO. The resulting outputs are the lateral and longitudinal vehicle speeds.

In Section 3.4 our proposal is presented, and how we have handled the problems inherent to kinematic-based-model observation schemes.

3.3.2 Dynamic Models

The dynamic models provide a more detailed explanation of the vehicle. Then, from (2.21), the single-track model is modified to be a function of the sideslip angle, hence,

$$\begin{aligned} m\dot{v}_x &= \sum_{j\in\mathcal{A}} F_{x_{1j}}\cos(\delta) - \sum_{j\in\mathcal{A}} F_{y_{1j}}\sin(\delta) + \sum_{j\in\mathcal{A}} F_{x_{2j}} - \frac{1}{2}\rho C_{Dx} S_x \bar{v}_x^2 - mg\sin(\theta_r) + \beta v_x \omega_z \\ m\dot{\beta} &= \frac{1}{v_x}\left[\sum_{j\in\mathcal{A}} F_{x_{1j}}\sin(\delta) + \sum_{j\in\mathcal{A}} F_{y_{1j}}\cos(\delta) + \sum_{j\in\mathcal{A}} F_{y_{2j}} - mg\sin(\phi_r)\cos(\theta_r)\right] - \omega_z \\ I_z\dot{\omega}_z &= l_1 m a_y - l\sum_{j\in\mathcal{A}} F_{y_{1j}} \end{aligned} \tag{3.32}$$

Several authors use different vehicle dynamical models, but the single-track model is the most common for the sideslip angle estimation problem. One common consideration among observers based on dynamical models is that longitudinal speed v_x is constant.

In [Bevly et al., 2001], on the one hand, the author proposes the use of GPS velocity measurements to determine the direction of travel. On the other hand, the vehicle heading is estimated by direct integration of a gyroscope in the z-axis while turning. The integration computation is reset and biased compensated during

straight driving. The sideslip angle is obtained from

$$\hat{\beta} = \psi_{GPS} - \hat{\psi}_{\int Gyro}$$

where ψ_{GPS} and $\hat{\psi}_{\int Gyro}$ are the orientation measured with the GPS and the orientation estimation given by the direct integration. Later on $\hat{v}_y = v_g^{GPS} \sin(\hat{\beta})$ the lateral speed is obtained.

In [Bevly et al., 2006], the author compares the approach presented in [Bevly et al., 2001], against a two GPS antenna approach. The two GPS antennas can accurately estimate the road bank angle and improve the sideslip angle estimation. Additionally, with a Kalman filter, the cornering stiffnesses for the front and rear axle are estimated.

In [**?**], the author describes a simple observer structure that contains a sliding mode term that includes robustness against output noises and parameter variations as sustained disturbances. The vehicle's nonlinear model is represented by an uncertain Takagi-Sugeno fuzzy model when the road adhesion conditions change, and the sideslip angle is unavailable for measurement. The stability conditions of such observers are expressed in linear matrix inequalities. The scheme is validated with numerical simulations. Moreover, in [**?**], the author can use the closed-loop observer to develop a closed-loop controller and validate it through simulation.

In [Stéphant et al., 2007], the authors develop a two stages observer; during the first stage, a SMO is developed based on the bicycle model, while assuming the lateral and longitudinal force time derivative as random walk variables. In this step, the yaw rate and the longitudinal and lateral forces at each tire are estimated. On the second stage, an EKF estimates the sideslip angle and the cornering stiffness. One advantage of using this type of structure is that the EKF filters the sliding modes observer's outputs and correct them.

In [You et al., 2009], a similar approach is taken into account. Still, lateral load transfer and traction/braking force are known values, improving the cornering stiffness and the sideslip angle estimations.

In [Zhao et al., 2011] the authors proposed a nonlinear observer for estimating the vehicle velocity with a bicycle model and Dugoff's tire model. The nonlinear observer complies with the observability criterion in the Lyapunov sense. The measurements required are the longitudinal and lateral acceleration, as the yaw rate.

In [Antonov et al., 2011], the authors consider a passenger vehicle equipped with standard vehicle dynamic control sensors, the propulsion, and the braking torques of the wheels are known. They use the planar two-track vehicle model as a

basis for the uncented Kalman filter (UKF) design. A method for the vertical tire forces calculation is developed, which additionally accounts for the tire stiffness. The simplified empirical Magic Formula is used for describing the tire/road interactions. Afterward, the performance of the augmented state UKF implementation is evaluated, employing real vehicle tests.

In [Nguyen et al., 2012], the heading measurement from a GPS is used to estimate the sideslip angle, also requires the steering angle and the yaw rate. The authors use the bicycle model to build its Kalman filter; here, the asynchronous measurement problem is addressed.

In [Yoon and Peng, 2013], the heading and roll angles to the inertial frame of reference are computed with a Kalman filter using a magnetometer sensor, the yaw rate, and the roll rate measurements. The sideslip angle is estimated using the previously obtained estimations and fusing them with the accelerometer measurements and the GPS sensor's velocities.

In [Chen et al., 2014] the authors use a SMO build over a vehicle dynamics 5-order model composed of the bicycle model and four single corner representations.

In [Gadola et al., 2014] an EKF is proposed to estimate the sideslip angle based on a single-track model using a family of curves representing a generic Pacejka magic tire model. Another critical part of this work is the way to update the $\mathbf{Q}$, $\mathbf{R}$ matrices with and optimization tool, over,

$$\min \left(|| \begin{bmatrix} a_y \\ \phi \end{bmatrix} - \mathbf{H}\hat{\mathbf{x}}^{-} ||_2 \right)$$

In [Zhang et al., 2016a, Zhang et al., 2016b], the estimation scheme is a LPV observer build over the lateral dynamics of the bicycle model. With this approach, the velocity is not considered constant. The observer gain is obtained through optimization by solving a linear matrix inequality (LMI) to comply with the stability constraints in the Lyapunov sense.

In [Katriniok and Abel, 2016], show a complete tire force estimation scheme, using the magic tire. The inputs are a_x, a_y, $\dot{\psi}$, v_g virtual measurements of the friction are added $\mu_x = 0$ if observable, $\mu_x = \mu_x$ if not. The same goes for μ_y. Observability is verified each iteration and if not observable choose between the values available of friction.

In [Naets et al., 2017], the estimation scheme is an EKF build over a bicycle model, complemented with Dugoff models boosted with cornering stiffness adaptation through the nonlinear least-squares method. This method requires the steering angle, lateral and longitudinal accelerations, yaw rate, tire angular speed, and the

actual car speed obtained through GPS.

In [Chen et al., 2018], the estimation scheme is a nonlinear Luenberger-structure observer over the lateral dynamics of the bicycle model, where the observer gain is found through Lyapunov functions. The scheme requires the IMU and GPS.

All the approaches mentioned above use kinematic equations somehow; however, some use the dynamical models that require prior knowledge on the vehicle mass, the cornering stiffness for the virtual front and rear tires. Our proposal has more similarity with [Grip et al., 2009, Madhusudhanan et al., 2016, Selmanaj et al., 2017b], but do not require load-bearing sensors nor heuristic methods to ensure the system's observability. We introduce the random walk variables into the observation matrix to solve the observability dilemma; besides, we compensate for the lateral speed estimation with gyroscope measurements and its rotation defined by quaternion operations.

3.3.3 Neural Network

Currently, the research community has been experiencing a rise in the use of machine learning techniques, especially neural networks, to solve complex problems. The vehicle sideslip angle estimation is no exception; several works can be found in the literature, see [Busnelli et al., 2017] and [De Martino et al., 2017].

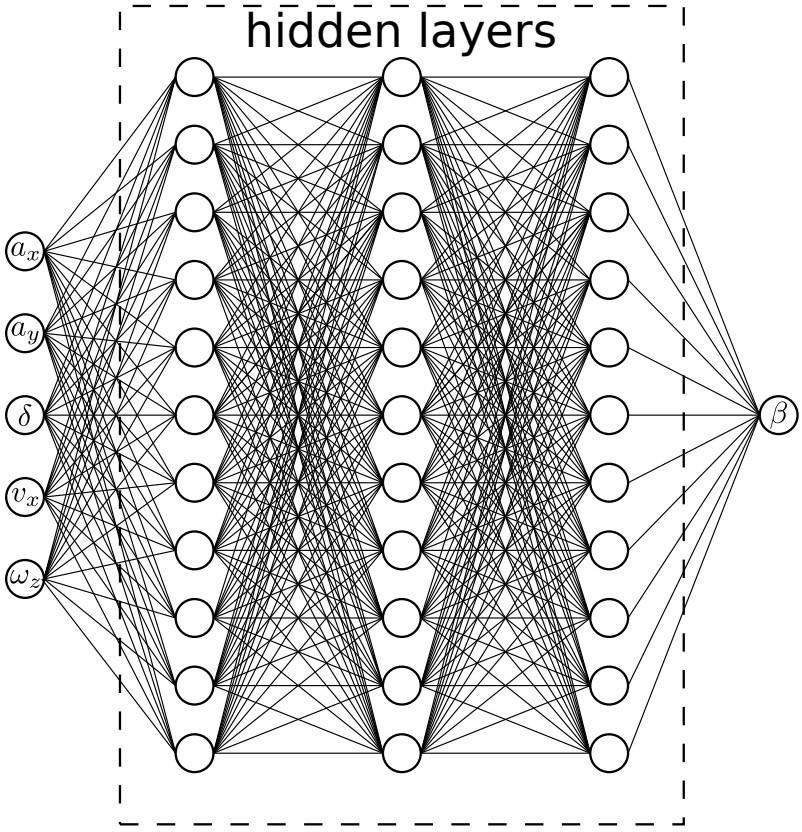

Figure 3.4 – Neural network structure

Figure 3.4 shows a generic neural network structure. In this particular case, the network's inputs are the longitudinal and lateral acceleration, a_x, and, a_y, respectively, the steering angle, δ, the longitudinal speed, v_x, is considered available, and the yaw rate, ω_z. This network has three hidden layers with 11 neurons each, and the sideslip angle, β, is the output. Nevertheless, a neural network structure could be modified to include more hidden layers, neurons, inputs, or outputs. Current advances in technology, specifically the increase in computational power, enable machine learning or neural networks to solve complex problems that were impossible to solve in the past.

The advantage of using a neural network approach is that you do not need information about the system. Through optimization, the network is trained to find the transfer function between the inputs and outputs. Nonetheless, to apply this technique successfully, vast amounts of data are required to perform its training. The training dataset has to represent the system behavior and scenarios; if not, the results might be inaccurate.

3.4 Contribution to the sideslip angle estimation

Sideslip angle estimation is a well-studied research topic, and small differences arise between the proposals found in the literature. In this work, we will focus on observer-based approaches and explain the method selected from this point forward.

The kinematic approach does not require specific information about the vehicle such as the cornering stiffness, the mass, the inertias; on the contrary, needs the position placement of the sensors, Ω_{ij}, ω_z, a_x, a_y, to be able to extrapolate the sideslip angle to a specific coordinate position in the vehicle body. The lateral speed estimation at the COG is a complicated task. The COG position on the vehicle is not constant, and it changes according to the vehicle's cargo distribution. Nonetheless, if the COG position is known in advance with a nonlinear transformation, the COG's lateral speed could be estimated. The COG position estimation is addressed in Chapter 4.

A dynamic-based-model observer needs to comply with the Newton-Euler laws of motion; the tire-ground forces are estimated using a force tire model formulations as the magic tire or the Dugoff's tire model. Nonetheless, the introduction of a model needs to include parameters that shall be identified. Similarly, the COG position and the vehicle's mass are considered known variables; moreover, several values that should be identified directly depend on the vehicle mass and its COG coordinates.

If we address a specific problem to solve, it becomes easier to decide how to arrive at a solution.

On the one hand, if we are trying to estimate the sideslip angle in racing Formula one car, see 3.5(a), it is accurate to say that the vehicle parameters could be identified in advance. Therefore, as the COG position and the vehicle mass are known, any of the approaches presented to solve the sideslip angle estimation problem are a good fit to solve this task. If the information provided's accuracy is addressed, a method that uses as much information possible will be the best.

On the other hand, if we deal with estimating the sideslip angle for mass-produced vehicles, the problem's complexity increases when considering the system's variability. With this type of vehicle, we could not expect to ask the driver for information about the vehicle's extra cargo, how many passengers and how many pieces of baggage, etc. Therefore, the estimation results will be inaccurate using dynamical models since the vehicle mass differs from the expected value. For sure, a closed-loop observer solves this problem; nevertheless, if we include these uncertainties at the observer design stage with classical approaches, the system

becomes unobservable. The unique solution presented so far is to use deflection sensors or tire-force transducers, but not many vehicles have deflection sensors, even less tire-force transducers. Using kinematic models, we require the COG position to successfully translate the sideslip angle from the estimation point to the COG; nonetheless, the sideslip angle at the axles could be accurately estimated since the axle position is known by design.

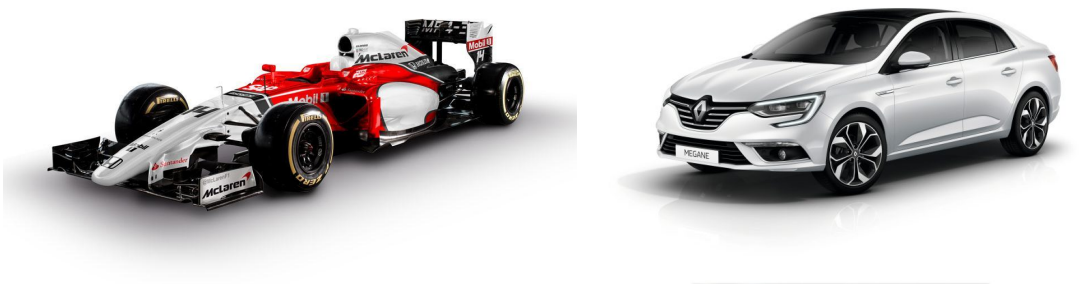

(a) Formula 1 vehicle (b) Renault Megane Sedan

Figure 3.5 – Vehicles for different purposes: Competition and daily life

This chapter aims to develop a black box able to reconstruct vehicle states for commercial vehicles; therefore, for our purposes, a kinematic model-based observer is simply a better fit. Nonetheless, if the COG position is not available, this uncertainty is addressed via proper observer tunning. For our purposes, we use an EKF to overcome the model uncertainty, sensor bias, and noise through appropriate tunning matrices $\mathbf{Q}$ and $\mathbf{R}$.

All the tests presented in this chapter are obtained from an experimental testbed; a 2011 Range Rover Evoque, see Figure 1.5; the test was performed at Lommel proving ground in Belgium under dry conditions. This vehicle is instrumented with two force transducers at the rear wheels, which measures the forces and torques at the longitudinal, lateral, and vertical directions. Additionally, it is instrumented with an IMU that measures the accelerations and angular rates for the x, y, and z axis.

3.4.1 Kinematic System Analysis

From the kinematic model (3.28) without considering a planar road, the following state-space representation is introduced:

$$\begin{aligned}\dot{\mathbf{x}}(t) &= \mathbf{A}(t)\mathbf{x}(t) + \mathbf{B}\mathbf{u}(t)\\ \mathbf{y}(t) &= \mathbf{C}\mathbf{x}(t)\end{aligned} \tag{3.33}$$

where:

$$\mathbf{A}(t) = \begin{bmatrix} 0 & \omega_z(t) \\ -\omega_z(t) & 0 \end{bmatrix};\ \mathbf{B} = \begin{bmatrix} 1 & 0 \\ 0 & 1 \end{bmatrix};\ \mathbf{C} = \begin{bmatrix} 1 & 0 \end{bmatrix}$$

with $\mathbf{x}(t) = \begin{bmatrix} v_x(t) & v_y(t) \end{bmatrix}^T$; $\mathbf{u}(t) = \begin{bmatrix} a_x(t) & a_y(t) \end{bmatrix}^T$. Two scenarios are important for (3.33), when ω_z equals zero, and all other values for ω_z. When $\omega_z = 0$, the observability of the system reduces to unity. Nonetheless, when $\omega_z \neq 0$, system (3.33) is fully observable. As mentioned in the literature review section, many authors have decided to use the bicycle model to deal with unobservable states, v_y, and others have modified the state matrix, $\mathbf{A}(t)$, to include a function that eliminates the observability problem.

3.4.1.1 Comparison between observers build from different models

In this section, a comparison between observers is based on different models. For each comparison, the difficulty degree of the maneuver is upgraded. Thus, we will start analyzing maneuvers on a plane road and increase the road complexity with unknown road profiles consisting of non-zero slope and bank angles.

In system (3.33) the output equation assumes knowledge on the longitudinal speed v_x, this measurement could be computed from the angular speed sensor at the wheels, with $v_x(t) \approx \frac{1}{2}\sum_{j=1}^{2}\Omega_{2j}(t)$. Usually, vehicles with front-wheel driven sets give an excellent computation of this state; nonetheless, it could fail during vehicle braking, since the wheels could be locked.

System (3.33) requires to be transformed into a discrete state-space equation, and we have decide to use the simple Euler discrete transformation $\dot{x} \approx \frac{x_{k+1}-x_k}{\Delta t}$

$$\mathbf{x}_{n|n} = \mathbf{\Phi}_n\mathbf{x}_{n-1|n-1} + \mathbf{\Gamma}_n\mathbf{u}_n \tag{3.34a}$$

$$\mathbf{y}_{n|n} = \mathbf{C}_n\mathbf{x}_{n|n} \tag{3.34b}$$

where

$$\begin{aligned}\mathbf{\Phi}_k &= \mathbf{I} + \Delta t \mathbf{A}_k \\ \mathbf{\Gamma} &= \Delta t \mathbf{B}\end{aligned}$$

here $\mathbf{I}$ is an identity matrix with proper dimensions such that matrix operations are consistent, and Δt is the sampling period.

The observer choose is an EKF,

$$\begin{aligned}\hat{\mathbf{x}}_{n|n} &= \mathbf{\Phi}_k \hat{\mathbf{x}}_{n-1|n-1} + \mathbf{\Gamma}\mathbf{u}_{n|n} + \mathbf{K}_n \left[\mathbf{z}_n - \mathbf{C}\left(\mathbf{\Phi}_k \hat{\mathbf{x}}_{n-1|n-1} + \mathbf{\Gamma}\mathbf{u}_{n|n}\right)\right] \\ \mathbf{P}_{n|n} &= \mathbf{\Phi}_n \mathbf{P}_{n-1|n-1} \mathbf{\Phi}_n^T + \mathbf{Q} - \mathbf{K}_n \mathbf{C}_n \left(\mathbf{\Phi}_n \mathbf{P}_{n-1|n-1} \mathbf{\Phi}_n^T + \mathbf{Q}\right)\end{aligned} \tag{3.35}$$

with

$$\mathbf{K}_n = \left(\mathbf{\Phi}_n \mathbf{P}_{n-1|n-1} \mathbf{\Phi}_n^T + \mathbf{Q}\right) \mathbf{C}^T \left[\mathbf{C}\left(\mathbf{\Phi}_n \mathbf{P}_{n-1|n-1} \mathbf{\Phi}_n^T + \mathbf{Q}\right) \mathbf{C}^T + \mathbf{R}\right]^{-1} \tag{3.36}$$

where $\mathbf{Q}$ and $\mathbf{R}$ represent the state process noise and the output noise matrices, respectively.

The first test is conducted with an ISO double lane change maneuver at 30 kph (kilometers per hour), in a flat and dry surface. Figure 3.6 shows the main accelerations, the steering angle evolution, and the vehicle trajectory. Notice that the accelerations levels are at maximum values of $\mid a_x \mid = 2$ and $\mid a_y \mid = 4$. For more information on the ISO double lane change, see Appendix B.

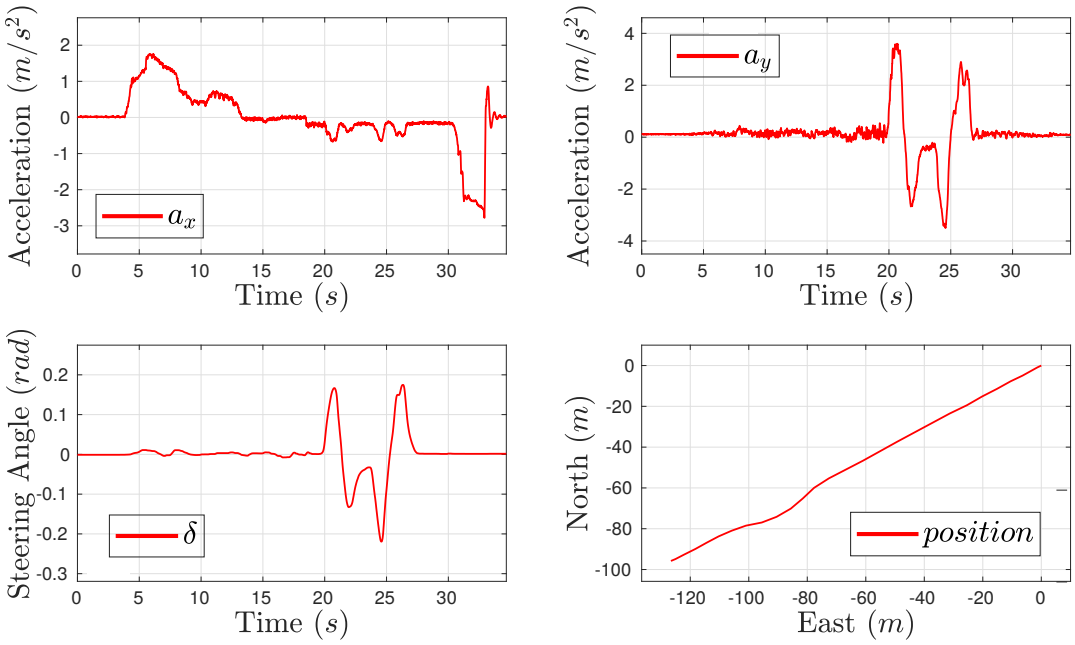

Figure 3.6 – ISO double lane change at 30 kph

Figure 3.7, shows the response of observer (3.35) applied to system (3.34). In Figure 3.7(a), the estimation for the longitudinal speed is depicted with a red-solid line and with a black-dashed line the actual longitudinal vehicle speed. Notice the accuracy of the longitudinal speed estimation, $\hat{v}_x$. Figure 3.7(b), shows a poor lateral estimation response, caused by the noise and bias from the measurements and second by the reduced observability during the straight driving part of the test. This was perceived in several works, see [Madhusudhanan et al., 2016, Selmanaj et al., 2017a, Grip et al., 2009]

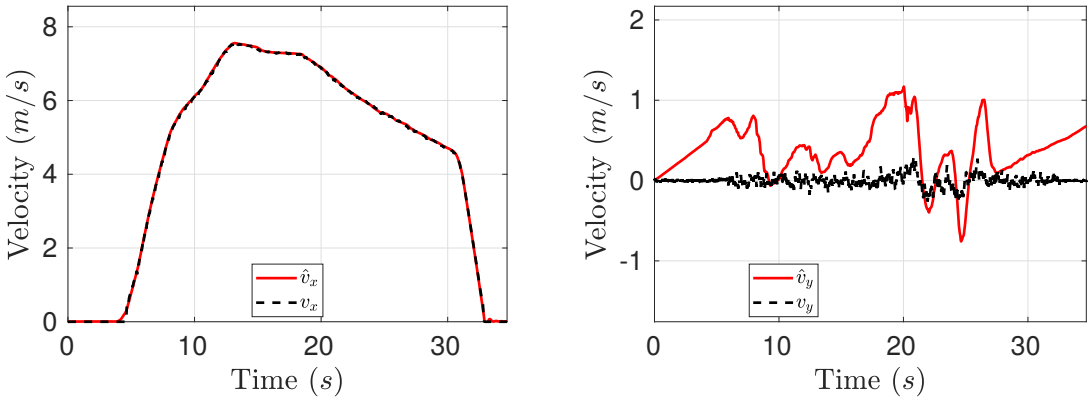

(a) Longitudinal speed comparison between observer response $\hat{v}_x$ and actual velocity v_x.

(b) Lateral speed comparison between observer response $\hat{v}_y$ and actual velocity v_y.

Figure 3.7 – Comparison of the longitudinal and lateral speeds for system (3.34a)-(3.34b) performing an ISO double lane change.

A vast number of complex solutions has been proposed to solve the issues of lateral speed estimatiop (observability, bias, and noise); with our proposal, the original process state-space system (3.34a) remains invariant; in exchange, we modify the output system to ensure system full-observability, even while the yaw rate, ω_z, is close to zero.

3.4.2 First solution [Consideration of $v_g = v_x$]

Lets consider the following linear time varying system:

$$\mathbf{x}_{n|n} = \mathbf{\Phi}_n \mathbf{x}_{n-1|n-1} + \mathbf{\Gamma}_n \mathbf{u}_n \tag{3.37a}$$

$$\mathbf{y}_{n|n} = \mathbf{C^1}_n \mathbf{x}_{n|n} \tag{3.37b}$$

where $\mathbf{\Phi}_n$, $\mathbf{x}_{n|n}$, $\mathbf{\Gamma}_n$, $\mathbf{u}_n$ are already defined in (3.34) and

$$\mathbf{C^1}_n = \begin{bmatrix} 1 & 0 \\ \hat{x}_{1,n|n-1} & \hat{x}_{2,n|n-1} \end{bmatrix}$$

which means that the measurement is $\mathbf{z} = \begin{bmatrix} v_x & v_x^2 \end{bmatrix}^T$. Last statement considers $v_x^2 \approx || \mathbf{v}_g ||_2^2$.

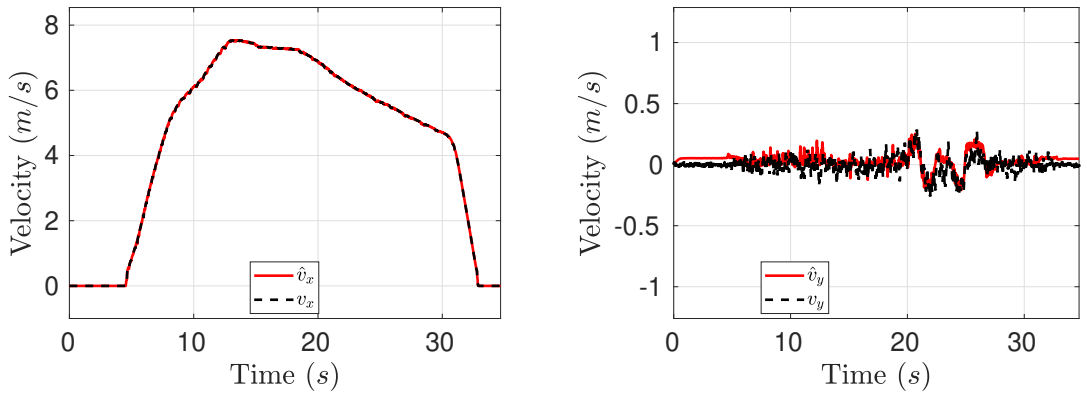

(a) Longitudinal speed comparison between observer response $\hat{v}_x$ and actual velocity v_x.

(b) Lateral speed comparison between observer response $\hat{v}_y$ and actual velocity v_y.

Figure 3.8 – Comparison of the longitudinal and lateral speeds for system (3.37) performing an ISO double lane change.

Figure 3.8 shows the Kalman filter (3.35) response to the same maneuver. Notice in Figure 3.8(b) the improvement for the lateral speed estimation. The system achieves full observability for all time with $\mathbf{C^1}_n$, the color and shapes are maintained to preserve readability. The filter solves the noise and bias problems with proper tunning. The estimation for the lateral speed is improved due to the imposed constraint added by the virtual measurement of $|| \mathbf{v}_g ||_2^2$. The error introduced with this consideration is also handled with proper tuning of the filter.

3.4.3 Second solution [Consideration of $v_y = 0$]

Section 3.4.2 solves the observability problem; nonetheless, the poor performance of the estimation gives room for improvement. Notice that the output matrix $\mathbf{C^1}_n$ is time-varying, which increases the computation time and optimality of our observations scheme. Another approach to ensure full-observability is to consider a virtual measurement for the lateral speed equal to zero, $v_y = 0$; in this case, the actual measurement is the amplitude of the virtual measurement noise. Thus, again

the output equation is modified to:

$$\mathbf{x}_{n|n} = \mathbf{\Phi}_n \mathbf{x}_{n-1|n-1} + \mathbf{\Gamma}_n \mathbf{u}_n \tag{3.38a}$$

$$\mathbf{y}_{n|n} = \mathbf{C^2} \mathbf{x}_{n|n} \tag{3.38b}$$

with

$$\mathbf{C^2} = \begin{bmatrix} 1 & 0 \\ 0 & 1 \end{bmatrix}$$

In this case $\mathbf{z} = \begin{bmatrix} v_x & 0 \end{bmatrix}^T$, which means $v_y = 0 + w_{v_y}$, with w_{v_y} as a random centered noise and v_y as a random walk variable.

Figure 3.9 displays the filter response for the same maneuver. Notice that in Fig. 3.9(b) the lateral speed estimation, $\hat{v}_y$, shows less noise at striaght driving when compared against the results in Fig. 3.8(b). The consideration presented in this section $v_y = 0$ is exactly the same as $|| \mathbf{v}_g ||_2^2$, the difference relies on the discrete handling of matrices $\mathbf{C^1}_n$ and $\mathbf{C^2}$.

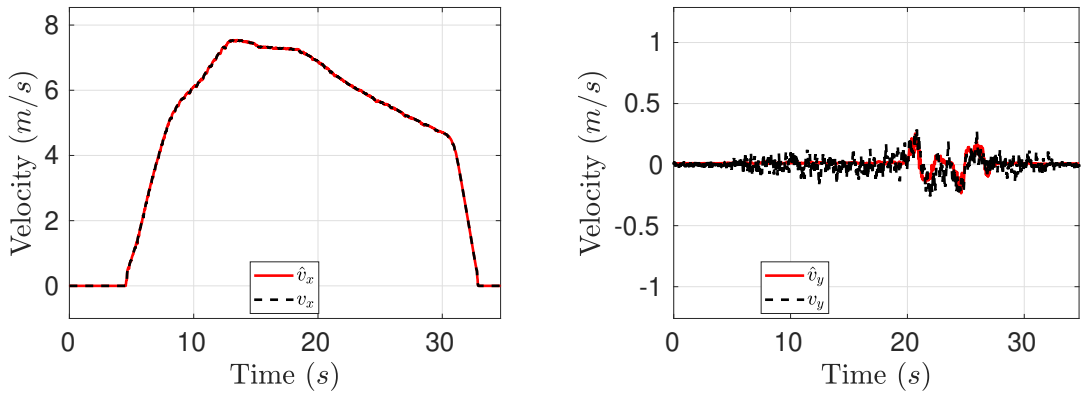

(a) Longitudinal speed comparison between observer response $\hat{v}_x$ and actual velocity v_x.

(b) Lateral speed comparison between observer response $\hat{v}_y$ and actual velocity v_y.

Figure 3.9 – Comparison of the longitudinal and lateral speeds for system (3.38) performing an ISO double lane change.

The tests presented up to this point are in flat roads; the observer's performance still has to be tested with at roads with bank and slope angles.

3.4.4 Considering bank and slope angle

This section introduces another degree of freedom; the maneuver now includes bank and slope angles. The road in which the new mission is performed has a different bank and slope angles. In this case, the vehicle drives the track two times.

During the first lap, medium speed is pursued; consequently, the maximum lateral acceleration achieved is 5 m/s^2. We aim to finish the second lap as soon as possible; therefore, the maximum lateral acceleration achieved is about 10 m/s^2. Figure 3.10 shows the described maneuver. Before modifying the system lets show how the observers build with system (3.37) and (3.38) perform with this maneuver. The mission is the following:

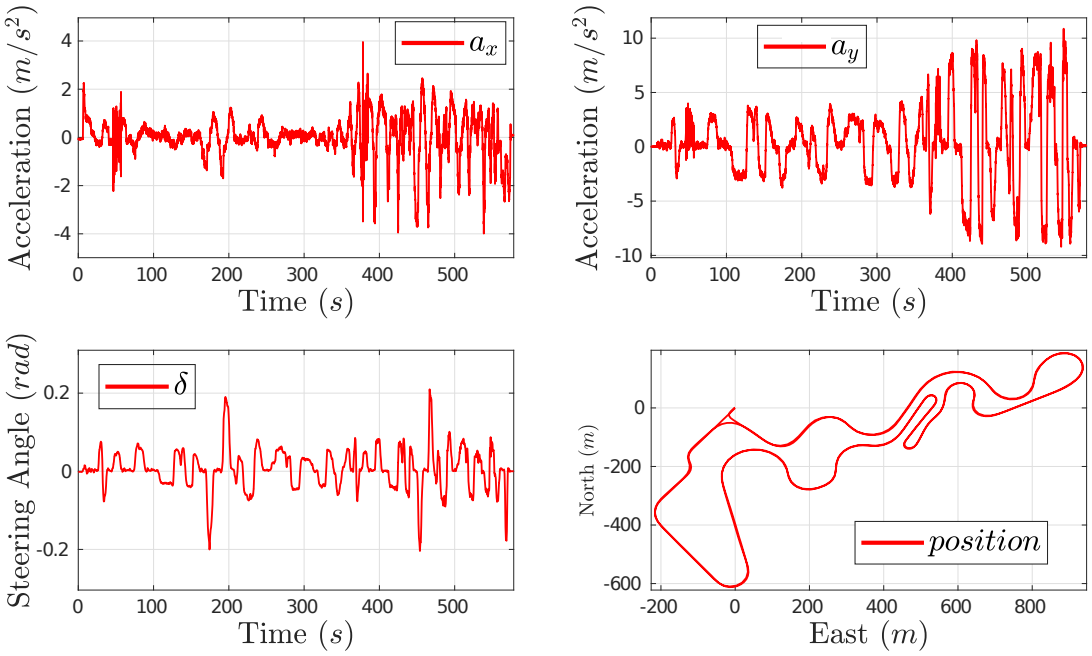

Figure 3.10 – Mission No. 2, test track with different road angles

vFigure 3.11, shows the sideslip-lateral force relationship. The upper figure shows the lateral TGF-sideslip angle relationship's linear behavior during the first lap, and the lower figure shows the same relationship during the second lap. An advantage of the kinematic approach is that no force is required in the observation scheme; thus, the saturation does not affect a kinematic-based observer's performance, and no special cases have to be considered.

First, let us consider systems () and () and its robustness against model uncertainty. Figure 3.12 shows a comparison between the estimated and actual lateral speeds. On the left figure, Fig. 3.12(a), the Kalman filter is build with (3.37), and on the right figure, Fig. 3.12(b), the filter is build with (3.38). Both approaches look-alike, nevertheless, the mean square error (MSE) has small differences, for the system pair (3.37), the MSE = 0.126889, on the other hand for the system pair (3.34a)-(3.38), the MSE = 0.118474. The model has to be modified to consider the road bank and slope angles to improve accuracy. Remember that the Kalman filter can deal with zero mean and Gaussian distribution uncertainty; nonetheless,

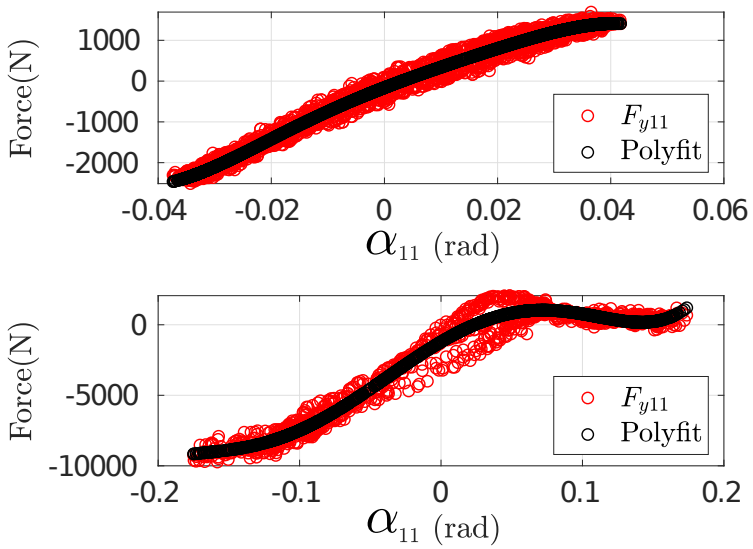

Figure 3.11 – Sideslip angle - Lateral Force Relation. Up: Linear relationship. Down: Non-linear relationship

road and slope do not fall within this category. Thus, to take into account the road angles, the system is modified into:

$$\mathbf{x}_{n|n} = \mathbf{\Phi^1}_n \mathbf{x}_{n-1|n-1} + \mathbf{\Gamma^1}\mathbf{u}_n \tag{3.39a}$$

$$\mathbf{y}_{n|n} = \mathbf{C^3}\mathbf{x}_{n|n} \tag{3.39b}$$

where

$$\mathbf{\Phi^1}_n = \begin{bmatrix} 1 & \Delta t\omega_{z,n} & g\Delta t & 0 & 0 & 0 \\ \Delta t\omega_{z,n} & 1 & 0 & 0 & -g\Delta t & 0 \\ 0 & 0 & 1 & \Delta t & 0 & 0 \\ 0 & 0 & 0 & 1 & 0 & 0 \\ 0 & 0 & 0 & 0 & 1 & \Delta t \\ 0 & 0 & 0 & 0 & 0 & 1 \end{bmatrix}; \quad \mathbf{\Gamma^1} = \begin{bmatrix} \Delta t & 0 \\ 0 & \Delta t \\ 0 & 0 \\ 0 & 0 \\ 0 & 0 \\ 0 & 0 \end{bmatrix}$$

$$\mathbf{C^3} = \begin{bmatrix} 1 & 0 & 0 & 0 & 0 & 0 \\ 0 & 0 & 0 & 1 & 0 & 0 \\ 0 & 0 & 0 & 0 & 0 & 1 \\ 0 & 1 & 0 & 0 & 0 & 0 \end{bmatrix}$$

with $\mathbf{x_{n|n}} = \begin{bmatrix} \hat{v}_{x,n} & \hat{v}_{y,n} & \hat{\theta}_n & \hat{\omega}_{y,n} & \hat{\phi}_n & \hat{\omega}_{x,n} \end{bmatrix}$, $\mathbf{z}_n = \begin{bmatrix} v_{x,n} & \omega_{y,n} & \omega_{x,n} & 0 \end{bmatrix}$, and $\mathbf{u}_n$ remains the same.

System (3.39) considers the slope and bank angles; notice that is its dimension increased and, subsequently, its complexity.

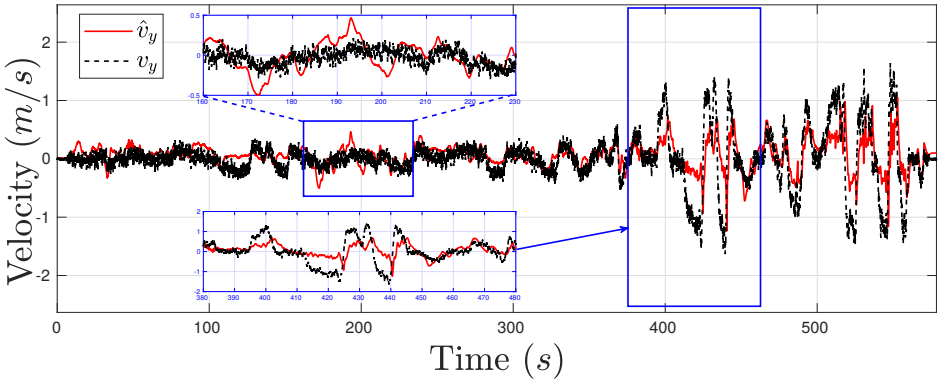

(a) Lateral speed comparison between observer response $\hat{v}_y$ and actual velocity v_y for system (3.37).

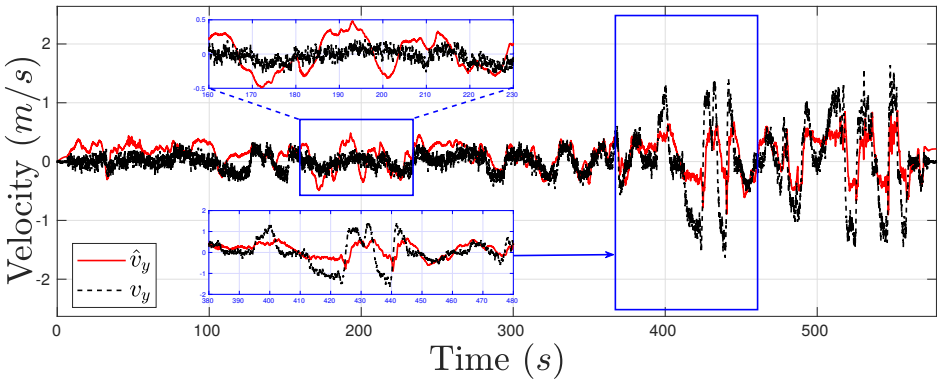

(b) Lateral speed comparison between observer response $\hat{v}_y$ and actual velocity v_y for system (3.38).

Figure 3.12 – Comparison of the longitudinal and lateral speeds for systems (3.37) and (3.38), performing Mission No. 2

Figure 3.13 shows the response of an extended Kalman filter based on system (3.39), the accuracy of the response increases when compared to Figure 3.12. Now our kinematic model can compensate for the gravity components that affect the sensor measurement.

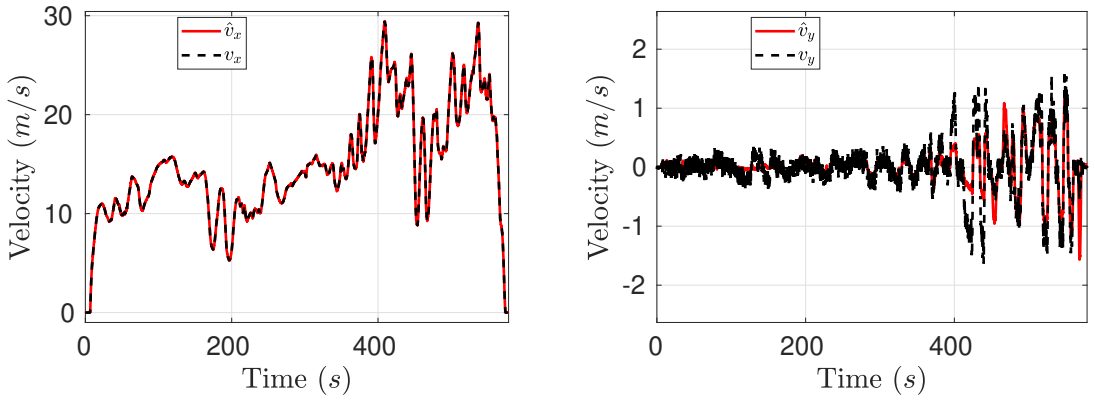

(a) Longitudinal speed comparison between observer response $\hat{v}_x$ and actual velocity v_x.

(b) Lateral speed comparison between observer response $\hat{v}_y$ and actual velocity v_y.

Figure 3.13 – Comparison of the longitudinal and lateral speeds for system (3.39) performing Mission No. 2.

3.4.5 Including the three Euler's angles

The Euler angles are the three angles that describe the orientation of a rigid body with respect to a fixed coordinate system. Any orientation can be achieved by composing three fundamental rotations about the axis of a coordinate system, in this case the angles ϕ, θ and ψ for the roll, pitch and yaw rotations, respectively.

Thus, by extending the kinematic system to $\mathbb{R}^3$ and compensating against gravity, gives:

$$\mathbf{a} = \dot{\mathbf{v}} + \boldsymbol{\omega} \times \mathbf{v} + \mathbf{R}_{\phi,\theta,\psi}\mathbf{g} \tag{3.40}$$

where $\mathbf{a} \in \mathbb{R}^3$ stands for the acceleration, $\mathbf{v} \in \mathbb{R}^3$ is the velocity, $\dot{\mathbf{v}}$ describes $\frac{d\mathbf{v}}{dt}$, $\boldsymbol{\omega} \in \mathbb{R}^3$ defines the angular rate, $\mathbf{g} \in \mathbb{R}^3$ means the gravity's acceleration, $\mathbf{R}_{\phi,\theta,\psi} \in \mathbb{R}^{3\times3}$ is a rotation matrix. Then, system (3.40) could be represented as:

$$\begin{aligned} a_x &= \dot{v}_x - \omega_z v_y + \omega_y v_z - g\sin(\theta) \\ a_y &= \dot{v}_y + \omega_z v_x - \omega_x v_z + g\sin(\phi)\cos(\theta) \\ a_z &= \dot{v}_z + \omega_y v_x - \omega_x v_y + g\cos(\phi)\cos(\theta) \end{aligned} \tag{3.41}$$

where coefficients x, y and z represents the body longitudinal, lateral and vertical axis and angles θ, ϕ means the angle between the body and an inertial frame

of reference; notice that the rotation matrix, $\mathcal{R}_{\phi,\theta,\psi}$ is defined such that the transformation from (3.40) to (3.41) holds. The discrete state-space representation is:

$$\begin{aligned} \mathbf{x}_{n|n} =& \mathbf{\Phi^2}_n \mathbf{x}_{n-1|n-1} + \mathbf{\Gamma^2}\mathbf{u}_n \\ \mathbf{y}_{n|n} =& \mathbf{C^4}\mathbf{x}_{n|n} \end{aligned} \tag{3.42}$$

where

$$\mathbf{\Phi^2} = \begin{bmatrix} 1 & \Delta t\omega_{z,n} & -\Delta t\omega_{y,n} & g\Delta t & 0 & 0 & 0 \\ -\Delta t\omega_{z,n} & 1 & \Delta t\omega_{x,n} & 0 & 0 & -g\Delta t & 0 \\ \Delta t\omega_{y,n} & -\Delta t\omega_{x,n} & 1 & 0 & 0 & 0 & 0 \\ 0 & 0 & 0 & 1 & \Delta t & 0 & 0 \\ 0 & 0 & 0 & 0 & 1 & 0 & 0 \\ 0 & 0 & 0 & 0 & 0 & 1 & \Delta t \\ 0 & 0 & 0 & 0 & 0 & 0 & 1 \end{bmatrix}$$

$$\mathbf{\Gamma^2} = \begin{bmatrix} \Delta t & 0 & 0 \\ 0 & \Delta t & 0 \\ 0 & 0 & \Delta t \\ 0 & 0 & 0 \\ 0 & 0 & 0 \\ 0 & 0 & 0 \\ 0 & 0 & 0 \end{bmatrix}; \quad \mathbf{C^4} = \begin{bmatrix} 1 & 0 & 0 & 0 & 0 & 0 & 0 \\ 0 & 0 & 0 & 1 & 0 & 0 & 0 \\ 0 & 0 & 0 & 0 & 0 & 1 & 0 \\ 0 & 1 & 0 & 0 & 0 & 0 & 0 \\ 0 & 0 & 1 & 0 & 0 & 0 & 0 \end{bmatrix}$$

with $\mathbf{x}_{n|n} = \begin{bmatrix} \hat{v}_x & \hat{v}_y & \hat{v}_z & \hat{\theta} & \hat{\omega}_y & \hat{\phi} & \hat{\omega}_x \end{bmatrix}^T$, $\mathbf{z}_n = \begin{bmatrix} v_x & \omega_y & \omega_x & 0 & 0 \end{bmatrix}$, and $\mathbf{u}_n = \begin{bmatrix} a_x & a_y & a_z \end{bmatrix}$.

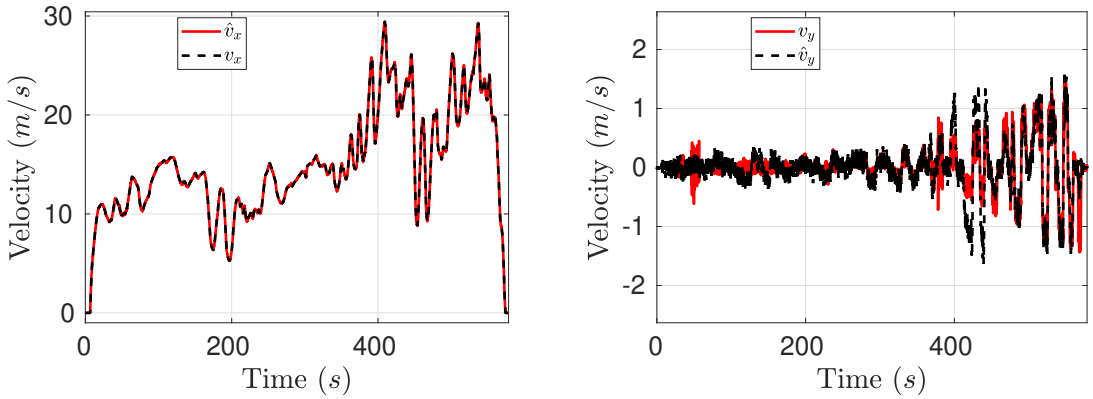

(a) Longitudinal speed comparison between observer response $\hat{v}_x$ and actual velocity v_x.

(b) Lateral speed comparison between observer response $\hat{v}_y$ and actual velocity v_y.

Figure 3.14 – Comparison of the longitudinal and lateral speeds for system (3.42) and Mission No. 2.

Figure 3.14, shows the estimation response with a red-solid line, and the actual measurement with a black dashed line. In this case the error difference is not noticeable at eye sight, further experimentation and analysis are introduced in further sections.

3.4.6 Quaternions

Another approach to handle rotations are quaternions. Quaternions are widely used on aerunautics and simulation software, since they have plenty of adavantages compared to Euler angles.

3.4.6.1 Fundamentals

Quaternions were discovered by William Rowan Hamilton in the 19th century. A quaternion has three imaginary units (i, j, k) and the following holds:

$$i^2 = j^2 = k^2 = ijk = -1;$$

$$jk = i; kj = -i; ki = j; ik = -j; ij = k; ji = -k;$$

A quaternion could be expressed as a couple composed of a real number and a vector as:

$$\mathbf{q} = \begin{bmatrix} q_0 & \bar{\mathbf{q}} \end{bmatrix}; \quad \mathbf{q} \in \mathbb{H}$$

with $q_0 \in \mathbb{R}$ and a vector $\bar{\mathbf{q}} = \begin{bmatrix} q_1 & q_2 & q_3 \end{bmatrix}^T \in \mathbb{R}^3$. For background on the properties and quaternion operations, see Appendix C.

Specifically, unit quaternions, provide a convenient mathematical notation for representing orientations and rotations of objects in three dimensions. Compared to Euler angles they are simpler to compose and avoid the problem of gimbal lock. Compared to rotation matrices they are more compact, more numerically stable, and more efficient. Quaternions have applications in computer graphics, [Shoemake, 1985], computer vision, robotics, [McCarthy, 1990], navigation, molecular dynamics, flight dynamics, [Katz, 1997], orbital mechanics of satellites, [Harrison, 1999], and crystallographic texture analysis, [Kunze and Schaeben, 2004].

When used to represent rotation, unit quaternions are also called rotation quaternions as they represent the 3D rotation group. When used to represent an orientation (rotation relative to a reference coordinate system), they are called orientation quaternions or attitude quaternions.

From (3.40), and if we replace the rotation matrix with unitary quaternions gives: using quaternions is obtained:

$$\begin{bmatrix} 0 \\ \mathbf{a} \end{bmatrix} = \begin{bmatrix} 0 \\ \dot{\mathbf{v}} \end{bmatrix} + \begin{bmatrix} 0 \\ \boldsymbol{\omega} \times \mathbf{v} \end{bmatrix} + \mathbf{q} \otimes \begin{bmatrix} 0 \\ \mathbf{g} \end{bmatrix} \otimes \mathbf{q}^* \tag{3.43}$$

with $\mathbf{q}$ and $\mathbf{q}^*$ as unitary quaternion and its conjugate, respectively, the operator $\otimes$ means the Hamiltonian product, see Appendix C for more information on quaternion specifics. Also representing system (3.43) in scalar form:

$$\begin{aligned} a_x =& \dot{v}_x + \omega_y v_z - \omega_z v_y - 2g(q_1 q_3 - q_0 q_2) \\ a_y =& \dot{v}_y + \omega_z v_x - \omega_x v_z - 2g(q_0 q_1 + q_2 q_3) \\ a_z =& \dot{v}_z + \omega_y v_x - \omega_x v_y - g(q_0^2 - q_1^2 - q_2^2 + q_3^2) \end{aligned} \tag{3.44}$$

where $\mathbf{q} = \begin{bmatrix} q_0 & q_1 & q_2 & q_3 \end{bmatrix}$ and the auqternionr time derivative is given by:

$$\dot{\mathbf{q}} = \frac{1}{2}\mathbf{q} \otimes \boldsymbol{\omega}$$

thus, the system composed by the Newton equation and its attitud equation is:

$$\begin{aligned} \begin{bmatrix} 0 \\ \mathbf{a} \end{bmatrix} =& \begin{bmatrix} 0 \\ \dot{\mathbf{v}} \end{bmatrix} + \begin{bmatrix} 0 \\ \boldsymbol{\omega} \times \mathbf{v} \end{bmatrix} + \mathbf{q} \otimes \begin{bmatrix} 0 \\ \mathbf{g} \end{bmatrix} \otimes \mathbf{q}^* \\ \dot{\mathbf{q}} =& \frac{1}{2}\mathbf{q} \otimes \boldsymbol{\omega} \end{aligned} \tag{3.45}$$

The discrete state-space representation of the kinematic system including its attitude

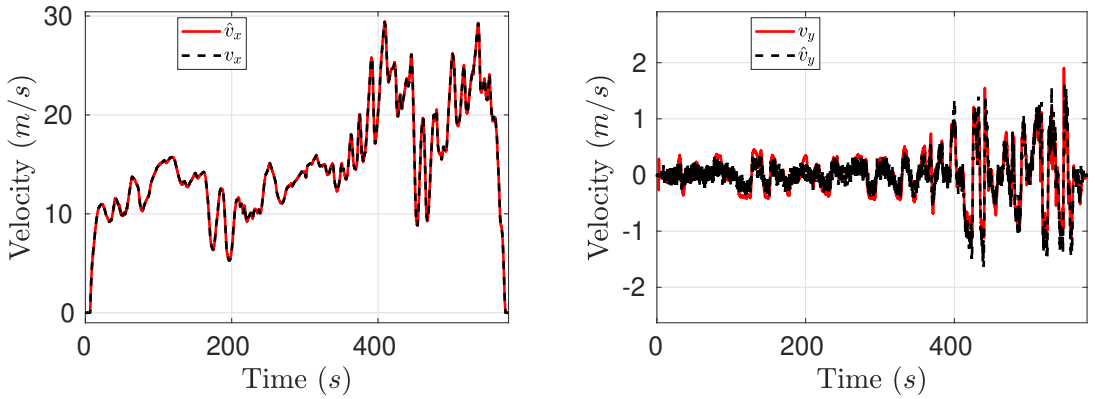

(a) Longitudinal speed comparison between observer response $\hat{v}_x$ and actual velocity v_x.

(b) Lateral speed comparison between observer response $\hat{v}_y$ and actual velocity v_y.

Figure 3.15 – Comparison of the longitudinal and lateral speeds for system (3.46).

is:

$$\begin{aligned} \mathbf{x}_{n|n} &= \mathbf{\Phi^3}_n \mathbf{x}_{n-1|n-1} + \mathbf{\Gamma^2}\mathbf{u}_n \\ \mathbf{y}_{n|n} &= \mathbf{C^5}\mathbf{x}_{n|n} \end{aligned} \tag{3.46}$$

where

$$\mathbf{C^5} = \begin{bmatrix} 1 & 0 & 0 & 0 & 0 & 0 & 0 \\ 0 & 1 & 0 & 0 & 0 & 0 & 0 \\ 0 & 0 & 1 & 0 & 0 & 0 & 0 \\ 0 & 0 & 0 & x_4 & x_5 & x_6 & x_7 \end{bmatrix}$$

$$\mathbf{\Phi^3} = \begin{bmatrix} 1 & \Delta t\omega_{z,n} & -\Delta t\omega_{y,n} & gx_6\Delta t & -gx_7\Delta t & gx_4\Delta t & -gx_5\Delta t \\ -\Delta t\omega_{z,n} & 1 & \Delta t\omega_{x,n} & -gx_5\Delta t & -gx_4\Delta t & -gx_7\Delta t & -gx_6\Delta t \\ \Delta t\omega_{y,n} & -\Delta t\omega_{x,n} & 1 & -gx_4\Delta t & gx_5\Delta t & gx_6\Delta t & -gx_7\Delta t \\ 0 & 0 & 0 & 1 & -\Delta t\frac{\omega_{x,n}}{2} & -\Delta t\frac{\omega_{y,n}}{2} & -\Delta t\frac{\omega_{z,n}}{2} \\ 0 & 0 & 0 & \Delta t\frac{\omega_{x,n}}{2} & 1 & \Delta t\frac{\omega_{z,n}}{2} & -\Delta t\frac{\omega_{y,n}}{2} \\ 0 & 0 & 0 & \Delta t\frac{\omega_{z,n}}{2} & \Delta t\frac{\omega_{y,n}}{2} & 1 & -\Delta t\frac{\omega_{x,n}}{2} \\ 0 & 0 & 0 & \Delta t\frac{\omega_{z,n}}{2} & \Delta t\frac{\omega_{y,n}}{2} & -\Delta t\frac{\omega_{x,n}}{2} & 1 \end{bmatrix};$$

with $\mathbf{\Gamma^2}$ is already defined in system (3.42), $\mathbf{x}_{n|n} = \begin{bmatrix} \hat{v}_x & \hat{v}_y & \hat{v}_z & \hat{q}_0 & \hat{q}_1 & \hat{q}_2 & \hat{q}_3 \end{bmatrix}^T$, $\mathbf{z}_n = \begin{bmatrix} v_x & 0 & 0 & 1 \end{bmatrix}^T$, and $\mathbf{u}_n = \begin{bmatrix} a_x & a_y & a_z \end{bmatrix}^T$.

Figure 3.15 shows the response obtained from observer based on system (3.46) against the actual velocities measurements. The improvement in the last case are easily noticed. The advantage of the quaternion approach is that uses the complete

model without requiring simplifications due to linearization, contrary to the use of sinus and cosinus operations. Figure 3.16 shows both estimation responses build with system (3.42), in Figure 3.16(a), and (3.46), in Figure 3.16(b). When comparing both results, we can state that the response obtained with the kinematic model using quaternions is better in terms of accuracy. In later sections the later will be re-validated with more manuevers and tests.

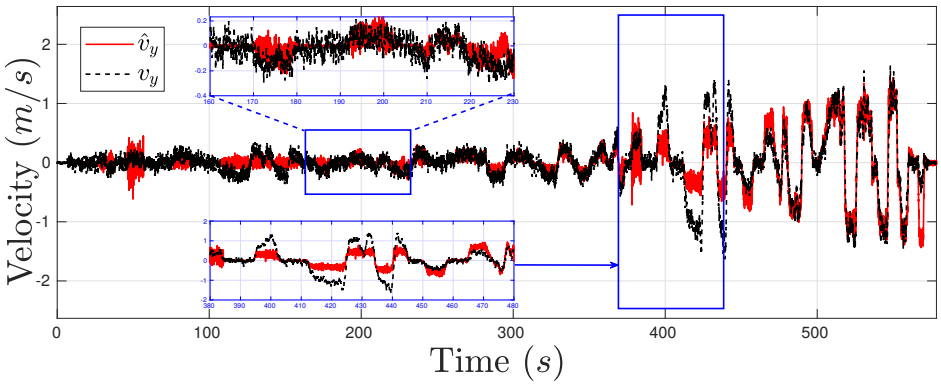

(a) Lateral speed comparison between observer response $\hat{v}_y$ and actual velocity v_y for system (3.42).

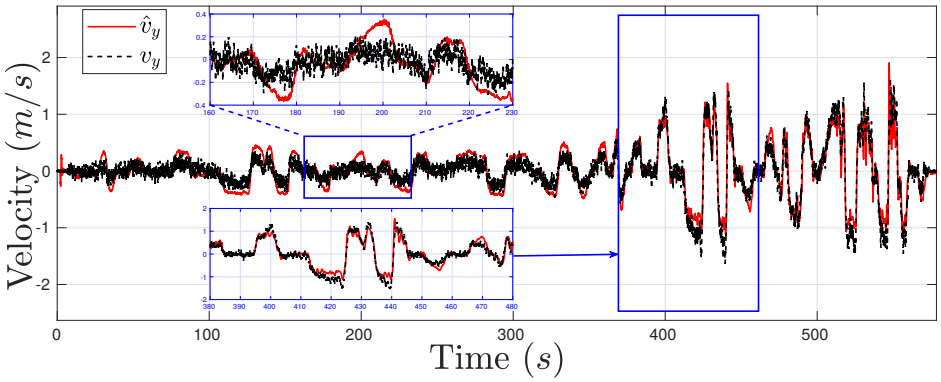

(b) Lateral speed comparison between observer response $\hat{v}_y$ and actual velocity v_y for system (3.46).

Figure 3.16 – Comparison of the longitudinal and lateral speeds for systems (3.42) and (3.46).

3.4.7 Wheels locked dilemma

In the previous section we have already and accurate estimation of the longitudinal speed, given the test results, this is explained due to we are considering that we can measure the longitudinal speed. Nonetheless, the longitudinal speed measurement that we use will not be correct 100% of the cases. The velocity is commonly computed with information of the wheel speed sensors; there exists a linear relationship between the linear and the angular velocity of the wheel, remember $v_x = r_e \Omega_{ij}$; poor accuracy is often the result of this relationship not holding.

Figure 3.17 shows the actual vehicle speed, v_x, versus the longitudinal speed computed from the angular wheel speed sensors, Ω_{ij}. Notice, in this case the front-right wheel is locked, and the measurement Ω_{12} goes to zero, while the other measurements Ω_{11}, Ω_{21}, Ω_{22} show that their respective tires behave regularly and comply with the longitudinal speed v_x. In some particular cases when braking, the tires could arrive to the saturation point, and the tires (or a single tire) could become into a locked state.

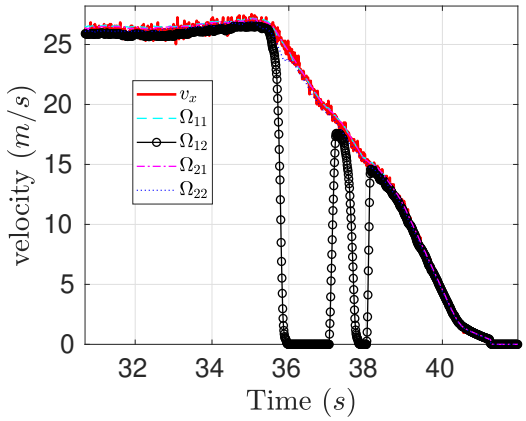

Figure 3.17 – Longitudinal speed of the vehicle compared against the longitudinal speed computed from the angular wheel speed.

Thus, in this case the longitudinal speed could not be estimated with a simple arithmetic mean. Let us define other different means that are more adequate for computing the longitudinal speed from angular wheel speed sensors.

The arithmetic mean is defined as the sum of a collection of numbers divided by the count of numbers in the collection, see [Jacobs, 1994],

$$\mu_A = \frac{1}{n}\sum_{i=1}^{n} x_i \tag{3.47}$$

where n is the number of elements in the set to compute the average, and $x_i \in \mathbb{R}$ is a real number.

The harmonic mean μ_H is defined as:

$$\mu_H = \left(\frac{1}{n}\sum_{i=1}^{n} x_i^{-1}\right)^{-1} \tag{3.48}$$

The harmonic mean is a Schur-concave function, and dominated by the minimum of its arguments, in the sense that for any positive set of arguments, $\min(x_1, \cdots, x_n) \leq \mu_H(x_1, \cdots, x_n) \leq n\min(x_1, \cdots, x_n)$. Thus, the harmonic mean cannot be made

arbitrarily large by changing some values to bigger ones (while having at least one value unchanged).

Finally, the contraharmonic mean of a set of positive numbers is defined as the arithmetic mean of the squares of the numbers divided by the arithmetic mean of the numbers:

$$\mu_C = \frac{\sum_{i=1}^{n} x_i^2}{\sum_{i=1}^{n} x_i} \tag{3.49}$$

notice that here $x_i \in \mathbb{R}^+$ and $(\mu_H + \mu_C)\frac{1}{2} = \mu_A$, Thus, the contraharmonic mean cannot be made arbitrarily small by changing some values to smaller ones (while having at least one value unchanged).

Figure 3.18 shows a comparison between the longitudinal speed, v_x, and the longitudinal speed computed with arithmetic mean, (3.47), the harmonic mean, (3.48), and the contraharmonic mean, (3.49), while the vehicle is having a demanding braking. The figure shows with a black-dashed line the arithmetic mean; notice that its accuracy is affected by the wheel locked phenomena, therefore using a simple mean affects our final estimation once the wheel lock phenomena occurs. On the one hand, the figure also displays with a pink dot-dashed line the response of the harmonic mean, notice that this result is simlar to the Ω_{12} measurement. On the other handm with a blue-dotted line, the figure shouws the contraharmonic mean response similar to the actual vehicle spee.

Once, depicted the different properties of each one of the means, $(\mu_A,\ \mu_H,\ \mu_C)$, a switched computation is proposed. Let us assume that we are able to detect when the vehicle is braking. Thus, the formula to compute the longitudinal speed is given by:

$$\begin{aligned} \hat{v}_x &= b\mu_C(\Omega_{ij}) + (1-b)\,\mu_H(\Omega_{ij}) \\ b &\in \chi := \{0, 1\} \end{aligned} \tag{3.50}$$

where b is a flag, with value one while braking and zero otherwise.

Equation (3.50), means that while braking the longitudinal speed estimation is computed with the contraharmonic mean, (3.49), otherwise, while accelerating is computed with the harmonic mean, defined in (3.48). Equation (3.50) also deals with effects that occur when a driving torque is higher than the tire's saturation constraint.

But, what happens when the four wheels are locked in an extreme situation? in this case, using equation (3.50) develop from the angular speed wheel sensor is

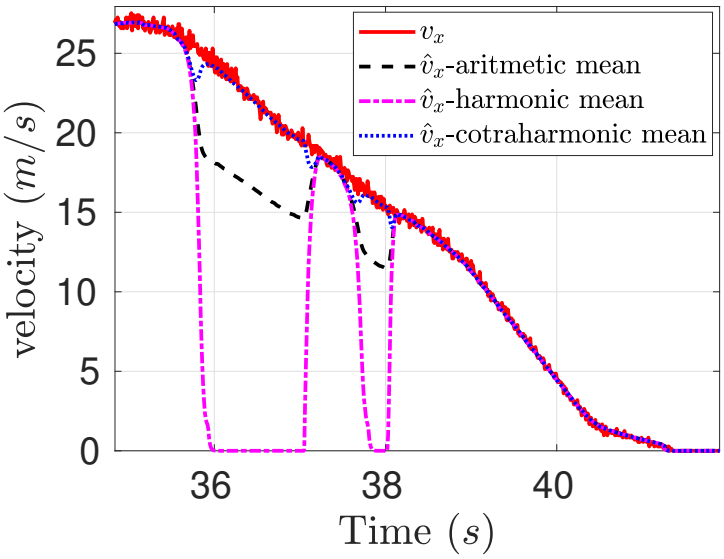

Figure 3.18 – Results comparing the harmonic, contraharmonic and arithmetic mean

not enough, thus, let us consider the following discrete state-space system:

$$\begin{aligned} \mathbf{x}_{n|n} =& \mathbf{\Phi^4}_n \mathbf{x}_{n-1|n-1} \\ \mathbf{y}_{n|n} =& \left(\mathbf{C^6}\left(1-b_n\right) + b_n \mathbf{C^7}\right)\mathbf{x}_{n|n} = \mathbf{C^8}\mathbf{x}_{n|n} \end{aligned} \tag{3.51}$$

where

$$\mathbf{\Phi^4} = \begin{bmatrix} 1 & \Delta t \\ 0 & 1 \end{bmatrix}; \quad \mathbf{C^6} = \begin{bmatrix} 1 & 0 \\ 0 & 1 \end{bmatrix}; \quad \mathbf{C^7} = \begin{bmatrix} 0 & 1 \end{bmatrix}; \tag{3.52}$$

with $\mathbf{x}_{n|n} = \begin{bmatrix} v_x & a_x \end{bmatrix}$, $\mathbf{z}_n = \begin{bmatrix} \hat{v}_{x,n} & a_{x,n} \end{bmatrix}(1-b_n) + a_{x,n}b_n$.

In system (3.51) we consider a system with a switched output equation. The switching mechanism is defined by the braking flag, moreover when the vehicle is not braking the dimension of the measurement, $\mathbf{z}$, is two, the measurement are the longitudinal speed computed with eq. (3.50) and the accelerometer; while braking the system relies on the acceleration measurement. Heuristically, to avoid a biased response, the flag signal is activated only when the following conditions occur:

- The braking flag is active
- The estimated velocity is greater than the measured velocity.

Figure 3.19 displays the results obtained from a Kalman filter observer base on system (3.51). Notice that while braking the v_x measurement is not available for the observer. The braking maneuvers are usually short, therefore, the deviation due to error integration is small, more over if the condition b **and** $(\hat{x}_{1,n} < \hat{v}_x)$ is true,

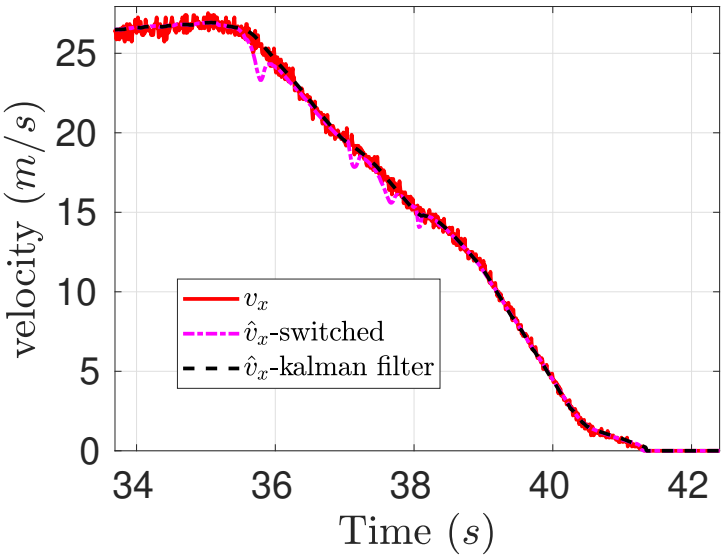

Figure 3.19 – Comparison between the longitudinal velocity, the estimation with the Kalman filter and the switched equation (3.50)

the estimation is again set to the actual velocity in a shorter amount of time. The algorithm to implement the developed Kalman filter is shown in Algorithm 3.2.

In some cases, an observer based on system (3.51) is not able to estimate accurately the longitudinal velocity, due to uncertainty in the model, or missing variables important for an accurate model. Thus, using the same principle as in system (3.51), the Newton-quaternion system (3.46) could be modified as:

$$\begin{aligned} \mathbf{x}_{n|n} &= \mathbf{\Phi^3}_n \mathbf{x}_{n-1|n-1} \\ \mathbf{y}_{n|n} &= \left(\mathbf{C^9}\left(1-b_n\right) + b_n \mathbf{C^{10}}\right)\mathbf{x}_{n|n} = \mathbf{C^{11}}\mathbf{x}_{n|n} \end{aligned} \tag{3.53}$$

with $\mathbf{\Phi}^3$ is already defined, $\mathbf{x}_{n|n} = \begin{bmatrix} \hat{v}_x & \hat{v}_y & \hat{v}_z & \hat{q}_0 & \hat{q}_1 & \hat{q}_2 & \hat{q}_3 \end{bmatrix}^T$,
$\mathbf{z}_n = \begin{bmatrix} \hat{v}_x & 0 & 0 & 1 \end{bmatrix}(1-b_n) + \begin{bmatrix} 0 & 0 & 1 \end{bmatrix} b_n$, and $\mathbf{u}_n = \begin{bmatrix} a_x & a_y & a_z \end{bmatrix}$

$$\mathbf{C^9} = \begin{bmatrix} 1 & 0 & 0 & 0 & 0 & 0 & 0 \\ 0 & 1 & 0 & 0 & 0 & 0 & 0 \\ 0 & 0 & 1 & 0 & 0 & 0 & 0 \\ 0 & 0 & 0 & x_4 & x_5 & x_6 & x_7 \end{bmatrix}; \quad \mathbf{C^{10}} = \begin{bmatrix} 0 & 1 & 0 & 0 & 0 & 0 & 0 \\ 0 & 0 & 1 & 0 & 0 & 0 & 0 \\ 0 & 0 & 0 & x_4 & x_5 & x_6 & x_7 \end{bmatrix}$$

The algorithm applied is the same as in Algorithm 3.2.

Algorithm 3.2: Longitudinal Velocity Estimator

Initialization
$\mathbf{x}_{0|0}$, $\mathbf{P}_{0|0}$, $\mathbf{Q}_1$, $\mathbf{R}_1$, $\mathbf{Q}_2$, $\mathbf{R}_2$, $\mathbf{\Phi} = \mathbf{\Phi^3}$, $\mathbf{C} = \mathbf{C^8}$
for$(n = 1 : \infty)$
Prediction stage (prediction stage)
    $\hat{\mathbf{x}}_{n|n-1} = \mathbf{\Phi}\hat{\mathbf{x}}_{n-1|n-1}$
    if b_n
        $\mathbf{P}_{n|n-1} = \mathbf{\Phi}\mathbf{P}_{n-1|n-1}\mathbf{\Phi}^T + \mathbf{Q}_2$
    else
        $\mathbf{P}_{n|n-1} = \mathbf{\Phi}\mathbf{P}_{n-1|n-1}\mathbf{\Phi}^T + \mathbf{Q}_1$
    end
Measurement update stage (correction stage)
    if b_n
        $\mathbf{k}_n = \mathbf{P}_{n|n-1}\mathbf{C}^T \left[\mathbf{C}\mathbf{P}_{n|n-1}\mathbf{C}^T + \mathbf{R_2}\right]^{-1}$
    else
        $\mathbf{k}_n = \mathbf{P}_{n|n-1}\mathbf{C}^T \left[\mathbf{C}\mathbf{P}_{n|n-1}\mathbf{C}^T + \mathbf{R_1}\right]^{-1}$
    end
    $\hat{\mathbf{x}}_{n|n} = \hat{\mathbf{x}}_{n|n-1} + \mathbf{k}_n \left[\mathbf{z}_n - \mathbf{C}\hat{\mathbf{x}}_{n|n-1}\right]$
    $\mathbf{P}_{n|n} = \mathbf{P}_{n|n-1} - \mathbf{k}_n\mathbf{C}\mathbf{P}_{n|n-1}$
end

3.5 Robustness analysis

In this section, we will proove that the algorithm has the same level of performance with different maneuvers and levels of exitation. First, we have to compare the estimator quality. The most common choices to measure model/estimator quality in terms of the fit between the estimated output, $\hat{\mathbf{B}}$, and the measured output, $\mathbf{B}$, are the mean squared error (MSE), the normalized mean squared error (NMSE) and the normalized root mean squared error (NRMSE).

$$MSE = \frac{1}{m} \mid\mid \mathbf{B} - \hat{\mathbf{B}} \mid\mid_2^2 \tag{3.54a}$$

$$NMSE = \frac{\mid\mid \mathbf{B} - \hat{\mathbf{B}} \mid\mid_2^2}{\mid\mid \bar{\mathbf{B}} \mid\mid_2^2} \tag{3.54b}$$

$$NRMSE = \frac{\mid\mid \mathbf{B} - \hat{\mathbf{B}} \mid\mid_2^2}{\mid\mid \bar{\mathbf{B}} - \mu(\bar{\mathbf{B}}) \mid\mid_2^2} \tag{3.54c}$$

A total of 57 missions were performed to validate the robustness of our approach, all of them with the land rover evoque experimental testbed. In the following subsections our results are presented.

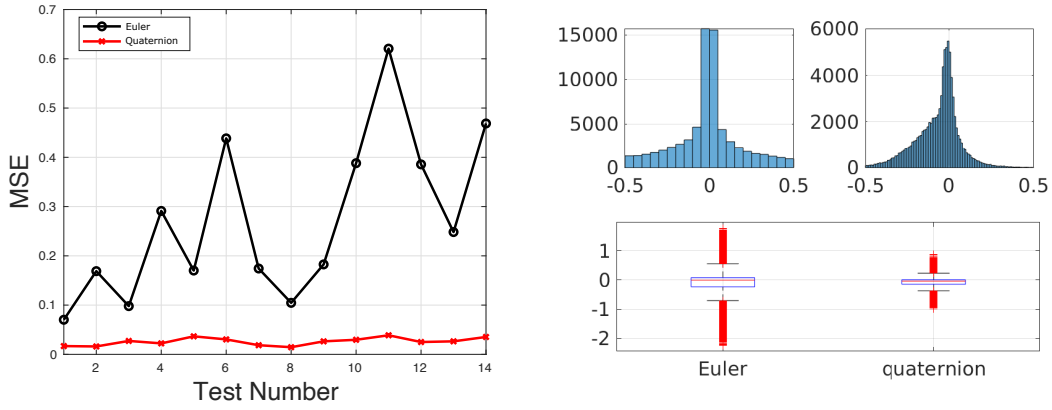

(a) MSE comparison for steady state cornering (b) Histogram and boxplot comparison

Figure 3.20 – Comparison between (3.42) and (3.53)

3.5.1 Steady State cornering ISO-4138

Steady state maneuvers reveals important information about the vehicles behavior. The results from this maneuver are used as reference values in several other test such as a sine with dwell and continuous sinusoidal input. This maneuver reveal the vehicle under/over-steer behavior, roll angle at steady state, steering and sideslip angle as function of lateral acceleration . The steady state cornering can be performed in three different ways, using constant radius, constant velocity or constant steering angle. More information regarding the maneuver is available in [ISO4138, 2012].

Figure 3.20(a) shows the MSE response of systems (3.42) and (3.46). The full Euler-model-based observer (EMBO) MSE response of each one of the 14 steady state cornering maneuvers is depicted with a black-solid line with circles. The quaternion-model-based observer (QMBO) MSE response is shown with a red-solid line with crosses. Notice the MSE error is lower for the QMBO, and also the error response has less variance within the samples.

A similar behavior is found in Figure 3.20(b) presents the statitucal analysis of the errors. Notice that the error resulting from the QMBO have less variance when compared against the EMBO.

The maneuver consist to drive a circular trajectory while mantainin a constan longitudinal acceleration until the vehicle becoms unstable. Table 3.1 presents the numerical results of the error analysis. The improvement for using the QMBO are quantitative and consistent.

Table 3.1 – MSE for different constant radius and longitudinal acceleration maneuvers

Radius (m)	direction	MSE v_y Euler	MSE v_y quaternion
30	counterclockwise	0.070279	0.016816
30	clockwise	0.168943	0.016066
60	counterclockwise	0.097955	0.027253
60	clockwise	0.291116	0.022299
100	counterclockwise	0.170159	0.036599
100	clockwise	0.438473	0.030370
30	clockwise	0.174269	0.018584
30	counterclockwise	0.104587	0.014540
60	counterclockwise	0.182624	0.026411
60	clockwise	0.388101	0.029618
100	clockwise	0.620598	0.038744
100	counterclockwise	0.385646	0.025060
60	counterclockwise	0.248291	0.026451
60	clockwise	0.468711	0.035321

3.5.2 Braking Maneuvers ISO 21994 and ISO 7975

In this section two maneuvers are considered the straight line braking and the brake in turn maneuvers. On the one hand straight line braking; ISO 21994, gives information about the braking distance. This test evaluates the stability performance of the vehicle while braking after a straight line maneuver. More information regarding the maneuver is available in [ISO21994, 2007]. On the other hand, the brake in turn maneuver give information regarding yaw stability and change in lateral acceleration compared to steady state. More information regarding the maneuver is available in [ISO21994, 2006].

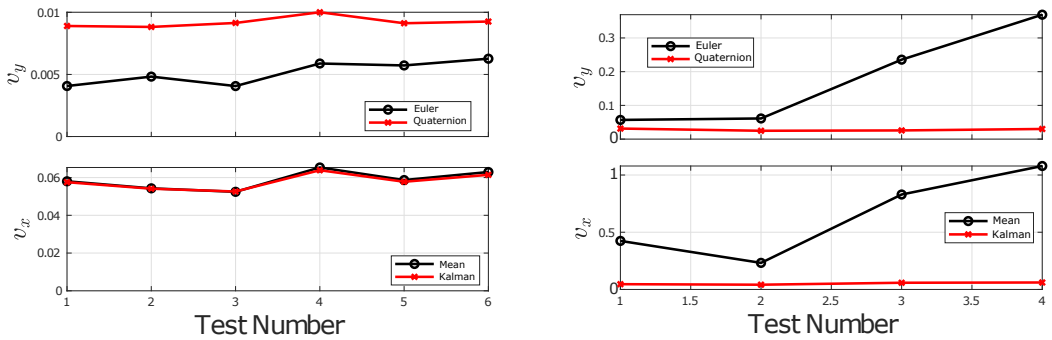

(a) MSE for straigth braking

(b) MSE for brake in turn

Figure 3.21 – Comparison between (3.42) and (3.53)

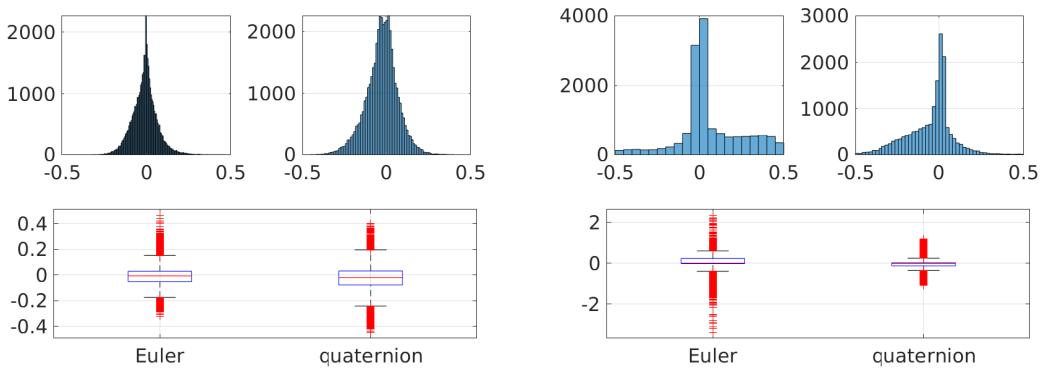

(a) Error histogram and boxplot for straigth braking

(b) Error histogram and boxplot for brake in turn

Figure 3.22 – Operation Region of equations (2.13) and (2.14)

Figure 3.21(a) shows the MSE error response obtained from both observers (lateral and longitudinal speed) for a series of straight braking maneuvers. Notice that,for the lateral speed the EMBO provides better results, but for the longitudinal speed there is no differences between the simple mean and the filtered state obtained with (3.51).

Figure 3.22 shows the error histograms and boxplot for the lateral speed of each one of the respective tests. Notice in Figure 3.22(b) the error response for the QMBO approach shows more accuracy compared with the EMBO, nonetheless Figure 3.22(a) shows the opposite.

While performing the straight line braking maneuvers the tires did not experience saturation, thus, the wheel lock phenomena was not present. Otherwise, while the brake and turn maneuver at least one of the tires arrived to the saturation point, and the wheel lock phenomena is easily noticed in Figure 3.21(b).

Figure 3.23 shows the error obtained at the longitudinal speed, for the straight-line braking maneuver both results are similar, nonetheless, for the brake and turn maneuver the improvement is perceived with ease, see Fig. 3.23(b).

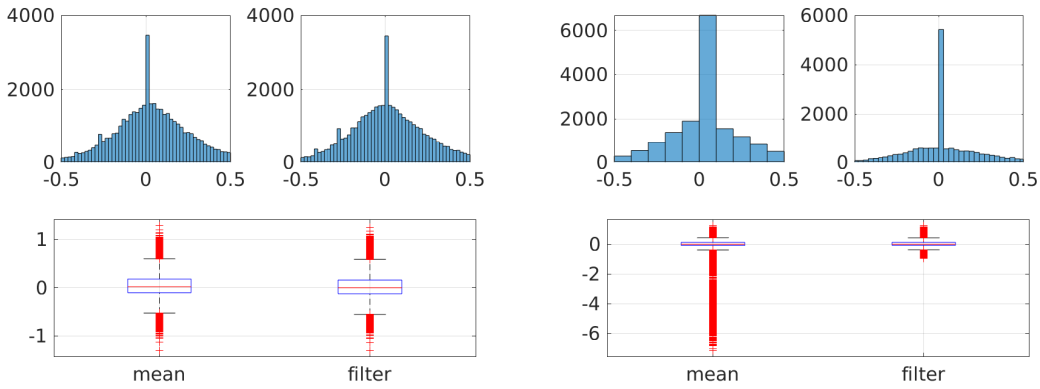

(a) Error histogram and boxplot for straigth braking

(b) Error histogram and boxplot for brake in turn

Figure 3.23 – Comparison between (3.42) and (3.53)

Table 3.2 show the MSE values for the stright-line maneuver while Table 3.3 depicts the values for the brake in turn maneuver, E means Euler and Q stands for quaternion.

Table 3.2 – MSE for different constant radius and longitudinal acceleration maneuvers

Pedal (%)	MSE v_y (E)	MSE v_y (Q)	MSE v_x filter	MSE v_x mean
20	0.004068	0.008902	0.057545	0.058018
40	0.004825	0.008825	0.054098	0.054291
60	0.004064	0.009146	0.052605	0.052449
100	0.005880	0.010009	0.063889	0.065338
100	0.005725	0.009122	0.057778	0.058676
100	0.006268	0.009260	0.061450	0.062937

Table 3.3 – MSE for brake in turn maneuver with a 100 meters constant radius at different speeds.

Velocity (kph)	Direction	MSE v_y (E)	MSE v_y (Q)	MSE v_x filter	MSE v_x mean
80	counterclockwise	0.056891	0.031292	0.046015	0.424291
80	clockwise	0.061238	0.024737	0.041473	0.232241
100	counterclockwise	0.235579	0.025738	0.058562	0.829700
100	clockwise	0.368966	0.030055	0.060807	1.078813

3.5.3 Lateral excitation maneuvers ISO 3888-1, ISO 7401, ISO 8725

In this section the lateral excitation maneuvers are analyzed: double lane change, step steer, sine with dwell and slaloms. The test presented here are far similar, this test are used to obtain information about the road holding ability of the vehicle, the lateral acceleration and yaw rates achieved at given steering angle and its rates. Also, the vehicle transient response to different inputs, including their overshoots, its gain and phase angles functions. These test are not fully representative of real driving but similar to aggressive overtake maneuvers. More information regarding these maneuvers are provided in [ISO3888-1, 1999] and [ISO7401, 2011].

Figure 3.24 shows the MSE response to a series of double lane change maneuvers. Notice that the results are similar for both analyzed approaches, EMBO and QMBO, and Table 3.4 depicts the test speed conditions and its respective MSE values.

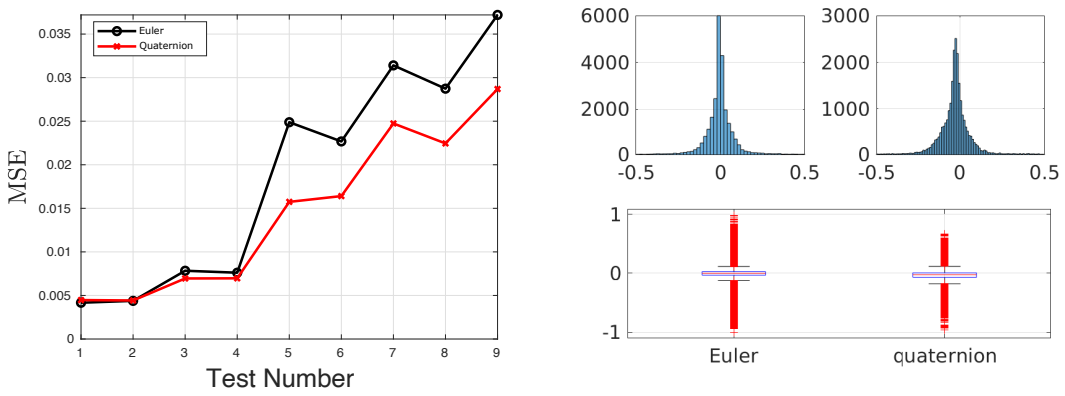

(a) Lateral velocity MSE for ISO double lane change

(b) Lateral velocity histogram for ISO double lane change

Figure 3.24 – Comparison between (3.42) and (3.53)

Figure 3.25, show the MSE response to a set of steep steer maneuvers at 80 kilometers per hour (kph), with different steering wheel angles as input. This test emulates the step response of the vehicle to a different amplitude step input. Table 3.5, shows the different responses of MSE for each test with different steering angle input.

Figure 3.26 shows the MSE response for the sine with dwell maneuvers, this series of maneuver are performed at 60 kph, with different steering wheel inputs, the behavior are similar for all the approaches, nonetheless, the QMBO approach present better accuracy accross the test. Look at Table 3.6 for the exact MSE.

Table 3.4 – MSE for ISO double lane change at different speeds.

Velocity (kph)	MSE v_y (E)	MSE v_y (Q)	MSE v_x filter	MSE v_x mean
30	0.004166	0.004470	0.020424	0.019668
30	0.004379	0.004423	0.021783	0.021045
40	0.007835	0.006950	0.024824	0.024464
40	0.007611	0.006966	0.024747	0.023676
50	0.024883	0.015741	0.034059	0.032239
50	0.022677	0.016405	0.034388	0.033974
55	0.031406	0.024740	0.034101	0.033617
55	0.028734	0.022450	0.032754	0.032200
55	0.037198	0.028691	0.037347	0.035959

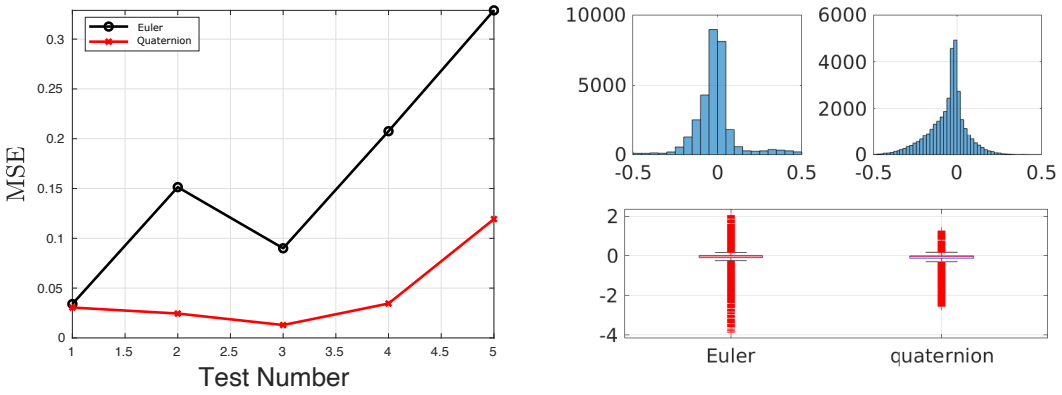

(a) Lateral velocity MSE for step steer

(b) Lateral velocity histogram for step steer

Figure 3.25 – Comparison between (3.42) and (3.53)

Table 3.5 – MSE for steep steer with different steering wheel angles at 80 kph.

Steer. wheel (^{o})	Direction	MSE v_y (E)	MSE v_y (Q)	MSE v_x filter	MSE v_x mean
40	counterclockwise	0.034006	0.030507	0.051315	0.051289
80	counterclockwise	0.151392	0.024463	0.049239	0.049329
40	clockwise	0.089987	0.012930	0.053981	0.053072
80	clockwise	0.207573	0.034528	0.054560	0.054229
120	clockwise	0.328881	0.119281	0.044419	0.044781

Table 3.6 – MSE for sine with dwell with different angles at 60 kph.

Steer. wheel (^{o})	MSE v_y (E)	MSE v_y (Q)	MSE v_x filter	MSE v_x mean
40	0.010844	0.014232	0.037233	0.036398
60	0.097562	0.036119	0.036126	0.035722
80	0.118307	0.049020	0.038272	0.037569
40	0.014041	0.018760	0.036695	0.035985
60	0.029260	0.023742	0.038574	0.036992
80	0.044139	0.025563	0.033110	0.032601

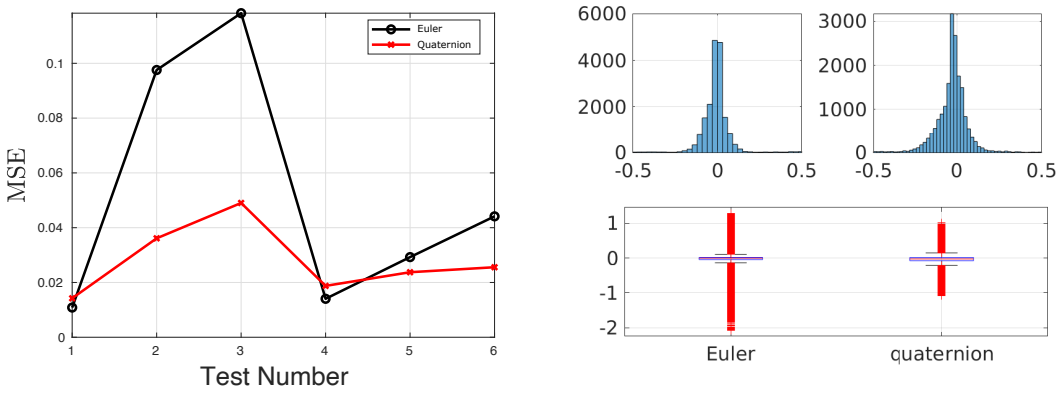

(a) Lateral velocity MSE for sine with dwell (b) Lateral velocity histogram for sine with dwell

Figure 3.26 – Comparison between (3.42) and (3.53)

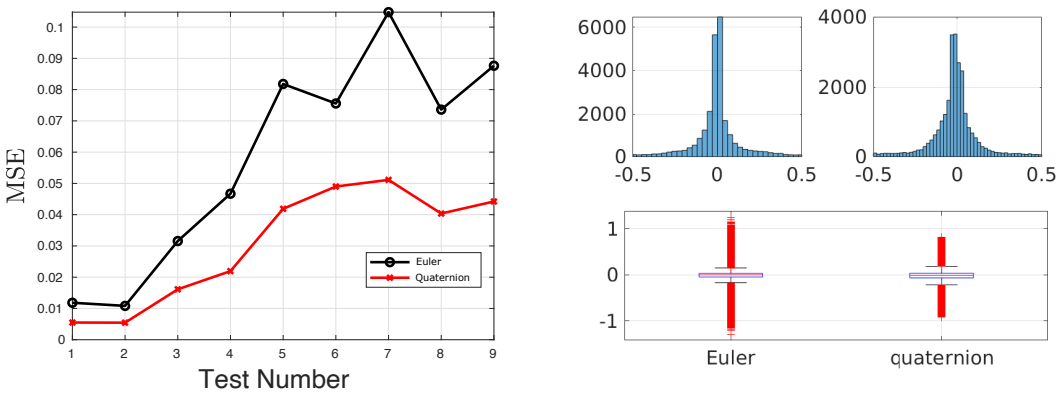

(a) Lateral velocity MSE for slalom (b) Lateral velocity histogram for slalom

Figure 3.27 – Operation Region of equations (2.13) and (2.14)

Finally, Figure 3.27 shows the MSE results obtained for the lateral speed estimation, the histogram and boxplots of a series of slalom maneuvers and Table 3.7 depicts the MSE obtained at each test.

3.5.4 Non planar road tests

The last set of test are performed on a regular track with different slop and road angles at different speeds. Also here, we will see the response of our algorithm to a couple of oval test with a high bank angle. Figure 3.28 shows the MSE for the lateral speed at eight laps on the same test track, the efficiency of the Newton-Euler base observer decreases as the vehicle speed increases, the same happens with the Newton-quaternion approach but the effects on the response are less noticeable.

Figure 3.29 shows the histograms and boxplots of both series of tests.

Table 3.7 – MSE for slalom maneuvers at different speeds

Velocity (kph)	MSE v_y (E)	MSE v_y (Q)	MSE v_x filter	MSE v_x mean
30	0.011824	0.005496	0.025754	0.025172
35	0.010823	0.005450	0.025652	0.024836
40	0.031559	0.016119	0.031195	0.030582
45	0.046704	0.021941	0.029019	0.028263
50	0.081802	0.041881	0.036033	0.035733
55	0.075563	0.048997	0.046760	0.049048
60	0.104775	0.051124	0.040413	0.040803
60	0.073598	0.040362	0.035311	0.034630
60	0.087631	0.044218	0.038369	0.037491

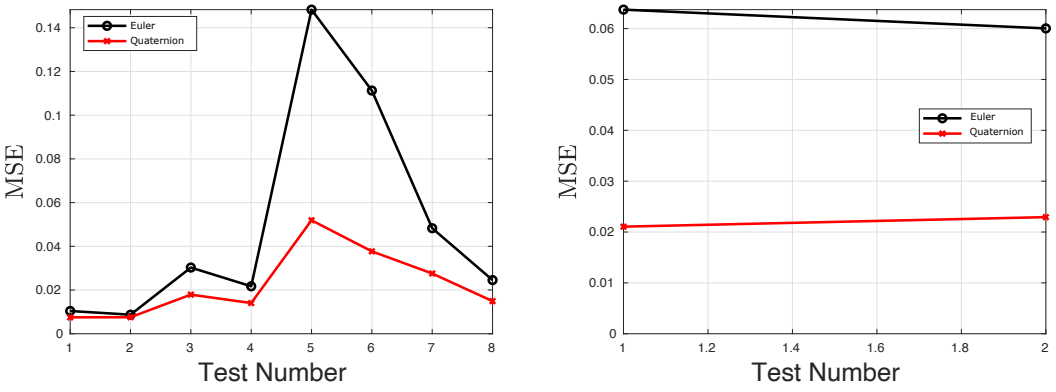

(a) Lateral velocity MSE for durability tests (b) Lateral velocity MSE for high slop roads

Figure 3.28 – Operation Region of equations (2.13) and (2.14)

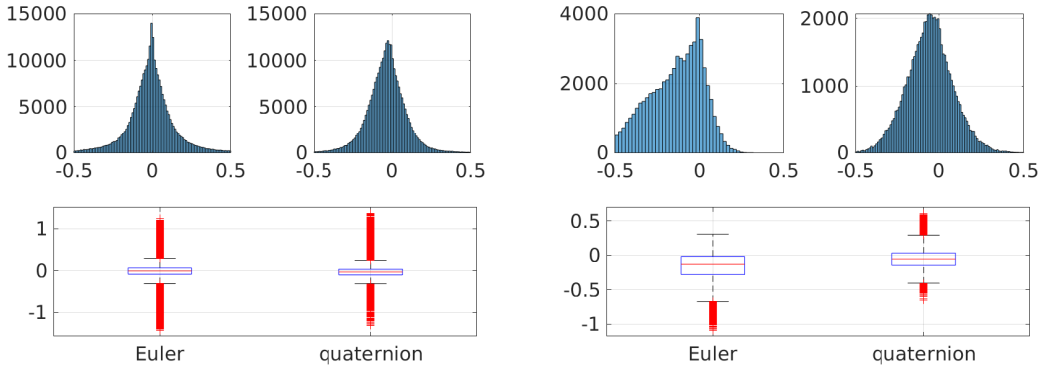

(a) Lateral velocity histogram for durability tests (b) Lateral velocity histogram for high slop roads

Figure 3.29 – Operation Region of equations (2.13) and (2.14)

Table 3.8 – MSE for track at different speeds

speed condition	MSE v_y (E)	MSE v_y (Q)	MSE v_x filter	MSE v_x mean
low	0.010399	0.007496	0.041330	0.041684
low	0.008714	0.007557	0.039841	0.040080
medium to high	0.030281	0.017894	0.061497	0.061017
medium to high	0.021714	0.014034	0.055285	0.055515
limit handling	0.148285	0.051917	0.079352	0.080250
limit handling	0.111260	0.037682	0.073168	0.071856
low and limit handling	0.048276	0.027570	0.060648	0.061618
medium to high	0.024548	0.014917	0.061359	0.061249

Table 3.9 – MSE for oval at high speed

MSE v_y (E)	MSE v_y (Q)	MSE v_x filter	MSE v_x mean
0.063728	0.021054	0.106145	0.106053
0.060040	0.022928	0.109358	0.109022

3.6 Conclusions

This chapter presents a proposal to estimate an automobile's lateral and longitudinal speed using wheel transducers and an inertial measurement unit.

The first section presents the state of the art for sideslip angle estimation and related research. After, we define this work's scope and select the kinematic model to base our observation scheme.

The second section develops our observation strategy, starts with the most simple model, and later considers the slope and bank angles. The system's attitude uses a quaternion ordinary-differential equation. Finally, we address the wheel locked phenomena for the longitudinal state estimation strategy. The results validate the excellent behavior of our proposal.

The third section validates the proposal under different standardized tests. The selected maneuvers are steady-state cornering, brake and turn, straight-line braking, sine with dwell, step steer, double lane change, and test tracks on roads with a different bank and slope angles.

Normal Tire-Ground Force Estimation

Contents

4.1 Introduction

In this section, we propose techniques to estimate the normal tire-ground forces. This variable's estimation is crucial for the overall estimation set-up since these variables are used as inputs to estimate the longitudinal and lateral tire-ground forces. Besides the normal tire-ground forces, our final implementation can provide vehicle parameters as the mass and the center of gravity position; these values are essential to ensure the excellent performance of controllers that relies on dynamic models. Model-based controllers usually use the single-track model, which requires the mass and center of gravity position; most of the literature's works consider these values constant; nevertheless, these parameters are not constant.

In Section 4.2, we present the preliminaries for normal tire-ground estimation. Section 4.3 describes different strategies to estimate the normal TGFs available in the literature. The contribution of this thesis that addresses normal TGFs is in Section 4.4. Finally, Section 4.5 presents the conclusions and perspectives.

4.2 Preliminaries

In this section, we introduce the formulations made from different models, described in Chapter 2; the single-track and hoverboard models, and further, we develop the equations required to build our estimation scheme.

4.2.1 Acceleration Measurement

Let us consider modeling the vehicle on a banked road; the roll angle contains the suspension roll angle and road bank angle, hence $\phi = \phi_v + \phi_r$. The acceleration measurement updates by: in [Kawashima et al., 2010, Piyabongkarn et al., 2008]:

$$\begin{aligned} \bar{a}_y &= a_y \cos(\phi) + g \sin(\phi) \\ \bar{a}_z &= -a_y \sin(\phi) + g \cos(\phi) \end{aligned} \tag{4.1}$$

Similarly, for a vehicle on a slope

$$\begin{aligned} \bar{a}_x &= a_x \cos(\theta) + g \sin(\theta) \\ \bar{a}_z &= -a_x \sin(\theta) + g \cos(\theta) \end{aligned} \tag{4.2}$$

4.2.2 Normal force equation from vehicle dynamics

The wheel load shifts according to the vehicle's acceleration. The vertical force on each tire can be computed separately under the consideration that the roll and pitch movement are decoupled. When the car moves forward, the positive acceleration causes a load shift from front to rear axle, given the vehicle body's pitch motion due to its inertia. Similarly, when the vehicle is turning left, the lateral acceleration causes a load shift from left to right wheels, given the roll motion. [Kiencke and Nielsen, 2005] presents the complete formulation.

On the one hand, using the simplified bicycle model (2.21), and after some algebraic manipulation, it follows the equation to compute the front and rear virtual wheel forces:

$$\sum_{j\in\mathcal{A}} F_{z_{ij}} = \frac{l_{i^c}}{l} mg\cos(\theta_r)\cos(\phi_r) + q^{i^c}\frac{h}{l} m\left(a_x + g\sin(\theta_r)\right) + q^{i}\frac{I_y}{l}\ddot{\theta}_v \tag{4.3}$$

On the other hand, from the hoverboard model (2.22), it is also possible to estimate the vertical contact forces at the virtual left and right wheels. Using some algebra gives:

$$\sum_{i\in\mathcal{A}} F_{z_{ij}} = \frac{e^c_j}{e} mg\cos(\theta_r)\cos(\phi_r) + q^{j}\frac{h}{l} m\left(a_y + g\sin(\phi_r)\cos(\theta_r)\right) + q^{j^c}\frac{I_x}{e}\ddot{\phi}_v \tag{4.4}$$

Applying the superposition principle to sets (4.3)-(4.4), we are able to compute the normal tire:

$$\begin{aligned}\hat{F}_{zij} =& q^j\frac{I_x}{2e}\ddot{\phi}_v + q^i\frac{I_y}{2l}\ddot{\theta}_v + \frac{1}{2gel}\Big(q^j l_{i^c} I_x\ddot{\phi}_v g\cos(\theta_r)\cos(\phi_r) + q^j e_{j^c} I_y\ddot{\theta}_v g\cos(\theta_r)\cos(\phi_r)\\ &+ q^i q^j h I_x\ddot{\phi}_v\left(a_x + g\sin(\theta_r)\right) + q^i q^j h I_y\ddot{\theta}_v\left(a_y + g\sin(\phi_r)\cos(\theta_r)\right)\\ &+ 2e_{i^c} l_{j^c} mg^2\cos^2(\theta_r)\cos^2(\phi_r) + 2q^{j^c} h l_{i^c} mg\cos(\theta_r)\cos(\phi_r)\left(a_y + g\sin(\phi_r)\cos(\theta_r)\right)\\ &+ 2q^i h e_{j^c} mg\cos(\theta_r)\cos(\phi_r)\left(a_x + g\sin(\theta_r)\right)\\ &- 2q^i q^j h^2 m\left(a_y + g\sin(\phi_r)\cos(\theta_r)\right)\left(a_x + g\sin(\theta_r)\right)\Big)\end{aligned} \tag{4.5}$$

with $q = -1$ and ^{c} stands for the complement operator, ($i \in A := \{1, 2\}$, thus, if $i = 2$; then $i^c = 1$).

The significant challenge for computing the set of equations (4.3)-(4.5) is the estimation of bank and slope angles as its respective angular accelerations. Some authors [Tseng, 2001, Ryu and Gerdes, 2004, Kawashima et al., 2010] have analyzed the influence of bank angle on the vehicle dynamics and concluded that for a correct estimation is critical to differentiate between road bank angle (ϕ_r) and

chassis roll angle (ϕ_v) relative to the environment coordinate system, $\phi = \phi_r + \phi_v$. When calculating the vertical load distribution, the most critical parameters are the lateral acceleration. The normal TGFs due to gravity and road bank angle affect the lateral accelerometer when the vehicle tilts around the x-axis [Nilsson and Lingefelt, 2011].

Nonetheless, for planar road conditions, the dynamics equations (4.3) are simplified to

$$\sum_{j\in\mathcal{A}} F_{z_{ij}} = \frac{l_{i^c}}{l} mg + q^i \frac{h}{l} m\bar{a}_x \tag{4.6}$$

the left and right virtual tires,(4.4), to

$$\sum_{i\in\mathcal{A}} F_{z_{ij}} = \frac{e_{j^c}}{e} mg + q^j \frac{h}{l} m\bar{a}_y \tag{4.7}$$

and finally the normal force at each tire, (4.5) is:

$$\hat{F}_{zij} = \frac{1}{gel}\left(e_{i^c} l_{j^c} mg^2 + q^{j^c} h l_{i^c} mg\bar{a}_y + q^i h e_{j^c} mg\bar{a}_x - q^i q^j h^2 m\bar{a}_y\bar{a}_x\right) \tag{4.8}$$

4.3 State of the art

The chassis controllers' design is a difficult problem; they should address several issues such as road handling, body motion, vehicle safety, and ride comfort. These algorithms are sensitive to changes in inertial vehicle parameters, including the vehicle's mass, the moments of inertia, and the COG location. Furthermore, observation/estimation schemes are substantially sensitive to these parameters.

The vehicle's mass is the most critical parameter since it directly affects the longitudinal, lateral, and suspension dynamics; this parameter can vary substantially during vehicle operation. The mass estimation methods could be classified based on the observed dynamics.

- Longitudinal Dynamics: Many researchers have capitalized on the relationship between vehicle mass, longitudinal forces, and the resulting longitudinal acceleration, see [Bae et al., 2001, Vahidi et al., 2005, Winstead and Kolmanovsky, 2005, Rhode et al., 2016].
- Powertrain Dynamics, see [Fremd, 1987].
- Suspension Dynamics: The mass' estimation problem is simplified when suspension deflection sensors are available. In [Kim and Ro, 2000], the

author estimates the vehicle mass with the quarter-car model. Furthermore, in [Rajamani and Hedrick, 1995] based on the same model has been developed as an adaptive observer to estimate suspension states and parameters.

In [Rajamani and Hedrick, 1995], based on a nonlinear adaptive observer, the estimation of the sprung mass is addressed; even though an experimental validation exists the experiment was carried on in a test-rig with scaled testbeds. The real-experiment signals are clean (without noise), what it helps the nonlinear observer convergence.

Patent [Genise, 1996] shows an approach that has been used in industry for mass estimation based on the velocity drop during a gearshift. The change in velocity before and during gearshift is used to calculate a mass estimate based on the longitudinal dynamics equation.

In [Bae et al., 2001], presents a system for estimating the road grade, mass, rolling resistance, and aerodynamic drag of a ground vehicle using recursive least squares and as inputs values of engine torque calculated by the engine map, a Global Positioning System (GPS) receiver, and, optionally, wheel speed or inertial sensors.

In [Vahidi et al., 2005], using the longitudinal vehicle dynamics and recursive least square (RLS) with multiple forgetting factors. The information required to apply such estimation technique is plenty: Velocity estimate, wheel angular speed, GPS velocity measurement, the engine torque, compression brake, transmission retarded torques, brake pressure, transmission gear ratio, and the final drive ratio. The method estimates the mass and the slope angle simultaneously. They used both simulation and test data to validate the estimation scheme, and even during the gear shift operation.

In [Winstead and Kolmanovsky, 2005], introduces an active on-line estimation method for road grade and vehicle mass. The scheme combines the estimation of parameters with an EKF and a model predictive control (MPC) scheme to control vehicle speed while enhancing parameters' identification. Nonetheless, the research results are constraint to simulations.

[Rhode et al., 2016] introduces a windup-stable Kalman filter, called Stenlund-Gustafsson M-Kalman filter to recursively solve the random-walk output error model with the presence of outliers and periods with low excitation to estimate the vehicle mass, the road grade, and the drag force.

4.4 Contribution to Normal TGF Estimation

This chapter aims to develop an algorithm capable of accurately estimate the normal TGFs, using available sensors of conventional mass-produced automobiles, like accelerometers and gyroscopes, diminishing the use of other transducers that regular vehicles do not have.

4.4.1 Normal equation method

A car can be described with equations more complex than the presented in (2.20). Equation (2.20) assumes a rigid body, and therefore is possible to represent the vehicle as four contact points (one for each wheel) with constant distances L_1, L_2, E_1 and E_2 for all time. Nonetheless, this model is still too complex to develop an estimator. To simplify it, we consider the following: the tire patch always touches the ground, the effects of sprung mass do not affect the vehicle dynamics. The car movement is mainly towards the longitudinal vehicle's direction, then, v_y is considered zero. The assumptions are:

- $a_z << \zeta << 1 \therefore a_z \approx 0$.
- $\ddot{\theta}_v << \zeta << 1 \therefore \ddot{\theta}_v \approx 0$.
- $\ddot{\phi}_v << \zeta << 1 \therefore \ddot{\phi}_v \approx 0$.
- $F_{Dy} << \zeta << 1 \therefore F_{Dy} \approx 0$ with $F_{Dy} = \frac{1}{2}\rho C_{Dy} S_y v_y$.

Thus, from the above assumptions system (2.20) becomes,

$$\begin{aligned}
ma_x =& \sum_{i\in\mathcal{A}} F^o_{x2i} + \sum_{i\in\mathcal{A}} F^o_{x1i}\cos(\delta) - \sum_{i\in\mathcal{A}} F_{y1i}\sin(\delta) - m_v g\sin(\theta_r);\\
ma_y =& \sum_{i\in\mathcal{A}} F_{y2i} + \sum_{i\in\mathcal{A}} F_{y1i}\cos(\delta) + \sum_{i\in\mathcal{A}} F^o_{x1i}\sin(\delta) - m_v g\sin(\phi_r)\cos(\theta_r);\\
0 =& \sum_{i\in\mathcal{A}} F_{z1i} + \sum_{i\in\mathcal{A}} F_{z2i} - m_v g\cos(\theta_r)\cos(\phi_r)\\
0 =& \sum_{i\in\mathcal{A}} F_{zi1} + \sum_{i\in\mathcal{A}} F_{zi2} - m_v g\cos(\phi_r)\cos(\theta_r);\\
I_z\ddot{\psi}_v =& l_1\left(\sum_{i\in\mathcal{A}} F_{y1i}\cos(\delta) - \sum_{i\in\mathcal{A}} F^o_{x1i}\sin(\delta)\right) - l_2\sum_{i\in\mathcal{A}} F_{y2i};\\
0 =& h\left(\sum_{i\in\mathcal{A}} F_{yi2} + \sum_{i\in\mathcal{A}} F_{y1i}\cos(\delta) + \sum_{i\in\mathcal{A}} F^o_{x1i}\sin(\delta)\right) - e_1F_{zl} + e_2F_{zd};\\
0 =& h\left(\sum_{i\in\mathcal{A}} F^o_{x2i} + \sum_{i\in\mathcal{A}} F^o_{x1i}\cos(\delta) + \sum_{i\in\mathcal{A}} F_{y1i}\sin(\delta)\right) + l_1\sum_{i\in\mathcal{A}} F_{z1i} - l_2\sum_{i\in\mathcal{A}} F_{z2i};
\end{aligned} \tag{4.9}$$

Thus, the rolling resistance, the drag force and the longitudinal force are included within the variable $F^o_{x1i} = F_{x1i} - F_{1i}(\omega_r) - \gamma_i F_{Dx}$ with $\gamma_1, \gamma_2 \geq 0$ and these variables satisfy $\gamma_1 + \gamma_2 = 1$.

4.4.1.1 Normal Forces Modeling

On the one hand, from (4.9) is developed an estimator set to compute the front and rear virtual wheel forces, here they are calculated as static and dynamic vertical force components, $\hat{F}_{z\nu s}$ and $\hat{F}_{z\nu d}$ respectively, defined as

$$\sum_{i\in\mathcal{A}} \hat{F}_{z2i} = \frac{l_1}{l}\hat{F}_{z\nu s} + \frac{h}{l}\hat{F}_{z\nu d} \tag{4.10a}$$

$$\sum_{i\in\mathcal{A}} \hat{F}_{z1i} = \frac{l_2}{l}\hat{F}_{z\nu s} - \frac{h}{l}\hat{F}_{z\nu d} \tag{4.10b}$$

with,

$$\hat{F}_{z\nu s} = mg\cos(\theta_r)\cos(\phi_r) \tag{4.11a}$$

$$\hat{F}_{z\nu d} = m(a_x + g\sin(\theta_r)) \tag{4.11b}$$

Notice that, $\hat{F}_{z\nu s}$ depends on the vehicle's mass (m) and the road's slope angle (θ_r), see (4.11a), while $\hat{F}_{z\nu d}$ includes also the acceleration on x's direction, a_x, see

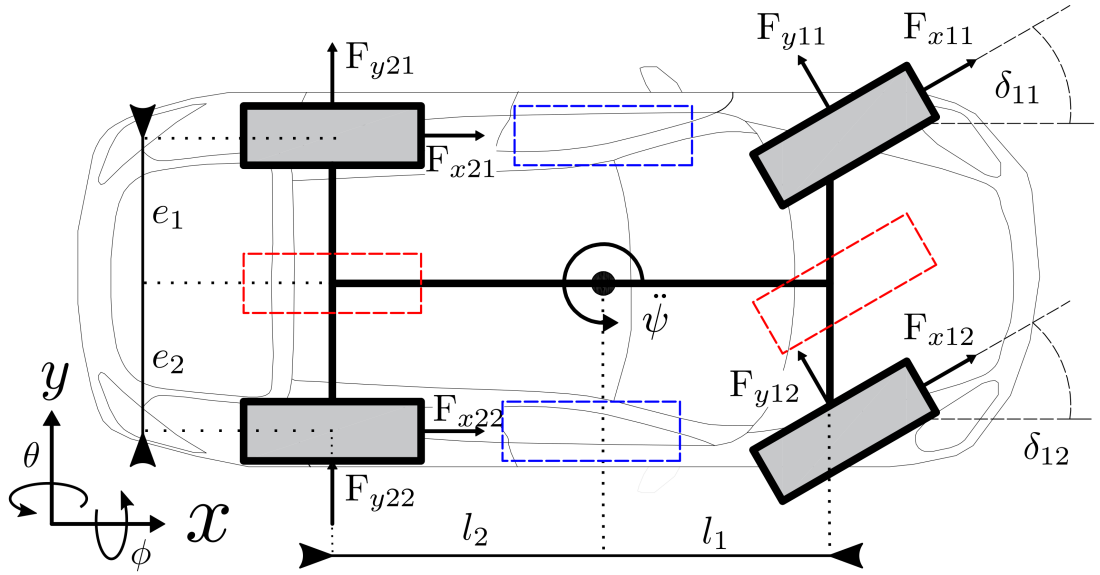

Figure 4.1 – Vehicle Model Draft - Double Track Model Superior View. Red dashed line shows the bicycle model and the blue dashed line refers to the hoverboard model

(4.11b).

On the other hand, from model (4.9), it is also possible to estimate the vertical contact forces at the virtual left and right wheels, $\sum_{i\in\mathcal{A}} \hat{F}_{zi1}$ and $\sum_{i\in\mathcal{A}} \hat{F}_{zi2}$ respectively. After some algebraic manipulation, gives

$$\sum_{i\in\mathcal{A}} \hat{F}_{z1i} = \frac{e_2}{e}\hat{F}_{z\eta s} - \frac{h}{e}\hat{F}_{z\eta d} \tag{4.12a}$$

$$\sum_{i\in\mathcal{A}} \hat{F}_{z2i} = \frac{e_1}{e}\hat{F}_{z\eta s} + \frac{h}{e}\hat{F}_{z\eta d} \tag{4.12b}$$

with,

$$\hat{F}_{z\eta s} = mg\cos(\phi_r)\cos(\theta_r) \tag{4.13a}$$

$$\hat{F}_{z\eta d} = m(a_y + g\sin(\phi_r)\cos(\theta_r) \tag{4.13b}$$

Here, $\hat{F}_{z\eta s}$ depends on vehicle's mass (m) and the road's bank angle (ϕ_r), see (4.13a), and for $\hat{F}_{z\eta d}$ definition also includes the lateral acceleration term a_y, see (4.13b). Observe that equations (4.10) and (4.12) are analogous addressing each one the longitudinal and lateral dynamics.

Equation sets (4.10) and (4.12) are used to compute the vertical forces at the front, rear, left and right virtual tires. However, our goal is to estimate the normal

forces at each wheel, not at virtual positions derived from bicycle and hover-board models; see Figure 4.1 to see the virtual tires with dotted lines. The estimation schemes obtained from sets (4.10) and (4.12) are used to develop the following linear system, thus,

$$\mathbf{A}\hat{\mathbf{F}}_z = \hat{\mathbf{F}}_k; \tag{4.14}$$

where:

$$\mathbf{A} = \begin{bmatrix} 1 & 1 & 0 & 0 \\ 0 & 0 & 1 & 1 \\ 1 & 0 & 1 & 0 \\ 0 & 1 & 0 & 1 \end{bmatrix} \tag{4.15}$$

$$\hat{\mathbf{F}}_z = \begin{bmatrix} \hat{F}_{z11} & \hat{F}_{z12} & \hat{F}_{z21} & \hat{F}_{z22} \end{bmatrix}^T \tag{4.16}$$

$$\hat{\mathbf{F}}_k = \begin{bmatrix} \sum_{i\in\mathcal{A}} \hat{F}_{z1i} & \sum_{i\in\mathcal{A}} \hat{F}_{z2i} & \sum_{i\in\mathcal{A}} \hat{F}_{zi1} & \sum_{i\in\mathcal{A}} \hat{F}_{zi2} \end{bmatrix}^T \tag{4.17}$$

with $\hat{F}_{z11}$ representing the vertical force estimation at the front left tire, $\hat{F}_{z12}$, $\hat{F}_{z21}$ and $\hat{F}_{z22}$ are the estimations for the front-right, rear-left, and rear-right tires respectively. Figure 4.1 shows the vertical forces in the middle of each wheel as a fill circled, representing a force vector that is perpendicular to the paper with direction towards the reader. System (4.14) is now used to calculate the normal TGFs, $\hat{F}_z$; nevertheless, as matrix $\mathbf{A}$ is singular, the linear system is singular. There exist plenty of vectors capable of transforming $\mathbf{A}$ into a full rank matrix, see [Lipschutz and Lipson, 2001] to look for suitable methods to find system eigenvectors; however, through in-depth analysis, we conclude that the required vectors to solve system (4.14) are $\mathbf{a}_1 = \begin{bmatrix} 1 & 0 & 0 & 1 \end{bmatrix}$ and $\mathbf{a}_2 = \begin{bmatrix} 0 & 1 & 1 & 0 \end{bmatrix}$, $F_{zDi} = \mathbf{a}_i\mathbf{F}_z$ is the sum of the normal contact forces between the front left and rear right tires and backwards.

4.4.1.2 Heuristic Estimator Model

Analyzing equations (4.10), (4.12) and (4.14), notice that, the static vertical force component remains constant and due to the dynamic component the load transfer occurs. Nevertheless, when the load is added to a tire due to vehicle dynamics, effects are also subtracted from another wheel to satisfy the mass conservation law because the total mass remains constant (neglecting fuel consumption), and the vertical movement is neglected. Thus from heuristic observations, the following

estimation model,

$$\begin{aligned}\hat{F}_{z_{11}} =& c_1 - c_2 a_x - c_3 a_y;\\ \hat{F}_{z_{12}} =& c_4 - c_5 a_x + c_6 a_y;\\ \hat{F}_{z_{21}} =& c_7 + c_8 a_x - c_9 a_y;\\ \hat{F}_{z_{22}} =& c_{10} + c_{11} a_x + c_{12} a_y;\end{aligned} \tag{4.18}$$

The coefficients $c_n \forall n \in [1, 12]$ are constants values which depends on initial weigh distribution, variables l_1, l_2, e_1, e_2, h and m. The just mentioned is noticeable when we compare equations (4.8) and (4.18). Then, if we consider a symmetric weight distribution of the vehicle means that $c_2 \approx c_{11}$, $c_5 \approx c_8$, $c_3 \approx c_{12}$, and $c_9 \approx c_{12}$. Thus, it follows that

$$\begin{aligned}\hat{F}_{z_{12}} + \hat{F}_{z_{21}} &= c_4 + c_7\\ \hat{F}_{z_{11}} + \hat{F}_{z_{22}} &= c_1 + c_{10}\end{aligned} \tag{4.19}$$

where c_1 stands for the initial vertical force condition at the front left tire, $\hat{F}_{z_{11}}(0)$, similarly the coefficients c_4, c_7 and c_{10} are defined by the initial vertical forces at $\hat{F}_{z_{12}}(0)$, $\hat{F}_{z_{21}}(0)$ and $\hat{F}_{z_{22}}(0)$, respectively; this also could be obtained from (4.5) or (4.8). Equations (4.19), means that $\hat{F}_{z_{11}} + \hat{F}_{z_{22}}$ and $\hat{F}_{z_{12}} + \hat{F}_{z_{21}}$ remains constant for all time.This assumption allows us to solve system (4.14); nonetheless, it holds when the automobile has a standard design and under regular use (by classic design, we mean a balanced car vehicle with the COG at the middle of the car). In Figure 4.2, a comparison between the response of consideration (4.19) and the actual measurements from wheel force transducers is presented. Here in solid line $c_1 + c_7$ is depicted, in dashed-dotted line $c_4 + c_{10}$ is displayed, in dashed line is shown the measurement for $F_{z11} + F_{z22}$ and the dotted line illustrates the measurement for $F_{z12} + F_{z21}$. Now, it is required to be developed a static vertical force estimator to compute $\left[\hat{F}_{z12}(0); \hat{F}_{z21}(0); \hat{F}_{z11}(0); \hat{F}_{z22}(0)\right]$.

4.4.1.3 Modeling using simplified quarter car suspension approach

A vehicle suspension system has multiple degrees of freedom; the suspension is a complex vibrations problem. Figure 4.3 represents a wheel that includes viscoelastic effects in the spring and damper suspension coefficients. Observe that the goal is to compute $\hat{F}_{z_{ij}}(0)$, which could be measured accurately at a stationary vehicle's condition. The model presented here uses just one degree of freedom; however, in subsection 4.4.1.4, more degrees of freedom are introduced. Thus, applying Newton laws of motion and from Figure 4.3, it follows that $\hat{F}_{z_{ij}} = k_{eq_{ij}} \cdot h_{ij} + c_{eq_{ij}} \cdot \dot{h}_{ij}$ where

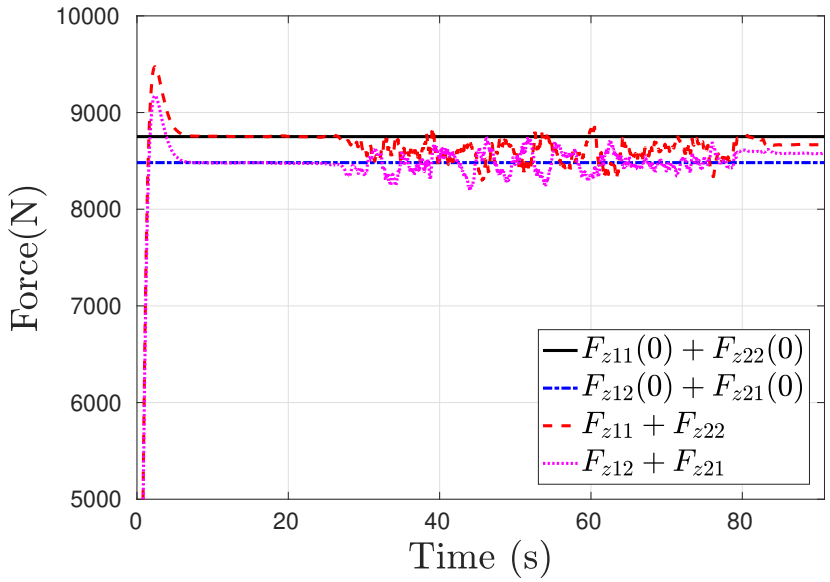

Figure 4.2 – Comparison between real and estimation of vertical forces addition ($\hat{F}_{z11} + \hat{F}_{z22}$; $\hat{F}_{z12} + \hat{F}_{z21}$) developed in equation (4.19), experimental measures are provided by dynamometric wheels installed on the experimental vehicle.

$k_{eq_{ij}}$ describes the spring coefficient, h_{ij} denotes mass' heigh, mg is the weight, $c_{eq_{ij}}$ stands for the damping coefficient and $\dot{h}_{ij}$ means the mass velocity on the vertical direction. Notice here, that our aim is to find the normal force at a static condition, thus, $\dot{h}_{ij} = 0$, an this implies that $\hat{F}_{z_{ij}}(0) = k_{eq_{ij}} \cdot h_{ij}$; where $h_{ij} = z_{ij} - z_{r_{ij}}$ and $\dot{h}_{ij} = \dot{z}_{ij} - \dot{z}_{r_{ij}}$.

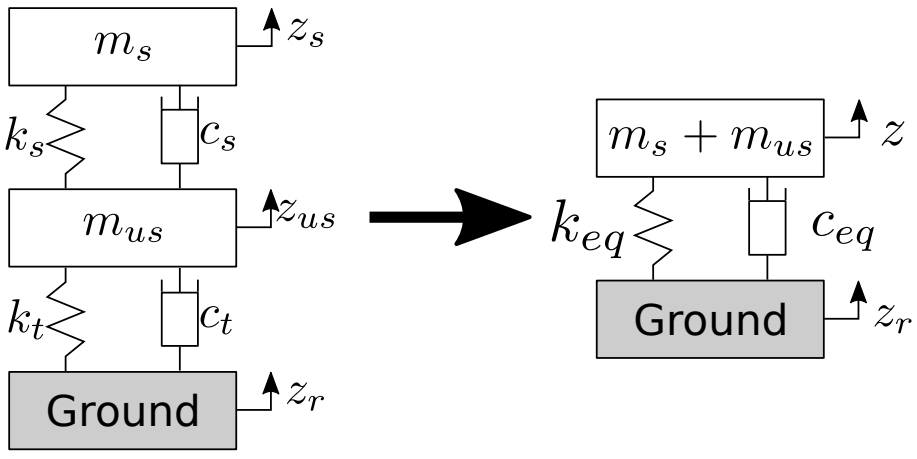

Figure 4.3 – Quart-Cart suspension model Sketch

4.4.1.4 Multi-model approach

We created a database from the data collected. We include measurement of the vehicle static and dynamic state; thus, using statistical software Minitab ※and the static collected data (h_{ij}), we obtain 18 regressions; each regression depends on the suspension deflection sensors. A brief sample of these models is in the following:

$$\begin{aligned}
\hat{F}_{z_{ij_1}}(0) =& 5566 - 3852h_{ij};\\
\hat{F}_{z_{ij_2}}(0) =& -12945 + 151394h_{ij} - 322525h_{ij}^2;\\
\vdots \quad =& \quad \vdots\\
\hat{F}_{z_{ij_{18}}}(0) =& 6737 - 3451h_{ij} + 5348h_{ij^c} - 15905h_{i^cj} + 2420h_{i^cj^c};
\end{aligned} \tag{4.20}$$

Each one of the models presented in (4.20) has a 95% confidence interval with a two tales normal distribution, and a different determination coefficient, R^2. A parallel Kalman filter is applied to the set of models. The intention is to find the most probable response for $\hat{F}_{z_{ij}}(0)$ by performing a fusion of the regressions. Figure 4.4 shows with blue-dashed line two regression responses with different covariance; the same figure also portrays with a red-solid line the fusion response of the Kalman filter.

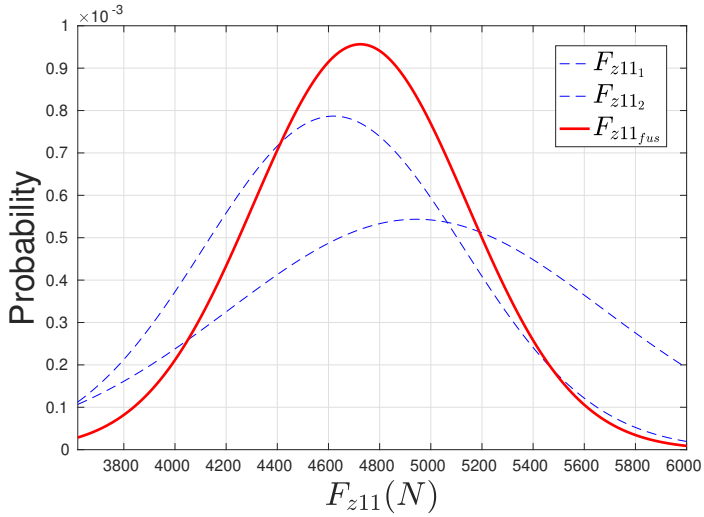

Figure 4.4 – Model responses with different covariance aiming to find the sweet spot

4.4.1.5 Vertical Force Estimator

Takin into account from vectors F_{zD1}, F_{zD2}; considering (4.19) and from linear system (4.14) and extended linear system is built; such system is:

$$\mathbf{A}_0\hat{\mathbf{F}}_z = \hat{\mathbf{F}}_{k_0} \tag{4.21}$$

where

$$\begin{aligned}
\mathbf{A}_0 &= \begin{bmatrix} 1 & 0 & 1 & 0 & 1 & 0 \\ 1 & 0 & 0 & 1 & 0 & 1 \\ 0 & 1 & 1 & 0 & 0 & 1 \\ 0 & 1 & 0 & 1 & 1 & 0 \end{bmatrix}^T \\
\hat{\mathbf{F}}_{k_0} &= \begin{bmatrix} \sum_{i\in\mathcal{A}} \hat{F}_{z_{1i}} & \sum_{i\in\mathcal{A}} \hat{F}_{z_{2i}} & \sum_{i\in\mathcal{A}} \hat{F}_{z_{i2}} & \sum_{i\in\mathcal{A}} \hat{F}_{z_{i1}} & \hat{F}_{zD1} & \hat{F}_{zD2} \end{bmatrix}^T
\end{aligned} \tag{4.22}$$

where $\hat{F}_{zD1} = \hat{F}_{z11}(0) + \hat{F}_{z22}(0)$; and $\hat{F}_{zD2} = \hat{F}_{z12}(0) + \hat{F}_{z21}(0)$. Observe that, $\hat{\mathbf{F}}_z$ remains the same as in (4.14), thus isolation $\hat{\mathbf{F}}_\mathbf{z}$ from linear system (4.21), gives

$$\hat{\mathbf{F}}_z = (\mathbf{A}_0^T\mathbf{A}_0)^{-1}\mathbf{A}_0^T\hat{\mathbf{F}}_{k_0} \tag{4.23}$$

Equation (4.23) defines our first estimation algorithm to compute wheel-ground contact vertical forces. In the following sections, its feasibility and accuracy under real-time experiments are proved.

4.4.1.6 Experimental results using the normal equation method

An experiment to validate our vertical forces estimation model is defined in equation (4.23). In this case, we consider prior knowledge of the initial weight distribution ($\hat{F}_{z11}(0)$, $\hat{F}_{z12}(0)$, $\hat{F}_{z21}(0)$, $\hat{F}_{z22}(0)$) due the multi-model approach applied with set of equations (4.20).

A slalom maneuver is performed with our experimental testbed, Dyna308, at a maximum of 60 kph. During this maneuver, the tires do not experiment saturation. Figure 4.6 shows the response of equation (4.23) with a red-solid line; the black-dashed line represents the actual force measured with the Kistler's sensors; finally, this figure shows with a pink-dotted line the response from algorithm presented in [Jiang et al., 2014].

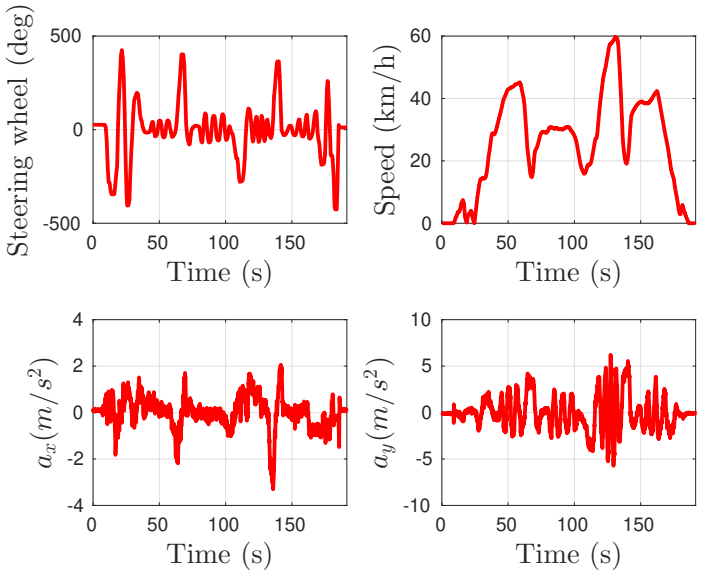

Figure 4.5 – Slalom maneuver carried out to validate the model at 60 km/h maximum velocity

4.4.2 Extension using the quarter-car model

The mass' estimation problem is simplified when suspension deflection sensors are available. In [Kim and Ro, 2000] employing the quarter-car model, the authors estimate the vehicle's mass. Furthermore, in [Rajamani and Hedrick, 1995] based on the same principle, an adaptive observer has been developed to estimate suspension states and parameters.

In Chapter 2, the quarter car model is introduced in equation (2.25); nonetheless this equation is already simplified to work at the equilibrium point of the suspension system, but to estimate the mass, we need the base model, thus:

$$m_{sij}\ddot{z}_{sij} = -k_{sij}(z_{sij} - z_{usij} - L_{sij}) - c_{sij}(\dot{z}_{sij} - \dot{z}_{usij}) - m_{sij}g \tag{4.24a}$$

$$\begin{aligned} m_{usij}\ddot{z}_{usij} = {} & k_{sij}(z_{sij} - z_{usij} - L_{sij}) + c_{sij}(\dot{z}_{sij} - \dot{z}_{usij}) \\ & - k_{tij}(z_{usij} - z_{rij} - R_{tij}) - c_{tij}(\dot{z}_{usij} - \dot{z}_{rij}) - m_{usij}g \end{aligned} \tag{4.24b}$$

where L_s is the nominal elongation of the spring, and R_t is the nominal elongation of the spring modeling the tire. If we analyze the equilibrium points of (4.24) we could obtain:

$$m_{sij} = -\frac{k_{sij}}{g}(z_{sij} - z_{usij} - L_{sij}) \tag{4.25a}$$

$$F_{zij}(0) = m_{usij}g - k_{sij}\left(z_{sij} - z_{usij} - L_{sij}\right) \tag{4.25b}$$

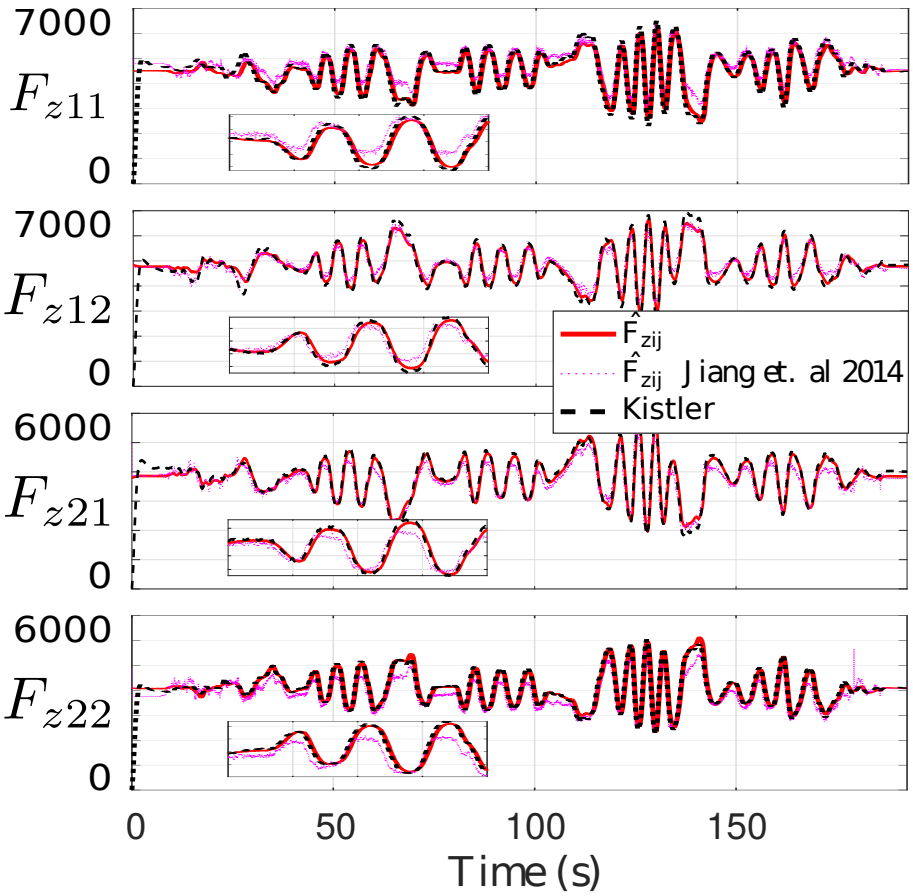

Figure 4.6 – F_{zij} measurement response versus the estimate $\hat{F}_{zij}$ at maximum speed of 60 km/h velocity.

notice that k_{sij} and L_{sij} are design variables; therefore prior knowledge is considered, deflection sensors measure $z_{sij} - z_{usij}$. Also, given this knowledge, it is possible to obtain the initial condition for the normal TGFs, given that the unsprung mass is also a design variable. Moreover, from model (2.26) we get:

$$m_s \ddot{z}_s = -\sum_{i\in\mathcal{A}}\sum_{j\in\mathcal{A}} \left(k_{sij}\left(z_{sij} - z_{usij} - L_{sij}\right) + c_{sij}\left(\dot{z}_{sij} - \dot{z}_{usij}\right)\right) - m_s g \tag{4.26}$$

here, m_s represents the vehicle sprung mass, and $\ddot{z}_s$ is the vertical acceleration at the COG of the whole vehicle sprung mass and calculating the equilibrium points, gives:

$$m_s g - \sum_{i\in\mathcal{A}}\sum_{i\in\mathcal{A}} k_{sij} L_{sij} = -\sum_{i\in\mathcal{A}}\sum_{j\in\mathcal{A}} k_{sij}\left(z_{sij} - z_{usij}\right) \tag{4.27}$$

and when setting our equilibrium point to zero, $(z_{sij} - z_{usij}) = 0$, we get:

$$m_s g = \sum_{i\in\mathcal{A}} \sum_{i\in\mathcal{A}} k_{sij} L_{sij} \tag{4.28a}$$

$$m_{sij} g = k_{sij} L_{sij} \tag{4.28b}$$

$$F_{zij}(0) = m_{usij} g + k_{sij} L_{sij} \tag{4.28c}$$

from (4.28c) and the single-track model (2.21), it follows:

$$\begin{aligned} \hat{l}_1 &= \frac{\sum_{i\in\mathcal{A}} \hat{F}_{z2i}(0) l - h\left(mg\sin(\theta_r(0))\right)}{mg\cos(\theta_r(0))\cos(\phi_r(0))} \\ \hat{l}_2 &= \frac{\sum_{i\in\mathcal{A}} \hat{F}_{zf}(0) l + h\left(mg\sin(\theta_r(0))\right)}{mg\cos(\theta_r(0))\cos(\phi_r(0))} \end{aligned} \tag{4.29}$$

with $m = \frac{1}{g}\sum_{i\in\mathcal{A}}\sum_{j\in\mathcal{A}} \hat{F}_{zij}(0)$. Analogously, taking into account the hoverboard vertical dynamics, gives

$$\begin{aligned} \hat{e}_2 &= \frac{\hat{\sum}_{i\in\mathcal{A}} F_{zi2}(0) E + hm(g\sin(\phi_r(0))\cos(\theta_r(0))}{mg\cos(\phi_r(0))\cos(\theta_r(0))} \\ \hat{e}_1 &= \frac{\sum_{i\in\mathcal{A}} \hat{F}_{zi1}(0) E - hm(g\sin(\phi_r(0))\cos(\theta_r(0))}{mg\cos(\phi_r(0))\cos(\theta_r(0))} \end{aligned}$$

Finally, the weight distribution and the COG computation increase its accuracy with lower excitation inputs and in particular situations as when $v_x = 0$; considering small road angles $\phi_r \approx \theta_r \approx 0$; simplifies the computation of variables $\hat{l}_i$ and $\hat{e}_i$, thus

$$\begin{aligned} \hat{l}_1 &= \frac{\sum_{i\in\mathcal{A}} \hat{F}_{z2i}(0)\cdot l}{m\cdot g};\ \ \hat{l}_2 = \frac{\sum_{i\in\mathcal{A}} \hat{F}_{z1i}(0)\cdot l}{m\cdot g}; \\ \hat{e}_1 &= \frac{\sum_{i\in\mathcal{A}} \hat{F}_{zi2}(0)\cdot e}{m\cdot g};\ \ \hat{e}_2 = \frac{\sum_{i\in\mathcal{A}} \hat{F}_{zi1}(0)\cdot e}{m\cdot g}; \end{aligned}$$

without requiring prior knowledge on the COG's altitude, h. This algorithm's accuracy at lower excitation environments is higher when compared against other responses obtained with different methodologies based exclusively on vehicle dynamics.

All of the approaches to estimating TGFs or even chassis controllers are sensitive to changes in the vehicle inertial parameters. The normal TGFs are the most

critical parameter in our scheme since they directly affect our estimations for the longitudinal and lateral TGFs.

4.4.2.1 Experimental results extension

A total of three tests are presented, the results validate the proposed algorithms; Figures 4.7, 4.8 and 4.9, represent part of the vehicle state in each one fo the test, respectively. The first two tests are slalom maneuvers at 55 kph and 70 kph maximum speed, respectively. Notice that during the first test, the absolute lateral acceleration is maintained below 5 m/s^2, while the second test the same variable reaches 10 m/s^2, see Figures 4.7, 4.8. During test No. 2, the tire experiments force saturation; this phenomenon increases the problem"s complexity. The test is conducted at 60 kph with a constant steering value to maintain a circular vehicle trajectory. During this maneuver, a low steering excitation is pursued; moreover, while performing the circle at the 150 seconds mark, the driver brakes while turning.

The first two tests can be divided into three main parts, an acceleration stage until we arrive at cruise speed where a slalom is done and, finally, the braking stage. During test No. 1, the schedule is the following:

- Acceleration phase from 25 to 40 seconds.
- Slalom from 40 to 60 s.
- Braking phase from 60 to 80 s.

The schedule for test No. 2 is:

- Acceleration phase from 25 to 38 seconds.
- Slalom from 38 to 55 s.
- Braking phase from 55 to 70 s.

The schedule for test No. 3 is:

- Constant steering from 20 s to 250 s.
- Braking phase from 140 s to 150 s.

Figure 4.10, shows the normal TGFs response to mission No. 1; here, the tire operation point is within the limits of its linear response. This figure depicts the proposed model response with a red-solid line; this predictor perfectly fits the actual normal TGFs portrayed with a black-dotted line.

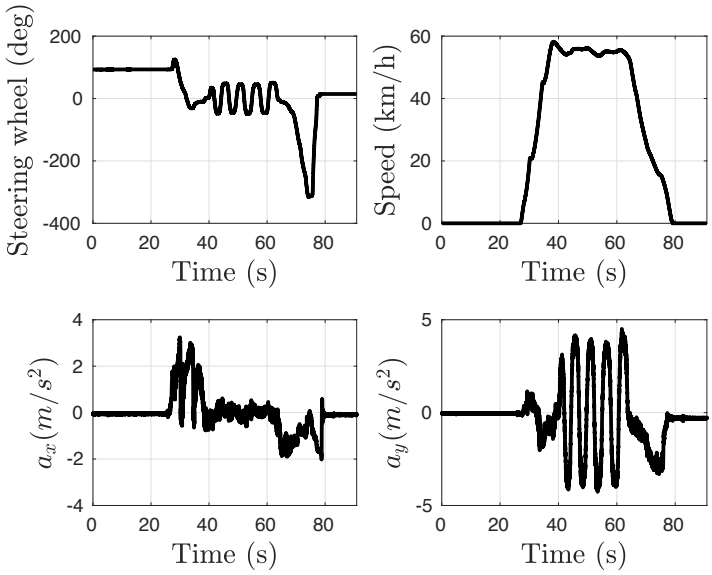

Figure 4.7 – Test No. 1 carried out to validate the longitudinal/lateral TGFs estimation scheme ($\max(v_x) = 60km/h$, $\max(\mid a_y \mid) = 4.7m/s^2$).

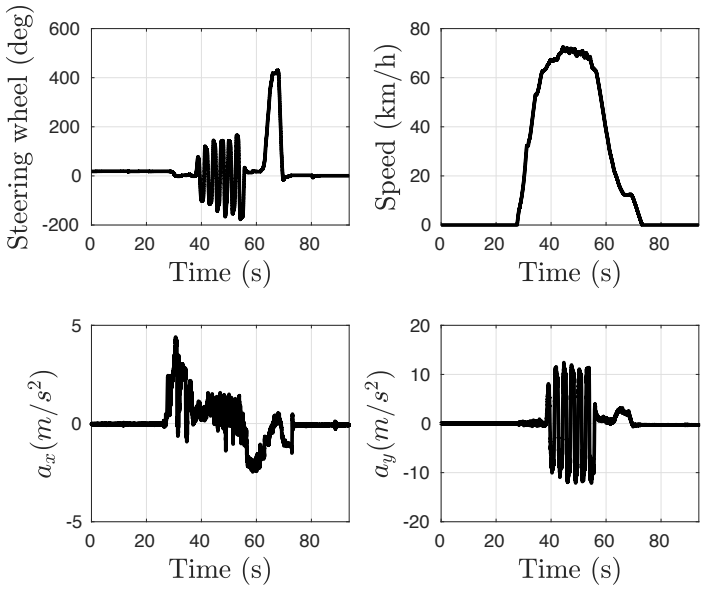

Figure 4.8 – Test No. 2 carried out to validate the longitudinal/lateral TGFs estimation scheme ($\max(v_x) = 71km/h$, $\max(\mid a_y \mid) = 10m/s^2$).

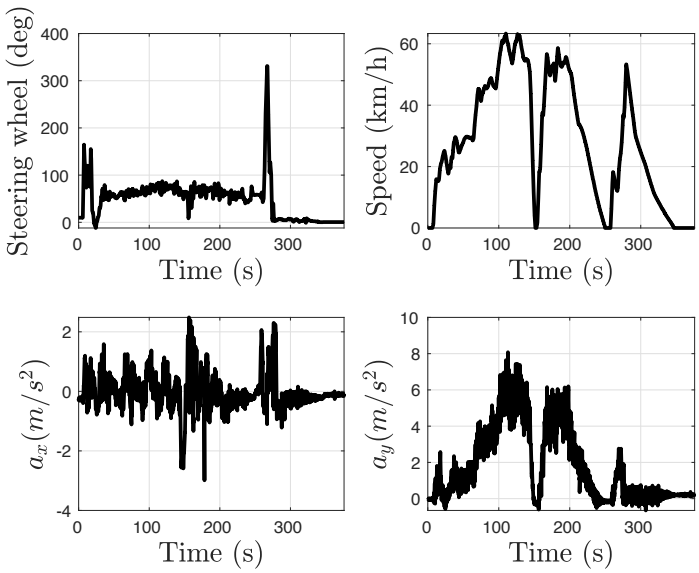

Figure 4.9 – Test No. 3 carried out to validate the longitudinal/lateral TGFs estimation scheme ($\max(v_x) = 60km/h$, $\max(\mid a_y \mid) = 6.5m/s^2$).

Figure 4.11 presents similar behavior; during this test, the tires experiment saturation. Notice that the proposed model shows a response overshoots at the front tires ($\hat{F}_{z_{11}}$ and $\hat{F}_{z_{12}}$); we attribute this phenomenon to the change from the linear operation region to the saturated one.

Finally, Figure 4.12 validate our algorithm during transient situations as maneuver No. 3. The estimation during maneuvers of this kind might suffer accuracy loss since they do not consider the vehicle chassis angles or low excitation levels.

4.4.2.2 Result Analysis

Once proposed and validated our algorithm, we have to make a quantitative assessment addressing the accuracy of our estimation; thus, we define the following error,

$$\tilde{F}_{z_{ij}} := \hat{F}_{z_{ij}} - F_{z_{ij}}$$

Figure 4.13 shows the error distribution after analyzing test No. 1 on the left side, test No. 2 on the center, and test No. 3 on the right side. In this analysis, the four wheels' errors are taken into account; the same figure shows the residual outliers for each one of the tests. The error has a normal distribution; the standard deviation for the test No. 1 is $\sigma_z = 210N$, with a mean value of $\mu_z = 68.35N$, and 0.76% of the data is considered an outlier. Similarly, for test No. 2, the error distribution has normal characteristics; during this test, the error standard deviation is $\sigma_z = 381N$, and its mean value is $\mu_z = 165.80N$, while the data outliers are 5.64%. Finally,

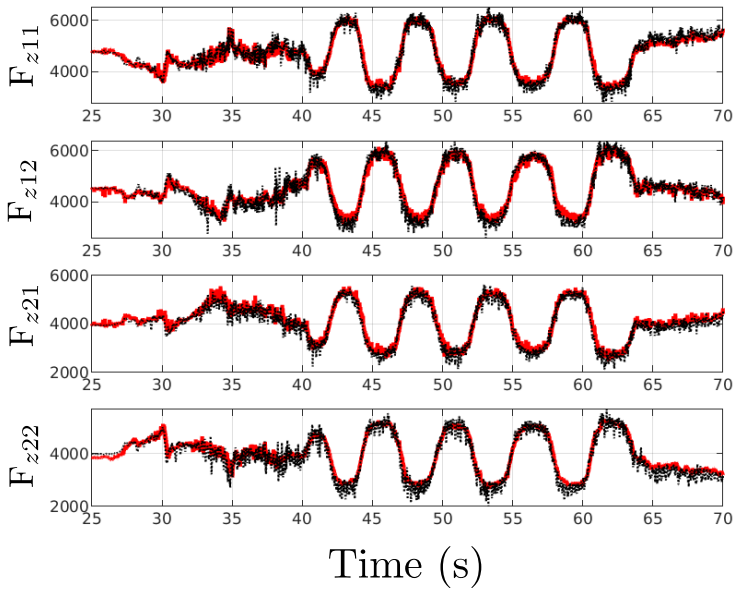

Figure 4.10 – Estimated Normal TGFs, $\hat{F}_{zij}$, response compared against the actual measurement given by Kysler dynamometers during test No. 1. Red-Solid line: $\hat{F}_{zij}$ - Proposition. Black-Pointed line: F_{zij} - Sensor Measurement

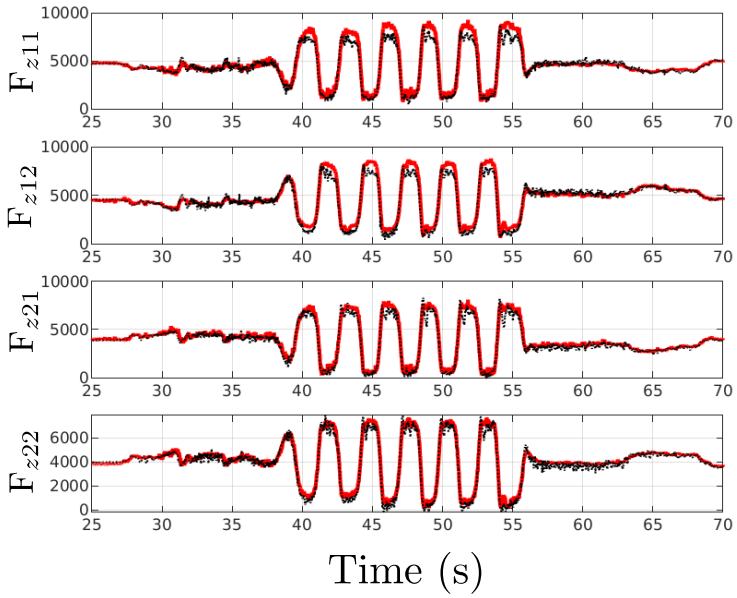

Figure 4.11 – Estimated Normal TGFs, $\hat{F}_{zij}$, response compared against the actual measurement given by Kysler dynamometers during test No. 2. Red-Solid line: $\hat{F}_{zij}$ - Proposal. Black-Pointed line: F_{zij} - Sensor Measurement

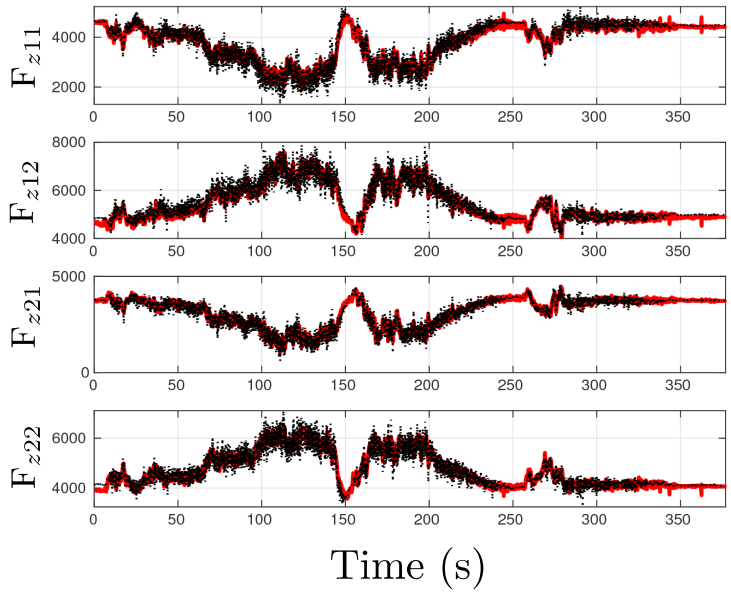

Figure 4.12 – Estimated Normal TGFs, $\hat{F}_{zij}$, response compared against the actual measurement given by Kysler dynamometers during test No. 3. Red-Solid line: $\hat{F}_{zij}$ - Proposal. Black-Pointed line: F_{zij} - Sensor Measurement

for the test No. 3 shows a standard deviation of $\sigma_z = 199N$, a mean error of $\mu_z = -15N$, and the error outliers are 1.98%.

4.4.3 Data fusion with Kalman filter

The normal TGFs are crucial for obtaining an accurate longitudinal and lateral TGFs estimation. So far, we have used vehicle and suspension models to compute the normal TGF's, but it is widely known that data fusion is a powerful tool to increase accuracy and add robustness. This section uses a Kalman filter to estimate these forces by fusing the bicycle, hoverboard, quarter-car, and seven degrees of freedom models. The use of a Kalman filter improves the estimation accuracy and adds robustness via statistical consensus of those mentioned models.

Data fusion strategy resembles the sensor redundancy concept (in this case is model redundancy); this allows us to an estimator able to estimate model parameters that up to this moment were considered known.

Figure 4.14 shows our strategy; first, we compute the normal TGFs obtained from the suspension model; we feed these results to an EKF based on the dynamic vehicle models; as an output, we get the normal TGFs, the mass, $\hat{m}$, and the COG position estimation ($\hat{E}_1$, $\hat{L}_1, \hat{h}$).

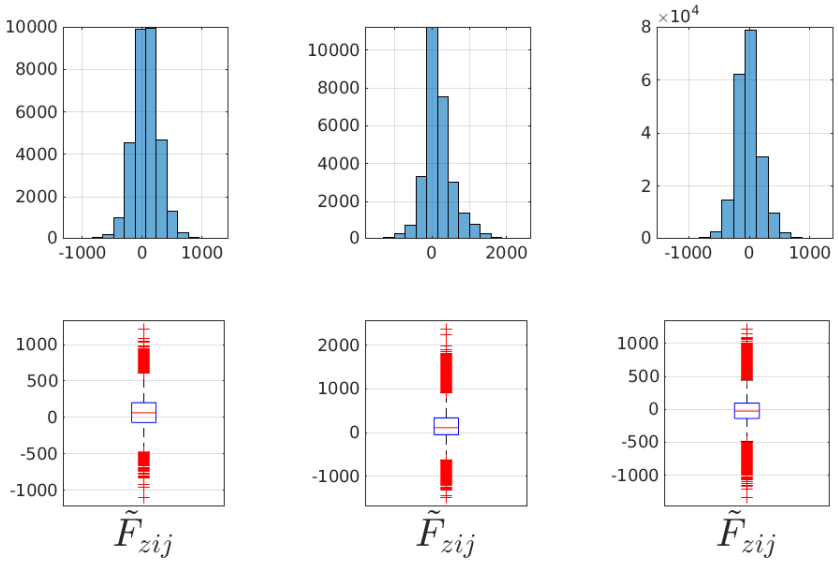

Figure 4.13 – Up: Distribution of the estimation error. Down: Boxplot graph obtained from the estimation error. Left: test No. 1. Center: test No. 2. Right: test No. 3.

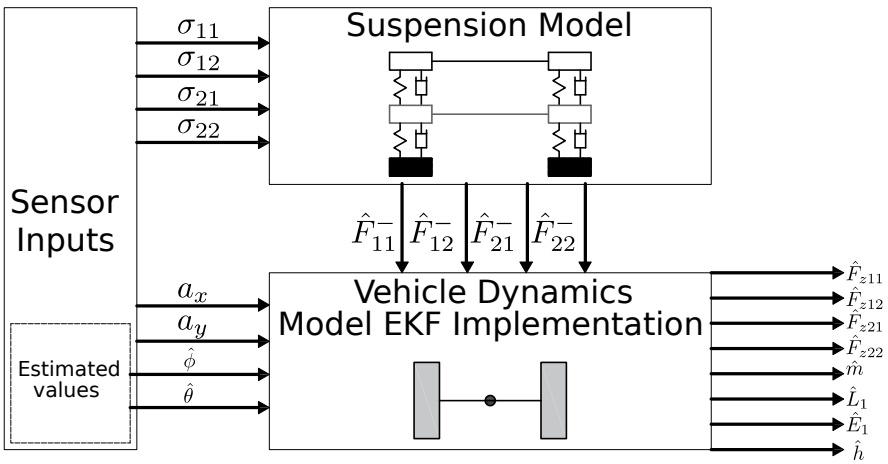

Figure 4.14 – Normal TGFs observation diagram

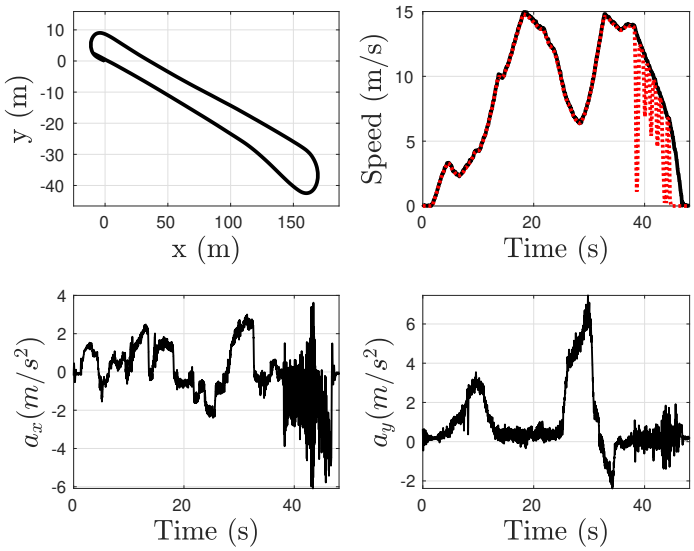

Figure 4.15 – Low friction coefficient mission. Upper-Left: gps measurement x, y coordinates. Upper-Right: Vehicle velocity –black-solid line –. Rear tires average velocity – red-dotted line –. Bottom-Left: Longitudinal acceleration. Bottom-Right: Lateral acceleration.

4.4.3.1 Experimental Results

This section presents experiments to validate our data fusion scheme. We carried out two experiments with Dyna308 to validate our proposals; the missions performed are depicted in Figures 4.15 and 4.16. During the first test, the road has low friction. Figure 4.15 shows with a black-solid line the vehicle speed measured with a GPS and with a red-dotted line the average angular rate obtained from the rear wheels; here, we show that exists a discrepancy between both sensors due to the wheel lock phenomena. Figure 4.16 shows the same maneuver but with high road friction; after a careful analysis of both tests, we can notice that during mission No. 2 the tires did not reach the saturation point during the braking operation.

The initial state of our filter uses data provided by the car manufacturer; this means that $\hat{m}(0)$, $\hat{E}_1(0)$, and $\hat{L}_1(0)$ are set with values of an empty car. As time passes, the estimated state converges to the actual state.

Figure 4.17 shows the response of our model fusion during test No. 1; this figure displays the estimation algorithm response in the red-solid line, and a black-dashed line represents the actual measurement from the force transducer. Notice that our algorithm has some pikes, caused by the noise and the sensibility of the input sensors; remember that this test is carried out in a road with low friction.

Figure 4.18 displays with a red-solid line the parameters estimated with our proposal and the real parameters are depicted with a black-dashed line. The initial values for the parameter estimation are $m = 1582$ kg, $L_1 = 1.0410$ m, $E_1 = 0.6958$

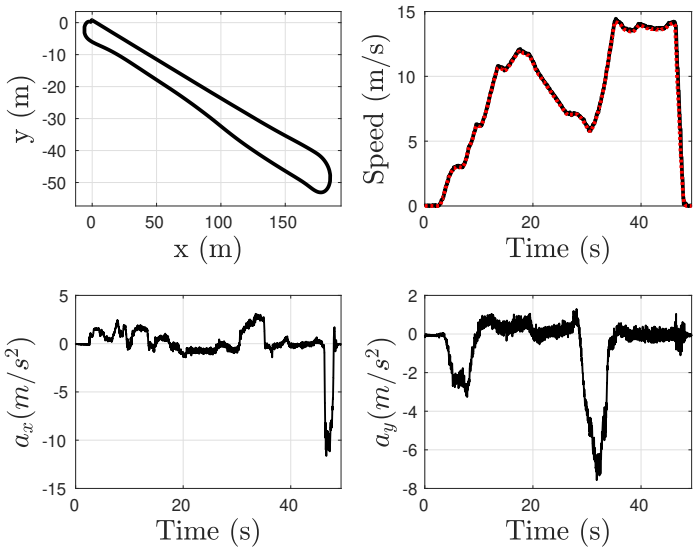

Figure 4.16 – High friction coefficient mission. Upper-Left: gps measurement x, y coordinates. Upper-Right: Vehicle velocity –black-solid line –. Rear tires average velocity – red-dotted line –. Bottom-Left: Longitudinal acceleration. Bottom-Right: Lateral acceleration.

m, and $h = 0.48$ m.

Figures 4.19 and 4.20 show the estimated state obtained with our proposal against the actual state. During this test, the road has high friction.

4.5 Conclusions

The chapter addresses the normal TGFs computation/estimation problem. The normal TGFs are the most crucial variable of the TGFs since it is used for the computation of the longitudinal and lateral TGFs estimation.

The first section presents state of the art for normal TGFs and related research. The most important works related to this are mentioned, and from that point, we start our proposal.

Our proposal could be divided into three stages, first solving the normal equation using only dynamic-vehicle models and a simplified quarter-car model. On a second stage, we use the quarter-car model to improve the estimator accuracy; here, we consider knowledge on design variables as the unsprung mass, the suspension stiffnesses, and damping coefficients. Finally, on the third stage, we implement a Kalman filter to fuse all the incoming information. We estimate the normal TGFs and the vehicle's mass and the center of gravity position (E_1, L_1, h).

Finally, we validate our proposal with tests that address different maneuvers and road conditions. On the one hand, we perform tests that consist of tire linear

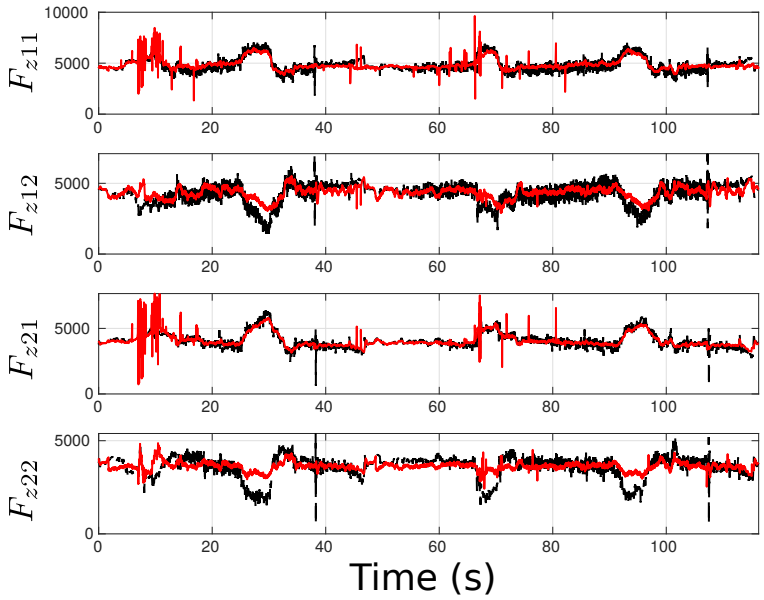

Figure 4.17 – Low Friction Mission. Normal TGFs comparison. Model Fusion Proposal: red-solid line. Sensor measurement: black-dashed line.

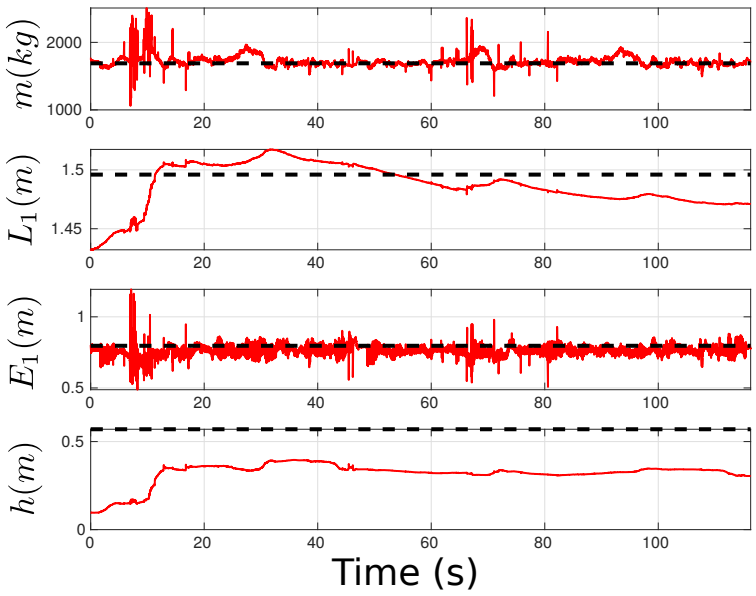

Figure 4.18 – Low Friction Mission. Normal TGFs comparison. Parameter Estimation: red-solid line. Sensor measurement: black-dashed line.

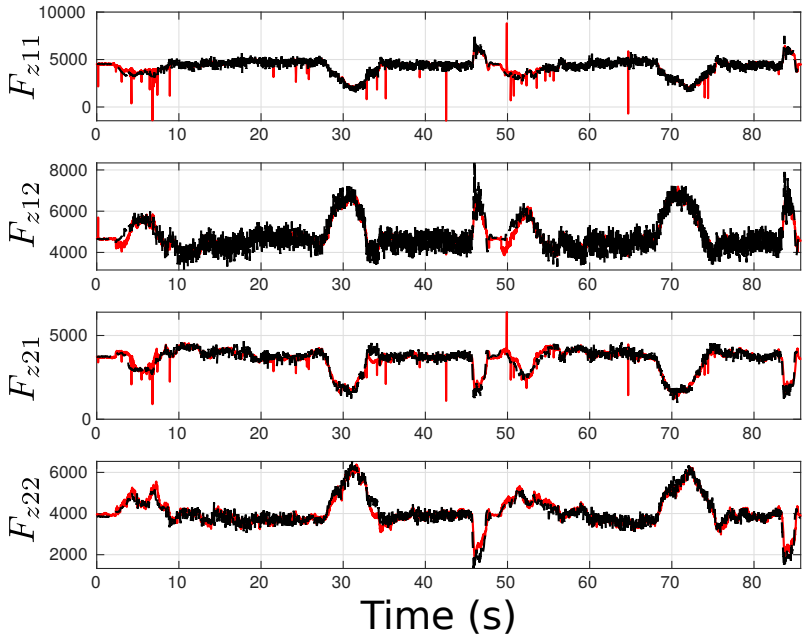

Figure 4.19 – High Friction Mission. Normal TGFs comparison. Model Fusion Proposal: red-solid line. Sensor measurement: black-dashed line.

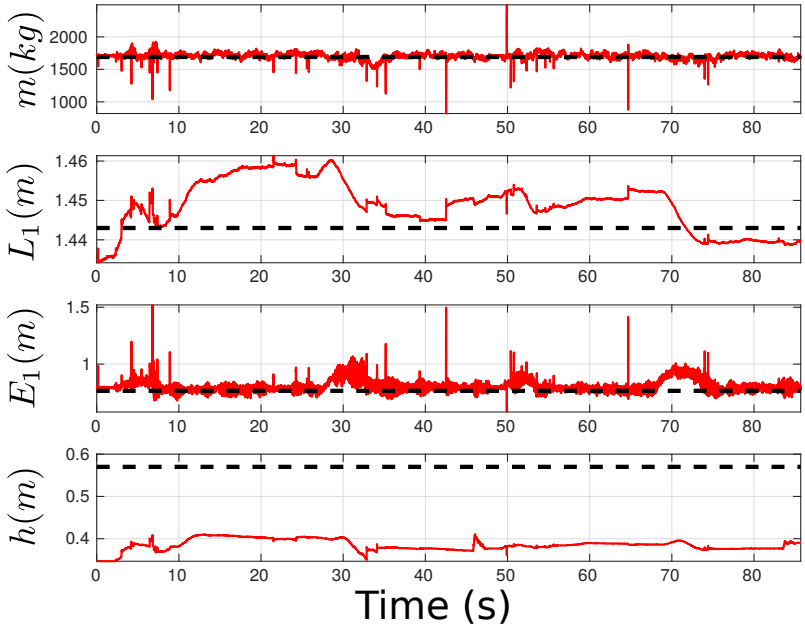

Figure 4.20 – High Friction Mission. Parameter Estimation. Proposal: red-solid line. Sensor measurement: black-dashed line.

and nonlinear behavior produced by an excess in vehicle speed. On the other hand, we validate our scheme to variable road friction—the proposed scheme's accuracy and robustness in all conditions.

Longitudinal and Lateral Tire Ground Force Estimation: Part 1

Contents

5.1 Introduction

The longitudinal and lateral tire-ground forces estimation is divided into two chapters, given that there exists a lot of differences between both methods. The organization of both strategies into a single chapter would have been confusing; therefore, in this first chapter, we present the estimation scheme based on vehicle models, notably the bicycle and hoverboard models. This chapter aligns with the existing literature because it follows more or less the standard approach, which is divided into three parts: An observer (LO, KF, SMO), based on a vehicle model (bicycle model, single corner) fused with a tire model (Dugoff, magic formula), such that, the system is fully observable.

Section 5.2 presents a review of different works addressing different strategies to estimate longitudinal and lateral TGFs. The contribution of this thesis that addresses longitudinal and lateral TGFs is seen in Sections 5.3, 5.4 and 5.5, these sections show the mathematical hypothesis to build our models, the overall scheme to estimate these TGFs and the experimental results, respectively. Finally, in Section 5.6, the conclusions, and perspectives are discussed.

5.2 State of the art on Longitudinal and Lateral Tire-Ground Force Estimation

One of the most widely used tire models is the magic tire model. Pacejka proposed this model in [Pacejka and Besselink, 1997b]. It is renowned as semi-empirical because its development is based on measured data and physical models; this approach can compute the longitudinal and lateral tire-ground forces. The magic tire model is arduous to implement into an embedded system. Its complexity is due to the requirement of some tire parameters, which are usually difficult to identify and might change due to use and tire wear. In [Dugoff, 1969], Dugoff provides a simpler formulation with the ability to describe forces in different situations as pure cornering, acceleration/braking, and combined maneuvers. Dugoff's model synthesizes all tire-vehicle properties required by the magic tire model into two constant parameters C_σ and C_α, known as longitudinal and cornering stiffness, respectively. Several authors had the idea of computing these tire-ground forces using observers built with dynamic models. In [Ray, 1995], a nonlinear state tire-ground force observer is developed and applied to a braking control system, where the tire-ground forces are computed for the virtual wheels proposed in the bicycle system. In [Wilkin et al., 2006], the tire-ground forces for the virtual centered

wheels are estimated using an Extended Kalman Filter. In [Dakhlallah et al., 2008], on a first stage, an EKF is used to estimate the lateral vehicle speed, v_y, at the vehicle's center of gravity, a transformation is made to determine the longitudinal and lateral speed at each tire position and compute the sideslip angle at each tire. The longitudinal/lateral tire-ground forces are estimated using the Dugoff's tire model on a second stage. In [Doumiati et al., 2012], a linear Kalman filter is implemented to estimate the forces at each wheel, to differentiate the front-left/right and rear-left/right wheels, the normal tire-ground forces are included in the estimation scheme. Also, Dugoff's tire model response is used to close the observation loop. [Rezaeian et al., 2015] presents a similar approach; however, in this work, the torque generated by the brakes and engine are known. In [Jiang et al., 2016], the longitudinal and lateral force transfer concept is introduced. This term improves accuracy at the force splitting stage. The virtual forces can be divided for each tire with this variable. In [Rhode et al., 2016], a tractive force estimation scheme is developed, taking into account the drag force; nevertheless, its goal is to estimate the total longitudinal tire-ground force produced in the vehicle.

5.3 Longitudinal/Lateral TGFs model

In this section, the longitudinal/lateral ground-force estimation methodology is introduced. Figure 5.1 displays the estimation scheme; observe that we require the acceleration in the lateral and longitudinal directions, the angular acceleration around the z axis, the steering angle, δ, the braking pressure P, and finally, the road bank and slope angles. The road angles are considered known variables, you can refer to our work [Acosta et al., 2017] or to [Ryu and Gerdes, 2004, Sebsadji et al., 2008, Grip et al., 2009].

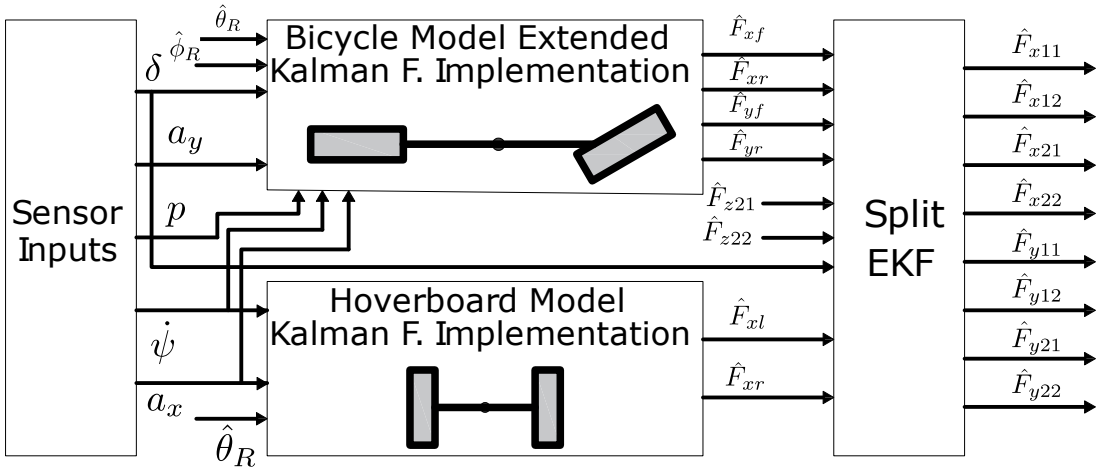

Figure 5.1 – Longitudinal/Lateral TGFs estimation scheme

5.3.1 Longitudinal and lateral TGFs using the bicycle model

Figure 5.1 shows our observation scheme; in this section, we develop the EKF that estimates the longitudinal and lateral TGFs for the front and rear-virtual tires of the single-track model. Thus, the bicycle model (2.21) can be rewritten as:

$$\mathbf{H} \cdot \mathbf{F}_{\mathbf{x|y:v}} = \mathbf{J} \tag{5.1}$$

where

$$\mathbf{H} := \begin{bmatrix} \cos\delta & 1 & -\sin\delta & 0 \\ \sin\delta & 0 & \cos\delta & 1 \\ L_1 \cdot \sin\delta & 0 & L_1 \cdot \cos\delta & -L_2 \end{bmatrix}$$

$$\mathbf{J} := \begin{bmatrix} m \cdot (a_x + g \cdot \sin\theta_r) + \gamma_x \cdot \bar{v}_x^2 \\ m \cdot (a_y + g \cdot \sin\phi_r \cdot \cos\theta_r) + \gamma_y \cdot \bar{v}_y^2 \\ I_{zz} \cdot \ddot{\psi} \end{bmatrix}$$

$$\mathbf{F}_{\mathbf{x|y:v}} := \begin{bmatrix} \sum_{i\in\mathcal{A}} \hat{F}_{x_{1i}} & \sum_{i\in\mathcal{A}} \hat{F}_{x_{2i}} & \sum_{i\in\mathcal{A}} \hat{F}_{y_{1i}} & \sum_{i\in\mathcal{A}} \hat{F}_{x_{2i}} \end{bmatrix}^T$$

with $\gamma_i = 0.5\rho C_{Di} S_i$ standing for the drag force.

Notice that matrix $\mathbf{H}$ is singular; therefore, its inverse, $\mathbf{H}^{-1}$, does not exist. A quick solution to isolate $\mathbf{F}_{\mathbf{x|y:v}}$; such as the pseudo-inverse, could be applied, but its response has low accuracy. To find a suitable solution, we can use our system's information to make considerations and simplify the problem.

In the literature, authors neglect the rear longitudinal TGF, $\sum_{i\in\mathcal{A}} F_{x_{2i}} = 0$;

this consideration is valid for academic purposes, however, in real scenarios the assumption does not hold. Developing an algorithm capable of computing the longitudinal TGFs is an arduous task because initially, the system (5.1) does not have a straightforward solution. Secondly, the powertrain configuration impacts the longitudinal TGFs distribution. There are at least 18 different powertrain configurations, but this work's scope only concerns the front-wheel-drive set, given that Dyna308 has this configuration.

The goal of this section is to isolate $\mathbf{F_{x|y:v}}$ in the system (5.1), thus, taking into account the powertrain set configuration, we have obtained a relationship between the front and rear wheels which is formulated as:

$$\sum_{i\in\mathcal{A}} F_{x_{2i}} \approx \eta \sum_{i\in\mathcal{A}} F_{x_{1i}} \tag{5.2}$$

In our previous work [Alatorre et al., 2017], η has been defined as a switched constant variable, negative when accelerating and positive while braking and always fulfilling $\mid \eta \mid < 1$. Notice that a linear switching relationship between the front and rear wheels does not capture the complete TGFs dynamics. This assumption is only valid at steady-state; therefore, this relationship is defined in the following sections.

5.3.1.1 Acceleration mode

During the vehicle's acceleration, a car with front-wheel drive set produces the torque required to move the automobile with its front wheels; meanwhile, the rear tires do not provide torque, but the rear tires deliver a force that opposes the vehicle movements. Thus, considering the single-corner model gives:

$$I_{\omega_{ij}}\dot{\omega}_{ij} = \tau_{ij} - r_{ij}\cdot F_{x_{ij}} - \zeta_{x_{ij}}\cdot \bar{v}_x^2 \tag{5.3}$$

where the suffixes $i, j \in \mathcal{A} := \{1, 2\}$. From (5.3) is obtained:

$$\begin{aligned}\sum_{i\in\mathcal{A}} F_{x_{1i}} =& \frac{1}{\bar{r}_1}\left(\sum_{i\in\mathcal{A}} \zeta_{x_{1i}}\bar{v}_x^2 - \sum_{i\in\mathcal{A}} I_{\omega_{1i}}\dot{\bar{\omega}}_1 + \sum_{i\in\mathcal{A}} \tau_{1i}\right)\\ \sum_{i\in\mathcal{A}} \hat{F}_{x_{2i}} =& \frac{1}{\bar{r}_2}\left(\sum_{i\in\mathcal{A}} \zeta_{x_{2i}}\bar{v}_x^2 - \sum_{i\in\mathcal{A}} I_{\omega_{2i}}\dot{\bar{\omega}}_2\right)\end{aligned}$$

where $\bar{r}_i = \frac{1}{2}\sum_{j\in\mathcal{A}} r_{ij}$, and $\dot{\bar{\omega}}_i = \frac{1}{2}\sum_{j\in\mathcal{A}} \omega_{ij}$; also considering the physical similarity between front and rear wheels, the following assumption, $\bar{r}_1 \approx \bar{r}_2$, is considered,

then

$$\begin{aligned}\sum_{i\in\mathcal{A}}\hat{F}_{x_{2i}} =& \frac{\sum_{i\in\mathcal{A}}\zeta_{x_{2i}}\bar{v}_x^2 - \sum_{i\in\mathcal{A}} I_{\omega_{2i}}\dot{\bar{\omega}}_2}{\sum_{i\in\mathcal{A}}\zeta_{x_{1i}}\bar{v}_x^2 - \sum_{i\in\mathcal{A}} I_{\omega_{1i}}\dot{\bar{\omega}}_1 + \sum_{i\in\mathcal{A}}\tau_{1i}}\sum_{i\in\mathcal{A}}\hat{F}_{x_{1i}} \\ =& \eta_a\sum_{i\in\mathcal{A}}\hat{F}_{x_{1i}}\end{aligned}$$

with

$$\eta_a = \frac{\sum_{i\in\mathcal{A}}\zeta_{x_{2i}}\bar{v}_x^2 - \sum_{i\in\mathcal{A}} I_{\omega_{2i}}\dot{\bar{\omega}}_2}{\sum_{i\in\mathcal{A}}\zeta_{x_{1i}}\bar{v}_x^2 - \sum_{i\in\mathcal{A}} I_{\omega_{1i}}\dot{\bar{\omega}}_1 + \sum_{i\in\mathcal{A}}\tau_{1i}}$$

and considering $\sum_{i\in\mathcal{A}}\tau_{1i} \approx m\cdot\bar{r}_1\cdot a_x$, $\dot{\bar{\omega}}_i \approx a_x/\bar{r}_i$, gives,

$$\eta_a \approx \frac{\sum_{i\in\mathcal{A}}\zeta_{x_{2i}}\bar{v}_x^2 - \frac{1}{\bar{r}_2}\sum_{i\in\mathcal{A}} I_{\omega_{2i}}a_x}{\sum_{i\in\mathcal{A}}\zeta_{x_{1i}}\bar{v}_x^2 - (\frac{1}{\bar{r}_1}\sum_{i\in\mathcal{A}} I_{\omega_{1i}} - m\cdot\bar{r}_1)a_x}$$

Approximating η_a with a second order Taylor series of expansion gives

$$\eta_a(\mathbf{\Phi}) \approx \eta_a(\mathbf{C}) + \eta_a'(\mathbf{C})(\mathbf{\Phi}-\mathbf{C}) + \eta_a''(\mathbf{\Phi}-\mathbf{C})^T(\mathbf{\Phi}-\mathbf{C})$$

where $\mathbf{\Phi} = \begin{bmatrix} a_x & \bar{v}_x \end{bmatrix}^T$ and $\mathbf{C}$ in this case represents the operation point, where approximation is done. We made the following consideration $\bar{v}_x \approx v_x$. To find the partial derivatives of η we use the least squares method, thus:

$$\eta_a \approx \bar{\eta}_a(\mathbf{\Phi_1}) = \mathbf{\Theta_1}\cdot\mathbf{\Phi_1}$$

with

$$\begin{aligned}\mathbf{\Theta_1} &= \begin{bmatrix} c_1 & c_2 & c_3 & c_4 & c_5 \end{bmatrix} \\ \mathbf{\Phi_1} &= \begin{bmatrix} a_x^2 & a_x & v_x^2 & v_x & 1 \end{bmatrix}\end{aligned}$$

here coefficients $c_1 - c_5$ are constant real numbers. Thus, while accelerating

$$\sum_{i\in\mathcal{A}}\hat{F}_{x_{2i}} \approx \bar{\eta}_a\sum_{i\in\mathcal{A}}\hat{F}_{x_i} \tag{5.4}$$

5.3.1.2 Braking mode

The torque produced during the braking process is distributed between the front and rear wheels. The torque distribution is set by design, thus each car has its own braking torque distribution. Thus, the braking system distributes the total torque

within the four wheels, then from (5.3), are obtained

$$\begin{aligned}\sum_{i\in\mathcal{A}} F_{x_{1i}} =& \frac{1}{\bar{r}_1}\left(\sum_{i\in\mathcal{A}} \zeta_{x_{1i}}\bar{v}_x^2 - \sum_{i\in\mathcal{A}} I_{\omega_{1i}}\dot{\bar{\omega}}_1 + \sum_{i\in\mathcal{A}} \tau_{1i}\right)\\ \sum_{i\in\mathcal{A}} F_{x_{2i}} =& \frac{1}{\bar{r}_2}\left(\sum_{i\in\mathcal{A}} \zeta_{x_{2i}}\bar{v}_x^2 - \sum_{i\in\mathcal{A}} I_{\omega_{2i}}\dot{\bar{\omega}}_2 + \sum_{i\in\mathcal{A}} \tau_{2i}\right)\end{aligned}$$

similarly, as in the acceleration case, $r_r \approx r_f$, hence

$$\begin{aligned}\sum_{i\in\mathcal{A}} F_{x_{2i}} =& \frac{\sum_{i\in\mathcal{A}} \zeta_{x_{1i}}\bar{v}_x^2 - \sum_{i\in\mathcal{A}} I_{\omega_{1i}}\dot{\bar{\omega}}_1 + \sum_{i\in\mathcal{A}} \tau_{1i}}{\sum_{i\in\mathcal{A}} \zeta_{x_{2i}}\bar{v}_x^2 - \sum_{i\in\mathcal{A}} I_{\omega_{2i}}\dot{\bar{\omega}}_2 + \sum_{i\in\mathcal{A}} \tau_{2i}} \sum_{i\in\mathcal{A}} F_{x_{1i}}\\ =& \eta_b \sum_{i\in\mathcal{A}} F_{x_{1i}}\end{aligned}$$

with

$$\eta_b = \frac{\sum_{i\in\mathcal{A}} \zeta_{x_{1i}}\bar{v}_x^2 - \sum_{i\in\mathcal{A}} I_{\omega_{1i}}\dot{\bar{\omega}}_1 + \sum_{i\in\mathcal{A}} \tau_{1i}}{\sum_{i\in\mathcal{A}} \zeta_{x_{2i}}\bar{v}_x^2 - \sum_{i\in\mathcal{A}} I_{\omega_{2i}}\dot{\bar{\omega}}_2 + \sum_{i\in\mathcal{A}} \tau_{2i}}$$

equivalently, as with η_a could be approximated a function $\bar{\eta}_b(\mathbf{\Phi_2})$. Thus,

$$\eta_b \approx \bar{\eta}_b(\mathbf{\Phi_2}) = \mathbf{\Theta_2}\cdot\mathbf{\Phi_2}$$

with

$$\begin{aligned}\mathbf{\Theta_2} &= \begin{bmatrix} c_6 & c_7 & c_8 & c_9 & c_{10}\end{bmatrix}\\ \mathbf{\Phi_2} &= \begin{bmatrix} a_x^2 & a_x & v_x^2 & v_x & 1\end{bmatrix}\end{aligned}$$

coefficients $c_6 - c_{10}$ are constant real numbers. Therefore, while braking

$$\sum_{i\in\mathcal{A}} F_{x_{2i}} \approx \bar{\eta}_b \cdot \sum_{i\in\mathcal{A}} F_{x_{1i}} \tag{5.5}$$

5.3.1.3 Switched rear TGF estimation model

The goal is to have a single relationship between the front and rear wheels; thus, the acceleration and braking modes (5.4) and (5.5) have to be fused. A braking flag is introduced, b_1, this variable represents the brake system status, $b_1 = 1$ when braking, and $b_1 = 0$ at any other condition. It follows:

$$\sum_{i\in\mathcal{A}} F_{x_{2i}} = \bar{\eta}_b \sum_{i\in\mathcal{A}} F_{x_{1i}}\cdot b_1 + \bar{\eta}_a \sum_{i\in\mathcal{A}} F_{x_{1i}}\cdot(1-b_1) \tag{5.6}$$

5.3.1.4 Brake pressure approach

Another approach used to estimate the TGFs while braking, is based on the brake's pressure. The formulation is quite simple, due to a linear relationship between the force and the system's pressure, it follows

$$F_{xj} = P \cdot K_j \tag{5.7}$$

where the suffix j has already been defined, P is the pressure produced by the braking system obtained through the CAN signal and K_j denotes a gain required to transform the applied pressure into a the longitudinal TGF.

5.3.1.5 Longitudinal virtual TGFs model using the hoverboard model

The hoverboard model ((2.22) provides the longitudinal TGF for the left and right virtual tires. Observe that the virtual left and right tires are exposed to the same phenomena when accelerating or braking; thus, a single approach to estimate the left and right virtual TGFs suffices our purposes. Hence, after isolating the TGFs in the hoverboard model (2.22) gives:

$$\bar{\mathbf{F}}_{\mathbf{x:v}} = \left(\mathbf{H}^{\mathbf{H}}\right)^{-1} \mathbf{J}^{\mathbf{H}} \tag{5.8}$$

with

$$\mathbf{H}^{\mathbf{H}} := \begin{bmatrix} 1 & 1 \\ E_2 & -E_1 \end{bmatrix}; \quad \bar{\mathbf{F}}_{\mathbf{x:v}} = \begin{bmatrix} \sum_{i\in\mathcal{A}} \hat{F}_{x_{i1}} \\ \sum_{i\in\mathcal{A}} \hat{F}_{x_{i2}} \end{bmatrix}$$
$$\mathbf{J}^{\mathbf{H}} := \begin{bmatrix} m \cdot (a_x + g \cdot \sin(\theta_r)) + \gamma_x \bar{v}_x^2 \\ I_{zz} \cdot \ddot{\psi} \end{bmatrix}$$

With the introduction of the virtual right and left longitudinal TGFs, we can replace the prior dependence on variables obtained through parameter identification that usually does not serve as a general solution since the overfits the response. One advantage of this proposal is the robustness improvement since variation on the road friction no longer affects the model response.

5.3.2 Longitudinal and lateral virtual TGFs division

The formulations presented can solve systems (5.1) and (5.8) for the virtual TGFs. Nevertheless, our final goal is to estimate the longitudinal and lateral forces at each one of the vehicle tires, front left/right and rear left/right, as depicted in Figure 4.1.

Several approaches have been used in literature to split these virtual forces. For example, in [Doumiati et al., 2012] the normal TGFs, the sideslip angle, and the Dugoff's tire model are used to divide the longitudinal and lateral TGFs. In the following, a proposal to split the virtual TGFs without using a tire model is presented.

5.3.2.1 Longitudinal virtual TGFs decoupling

The proposal based on [Jiang et al., 2016], where the difference between left and right longitudinal TGFs is defined as longitudinal force transfer as:

$$T_{xf} = F_{x11} - F_{x12} \approx g_1 \frac{\dot{\psi}}{v_x} + g_2 a_y + g_3 \delta \tag{5.9a}$$

$$T_{xr} = F_{x21} - F_{x22} \approx g_4 \frac{\dot{\psi}}{v_x} + g_5 a_y \tag{5.9b}$$

where the coefficients $g_k \forall k \in \{1, ..., 5\}$ are computed using a regression (parameter identification). The performance of the estimation scheme using this set of equations is overwhelming for controlled experiments. Nevertheless, after a deep analysis, it is concluded that the coefficients' value is strictly related to road friction, μ. Thus, to maintain the same degree of accuracy, the coefficients must be re-identified with a new set of data with current environmental conditions, translating into an extenuating series of experimentation that will take lots of time and money.

In this work, the rear longitudinal force transfer T_{xr}, the concept is used, but re-defined as an independent function such that modifications on the environmental conditions do not affect the algorithm response. Equation (5.9a) is not taken into account in this proposal.

Considering our previous work [Alatorre et al., 2017], we have deduced an equation that defines the rear-right/left wheel longitudinal TGFs:

$$\sum_{i \in \mathcal{A}} F_{x_{2i}} = \xi_{x_{2i}} a_{x_{2i}} + (-1)^{i+1} \cdot \xi_{y_{2i}} a_{y_{2i}} - \gamma_x \bar{v}_x^2 \tag{5.10}$$

if we apply (5.10) to the longitudinal for transfer definition, yields

$$T_{xr} = \xi_{x_{21}} a_{x_{21}} + \xi_{y_{21}} a_{y_{21}} - \gamma_x \bar{v}_x^2 - \xi_{x_{22}} a_{x_{22}} + \xi_{y22} a_{y_{22}} + \gamma_x \bar{v}_x^2$$

From classical mechanics, we can use the motion of a particle on a rigid body,

$$T_{xr} = (\xi_{x21} - \xi_{x_{22}}) E \dot{\psi} + \xi_{y_{21}} a_{y_{21}} + \xi_{y_{22}} a_{y_{22}}$$

it follows

$$T_{xr} = (\xi_{y21} + \xi_{y22})\frac{1}{2}\sum_{i\in\mathcal{A}} a_{y2i} + (\xi_{y21} - \xi_{y22})\dot{\psi}^2 E + (\xi_{x21} - \xi_{x22})\dot{\psi}E$$

Since, the terms $(\xi_{y21} - \xi_{y22}) = \Delta_\xi$ and $(\xi_{x21} - \xi_{x_{22}})$ are too small,they do not contribute to the longitudinal force transfer model, T_{xr}. The following is obtained:

$$T_{xr} = \varepsilon^{-1}\sum_{i\in\mathcal{A}} F_{z_{2i}}\frac{1}{2}\sum_{i\in\mathcal{A}} a_{y_{2i}} \approx \varepsilon^{-1}\cdot\sum_{i\in\mathcal{A}} F_{y_{2i}} \tag{5.11}$$

with

$$\sum_{i\in\mathcal{A}} F_{z_{2i}} = \varepsilon\sum_{i\in\mathcal{A}} \xi_{y_{2i}}$$

where ε is defined as constant and could be obtained through a regression. It has to be remarked that ε does not require adjustments due to different environmental conditions.

5.3.2.2 Lateral virtual TGFs decoupling

The solution provided in [Jiang et al., 2016] for the rear lateral force transfer is adequate for our proposal and will be re-used.

$$\hat{T}_{yr} = F_{y21} - F_{y22} = \frac{\hat{F}_{z21} - \hat{F}_{z22}}{\hat{F}_{zr}}\cdot\hat{F}_{yr} \tag{5.12}$$

Our solution does not take into account the front lateral force transfer, T_{yf}. Notice that is necessary to include the rear wheels normal TGFs estimation.

5.4 Observer design

The TGFs models previously obtained could be solved with probabilistic estimation techniques. We prioritize the Kalman filter to take into account the uncertainties associated with the model and the measures. Finally, considering the linear nature of the systems (bicycle, hoverboard, force split), it has been chosen to use a KF or EKF accordingly.

5.4.1 Bicycle model EKF implementation

The first step towards the implementation is to represent set of eqs. (5.1), as a discrete state-space system. Thus, eq. (5.1), becomes

$$\begin{aligned} \mathbf{x}_{k+1} &= (\mathbf{I}_{6\times 6} + T_s \cdot \mathbf{A}_1(k)) \cdot \mathbf{x}_k + T_s \cdot \mathbf{B_1} \cdot \mathbf{u} + T_s \cdot \mathbf{w_k} \\ \mathbf{y}_k &= \mathbf{C}_1(k) \cdot \mathbf{x}_k + \nu_\mathbf{k} \end{aligned} \tag{5.13}$$

where

$$\mathbf{x}_k = \begin{bmatrix} x_1 & x_2 & x_3 & x_4 & x_5 & x_6 \end{bmatrix}^T$$

$$\mathbf{A}_1(k) = \begin{bmatrix} 0 & 0 & 0 & 0 & 0 & 0 \\ -\cos\delta_k & 0 & -\sin\delta_k & 0 & 0 & \cos\delta_k \\ 0 & 0 & 0 & 0 & 0 & 0 \\ \sin\delta_k & 0 & -\cos\delta_k & 0 & 0 & -\sin\delta_k \\ 0 & 0 & 0 & 0 & 0 & 0 \\ 0 & 0 & 0 & 0 & 0 & 0 \end{bmatrix}$$

$$\mathbf{B_1} \cdot \mathbf{u} = \begin{bmatrix} 0 \\ \cos\delta_k \cdot m \cdot a_x(k) + \sin\delta_k \cdot m \cdot a_y(k) \\ \frac{1}{L} \cdot (-I_{zz} \cdot \ddot{\psi}(k) + L_1 \cdot m \cdot a_y(k)) \\ \cos\delta_k \cdot m \cdot a_y(k) - \sin\delta_k \cdot m \cdot a_x(k) \\ 0 \\ 0 \end{bmatrix}$$

$$\mathbf{C}_1(k) = \begin{bmatrix} 1 & \cos\delta_k & 0 & -\sin\delta_k & 0 & 0 \\ 0 & \sin\delta_k & 1 & \cos\delta_k & 0 & 0 \\ 0 & L_1 \cdot \sin\delta_k & -L_2 & L_1 \cdot \cos\delta_k & 0 & 0 \\ 1 & -x_5 & 0 & 0 & 0 & 1 \\ 1 & 0 & 0 & 0 & -x_2 & 1 \\ 0 & 0 & 0 & 0 & 1 & 0 \\ 0 & 0 & 0 & 0 & 0 & 1 \\ b_1(k) & 0 & 0 & 0 & 0 & 0 \\ 0 & b_1(k) & 0 & 0 & 0 & 0 \end{bmatrix}$$

with $x_1 = \sum_{i\in\mathcal{A}} \hat{F}_{x_{2i}}$, $x_2 = \sum_{i\in\mathcal{A}} \hat{F}_{x_{1i}}$, $x_3 = \sum_{i\in\mathcal{A}} \hat{F}_{y_{2i}}$, $x_4 = \sum_{i\in\mathcal{A}} \hat{F}_{y_{1i}}$, $x_5 = \eta$ and $x_6 = \zeta \cdot \bar{v}_x^2$. System (5.13) is non-linear, and observable; its observability has been verified by means of the criterion proposed in [Sontag, 1998] and presented in Definition 3.2.5.

5.4.2 Hoverboard model KF implementation

The second step for completing the TGFs observation scheme as shown in Figure (5.1), is to represent model (5.8) with a state-pace realization. Then,

$$\begin{aligned} \mathbf{x}_{k+1} &= (\mathbf{I}_{3\times 3} + T_s \cdot \mathbf{A}_2(k)) \cdot \mathbf{x}_k + T_s \cdot \mathbf{B_2} \cdot \mathbf{u} + T_s \cdot \mathbf{w_k} \\ \mathbf{y}_k &= \mathbf{C}_2(k) \cdot \mathbf{x}_k + \nu_{\mathbf{k}} \end{aligned} \tag{5.14}$$

where

$$\mathbf{x}_k = \begin{bmatrix} x_1 \\ x_2 \\ x_3 \end{bmatrix}; \mathbf{A}_2(k) = \begin{bmatrix} 0 & -1 & 1 \\ \frac{E_2}{E_1} & 0 & 0 \\ 0 & 0 & 0 \end{bmatrix} \mathbf{B_2} \cdot \mathbf{u} = \begin{bmatrix} m \cdot a_x(k) \\ I_{zz} \cdot \ddot{\psi}(k) \\ 0 \end{bmatrix}; \mathbf{C}_2(k) = \begin{bmatrix} 1 & 1 & -1 \\ -E_2 & E_1 & 0 \\ 0 & 0 & 1 \end{bmatrix}$$

with $x_1 = F_{xl}$, $x_2 = F_{xd}$ and $x_3 = \zeta \cdot \bar{v}_x^2$. The observability of system (5.14) is verified with the full column rank of its observability matrix,

$$rank[\mathbf{O}] = \dim(\mathbf{x})$$

where

$$\mathbf{O} = \begin{bmatrix} \mathbf{C^T} & (\mathbf{C} \cdot \mathbf{A})^\mathbf{T} & (\mathbf{C} \cdot \mathbf{A^2})^\mathbf{T} \end{bmatrix}^T$$

5.4.3 Tire-ground force split EKF implementation

The final step of our scheme is the TGFs splitting stage, which uses TGFs estimation response obtained from the bicycle-hoverboard models and the TGFs transfer equations (5.11)-(5.12) as measurements. Therefore,

$$\begin{aligned} \mathbf{x}_{k+1} &= \mathbf{I}_{8\times 8} + \mathbf{w_k} \\ \mathbf{y}_k &= \mathbf{C}_3(k) \cdot \mathbf{x}_k + \nu_{\mathbf{k}} \end{aligned} \tag{5.15}$$

where

$$\mathbf{x}_k = \begin{bmatrix} x_1 & x_2 & x_3 & x_4 & x_5 & x_6 & x_7 & x_8 \end{bmatrix}^T$$

$$\mathbf{C}_3(k) = \begin{bmatrix} 1 & 0 & \cos\delta_k & 0 & 0 & 0 & 0 & 0 \\ 1 & 0 & 0 & \cos\delta_k & 0 & 0 & 0 & 0 \\ 0 & 1 & 1 & 0 & 1 & 0 & 0 & 0 \\ 0 & 1 & 0 & 1 & -1 & 0 & 0 & 0 \\ 0 & 0 & -\sin\delta_k & 0 & 0 & 1 & 0 & 0 \\ 0 & 0 & 0 & -\sin\delta_k & 0 & 1 & 0 & 0 \\ 0 & 0 & 0 & 0 & 0 & 0 & 1 & 1 \\ 0 & 0 & 0 & 0 & 0 & 0 & 1 & -1 \end{bmatrix}^T$$

with $x_1 = F_{x_{11}}$, $x_2 = F_{x_{12}}$, $x_3 = F_{x_{21}}$, $x_4 = F_{x_{22}}$, $x_5 = F_{y_{11}}$, $x_6 = F_{y_{12}}$, $x_7 = F_{y_{21}}$ and $x_8 = F_{y_{22}}$.

The constrains

$$\left(\mu \cdot F_{z_{ij}}\right)^2 \geq F_{x_{ij}}^2 + F_{y_{ij}}^2$$

are included in the EKF implementation for the bicycle model and the split TGFs stage, in the observation matrix.

5.5 Experimental Results

Our proposal is validated with real data; three special cases were selected. These test cases validate our proposal's robustness at low and high lateral excitation levels as when the tires experiment force saturation.

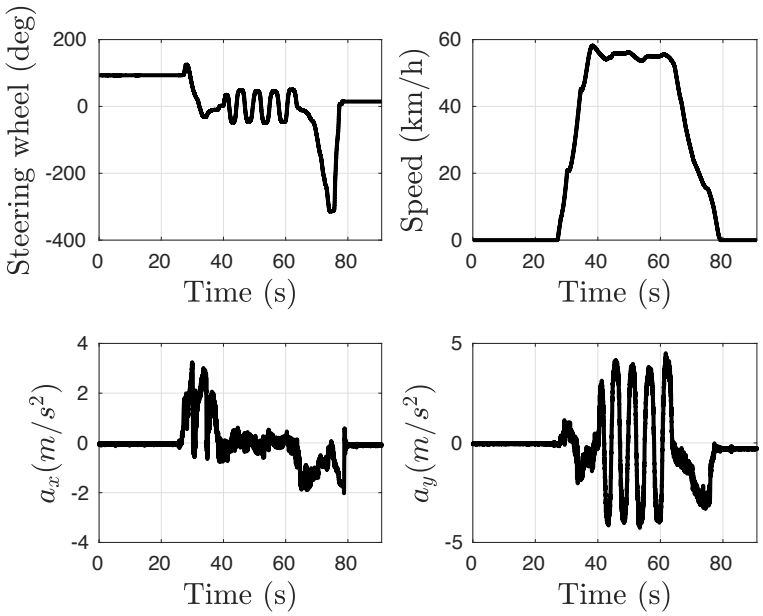

Figure 5.2 – No. 1 carried out to validate the longitudinal/lateral TGFs estimation scheme ($\max(v_x) = 60km/h$, $\max(\mid a_y \mid) = 4.7m/s^2$).

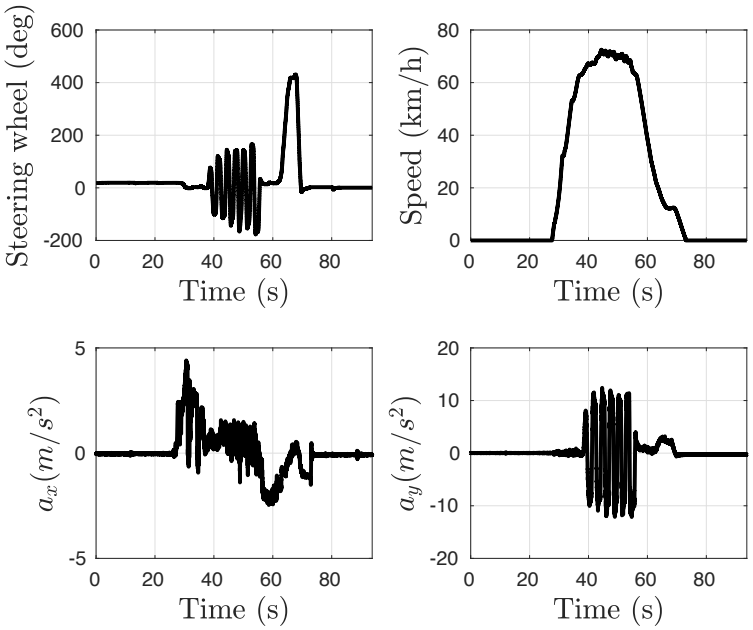

Figure 5.3 – Test No. 2 carried out to validate the longitudinal/lateral TGFs estimation scheme ($\max(v_x) = 71km/h$, $\max(\mid a_y \mid) = 7m/s^2$).

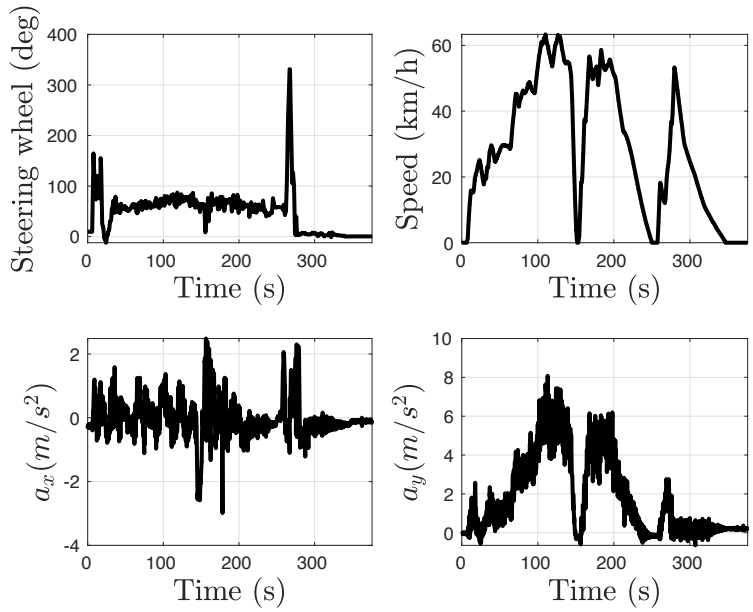

Figure 5.4 – Test No. 3 carried out to validate the longitudinal/lateral TGFs estimation scheme ($\max(v_x) = 60km/h$, $\max(\mid a_y \mid) = 6.5m/s^2$).

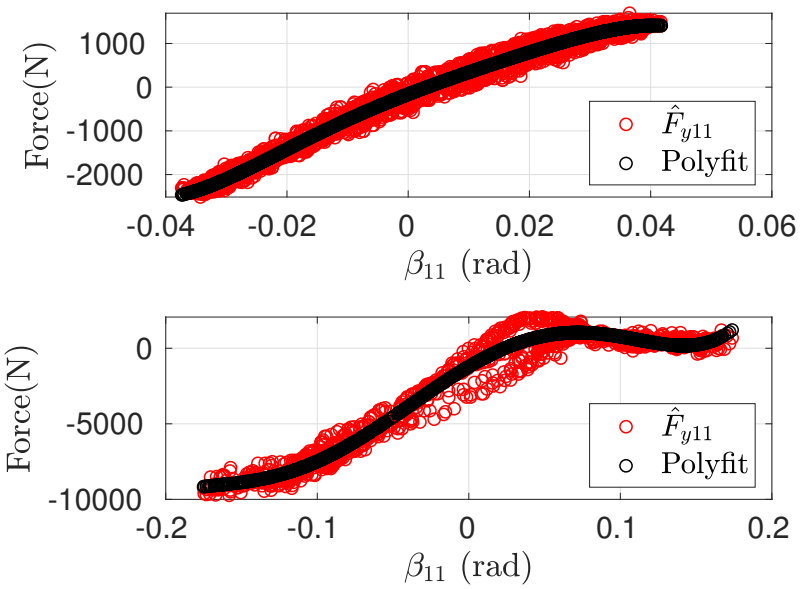

Figure 5.5 – Saturation level comparison between test No. 1 and 2. Up: Test No. 1. Down: Test No. 2

5.5.1 Tests Description

Three tests are carried out to validate the proposed algorithms, the tests performed are depicted in Figures 5.2, 5.3 and 5.4, respectively. During the first two tests, the vehicle is subjected to a slalom maneuver at 55 km/h and 70 km/h maximum speed, respectively. The difference between performed tests is noticed when the maximum lateral acceleration is compared. During test No. 1, the lateral acceleration is maintained below 5 m/s^2, during test No. 2, the lateral acceleration achieved is up to 10 m/s^2, see Figs. 5.2 and 5.3. Nevertheless, the main difference is noticed when comparing the sideslip-lateral TGF relationship, see Figure 5.5; this figure shows with red circles the lateral TFG, and with black circles, a polynomial data fit to see the graph trend easily. During test No. 2, the tire was being subjected to force saturation. The third test is conducted at 60 kph with constant steering such that the vehicle path is a circle; during the last maneuver, we look to validate our proposal against maneuvers with low lateral excitation.

The first two tests can be divided into three main parts, an acceleration stage until we arrive at cruise speed where a slalom maneuver is done, and finally, the braking stage. The schedule for test 1 is:

- Acceleration phase from 25 to 40 seconds.
- Slalom maneuver at 55 kph cruise speed from 40 to 60 seconds.
- Braking phase from 60 to 80 seconds.

The schedule for test No. 2 is:

- Acceleration stage from 25 to 38 seconds.
- Slalom section from 38 to 55 seconds.
- Braking phase from 55 to 70 seconds.

The schedule for test No. 3 is:

- Constant steering from 20 s to 140 seconds.
- Braking phase from 140 s to 150 seconds.
- Constant steering from 150 to 250 seconds

5.5.2 Results

The first two tests were selected to present our proposal working under linear TGFs-Sideslip relationship (test No. 1) and also with a non-linear lateral TGFs-Sideslip behavior (test No. 2). The third test shows the performance of our proposal with a low lateral excitation.

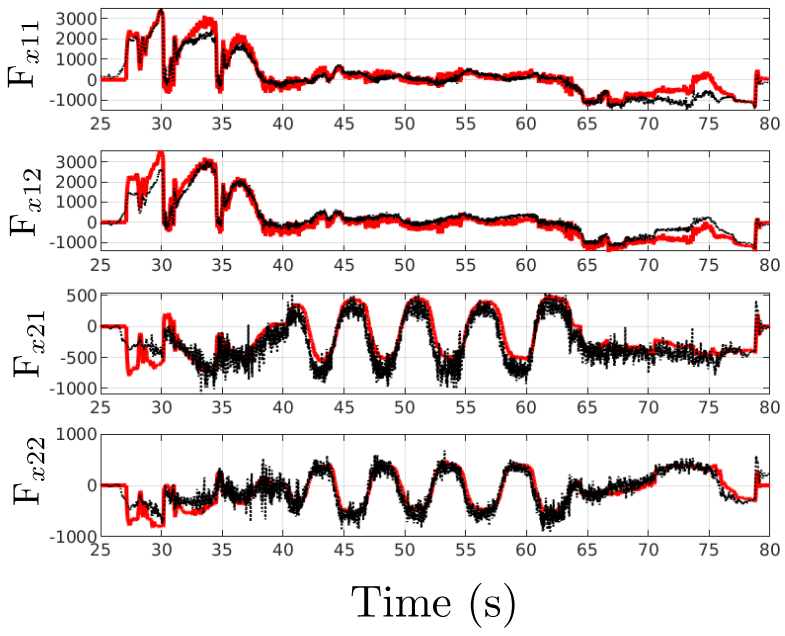

Figure 5.6 – Estimated Longitudinal TGFs, $\hat{F}_{xij}$, response compared against the actual measurement given by Kysler dynamometers during test No. 1. Red-Solid line: $\hat{F}_{xij}$ - Proposal. Black-Pointed line: F_{xij} - Sensor Measurement

Figure 5.6 portrayed the estimation response with a red-solid line and compared it against the sensor measurement with a black-dotted line. Observe the existing

error during the acceleration stage due to uncertainties introduced by the rubber and the steering system. Remember that the longitudinal and lateral dynamics fo the front wheels are tightly coupled.

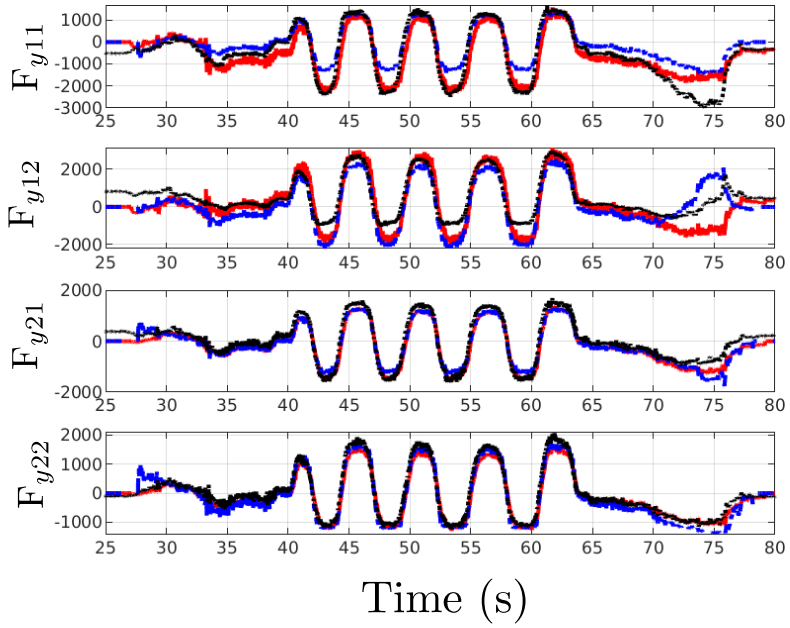

Figure 5.7 – Estimated Lateral TGFs, $\hat{F}_{yij}$, response compared against a response obtained using a Dugoff's tire model and the actual measurement given by Kysler dynamometers during test No. 1. Red-Solid line: $\hat{F}_{yij}$ - Proposition. Blue-Dashed line: $\hat{F}_{yij}$ - Dugoff's Tire model. Black-Pointed line: F_{yij} - Sensor Measurement

Figure 5.7 depicts our results for lateral TGFs estimation; with a red-solid line, we present our proposal response; with a black-dotted line, the lateral TGF transducers data; finally, with a blue-dashed line, the result of a Dugoff's tire model. We compute the Dugoff's tire model using the normal TGFs measurements, $F_{z_{ij}}$, and the sideslip angle measurement, α, to compare against our proposal.

The longitudinal/lateral front-left/right and right-left/right TGFs responses obtained from test No. 2 are displayed from Figure 5.8 and 5.9, respectively. The results obtained are accurate, and the estimated variables correspond to those measured by the sensors; nonetheless, the overall performance is degraded. Notice that the Dugoff's tire model performance has also been degraded, see Figure 5.9, due to nonlinear tire behaviors.

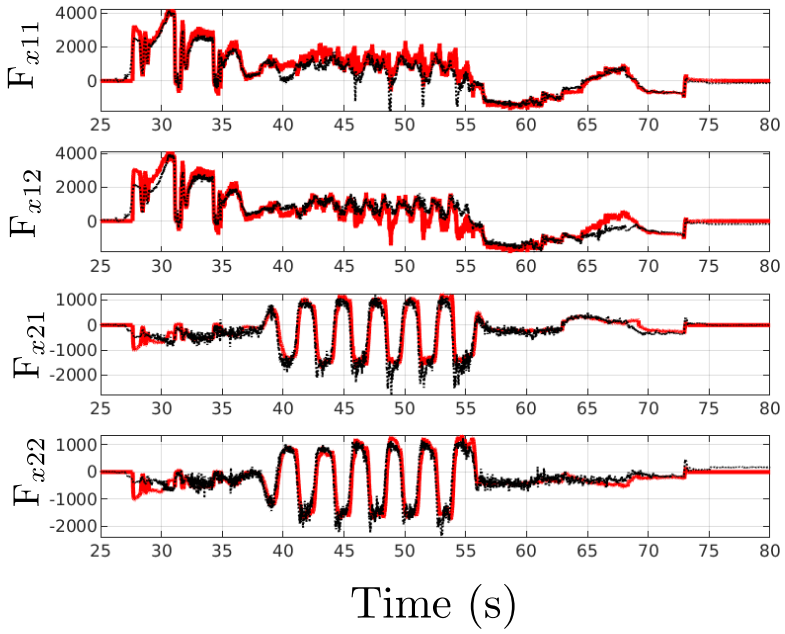

Figure 5.8 – Estimated Longitudinal TGFs, $\hat{F}_{xij}$, response compared against the actual measurement given by Kysler dynamometers during test No. 2. Red-Solid line: $\hat{F}_{xij}$ - Proposal. Black-Pointed line: F_{xij} - Sensor Measurement

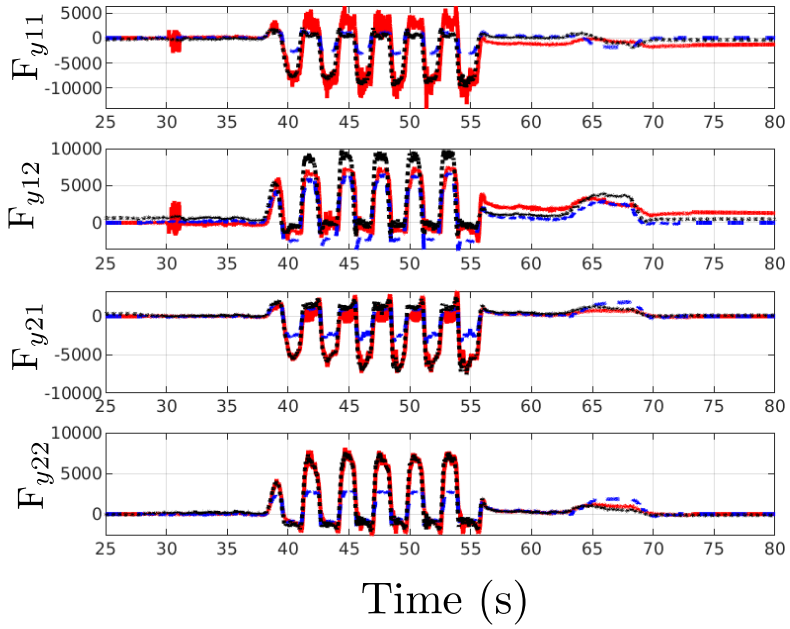

Figure 5.9 – Estimated Lateral TGFs, $\hat{F}_{yij}$, response compared against a response obtained using a Dugoff's tire model and the actual measurement given by Kysler dynamometers during test No. 2. Red-Solid line: $\hat{F}_{yij}$ - Proposition. Blue-Dashed line: $\hat{F}_{yij}$ - Dugoff's Tire model. Black-Pointed line: F_{yij} - Sensor Measurement

Finally, the results obtained from test No. 3 are presented in Figures 5.10 and

5.11. After analyzing the results, we can state that our proposal is more robust and accurate than those presented in the literature, see [Doumiati et al., 2012, Jiang et al., 2016, Alatorre et al., 2017]. A remark that should be addressed is that the proposed scheme does not require the sideslip angle estimation nor a tire model. Still, the observation scheme remains a closed-loop observer; the later is one of the main differences between this proposal and [Jiang et al., 2016].

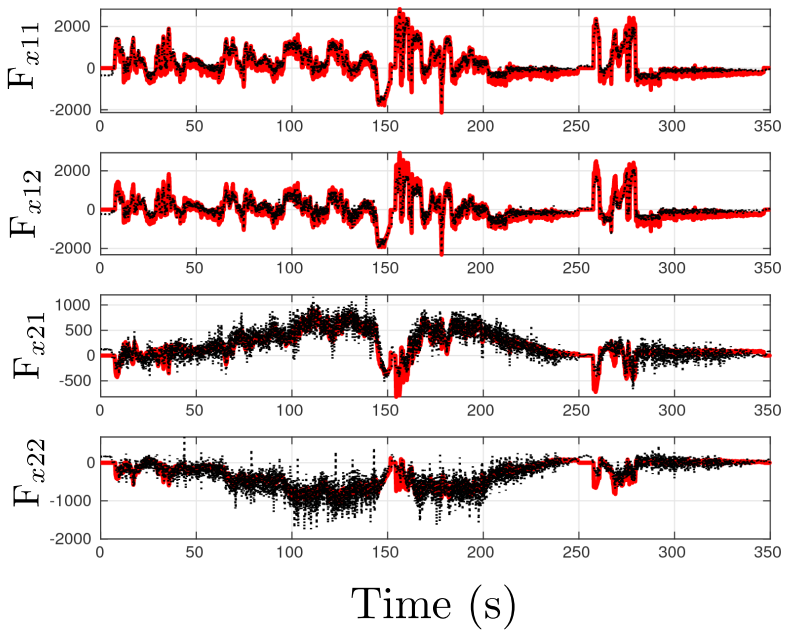

Figure 5.10 – Estimated Longitudinal TGFs, $\hat{F}_{xij}$, response compared against the actual measurement given by Kysler dynamometers during test No. 3. Red-Solid line: $\hat{F}_{xij}$ - Proposal. Black-Pointed line: F_{xij} - Sensor Measurement

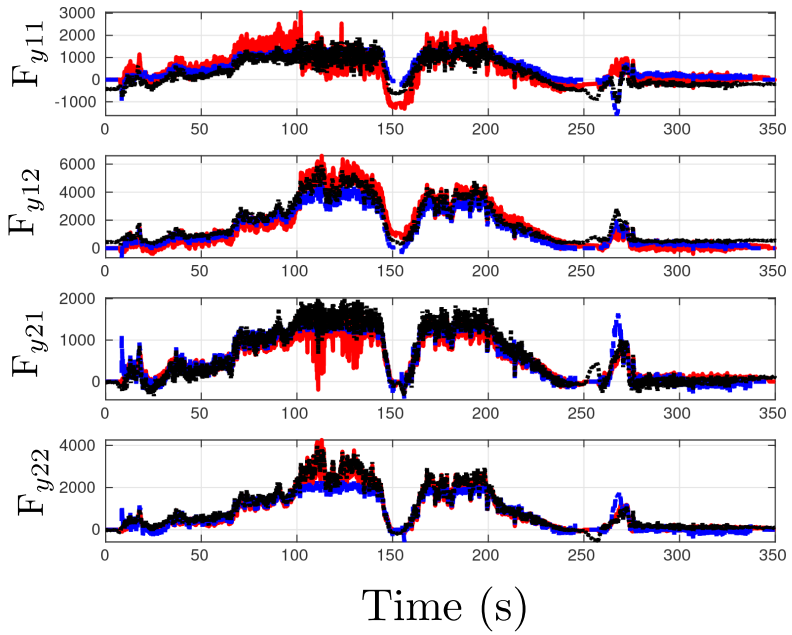

Figure 5.11 – Estimated Lateral TGFs, $\hat{F}_{yij}$, response compared against a response obtained using a Dugoff's tire model and the actual measurement given by Kysler dynamometers during test No. 3. Red-Solid line: $\hat{F}_{yij}$ - Proposition. Blue-Dashed line: $\hat{F}_{yij}$ - Dugoff's Tire model. Black-Pointed line: F_{yij} - Sensor Measurement

5.5.3 Results Analysis

Once proposed and validated our algorithm, we have to make a quantitative assessment addressing the accuracy of our estimation; thus, we define the following error,

$$\tilde{F}_{p_{ij}} := \hat{F}_{p_{ij}} - F_{p_{ij}}$$

where $p := x, y$, and i, j are already defined.

Figure 5.12 shows the longitudinal and lateral TGFs error distributions obtained from test No. 1; here, the errors have a normal distribution; this figure also shows a boxplot of the residual errors. The error function for the longitudinal TGFs has a standard deviation $\sigma_x = 250$ and a mean value of $\mu_x = 29.16$ and just 3.14% of the evaluated data are considered outliers. For the lateral TGFs the standard deviation is $\sigma_y = 385$, the mean value is $\mu_x = -170$ and 7.72% of the data are outliers. On the other hand, the Dugoff's tire model response has a standard deviation of 531 N, a mean error of -62 N, and 10% of the data is considered an outlier.

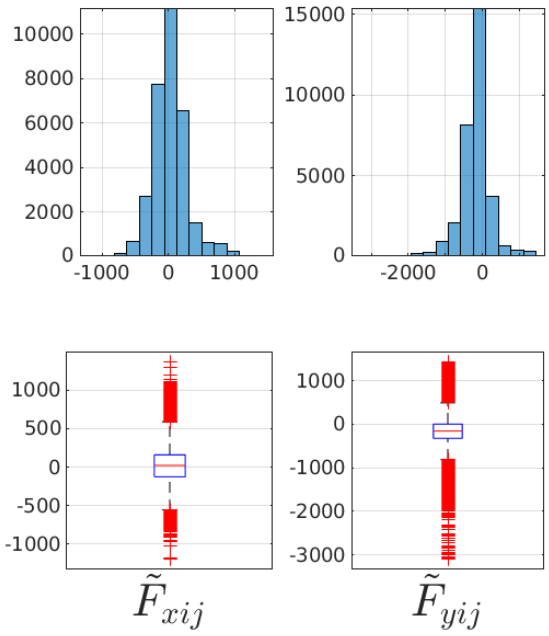

Figure 5.12 – Up: Distribution of the estimation error for the TGFs during test No. 1. Down: Boxplot graph obtained from the estimation error for the TGFs during test No. 1.

Similarly, Figure 5.13 shows the error analysis of test No. 2; in this figure, the error distribution is normal. In this case, the statistical values of the error are: a standard deviations of $\sigma_x = 369$ N, $\sigma_y = 1198$ N, $\mu_x = 49.90$ N, $\mu_y = -148.39$ N, the data outliers are 6.48 and 7.11% for the x, and y directions, respectively. The residuals from the Dugoff's tire model have a standard deviation of $\sigma_d = 1609$, a mean error of $\mu_d = 5.6450$, and 16% of the data is considered an outlier, see the center of Figure 5.15.

Finally, Figure 5.14 displays the error analysis of test No. 3; this figure shows that the error has normal distribution, and the statistical values of the error are $\sigma_x = 165$, $\sigma_y = 326$, $\mu_x = -44.14, \mu_y = -41.68$, the data outliers are 1.56%, 3.52%, for the x, and y directions, respectively. On the other hand, the right figures of Figure 5.15 show the residuals from the Dugoff's tire model, the residuals have a normal distribution of $\sigma_d = 409$ N, a mean of $\mu_d = -67$ N, and 4.87% of the data is considered an outliers; if we analyze particularly the braking phase, the analitycal resuls are the following: $\sigma_x = 137$ N, $\mu_x = -55.01$ N, $\sigma_y = 457$ N, $\mu_y = 18.67$ N and the data outliers are 1.79%, 0.39% for the x and y directions, respectively. The statistical error analysis from the Dugoff's tire model is modified to $\sigma_d = 640$ N, $\mu_d = 143$ N, and 4.56% of the data is considered an outlier.

Observe that during the three tests, Dugoff's tire model response has lower accuracy levels than our proposal; these results are obtained even when the

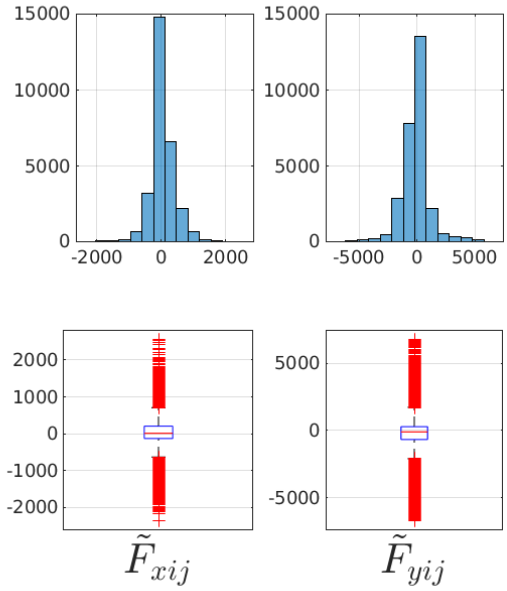

Figure 5.13 – Up: Distribution of the estimation error for the TGFs during test No. 2. Down: Boxplot graph obtained from the estimation error for the TGFs during test No. 2.

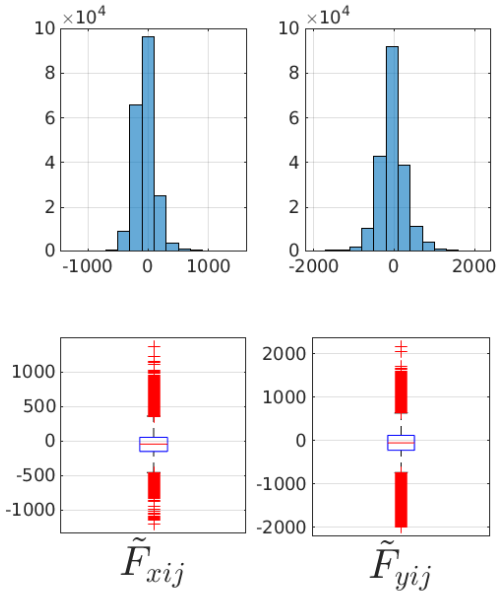

Figure 5.14 – Up: Distribution of the estimation error for the TGFs during test No. 3. Down: Boxplot graph obtained from the estimation error for the TGFs during test No. 3.

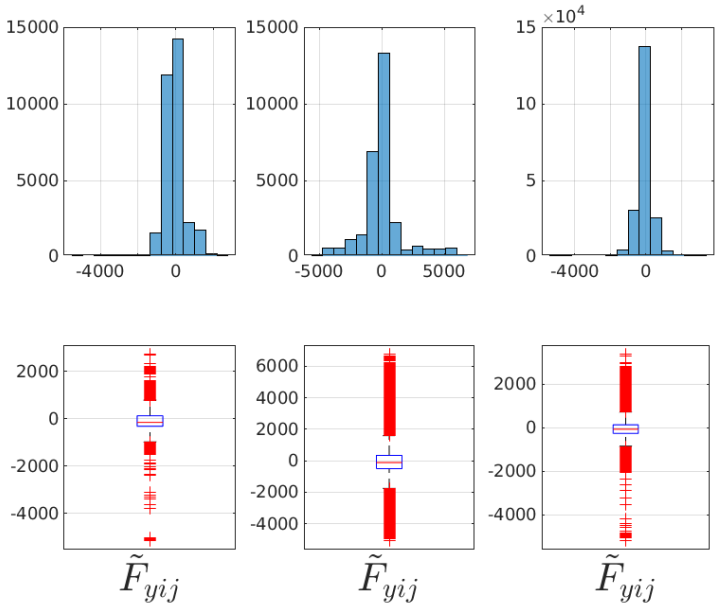

Figure 5.15 – Up: Distribution of the estimation error for the lateral TGFs using Dugoff's tire model. Down: Boxplot graph obtained from the estimation error obtained using Dugoff's formulation. Left: test No. 1. Center: test No. 2. Right: test No. 3.

Dugoff's tire model is fed with the sideslip angle and normal tire-ground forces measurements.

5.5.4 Mass Sensitivity Analysis

One of the most important parameters for TGFs estimation or control schemes is the vehicle's mass. In our scheme, we use the mass, computed by eq. (4.28c), as input. Thus, it becomes mandatory to analyze how sensitive our proposal is to miss-calculations of this variable. Thus, is defined $\tilde{m} = m - \hat{m}$ as the mass' estimation error. Now, we compute the following cost function

$$e = \sum_{n_m=1}^{3} \left(\frac{1}{n} \sum_{n=1}^{n_\infty} \left(\sum_{i \in \mathcal{A}} \sum_{j \in \mathcal{A}} (E_x + E_y) \right) \right) \tag{5.16}$$

with

$$E_x = \frac{\left(\hat{F}_{x_{ij}} - F_{x_{ij}} \right)^2}{\max \mid F_{x_{ij}} \mid^2}; \quad E_y = \frac{\left(\hat{F}_{y_{ij}} - F_{y_{ij}} \right)^2}{\max \mid F_{y_{ij}} \mid^2}$$

where n_m stands for the test number. The observation scheme is feed with different mass values in the range [-300, 300] kg and the error obtained from computing (5.16) is show in Figure 5.16.

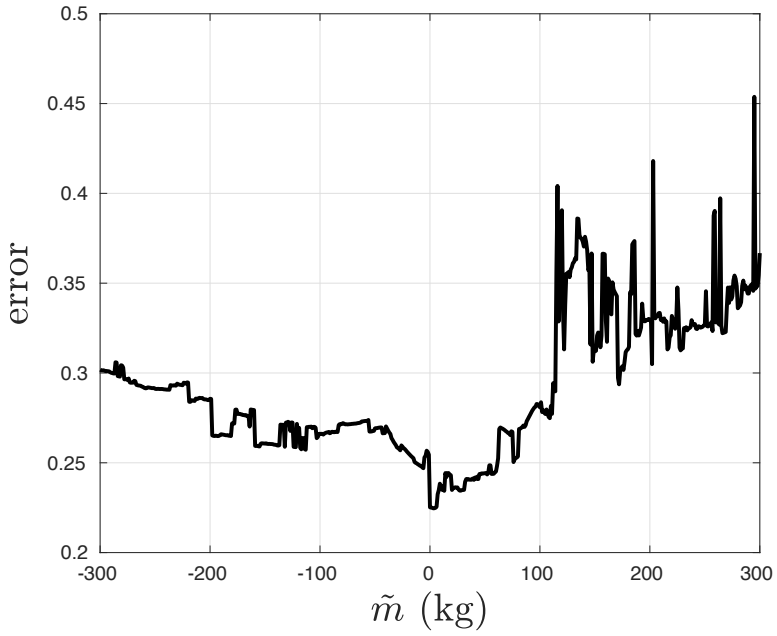

Figure 5.16 – Observation Scheme mass' sensitivity

Figure 5.16 shows the algorithms robustness against mass uncerteinty, the error defined in (5.16) varies from 0.25 to 0.4 with translates into an increase of 76%.

5.6 Conclusions

This chapter presents the first part of our solution to address the longitudinal and lateral tire-ground forces state estimation problem.

The first section of this chapter presents state of the art for longitudinal and lateral tire-ground estimation. The main contributions in the literature are stated, and our contribution is remarked.

After, during the second section, the observer scheme is built. We started with two lumped models, an extended Kalman filter for the single-track model, and a linear Kalman filter for the hoverboard model. A different model for accelerating and braking is obtained for the single-track model, and both models are fused using a braking flag. Finally, an extended Kalman filter splits the virtual tire-ground forces into the tires.

The robustness of our scheme is validated with real-data for maneuvers with and without tire force saturation. Finally, a sensibility analysis against variations in the mass is presented.

Longitudinal and Lateral Tire Ground Force Estimation: Part 2

Contents

6.1 Introduction

In this chapter other approach is taken into account to compute the longitudinal and lateral tire-ground forces; even though we did not find a single matricial representation for the $x, y,$ and z axis. Nonetheless, the we think that the results are good enough to present this contribution.

Section 6.2 presents the background required to develop the estimator for longitudinal and lateral TGFs. The strategy itself is presented in Section 6.3, the validation of the TGF computation is presented in Section 6.4. Finally in Section 6.5 the conclusions and perspectives are discussed.

6.2 Preliminaries

6.2.1 Relative Motion

An accelerometer measures the specific forces applied to a specific mass in a sensor. This particular force is the sensor acceleration minus the gravity field, $\mathbf{g}$. The acceleration measured by an accelerometer could be expressed using the rotational speed $\boldsymbol{\omega}$ and angular acceleration $\dot{\boldsymbol{\omega}}$ of the vehicle, see [Brunner et al., 2015]:

$$\begin{aligned}\mathbf{a}_{\mathbf{s}}^{\mathbf{I}} - GM\frac{\mathbf{d_{sE}}}{||\,\mathbf{d_{sE}}\,||^3} =& \mathbf{a}_{\mathbf{B}}^{\mathbf{E}} - GM\frac{\mathbf{d_{BE}}}{||\,\mathbf{d_{BE}}\,||^3} + \dot{\boldsymbol{\omega}}^{BE}\times\mathbf{d_{sB}} + \boldsymbol{\omega}^{BE}\times\left(\boldsymbol{\omega}^{BE}\times\mathbf{d_{sB}}\right)\\ &+\boldsymbol{\omega}^{EI}\times\left(2\left(\mathbf{v}_B^E+\boldsymbol{\omega}^{BE}\times\mathbf{d_{sB}}\right)+\boldsymbol{\omega}^{EI}\times\mathbf{d_{sI}}\right)\end{aligned} \tag{6.1}$$

where $\mathbf{a}_{\mathbf{s}}^{\mathbf{I}}$ is the acceleration at some point of a rigid body, G is the gravitational constant and M is the mass of the earth, $\mathbf{d_{sE}}$ stands for the distance between point $\mathbf{a}_{\mathbf{s}}^{\mathbf{I}}$ and the center of the earth, $\mathbf{a}_{\mathbf{B}}^{\mathbf{E}}$ is the acceleration at a different point of the same rigid body, but different than $\mathbf{a}_{\mathbf{s}}^{\mathbf{I}}$, $\mathbf{d_{BE}}$ defines the distance between a point $\mathbf{a}_{\mathbf{B}}^{\mathbf{E}}$ and the center of the earth, $\dot{\boldsymbol{\omega}}^{BE}\times\mathbf{d_{sB}}+\boldsymbol{\omega}^{BE}\times\left(\boldsymbol{\omega}^{BE}\times\mathbf{d_{sB}}\right)$ represents the acceleration due to the position difference between point $\mathbf{a}_{\mathbf{s}}^{\mathbf{I}}$ and $\mathbf{a}_{\mathbf{B}}^{\mathbf{E}}$ and $\boldsymbol{\omega}^{EI}\times\left(2\left(\mathbf{v}_B^E+\boldsymbol{\omega}^{BE}\times\mathbf{d_{sB}}\right)+\boldsymbol{\omega}^{EI}\times\mathbf{d_{sI}}\right)$ means the acceleration involved by the earth rotation. The acceleration given by the rotation of the earth, is really small in the context of intelligent vehicles, and the distance between the both points and the center of the earth could be considered equal, the later means that gravity affects both points equally. After applying the above mentioned consideration gives:

$$\mathbf{a}_{\mathbf{s}}^{\mathbf{I}} = \mathbf{a}_{\mathbf{B}}^{\mathbf{E}} + \dot{\boldsymbol{\omega}}^{\mathbf{BE}}\times\mathbf{d_{sB}} + \boldsymbol{\omega}^{\mathbf{BE}}\times\left(\boldsymbol{\omega}^{\mathbf{BE}}\times\mathbf{d_{sB}}\right) \tag{6.2}$$

Figure 6.1 – Isometric tire

Specifically, in this section, we aim to compute the acceleration at the ij^{th} tire; therefore, we consider prior knowledge of the vehicle longitudinal and lateral accelerations, a_x and a_y, and the vehicle yaw rate, $\dot{\psi}$; these measurements are obtained from an inertial measurement unit; where $\mathbf{a_s^I} = \begin{bmatrix} a_{x_{ij}} & a_{y_{ij}} & a_{z_{ij}} \end{bmatrix}^T$ is the tire acceleration vector, $\mathbf{a_B^E} = \begin{bmatrix} a_x & a_y & a_z \end{bmatrix}^T$ means the vehicle's acceleration vector – or the acceleration vector at the sensor position – $\boldsymbol{\omega}^{\mathbf{BE}} = \begin{bmatrix} \dot{\phi} & \dot{\theta} & \dot{\psi} \end{bmatrix}^T$ defines the vector of angular rates, $\dot{\boldsymbol{\omega}}^{\mathbf{BE}} = \begin{bmatrix} \ddot{\phi} & \ddot{\theta} & \ddot{\psi} \end{bmatrix}^T$ is the angular acceleration vector, $\mathbf{d_{sB_{ij}}} = \begin{bmatrix} (-1)^{1+i} L_i & (-1)^{1+j} E_j & -h \end{bmatrix}^T$ represents the distance between the sensor and the ij^{th} tire. Specifically, we require the angular acceleration vector, but there is no sensor able to provide such measurements; therefore, $\dot{\omega}$ is estimated using an EKF as in [Brunner et al., 2017].

6.3 Tire Dynamics

At this point, the normal tire-ground forces are available. From the literature, we could notice that most works use the bicycle model to compute the longitudinal and lateral TGFs, see [Ray, 1995, Wilkin et al., 2006, Doumiati et al., 2012, Alatorre et al., 2017]. In some special cases [Rezaeian et al., 2015, Regolin et al., 2017], a piece of the tire dynamics is used to boost the vehicle model implementations. In this section, we propose a different approach that takes advantage of the vehicle dynamics to promote the dynamic tire system by means of local accelerations $\mathbf{a_{i,j}}$, and equivalent masses.

6.3.1 Lateral tire-ground force computation

This concept is based on a tire as a system; therefore, we first model the dynamic behavior of the tire, thus

$$\begin{aligned} m_{ij}a_{x_{ij}} &= F_{x_{ij}} - /tau_{x_{ij}}r_{e_{ij}} \\ m_{ij}a_{y_{ij}} &= F_{y_{ij}} \\ m_{ij}a_{z_{ij}} &= F_{z_{ij}} \end{aligned} \tag{6.3}$$

then, from (6.3) we define our equivalent mass as:

$$m^*_{ij} = \frac{F_{z_{ij}}}{a_{z_{ij}}} \tag{6.4}$$

where $a_{z_{ij}} \approx g$. Now for the y-axis we will separate the analysis for front and rear wheels.

The front and rear wheels analysis is similar; nevertheless, the steering subsystem introduces some differences between the definitions. The rear tires are considered to be parallel with the vehicle orientation; thus, the small steering angles are neglected to simplify our mathematical manipulations; thus,

$$m_{2j}a_{y_{2j}} = F_{y_{2j}} \tag{6.5}$$

by introducing the equivalent mass defined in (6.4) into equation (6.5), gives

$$F_{y_{2j}} = \frac{F_{z_{2j}}a_{y_{2j}}}{a_{z_{1j}}} \approx \frac{F_{z_{2j}}a_{y_{2j}}}{g} \tag{6.6}$$

and finally, the computation for the rear lateral TGFs is defined by:

$$F_{y_{2j}} = \frac{F_{z_{2j}}}{g}\left(a_y + \dot{\omega}_x h - \dot{\omega}_z l_2 + \omega_z(q^{1+j}e_j\omega_z - h\omega_y) + \omega_x(q^{1+j}e_j\omega_x - l_2\omega_y)\right)$$

with $q = -1$. Considering small angles for roll and pitch, we can consider small roll and pitch rates and accelerations, giving

$$F_{y_{2j}} = \frac{F_{z_{2j}}}{g}\left(a_y - \dot{\omega}_z l_2 + q^{1+j}e_j\omega_z^2\right) \tag{6.7}$$

For the front wheels the approach is similar, nonetheless the effect of the steering angle is added, thus

$$F_{y_{1j}} = \frac{F_{z_{1j}}}{g}\left(a_y + \dot{\omega}_x h + \dot{\lambda}_j l_1 + \lambda_j(q^{1+j}e_j\lambda_j - h * \omega_y) + \omega_x(q^{1+j}e_j\omega_x + l_1\omega_y)\right)$$

with $\lambda_j = \omega_z + \dot{\delta}_j$. And finally

$$F_{y_{1j}} = \frac{F_{z_{1j}}}{g}\left(a_y - \dot{\lambda}_j l_1 + q^{1+j} e_j \lambda_j^2\right) \tag{6.8}$$

6.3.2 Longitudinal tire-ground force

In this case the heuristic formula that was develop is the following for the front tires

$$F_{x_{1j}} = (1+\chi)\frac{F_{z_{1j}} + \frac{1}{2}\sum_{i\in\mathcal{A}} F_{z_{1j}}}{g}\left(a_x + q^{1+j}\dot{\omega}_z e_j - \dot{\omega}_y h - \omega_y(q^{1+j} e_j \omega_x + l_1\omega_y) - \omega_z(h\omega_x + l_1\omega_z)\right)$$

and the simplified version

$$F_{x_{1j}} = (1+\chi)\frac{F_{z_{1j}} + \frac{1}{2}\sum_{i\in\mathcal{A}} F_{z_{1j}}}{g}\left(a_x + q^{1+j}\dot{\omega}_z e_j - l_1\omega_z^2\right) \tag{6.9}$$

and for the rear tires

$$F_{x_{2j}} = \chi\frac{F_{z_{1j}} + \frac{1}{2}\sum_{i\in\mathcal{A}} F_{z_{1j}}}{g}\left(a_x + q^{1+j}\dot{\omega}_z e_j - l_1\omega_z^2\right) \tag{6.10}$$

with $\mid \chi \mid$ a value lower than the unity.

6.4 Experimental Results

In this section, we present the designed experiments to validate our TGFs computation/estimation scheme. In order to strengthen the advantages of our approach, the validation is carried out using two different vehicles. On the one hand, a Peugeot 308sw, with a gasoline combustion engine and a front-driven powertrain. On the other hand, a modified Land Rover Evoque is used to validate our approach; this vehicle has two in-wheel electric motors at the rear wheels.

6.4.1 Peugeot 308sw

The experimental testbed was already presented in Chapter 1.

Two test were performed; the same as in section 4.4.3.1; recalling those tests, see Figures 6.2 and 6.3. During the first mission, the road has low friction. Figure 6.2 shows at the upper-right corner with a black-solid line the vehicle speed measured with a GPS and with a red-dotted line is depicted the average angular speed obtained from the rear wheels speed sensors. Here we show that the rear tires were locked during braking due to tire force saturation. Figure 6.3 shows the

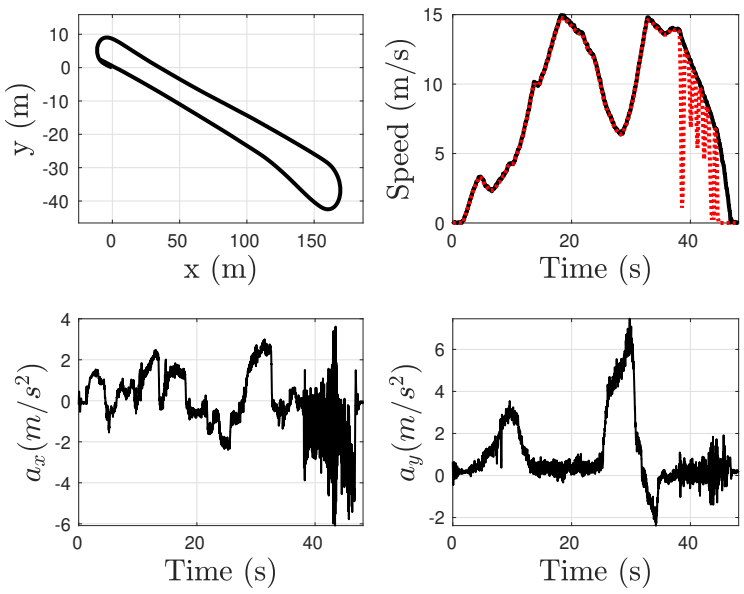

Figure 6.2 – Low friction coefficient mission. Upper-Left: gps measurement x, y coordinates. Upper-Right: Vehicle velocity –black-solid line –. Rear tires average velocity – red-dotted line –. Bottom-Left: Longitudinal acceleration. Bottom-Right: Lateral acceleration.

same maneuver at a different road with high friction; analyzing the differences between missions No.1 and No.2, we could notice that during mission No. 2, the tires did not reach the saturation operation region during the braking operation.

The lateral TGFs computation results are compared against the Dugoff's and the magic tire models; for more information on both approaches, see [Dugoff, 1969] and [Pacejka and Bakker, 1993], respectively. Using the correvit S400 transducer, we obtain the vehicle sideslip angle, which is feed to both tire models. Notice that we have to translate the vehicle speeds (v_x, v_y), from the correvit position at each one of the tires using

$$\mathbf{v_{ij}} = \mathbf{v_c} + \omega \times \mathbf{\Xi_{ij}}$$

where $\mathbf{v_{ij}} = \begin{bmatrix} v_{xij} & v_{yij} & v_{zij} \end{bmatrix}$ means the velocity vector at the ij^{th} tire, $\mathbf{v_c} = \begin{bmatrix} v_{xc} & v_{yy} & v_{zc} \end{bmatrix}$ stands for the velocity at the correvit position and $\Xi_{ij} = \begin{bmatrix} \pm l_{ij} & \pm e_{ij} & \pm s \end{bmatrix}$ defines de distances between the tires and the sideslip transducer position in the longitudinal, lateral, and vertical directions, respectively.

On the one hand, to compute the lateral TGFs, the Dugoff model needs for its computation prior knowledge on C_σ, C_α, μ, and the normal TGFs, F_{zij}, see [Dugoff, 1969]. On the other hand, the magic tire model requires prior knowledge of variables B, C, D, E, S_h, S_v and F_{zij}, see [Pacejka and Bakker, 1993]. In both cases, the normal TGFs and the sideslip angle are used directly from the transducers. The other parameters are identified using particle swarm optimization (PSO).

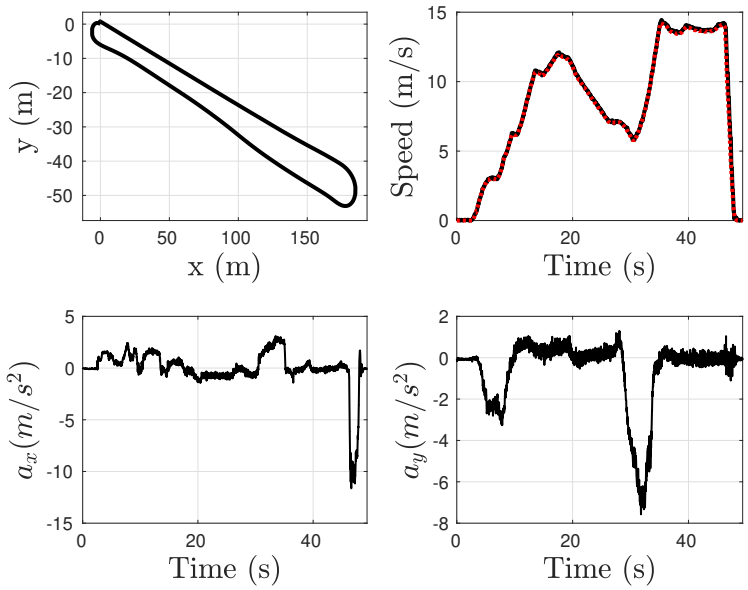

Figure 6.3 – High friction coefficient mission. Upper-Left: gps measurement x, y coordinates. Upper-Right: Vehicle velocity –black-solid line –. Rear tires average velocity – red-dotted line –. Bottom-Left: Longitudinal acceleration. Bottom-Right: Lateral acceleration.

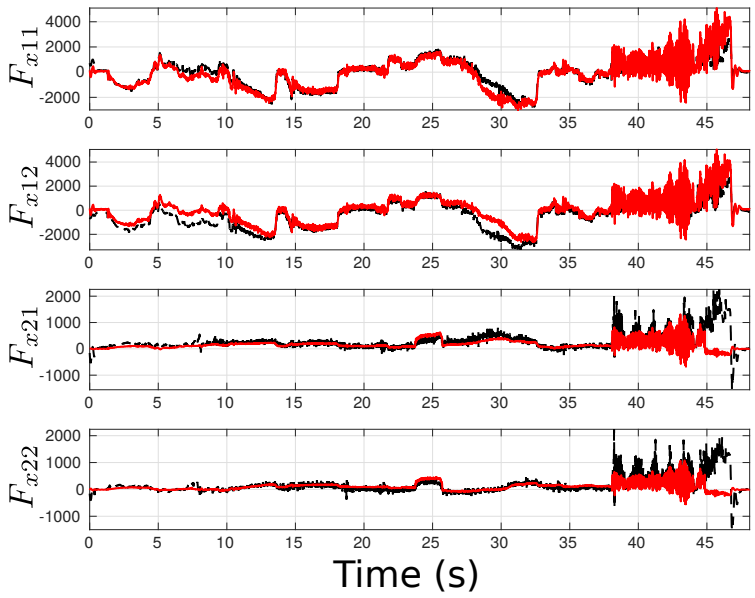

Figure 6.4 – Low Friction Mission. Longitudinal TGFs comparison. Model Fusion Proposal: red-solid line. Sensor measurement: black-dashed line.

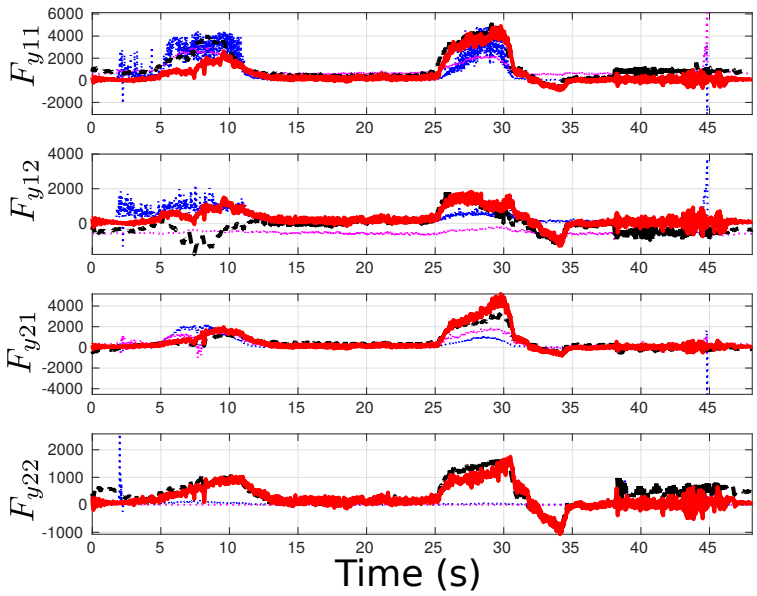

Figure 6.5 – Low Friction Mission. Lateral TGFs comparison. Mass equivalent method: red-solid line. Sensor measurement: black-dashed line. Dugoff tire model: blue-dotted line. Magic Tire Model: pink-dotted line

Figures 6.4 and 6.5 show the response of our proposal during the low friction test. Figure 6.4 shows the longitudinal response obtained from our proposal with a red-solid line and compared against the actual longitudinal TGFs with a black-dotted-dashed line. The proposal delivers an accurate computation of the forces; at the end of the mission, the rear wheels experimented an error due to the locked tires at a slow speed below 4 m/s present in Figure 6.2 around the 40 seconds mark.

Figure 6.5 displays the lateral TGFs comparison. A blue-dotted line is presented with the Dugoff's tire model, and with a pink-dotted line is depicted the magic tire model's respective responses. Here, we see that it is difficult for the tire models to deliver a good response for all the tires; the problem appears while translating the sideslip angle to the actual tire position coherently for all the tires. With our proposal, those problems disappear, since our algorithm is not dependent on the sideslip angle, nonetheless for F_{y12} at [5,10] seconds time frame, a discrepancy between the estimated force and the actual force appears; this is explained due to the low vehicle speed. The force components due to camber, conicity, plysteer, radial run-out, and lateral run-out are stronger than the force produced due to vehicle dynamics. These effects are not considered in our proposal; thus, it is not possible to estimate the TGFs produced purely with those effects.

Figures 6.6-6.7 presents the same responses, but in this case, the tire-ground friction is high, and we drive two laps. Our approach's accuracy is again validated,

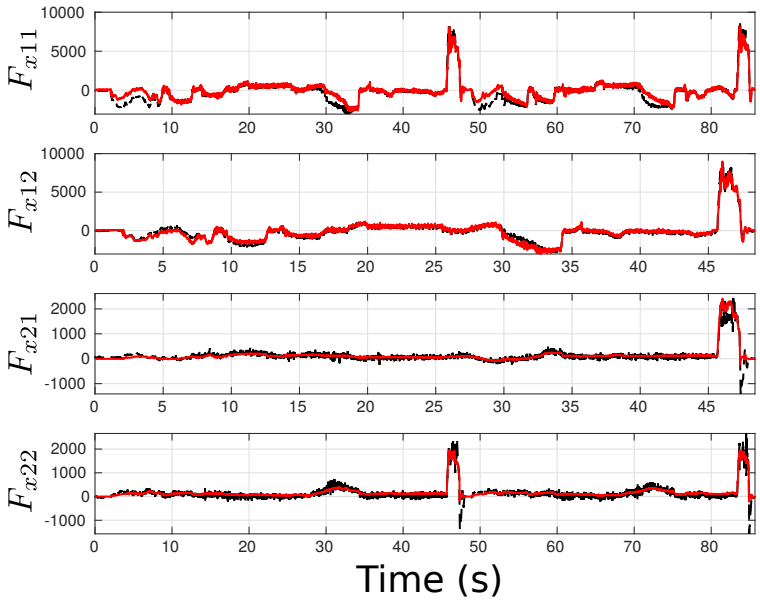

Figure 6.6 – High Friction Mission. Longitudinal TGFs comparison. Mass equivalent method: red-solid line. Sensor measurement: black-dashed line.

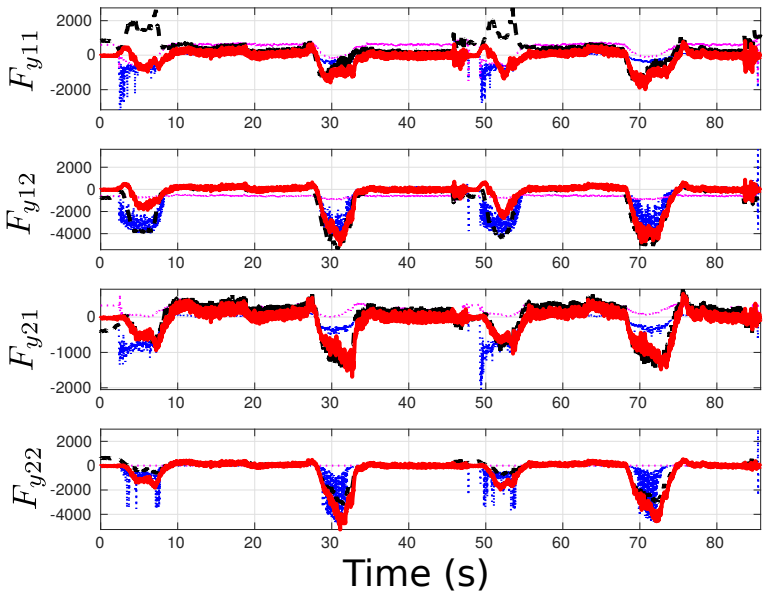

Figure 6.7 – High Friction Mission. Lateral TGFs comparison. Mass equivalent method: red-solid line. Sensor measurement: black-dashed line. Dugoff tire model: blue-dotted line. Magic Tire Model: pink-dotted line

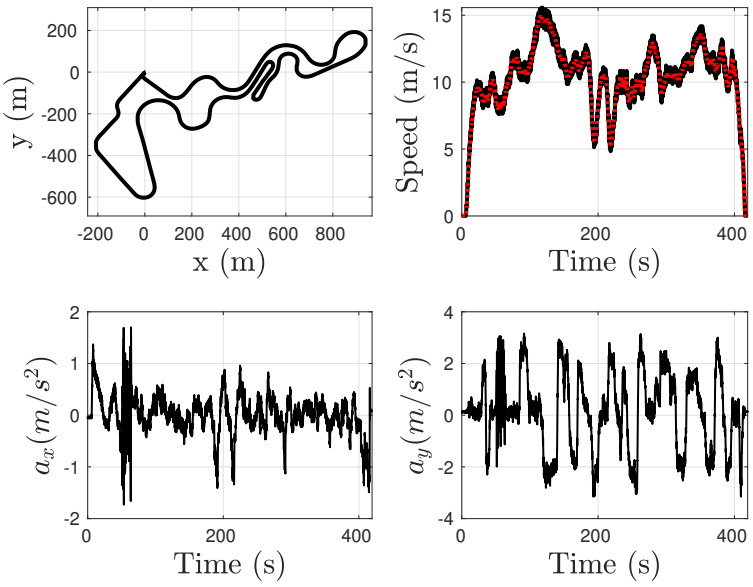

Figure 6.8 – Mission No. 3. Low Speed lap to Lommel proving ground. Maximum lateral acceleration, a_y about 3 m/s^2

and even more, we could see a more significant difference between its response and the one obtained from the tire models. Notably, in Figure 6.7, between [0, 10] seconds and [50,60] seconds, our response deviates from the actual force; this is explained due to the low vehicle speed (less than 5 m/s); at a low rate, the tire disturbances, such as camber, are more potent than the effects of the moving vehicle.

6.4.2 Land Rover Evoque

The second experimental testbed is a 2011 Range Rover Evoque; the test is performed at Lommel proving ground in Belgium under dry conditions. This vehicle is instrumented with two force transducers at the rear wheels which measures the forces and torques at the longitudinal, lateral and vertical directions. Additionally, it is instrumented with an IMU that measures the accelerations and angular rates for the x, y, and z axis. Two tests are presented here: one lap at low speed and another at the limit handling speed. Figure 6.8 shows Mission No.3 with the velocity profile at a maximum speed of 15 m/s; mission No. 4 followed the same route, but, the velocity profile was scaled showing a maximum speed of 22 m/s, the difference between mission No. 3 and 4 is that during mission No. 4 the tire experiment the saturation phenomena. It should be mentioned that a professional driver was required to conduct these tests.

Figure 6.10 shows the rear tire's algorithm responses for the longitudinal and

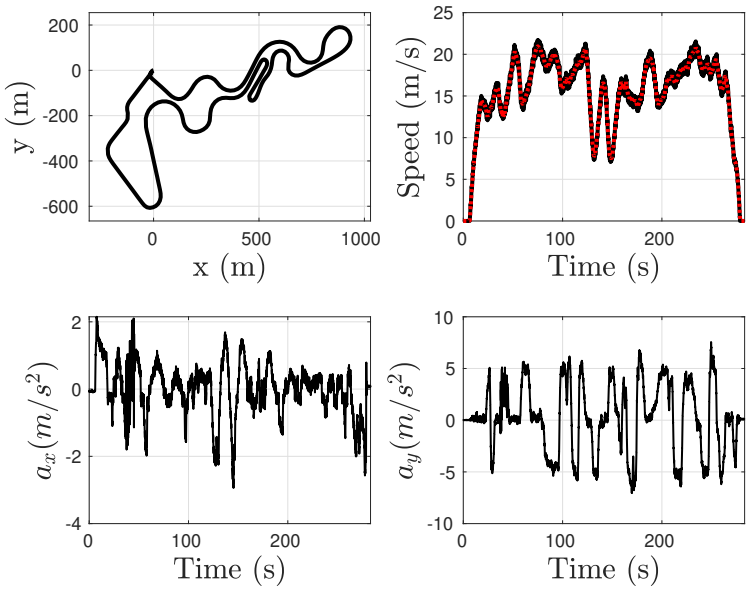

Figure 6.9 – Mission No. 4. High Speed lap to Lommel proving ground. Maximum lateral acceleration, a_y about 3 m/s^2

lateral TGFs during mission No. 3; here, on the one hand for the longitudinal TGFs exist a region of maximum noise between the 50 and 70 seconds – given by the longitudinal accelerometer –. On the other hand, for the lateral TGFs, this figure compares our proposal, the Dugoff, and magic tire models; notice here, the excellent response of the three computations.

Figure 6.11 shows the rear tire's algorithm responses for the longitudinal and lateral TGFs during mission No. 4; here, for the longitudinal TGFs exist a region of maximum noise between the 30 and 50 seconds – given by the longitudinal accelerometer –. For the lateral TGFs, this figure compares our proposal, the Dugoff, and magic tire models; notice here, the inadequate response of the Dugoff and magic tire models computation. Based on these inadequate responses, given by the tire models, we conclude, that with this approach, the values C_σ and C_α for the Dugoff tire model and B, C, D, and E for the magic tire model varies with the vehicle velocity and the level of lateral excitation. On the contrary, our approach displays robustness, since algorithm tunning is not required to obtain similar accuracy.

6.4.3 Estimation Scheme Response Analysis

In order to analyze the estimation performance of our proposal, the following error is defined

$$\tilde{F}_{p_{ij}} := \hat{F}_{p_{ij}} - F_{p_{ij}}; \forall p \in \{x, y\}$$

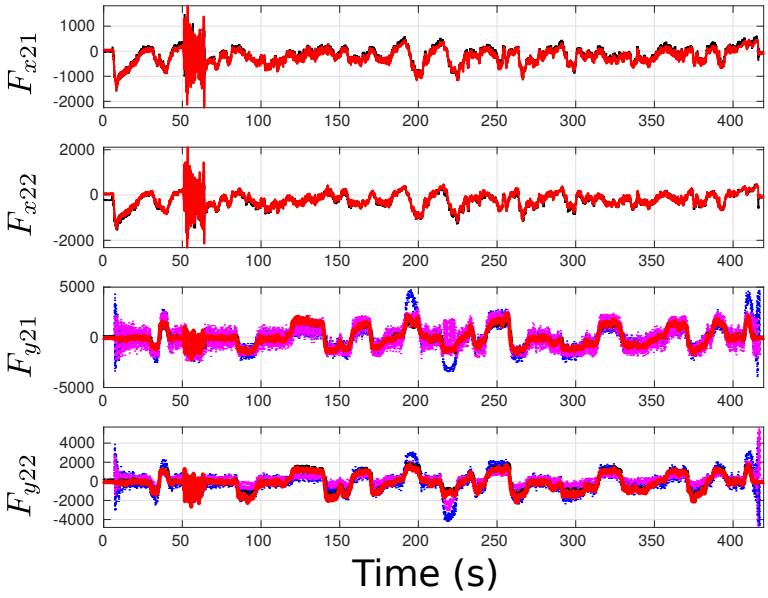

Figure 6.10 – Low Speed Mission. Longitudinal and Lateral TGFs comparison for the rear wheels. Mass equivalent proposal: red-solid line. Sensor measurement: black-dashed line. Dugoff tire model: blue-dotted line. Magic Tire Model: pink-dotted line

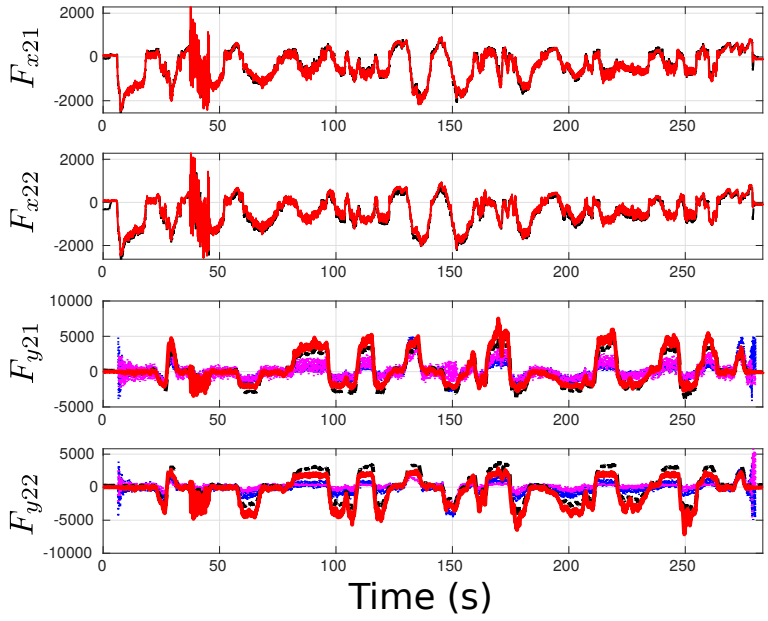

Figure 6.11 – High Speed Mission. Longitudinal and Lateral TGFs comparison for the rear wheels. Mass equivalent proposal: red-solid line. Sensor measurement: black-dashed line. Dugoff tire model: blue-dotted line. Magic Tire Model: pink-dotted line

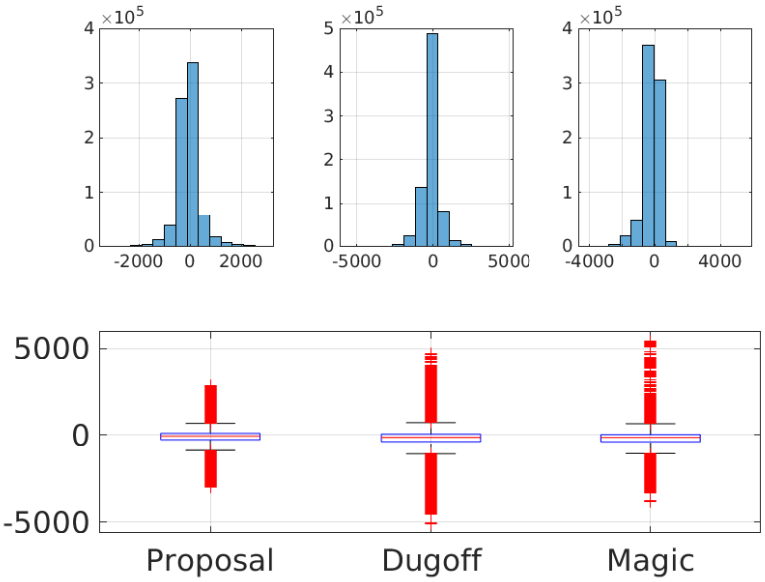

Figure 6.12 – Mission No. 1 Lateral TGFs comparison. Analysis made using our proposal, the Dugoff's model and magic tire model. Up: Distribution of the estimation error. Down: Boxplot graph obtained from the estimation error for the TGFs.

also the responses of each tire are concatenated to its further analyze. The index selected to analyze the performance of our proposal are the mean error, μ_p, the standard deviation of the error, σ_p, the maximum absolute error, $\max\left(\mid \tilde{F}_{pij} \mid\right)$, and the percentage of outliers.

Table 6.1 shows the response analysis for the longitudinal TGFs during the four missions. This result's primary concern is the high value for the absolute error, which could be explained due to the high convergence time required by the observer to follow high excitation inputs (accelerating, braking). Nonetheless, observe that the standard deviation remains small.

Table 6.2 presents a comparison between the response obtained with our proposal (P) against the Dugoff's (D) and magic tire (M) models. Notice that our results are better for the most important parameters (σ_y, $\max\left(\mid \tilde{F}_{yij} \mid\right)$) in all

Table 6.1 – Longitudinal TGFs error response analysis

Mission	μ_x (N)	σ_x (N)	$\max(\mid \tilde{F}_{xij} \mid)$ (N)	outliers (%)
No. 1	48	375	5191	15.26
No. 2	45	299	3213	14.44
No. 3	-7.9	145	2809	1.81
No. 4	39	186	2953	1.73

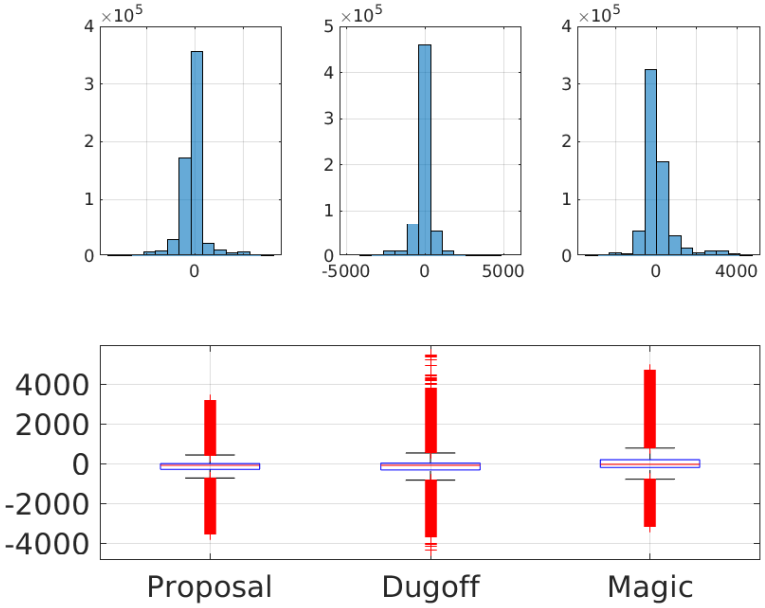

Figure 6.13 – Mission No. 2 Lateral TGFs comparison. Analysis made using our proposal, the Dugoff's model and magic tire model. Up: Distribution of the estimation error. Down: Boxplot graph obtained from the estimation error for the TGFs.

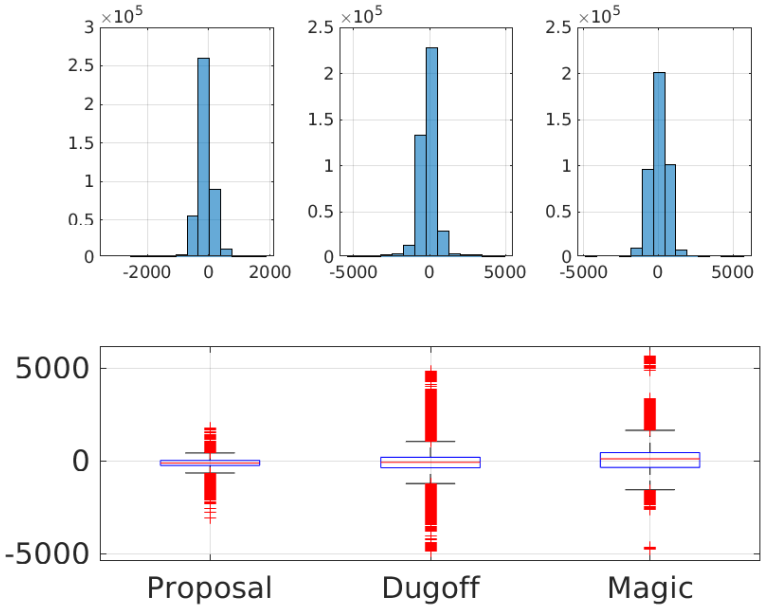

Figure 6.14 – Mission No. 3 Lateral TGFs comparison. Analysis made using our proposal, the Dugoff's model and magic tire model. Up: Distribution of the estimation error. Down: Boxplot graph obtained from the estimation error for the TGFs.

Table 6.2 – Lateral TGFs error response analysis

Mission	μ_y (P/D/M) (N)	σ_y (P/D/M) (N)	$\max(\mid \tilde{F}_{yij} \mid)$ (P/D/M) (N)	outliers (P/D/M) (%)
No. 1	-64/-146/-214	436/543/472	2949/5084/5445	6.06/7.19/6.56
No. 2	-92/-91/-128	570/595/814	3501/5506/4739	12.36/11.27/12.9
No. 3	-108/-82/-63	243/681/634	3053/4860/5647	2.17/4.95/1.23
No. 4	-194/-115/-67	744/1415/1480	4215/5239/5505	0.52/0.49/0.27

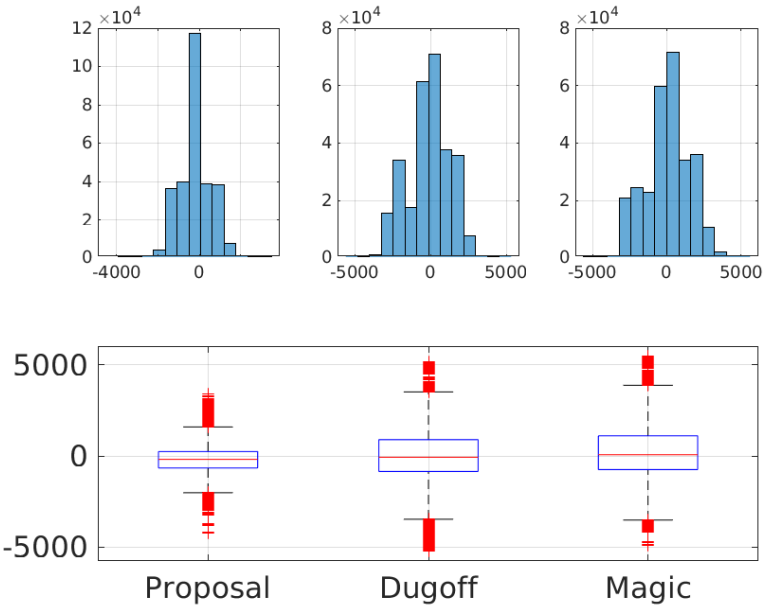

Figure 6.15 – Mission No. 1 Lateral TGFs comparison. Analysis made using our proposal, the Dugoff's model and magic tire model. Up: Distribution of the estimation error. Down: Boxplot graph obtained from the estimation error for the TGFs.

missions by a significant margin that means that our results are more accurate and at high speed as in mission No. 4 the results given with our proposal overthrow the Dugoff's or the magic tire responses.

On the other hand, Figures 6.12-6.15, display the response comparison between our proposal, the Dugoff, and the magic tire models for mission No. 1 through No. 4, respectively. The numbers presented in Table 6.2 are more precise, and the improvement obtained from the proposed approach could be verified with ease. In all cases, the resulting boxplot is more compact with smaller outliers and quartiles. Notice in Figure 6.15, that the values considered outliers from our proposal would not have this tag with the Dugoff or the magic tire formulations.

6.5 Conclusions

This chapter presents a novel longitudinal and lateral TGFs approach; this model computes the TGFs without requiring a tire model or vehicle model.

The model is obtained directly from the tire representation and the use of equivalent masses and local accelerations. This method follows the simple Newton laws of motion and does not require the sideslip angle to compute the TGFs.

The algorithm is validated with experimental data, and the method's robustness is tested for variation in friction and tire operation region. The saturation is taken into account intensely since the acceleration is the force's product and not backward.

The results tell us that this approach is more robust and accurate than other methods found in the literature.

Application of TGFs to vehicle subsystem controllers

Contents

7.1 Introduction

This chapter includes some applications that could consist of estimating the tire-ground forces or even the parameter estimation. Here two applications are presented first, the road profile estimation and later the control of an active suspension system to improve passenger comfort. Even though we give two applications, many systems will significantly improve their performance, i.e., the braking system, optimal controllers to improve energy efficiency, and electronic stability controllers.

7.2 Road Profile Estimation

In later years, active or semi-active suspension systems have been introduced and integrated into intelligent vehicles with the Advanced Driver Assistance System. These suspensions modify the mechanical properties using actuators that actively move the vehicle chassis through the vertical direction (active suspension) or using a magnetorheological damper (semi-active suspension) modifies the system response by varying the actual damping in the system. The correct behavior of this system can improve the maneuverability, comfort, and stability of the vehicle.

In the literature, most of the approaches to control the suspension system considers complete knowledge of the state; just a few works have addressed the state estimation problem in the close loop control scheme, see [Pletschen and Badur, 2014, Wang et al., 2017]. This work's scope is the estimation problem, including the suspension states, the unknown inputs, and the load transfer that actively affect the ride comfort and safety. Suspension state estimation is an arduous task; the introduction of unknown inputs such as road profile, transfer load, the use of equivalent parameters that can vary according to the system state, among others, increases the problem's complexity. The road profile is one of the most important variables that determine the dynamic suspension performance. Knowledge of the road profile is essential for vehicle dynamics and active controllers, see [Chokor et al., 2016, Shin et al., 2014, Savaresi et al., 2010a, Gillespie, 1992, Sayers and Karamihas, 1998, Bastow et al., 2004, ElMadany and Abduljabbar, 1999]. Road profile and accurate state estimation provides useful information to design active controllers and improve passenger's safety and comfort. Nowadays, there is no low-cost sensor able to measure the road irregularities; thus, developing a virtual sensor to reconstruct the road profile is of great importance. There are methods to measure road profiles by doing visual inspections as in [Kim et al., 2002], and recently Mercedes-Benz introduced stereo cameras to perform this operation.

However, these approaches are sensitive to weather and light conditions, without mentioning the computational burden required to perform its computation. In [Doumiati et al., 2011], a quarter-car representation is proposed to estimate the road profile using a Kalman filter. In [Doumiati et al., 2017], the road profile estimation is performed by an adaptive Youla-Kučera parameterization technique. In [Imine et al., 2005], estimation techniques based on sliding mode observers are proposed.

This work's main contribution consists of the development of an embedded estimation algorithm to estimate not only the road profile but the suspension states, and the load transfer as well, using a single observer structure. The quarter-car model is boosted using the vehicle dynamics so that an approximation for the road profile time derivative is defined. The estimation procedure is validated with a high order vehicle model using a professional automotive simulator OKTAL-SCANeR studio-Callas, and the primary vehicle dynamics considerations that empower SCANeR suspension model are validated using experimental data from our testbed.

The most known vehicle suspension model is the quarter-car model,

$$\begin{aligned} m_{sij}\ddot{z}_{sij} &= -k_{sij}(z_{sij}-z_{usij}) - c_{sij}(\dot{z}_{sij}-\dot{z}_{usij}) \\ m_{usij}\ddot{z}_{usij} &= k_{sij}(z_{sij}-z_{usij}) + c_{sij}(\dot{z}_{sij}-\dot{z}_{usij}) - k_{tij}(z_{usij}-z_{rij}) - c_{tij}(\dot{z}_{usij}-\dot{z}_{rij}) \end{aligned} \tag{7.1}$$

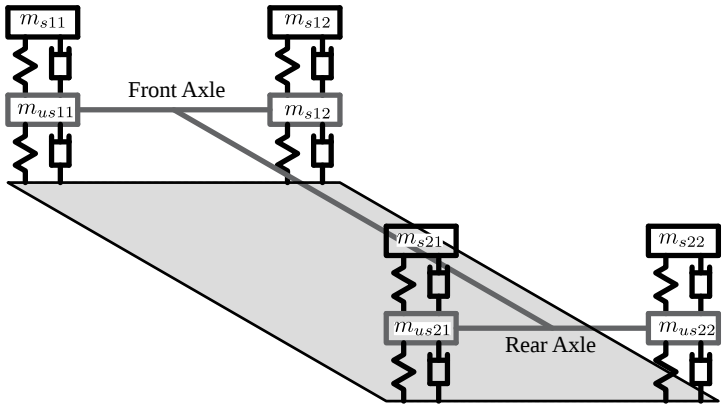

Figure 7.1 – Coupled Corner Suspension Model

The quarter-car model defined in equation set (7.1) is a linear model that neglects the interaction between vehicle corners. According to [Kim and Ro, 2000], this simple two-mass model misrepresents the suspension dynamics; In [Kim and

Ro, 2000], a 32 order linear model based on ADAMS is introduced. Nonetheless, designing an observer/controller for a system of such dimension is inconceivable; besides, this 32-order model requires variables that are only available through simulation. The quarter-car model is not enough to estimate the vehicle mass; thus, a coupled-corner representation is proposed in Figure 7.1. Thus, from Figure 7.1, and to comply with the conservation of angular momentum law, the coupled-corner model is modified as:

$$\begin{aligned} m_{sij}\ddot{z}_{sij} &= -\sum_{\alpha\in\mathcal{A}}\sum_{\beta\in\mathcal{A}}\left(k_{sij\alpha\beta}(z_{s\alpha\beta}-z_{us\alpha\beta})+c_{sij\alpha\beta}(\dot{z}_{s\alpha\beta}-\dot{z}_{us\alpha\beta})\right) \\ m_{usij}\ddot{z}_{usij} &= \sum_{\alpha\in\mathcal{A}}\sum_{\beta\in\mathcal{A}}\left(k_{sij\alpha\beta}(z_{s\alpha\beta}-z_{us\alpha\beta})+c_{sij\alpha\beta}(\dot{z}_{s\alpha\beta}-\dot{z}_{us\alpha\beta})\right) \\ &\quad -\sum_{\alpha\in\mathcal{A}}\sum_{\beta\in\mathcal{A}}\left(k_{tij\alpha\beta}(z_{us\alpha\beta}-z_{r\alpha\beta})+c_{tij\alpha\beta}(\dot{z}_{us\alpha\beta}-\dot{z}_{r\alpha\beta})\right) \end{aligned} \tag{7.2}$$

where suffixes $\alpha,\beta\in\mathcal{A}$ represents the suspension spring stiffness given by the interaction between corners – i.e., k_{s1111} means the spring stiffness for the front-left wheel and k_{s1112} signify the stiffness related to the dynamics between the front-right and front-left wheel. Thus, after an insightful analysis, the load transfer is defined as:

$$\Xi F_{zij}=\sum_{\alpha\in\mathcal{A}}\sum_{\beta\in\mathcal{A}}\left(k_{tij\alpha\beta}(z_{us\alpha\beta}-z_{r\alpha\beta})+c_{tij\alpha\beta}(\dot{z}_{us\alpha\beta}-\dot{z}_{r\alpha\beta})\right)$$

Then, assuming a plane road ($z_r=\dot{z}_r=0$) and the vehicle at a steady condition ($a_z=a_x=a_y=0$); the initial normal force condition is obtained from (7.2), and defined:

$$F_{zij}(0)=\sum_{\alpha\in\mathcal{A}}\sum_{\beta\in\mathcal{A}}\left(k_{s\alpha\beta}\cdot(h_{s\alpha\beta}-l_{s\alpha\beta})\right)+m_{usij}\cdot g \tag{7.3}$$

where $h_{s\alpha\beta}=z_{s\alpha\beta}-z_{us\alpha\beta}$, $l_{s\alpha\beta}$ means the nominal elongation of the $\alpha\beta^{th}$ spring. Notice that, m_{usij} is a design known variable. The only fluctuating mass is at the chassis, m_{sij} and $m_{sij}\approx F_{zij}(0)/g$. The variables that defines the center of gravity position E_1, L_1, could be easily identified given the vehicle's weight distribution. E_1 and L_1 are defined in later sections of the paper.

7.2.1 Observer Design and Analysis

This section presents an analysis of the system uncertainty and observer design. First, as mentioned in the last section, the quarter car model has its flaws; however, its accuracy-simplicity trade-off is higher than the coupled-corner model. In the

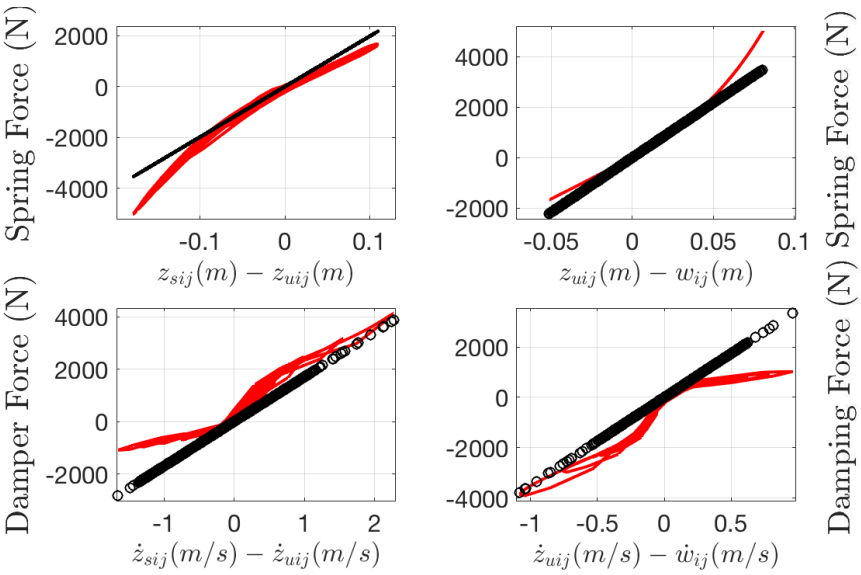

Figure 7.2 – Up-left: Suspension deflection against spring force at the suspension. Up-right: Tire deflection against the spring force at the tire. Down-left: Suspension deflection speed against the damping force at the suspension. Down-right: Tire deflection speed against the damping force at the tire.

previous section, the coupled corner model helps to compute the system's mass and the COG position.

The quarter-car model allows studying a vehicle's vertical behavior according to its suspension type (passive or controlled). However, the road profile, z_r, is an unknown input that results in undesired vibrations if it is not considered at the controller design stage. These vibrations affect vehicle stability and reduce passengers' comfort. Thus, it is crucial to provide the road profile for its inclusion into the closed-loop controller strategy to profit from a semi-active or active suspension fully.

Figure 7.2 shows in red-solid line the actual force produced at the suspension spring and dampers (left figures) and the actual force produced by the tire represented by a series of springs and dampers (right figures). Also, displays with black circles the linear approximation of such forces using the equivalent parameters (k_s, c_s, k_t and c_t). Notice that this linear approximation lacks accuracy at the edges of the graphs. Moreover, the presence of such uncertainties increases the estimation problem complexity.

To overcome these uncertainties, we choose to develop a closed-loop stochastic observer. Then, let us consider a general nonlinear suspension model:

$$\begin{aligned} \dot{\mathbf{z}}_{\mathbf{ij}} &= \mathbf{f}(t, \mathbf{z}_{\mathbf{ij}}, \mathbf{z}_{\mathbf{rij}}) \\ \mathbf{y} &= \mathbf{h}(t, \mathbf{z}_{\mathbf{ij}}, \mathbf{z}_{\mathbf{rij}}) \end{aligned} \tag{7.4}$$

Thus, from (7.4) is possible to obtain the state-space representation

$$\begin{aligned} \dot{\mathbf{x}} &= \mathbf{A}\mathbf{x} + \mathbf{d}(t,\mathbf{x}) \\ \mathbf{y} &= \mathbf{C}\mathbf{x} + \mathbf{g}(t,\mathbf{x}) \end{aligned} \tag{7.5}$$

where $\mathbf{x}^T = \begin{bmatrix} \mathbf{z_{ij}}^T & \mathbf{z_{rij}}^T & \Delta F_{zij} \end{bmatrix}$ with errors $\mathbf{d}(t,\mathbf{x}) = \mathbf{f}(t,\mathbf{x}) - \mathbf{A}\mathbf{x}$ and $\mathbf{g}(t,\mathbf{x}) = \mathbf{h}(t,\mathbf{x}) - \mathbf{C}\mathbf{x}$ bounded by the $\mathcal{L}_2$-norm $\| \mathbf{d}(t,\mathbf{x}) \|^2 \leq \mathbf{M}_1 < \infty$, and $\| \mathbf{g}(t,\mathbf{x}) \|^2 \leq \mathbf{M}_2 < \infty$. Matrices $\mathbf{M}_1$ and $\mathbf{M_2}$ are composed of elements in positive real space, $\mathbb{R}^+$, and $\mathbf{M_1} > 0$, $\mathbf{M_2} > \mathbf{0}$. With $\mathbf{z_{ij}}^T = [z_{sij}, \dot{z}_{zij}, z_{usij}, \dot{z}_{usij}]$, $\mathbf{z}_{rij}^T = [z_{rij}, \dot{z}_{rij}]$. Also the following property holds

$$\| \mathbf{d}(t,\mathbf{x}) \|^2 = \mathbf{Q}(t,\mathbf{x}) \leq \mathbf{Q}_{max} \sim \mathcal{N}(0, \sigma_d)$$

$$\| \mathbf{g}(t,\mathbf{x}) \|^2 = \mathbf{R}(t,\mathbf{x}) \leq \mathbf{R}_{max} \sim \mathcal{N}(0, \sigma_g)$$

where $\mathbf{Q}_{max}$ and $\mathbf{R}_{max}$ are the covariance process and the output noise matrices, respectively. The elements of matrix $\mathbf{A} \in \mathbb{R}^{7\times7}$ and $\mathbf{C} \in \mathbb{R}^{4\times7}$ are defined in the following subsections.

7.2.1.1 Sprung mass height at the inertial frame

The body attitude with respect to the inertial frame could be estimated using an inertial measurement unit. Then, if we translate the vertical velocity of the vehicle to each one of the tires, gives:

$$v_{zij} = v_{zcog} \pm L_i\dot{\theta} \pm E_j\dot{\phi} \tag{7.6}$$

where v_{zij} means the vertical speed at the ij^{th} corner, v_{zcog} is the vertical speed at the center of gravity, L_i means the smallest distance between the COG and the front or rear axle, respectively. The variable $\dot{\theta}$ means the pitch angular rate measured by an IMU. E_i stands for the distance in the $y - body$ plane between the tire and the COG, and finally, $\dot{\phi}$ represents the angular roll rate given by the IMU. The ground vehicle is a non-holonomic system, thus, it is correct to consider $v_{zij} = v_{zcog} \pm \dot{z}_{ij}$. Then, from (7.6), gives

$$\dot{z}_{sij} = \pm L_i\dot{\theta} \pm E_j\dot{\phi} \tag{7.7}$$

finally, integrating (7.7) it comes

$$z_{sij} = \pm L_i\theta \pm E_j\phi \tag{7.8}$$

The decision for using eq. (7.7) or (7.8) in our observation scheme depends entirely on the IMU's quality. It is necessary to avoid bias in the estimations due to high noise within the gyroscopes measurements; however, we prefer to use (7.8) because of an increase in the system observability index.

7.2.2 Sprung mass height at the body frame

The roll dynamics at the vehicle body frame could be modeled as a second-order system as

$$\begin{aligned} I_\phi \ddot{\phi}_v &= -k_\phi \phi_v - c_\phi \dot{\phi}_v - \gamma_y a_y \\ \frac{\phi_v(s)}{a_y(s)} &= \frac{\gamma_y}{I_\phi s^2 + c_\phi s + k_\phi} \end{aligned} \tag{7.9}$$

The pitch body dynamics model is nonlinear; the approximation is a third-order polynomial. Thus,

$$I_\theta \ddot{\theta}_v = f_\theta(\theta_v, \dot{\theta}_v, a_x) \tag{7.10}$$

we are able to compute ϕ_v, $\dot{\phi}_v$, θ_v and $\dot{\theta}_v$ using (7.9) and (7.10). Finally, applying the same concept as in (7.7), we get the following set

$$\begin{aligned} \dot{z}_{ij} - \dot{z}_{rij} &= \pm L_i \dot{\theta}_v \pm E_j \dot{\phi}_v \\ z_{ij} - z_{rij} &= \pm L_i \theta_v \pm E_j \phi_v \end{aligned} \tag{7.11}$$

7.2.3 Normal Tire-Ground forces obtained from vehicle dynamics

The vertical vehicle dynamics affect the suspension system. In this subsection are two representations of a vehicle, presented in Chapter 2, the bicycle and hoverboard models. Eventually, using both models is possible to obtain the normal TGFs, as depicted in 4. Thus, normal TGFs are defined as:

$$\hat{F}_{zij} = \frac{1}{gel}\left(e_{i^c} l_{j^c} mg^2 + q^{j^c} h l_{i^c} mg\bar{a}_y + q^i h e_{j^c} mg\bar{a}_x - q^i q^j h^2 m\bar{a}_y\bar{a}_x\right) \tag{7.12}$$

with $q = -1$ and ^{c} stands for the complement operator, (i.e $i = 2 \in \mathcal{A} := \{1, 2\}$, then, $i^c = 1$). Then,

$$\Delta F_{zij} = F_{zij} - (m_s + m_{us})\, g \tag{7.13}$$

From the quarter-car model is possible to obtain the load transfer, then from (7.1) analogously to (7.3), the load transfer is redefined as:

$$\Delta F_{zij} = k_{tij}\left(z_{uij} - z_{rij}\right) + c_{tij}\left(\dot{z}_{uij} - \dot{z}_{rij}\right) \tag{7.14}$$

Hence, from (7.14) and considering prior knowledge of the load transfer given by (7.13) is possible to obtain,

$$\dot{z}_{rij} = \frac{k_{tij}}{c_{tij}}\left(z_{uij} - z_{rij}\right) + \dot{z}_{uij} - \frac{1}{c_{tij}}\Delta\hat{F}_{zij} \tag{7.15}$$

Equation (7.15) approximates the road irregularities time derivative, obtained by the mixture between the suspension and vehicle dynamic models.

As mentioned earlier, the suspension model (7.5) is not perfect, and to overcome the mentioned uncertainties, we develop an observer based on the Kalman filter technique in the next section.

7.2.4 Kalman filter implementation

Let us consider the models presented in the previous section in a discrete state-space form, as follows:

$$\begin{aligned} \mathbf{x}_k &= \bar{\mathbf{A}}_k\mathbf{x}_{k-1} + \bar{\mathbf{w}}_k \\ \mathbf{y}_k &= \mathbf{C}_k\mathbf{x}_k + \bar{\mathbf{v}}_k \end{aligned} \tag{7.16}$$

with $\mathbf{x}_k$ as defined in equation (7.5), $\bar{\mathbf{A}} = \mathbf{I} + \mathbf{A} * t_s$, $\mathbf{I}$ is an identity matrix, $\mathbf{I} \in \mathbb{R}^{7\times7}$, t_s defines the sampling period of the discrete system. Also here $\bar{\mathbf{w}}_k$ is the system

uncertainty, and $\bar{\mathbf{v}}_k$ represents the measurement noise and uncertainty.

$$\mathbf{A} = \begin{bmatrix} \mathbf{\Omega}_{4\times4} & \mathbf{B}_{4\times2} & \mathbf{0}_{5\times1} \\ \mathbf{\Theta}_{3\times4} & \mathbf{\Phi}_{3\times2} & \mathbf{J}_{2\times1} \end{bmatrix}; \quad \mathbf{C} = \begin{bmatrix} \mathbf{L}_{4\times4} & \mathbf{M}_{4\times3} \\ \mathbf{0}_{1\times6} & 1_{1\times1} \end{bmatrix}$$

$$\mathbf{\Omega} = \begin{bmatrix} 0 & 1 & 0 & 0 \\ -m_s^{-1}k_s & -m_s^{-1}c_d & m_s^{-1}k_s & m_s^{-1}c_d \\ 0 & 0 & 0 & 1 \\ m_{us}^{-1}k_s & m_{us}^{-1}c_d & -m_{us}^{-1}(k_s+k_t) & -m_{us}^{-1}(c_d+c_t) \end{bmatrix}$$

$$\mathbf{B} = \begin{bmatrix} 0 & 0 & 0 & m_s^{-1}k_t \\ 0 & 0 & 0 & m_{us}^{-1}c_t \end{bmatrix}^T; \quad \mathbf{J} = \begin{bmatrix} -c_t^{-1} \\ 1 \end{bmatrix}$$

$$\mathbf{\Theta} = \begin{bmatrix} 0 & 0 & 0 & 0 \\ 0 & 0 & k_t c_t^{-1} & 1 \\ 0 & 0 & 0 & 0 \end{bmatrix}; \quad \mathbf{\Phi} = \begin{bmatrix} 0 & 1 \\ -k_t c_t^{-1} & 0 \\ 0 & 0 \end{bmatrix}$$

$$\mathbf{L} = \begin{bmatrix} 1 & 0 & -1 & 0 \\ 0 & 1 & 0 & -1 \\ 1 & 0 & 0 & 0 \\ 1 & 0 & 0 & 0 \end{bmatrix}; \quad \mathbf{M} = \begin{bmatrix} 0 & 0 & 0 \\ 0 & 0 & 0 \\ 0 & 0 & 0 \\ -1 & 0 & 0 \end{bmatrix}$$

with $\mathbf{0}_{m\times n} \in \mathbb{R}^{m\times n}$ as a matrix full of zeros with adequate dimensions. Figure 7.3 shows the overall observation scheme, with the inputs required to obtain the complete suspension state, and its road profile.

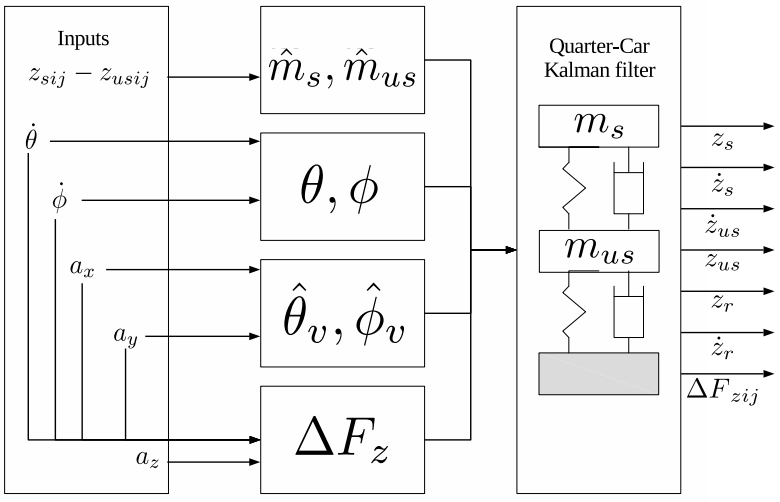

Figure 7.3 – Overall observation scheme

7.2.5 Simulation Results

In this section, a set of simulations are performed to validate the proposed scheme using automotive simulation environment OKTAL-SCANeRstudio with a high order vehicle dynamic model Callas. The system response is directly obtained from the simulator, and the observer is implemented using a Matlab script. Two maneuvers where carried out: 1) The first one was to follow a straight line at a constant speed with a road profile defined as $z_r = 0.1 \cdot \sin\left(\frac{1}{7} \cdot 2 \cdot \pi \cdot x_{pos}\right)$ where x_{pos} means the longitudinal vehicle position within the trajectory. The road profile z_r, in this case, has a sinusoidal periodicity every 7 meters. A set of 5 missions were performed at 10, 15, 20, 25, and 30 kph. 2) The second maneuver is a slalom. A set of 10 slaloms are performed at different speeds from 50 to 100 kph in a flat road.

7.2.6 Observation schemes performance

There are other approaches able to compute the road profile. A classic approach is to consider the road profile time derivative as a random walk variable ($\dot{z}_{rij} = 0$). Table 7.1 shows a comparison between the mean square error of our contribution and the classical observer considering $\dot{z}_{rij} = 0$. The matrices $\mathbf{R}$ and $\mathbf{Q}$ for the Kalman filter are selected after an optimization process known as PSO. Thus, both approaches (proposal and random walk definition) have the best possible choice for $\mathbf{R}$ and $\mathbf{Q}$ matrices. Notice that our proposal delivers an improved performance according to the mean square error results in most cases.

In Table 7.2, the mean estimation errors and the standard deviation of the estimation errors for each one of the test are presented. Figure 7.4, shows the road profile estimation response with a red-solid line and with black dots the actual road. Table 7.2 shows that the maximum standard deviation for $\tilde{z}_{sij} := z_{sij} - \hat{z}_{sij}$ is 1.5 centimeters, from now on the symbol $\tilde{}$ means an error and the symbol $\hat{}$ represents an estimation, for $\tilde{z}_{uij}$ is 1.7 centimeters and for the standard deviation of the road profile error, $\tilde{z}_{rij}$, is 1.8 centimeters. The main difference between our proposal and the random walk approach relies upon the slalom stage since the random walk consideration, $\dot{z}_r = 0$, is, on the one hand, unconstrained and the filter is not able to differentiate between noise or model uncertainty. The measured input, $z_{sij} - z_{usij}$, has the same order of magnitude for both maneuvers; nonetheless, the road profile is equal to zero for all the slalom maneuvers. On the other hand, in our proposal $\dot{z}_{rij}$ is constrained by equation (7.15).

Figure 7.5, shows the $\hat{z}_{sij}$ response of our observer with a red-solid line, while depicts the actual z_{sij} using black dots. Notice that the estimation error requires time to adjust and converge to zero.

Table 7.1 – Comparison between the proposal presented in this work and the known random walk technique

	MSE					
Approach	$\tilde{z}_{sij}$	$\dot{\tilde{z}}_{sij}$	$\tilde{z}_{uij}$	$\dot{\tilde{z}}_{sij}$	$\tilde{w}_{sij}$	$\dot{\tilde{w}}_{sij}$
V. Dyn.	0.0001	0.0239	0.0001	0.0239	0.0002	0.0977
R. Walk	0.0002	0.0249	0.0002	0.0249	0.0003	0.0835

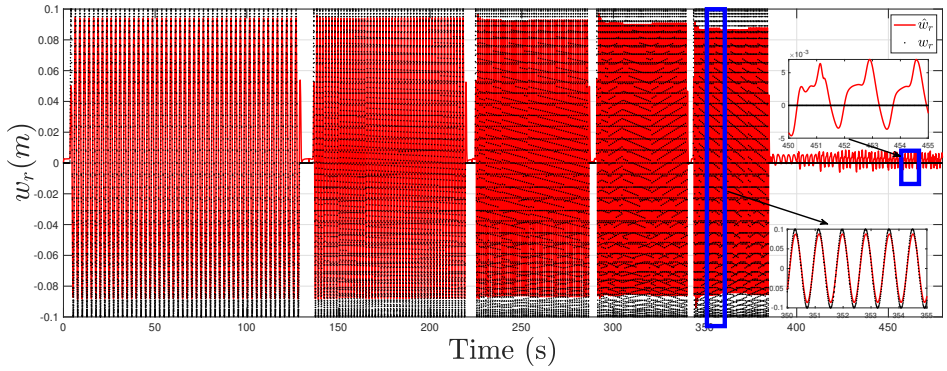

Figure 7.4 – Road profile estimation, $\hat{z}_{rij}$ against the actual road profile, z_{rij}. The first 134 seconds the vehicle speed is 10 km/h, from 134 to 222 seconds the velocity is 15 km/h, from 222 to 289 s. $v = 20$ km/h, from 289 to 342 s. the vehicle speed is 25 km/h, from 340 to 386 s. the velocity is 30 km/h. Until second 386 the road is described by $z_r = 0.1 \cdot \sin\left(\frac{1}{7} \cdot 2 \cdot \pi \cdot x_{pos}\right)$ where x_{pos}. From 386 to 480 seconds, the road profile is zero and the vehicle is performing the slalom maneuvers at different speeds from 50 to 100 km/h.

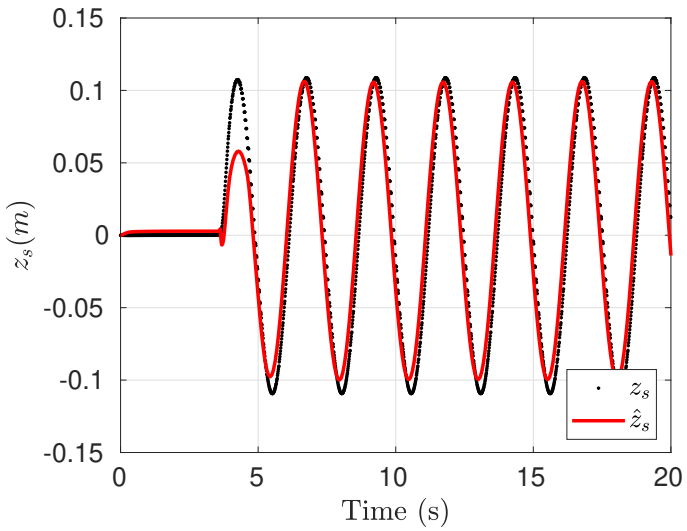

Figure 7.5 – $\hat{z}_{sij}$ response compared against z_{sij} for the mission at 10 km/h speed with a standard deviation of 1.5 cm

Table 7.2 – Error analysis: Withing the first five tests the road is described by $z_r = 0.1 \cdot \sin\left(\frac{1}{7} \cdot 2 \cdot \pi \cdot x_{pos}\right)$. The others $z_r = 0$

v_x km/h	$\mu_{\tilde{z}_s}$ / $\sigma_{\tilde{z}_s}$ m	$\mu_{\dot{\tilde{z}}_s}$ / $\sigma_{\dot{\tilde{z}}_s}$ m/s	$\mu_{\tilde{z}_{us}}$ / $\sigma_{\tilde{z}_{us}}$ m	$\mu_{\dot{\tilde{z}}_{us}}$ / $\sigma_{\dot{\tilde{z}}_{us}}$ m/s	$\mu_{\tilde{z}_r}$ / $\sigma_{\tilde{z}_r}$ m	$\mu_{\dot{\tilde{z}}_r}$ / $\sigma_{\dot{\tilde{z}}_r}$ m/s
10	0.0024 / 0.0153	0.0002 / 0.1666	0.0023 / 0.0169	0.0002 / 0.1666	0.0023 / 0.0178	0.0004 / 0.2098
15	0.0033 / 0.0084	0.0004 / 0.1808	0.0017 / 0.0093	0.0004 / 0.1808	0.0024 / 0.0122	0.0013 / 0.2935
20	0.0050 / 0.0069	0.0014 / 0.1813	0.0000 / 0.0054	0.0014 / 0.1813	0.0025 / 0.0091	0.0025 / 0.3782
25	0.0054 / 0.0088	0.0025 / 0.1629	-0.0028 / 0.0059	0.0025 / 0.1629	0.0024 / 0.0091	-0.0016 / 0.4593
30	-0.0026 / 0.0100	0.0005 / 0.1295	-0.0021 / 0.0075	0.0005 / 0.1295	0.0014 / 0.0112	-0.0213 / 0.5282
50	0.0040 / 0.0035	-0.0007 / 0.0244	0.0008 / 0.0034	-0.0007 / 0.0244	0.0028 / 0.0022	-0.0003 / 0.0408
60	0.0037 / 0.0049	-0.0003 / 0.0428	-0.0008 / 0.0049	-0.0003 / 0.0428	0.0027 / 0.0028	-0.0033 / 0.0514
65	0.0035 / 0.0059	0.0003 / 0.0565	-0.0016 / 0.0061	0.0003 / 0.0565	0.0027 / 0.0032	-0.0037 / 0.0578
70	0.0020 / 0.0070	-0.0000 / 0.0821	-0.0031 / 0.0070	-0.0000 / 0.0821	0.0025 / 0.0035	-0.0073 / 0.0617
75	0.0017 / 0.0070	0.0007 / 0.0842	-0.0033 / 0.0069	0.0007 / 0.0842	0.0025 / 0.0034	-0.0082 / 0.0613
80	0.0008 / 0.0069	0.0003 / 0.0877	-0.0039 / 0.0065	0.0003 / 0.0877	0.0022 / 0.0033	-0.0114 / 0.0589
85	0.0005 / 0.0067	0.0000 / 0.0898	-0.0043 / 0.0062	0.0000 / 0.0898	0.0021 / 0.0032	-0.0125 / 0.0562
90	0.0003 / 0.0065	-0.0005 / 0.0915	-0.0044 / 0.0059	-0.0005 / 0.0915	0.0020 / 0.0031	-0.0127 / 0.0542
95	0.0004 / 0.0064	0.0002 / 0.0931	-0.0044 / 0.0059	0.0002 / 0.0931	0.0020 / 0.0030	-0.0116 / 0.0527
100	0.0002 / 0.0064	0.0008 / 0.0963	-0.0046 / 0.0058	0.0008 / 0.0963	0.0017 / 0.0029	-0.0124 / 0.0520

7.3 Active suspension control

The driver comfort, J_D, and road holding, J_R, performances criteria are defined as

$$J_D = \int_0^{12} \frac{z_s}{z_r(\omega j)} d\omega; \quad J_R = \int_{10}^{20} \frac{\ddot{z}_s}{z_r(\omega j)} d\omega \tag{7.17}$$

As mentioned before, both criteria can not be optimized at the same time, and, according to [Savaresi et al., 2010b] and [Sename et al., 2013], the maximum effect of the road profile on driver's comfort and road holding are in the closed frequency domains from [0 Hz, 12 Hz] and [10 Hz, 20 Hz], respectively. The latter means that even though J_D and J_R have a trade-off relationship, they could be optimized both at different frequencies and, this way, obtained the best possible performance from our closed-loop system.

Another aspect in this work to take into account is the fact that state variables $\mathbf{z}$ defined in equation (7.4), and the road profile, $\hat{z}_r$, are not directly available for its use in the control design, however, estimation of these variables is developed in the last section and now are available and ready to be implemented into the controller. The motivation behind using robust controllers is to deal with non-modeled or non-measured disturbances as z_r, but besides, we want to avoid the uncertainty introduced by these variables. In this section, an MPC and linear quadratic regulator (LQR) designs are proposed and compared to be implemented on the system (7.4), since this type of scheme is used several domains of technology, see [Garcia et al., 1989, Qin and Badgwell, 2003, Bemporad and Morari, 1999].

7.3.1 Model predictive control

Model predictive control is an advanced control methodology that can optimize closed-loop performance subject to operating constraints on input and output variables. Lately, MPC has gathered plenty of attention from researchers because the controllers can handle multi-variate control problems as if it was a single variable problem; it also addresses actuator limitations, leading to optimal operation.

Let us consider the following discrete, linear time-invariant system:

$$\begin{aligned} \mathbf{x}(t+1) =& \mathbf{A}\mathbf{x}(t) + \mathbf{B}\mathbf{u}(t) \\ \mathbf{y}(t) =& \mathbf{C}\mathbf{x}(t) + \mathbf{D}\mathbf{u}(t) \end{aligned} \tag{7.18}$$

with $\mathbf{A} \in \mathbb{R}^{n\times n}$, $\mathbf{B} \in \mathbb{R}^{n\times p}$, $\mathbf{C} \in \mathbb{R}^{q\times n}$ and $\mathbf{D} \in \mathbb{R}^{q\times p}$ constant matrices, and pair of matrices $(\mathbf{A}, \mathbf{B})$ are stabilizable.

Also lets consider a cost function

$$J(\mathbf{x}, \mathbf{u}) = \sum_{j=0}^{N-1} J_t(\mathbf{x}_j, \mathbf{u}_j) + J_N(\mathbf{x}_N, \mathbf{u}_N) \tag{7.19}$$

where

$$J_t(\mathbf{x}_j, \mathbf{u}_j) = \frac{1}{2} \mid\mid \mathbf{x}_j \mid\mid_Q^2 + \frac{1}{2} \mid\mid \mathbf{u}_j \mid\mid_R^2; \quad \forall j \in \{0, 1, ..., N-1\}$$

is the quadratic cost, with weight matrices $\mathbf{Q} \in \mathbb{R}^{n\times n} > 0$ and $\mathbf{R} \in \mathbb{R}^{p\times p} > 0$; and a terminal cost defined by

$$J_N(\mathbf{x}_N, \mathbf{u}_N) = \frac{1}{2} \mid\mid \mathbf{x}_N \mid\mid_P^2$$

where P is the weight on terminal state.

Rewriting the cost junction (7.19) in matricial form, gives:

$$J(\mathbf{x}, \mathbf{u}) = \frac{1}{2}\mathbf{X}^T\hat{\mathbf{Q}}\mathbf{X} + \frac{1}{2}\mathbf{U}^T\hat{\mathbf{R}}\mathbf{U} \tag{7.20}$$

where

$$\mathbf{X} = \begin{bmatrix} \mathbf{x}(t) \\ \mathbf{x}(t+1) \\ \dots \\ \mathbf{x}(t+N-1) \\ \mathbf{x}(t+N) \end{bmatrix}; \quad \hat{\mathbf{Q}} = \begin{bmatrix} \mathbf{Q} & \mathbf{0} & \dots & \mathbf{0} & \mathbf{0} \\ \mathbf{0} & \mathbf{Q} & \dots & \mathbf{0} & \mathbf{0} \\ \vdots & & \ddots & & \vdots \\ \mathbf{0} & \mathbf{0} & \dots & \mathbf{Q} & \mathbf{0} \\ \mathbf{0} & \mathbf{0} & \dots & \mathbf{0} & \mathbf{P} \end{bmatrix}$$

$$\mathbf{U} = \begin{bmatrix} \mathbf{u}(t) \\ \mathbf{u}(t+1) \\ \dots \\ \mathbf{u}(t+N-2) \\ \mathbf{u}(t+N-1) \end{bmatrix}; \quad \hat{\mathbf{R}} = \begin{bmatrix} \mathbf{R} & \mathbf{0} & \dots & \mathbf{0} \\ \mathbf{0} & \mathbf{R} & \dots & \mathbf{0} \\ \vdots & & \ddots & \vdots \\ \mathbf{0} & \mathbf{0} & \dots & \mathbf{R} \end{bmatrix}$$

Developing (7.20), gives

$$\begin{aligned} J(\mathbf{x},\mathbf{u}) =& \frac{1}{2}\left[\mathbf{A}_N\mathbf{X}_0 + \mathbf{B}_N\mathbf{U}\right]^T \hat{\mathbf{Q}}\left[\mathbf{A}_N\mathbf{X}_0 + \mathbf{B}_N\mathbf{U}\right] + \frac{1}{2}\mathbf{U}^T\hat{\mathbf{R}}\mathbf{U} \\ =& \frac{1}{2}\mathbf{U}\left(\mathbf{B}_N^T\hat{\mathbf{Q}}\mathbf{B}_N + \hat{\mathbf{R}}\right)\mathbf{U} + \left(\mathbf{X}_0^T\mathbf{A}_N^T\hat{\mathbf{Q}}\mathbf{B}_N\right)^T\mathbf{U} + \frac{1}{2}\mathbf{X}_0^T\mathbf{A}_N^T\hat{\mathbf{Q}}\mathbf{A}\mathbf{X}_0 \end{aligned}$$

Model predictive control finds a controller $\mathbf{u}$ such that the cost function (7.20) is minimized. Particularly, if the system has some constraints or even the actuator is saturated, it requires an iterative optimization method, such as the inner-point method, to solve the quadratic programming problem. If the system has no constraints, the analytical solution could be applied, therefore,

$$\nabla_{\mathbf{U}} J(\mathbf{x},\mathbf{u}) = \left(\mathbf{B}_N^T\hat{\mathbf{Q}}\mathbf{B}_N + \hat{\mathbf{R}}\right)\mathbf{U} + \left(\mathbf{X}_0^T\mathbf{A}_N^T\hat{\mathbf{Q}}\mathbf{B}_N\right)^T \tag{7.21}$$

and finally:

$$\mathbf{U} = -\left(\mathbf{B}_N^T\hat{\mathbf{Q}}\mathbf{B}_N + \hat{\mathbf{R}}\right)^{-1}\left(\mathbf{X}_0^T\mathbf{A}_N^T\hat{\mathbf{Q}}\mathbf{B}_N\right)^T \tag{7.22}$$

7.3.2 Linear quadratic regulator

A set of linear differential equations describes the system dynamics, and the cost is characterized by a quadratic function called the linear quadratic (LQ) problem. One of the main results, in theory, is that the solution is provided by the linear–quadratic regulator, a feedback controller whose equations are given below. The LQR is an integral part of the LQG (linear–quadratic–Gaussian) problem. Like the LQR problem itself, the LQG problem is one of the most basic controls theory problems.

7.3.2.1 Finite-Horizon, discrete-time LQR

Let us consider the following discrete, linear time-invariant system:

$$\begin{aligned}\mathbf{x}(t+1) =& \mathbf{A}\mathbf{x}(t) + \mathbf{B}\mathbf{u}(t)\\ \mathbf{y}(t) =& \mathbf{C}\mathbf{x}(t) + \mathbf{D}\mathbf{u}(t)\end{aligned} \tag{7.23}$$

with $\mathbf{A} \in \mathbb{R}^{n\times n}$, $\mathbf{B} \in \mathbb{R}^{n\times p}$, $\mathbf{C} \in \mathbb{R}^{q\times n}$ and $\mathbf{D} \in \mathbb{R}^{q\times p}$ constant matrices, and pair of matrices $(\mathbf{A}, \mathbf{B})$ are stabilizable, and consider the cost function (7.20), thus:

$$J(\mathbf{x}, \mathbf{u}) = \frac{1}{2}\mathbf{X}^T\hat{\mathbf{Q}}\mathbf{X} + \frac{1}{2}\mathbf{U}^T\hat{\mathbf{R}}\mathbf{U}$$

the optimal control minimizing the performance index is given by:

$$\mathbf{u}(t) = -\mathbf{K}(t)x(t)$$

where

$$\mathbf{K}(t) = \left(\hat{\mathbf{R}} + \mathbf{B}^T\mathbf{P}(t+1)\mathbf{B}\right)^{-1}\left(\mathbf{B}^T\mathbf{P}(t+1)\mathbf{A}\right)$$

and $\mathbf{P}(t)$ is found iteratively in time by solving the dynamic Riccati equation

$$\mathbf{P}(t-1) = \mathbf{A}^T\mathbf{P}(t)\mathbf{A} - \left(\mathbf{A}^T\mathbf{P}(t)\mathbf{B}\right)\left(\left(\hat{\mathbf{R}} + \mathbf{B}^T\mathbf{P}(t+1)\mathbf{B}\right)^{-1}\left(\mathbf{B}^T\mathbf{P}(t+1)\mathbf{A}\right)\right) + \mathbf{Q}$$

7.3.3 MPC with known disturbances

Let us consider the following discrete, linear time-invariant system:

$$\begin{aligned}\mathbf{z}(t+1) =& \mathbf{A}\mathbf{z}(t) + \mathbf{B}\mathbf{u}(t) + \mathbf{D}\mathbf{z}_r(t)\\ \mathbf{y}(t) =& \mathbf{C}\mathbf{z}(t)\end{aligned} \tag{7.24}$$

with $\mathbf{A} \in \mathbb{R}^{4\times 4}$, $\mathbf{B} \in \mathbb{R}^{4\times 1}$, $\mathbf{C} \in \mathbb{R}^{2\times n}$ and $\mathbf{D} \in \mathbb{R}^{4\times 1}$ constant matrices, and pair of matrices $(\mathbf{A}, \mathbf{B})$ are stabilizable, and consider the cost function (7.20), thus:

$$J(\mathbf{z}, \mathbf{u}) = \frac{1}{2}\mathbf{Z}^T\hat{\mathbf{Q}}\mathbf{Z} + \frac{1}{2}\mathbf{U}^T\hat{\mathbf{R}}\mathbf{U}$$

following the same procedure as in the MPC section we have:

$$\mathbf{U} = -\left(\mathbf{B}_N^T\hat{\mathbf{Q}}\mathbf{B}_N + \hat{\mathbf{R}}\right)^{-1}\left(\mathbf{Z}_0^T\mathbf{A}_N^T\hat{\mathbf{Q}}\mathbf{B}_N + \mathbf{Z}_r^T\mathbf{D}_N^T\hat{\mathbf{Q}}\mathbf{B}_N\right)^T \tag{7.25}$$

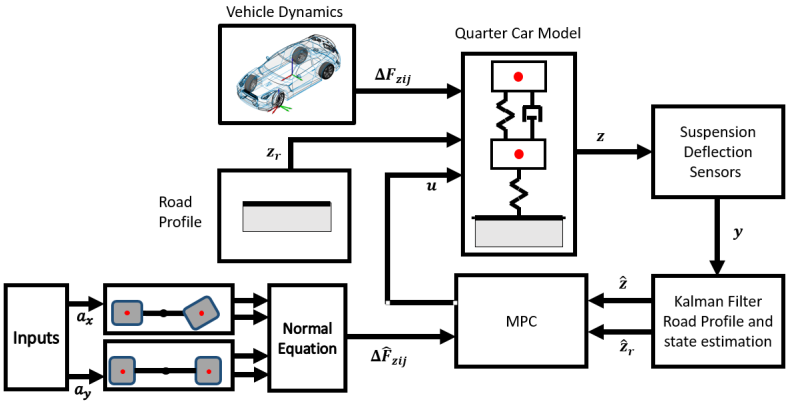

Figure 7.6 – Closed loop quarter car system with load transfer and road profile disturbance and MPC with observation scheme for the load transfer and road profile.

7.3.4 Simulation results

It should be mentioned that a difference arises when the controllers for a front or a rear-wheel are compared; however, the design procedure and control structure is the same in both cases. The difference lies in the assumptions made. The suspension system at the front tire presented in this work has no means to estimate the road profile ahead since the sensors used to design the observer scheme cannot predict the future. The method to estimate the road profile is based on system dynamics, and the excitation exerted from the road to the quarter-car model. There are other approaches with which it is possible to estimate the road beforehand; these approaches use vision systems to predict the road profile before the system be exited by it. We do not implement the later in our proposal; thus, to solve this dilemma (road profile prediction), the controller for a front-wheel will assume low-frequency disturbances $\bar{\mathbf{z}}_r$, such that the following assumption is considered truth

$$\bar{\mathbf{z}}_{rk} = \begin{bmatrix} z_{rk} & z_{rk} & \cdots & z_{rk} \end{bmatrix}^T \in \mathbb{R}^n$$

For the rear wheels suspension systems, the control law remains as presented in the MPC or the LQR subsections, and the receding horizon should be selected depending on vehicle velocity and defined as

$$n = \frac{L}{T_s v_x}$$

with T_s as the sampling period, and v_x represents the longitudinal velocity. A block diagram of the control scheme is presented in Figure 7.6

We aim to improve vehicle comfort; in the literature, it could be found the

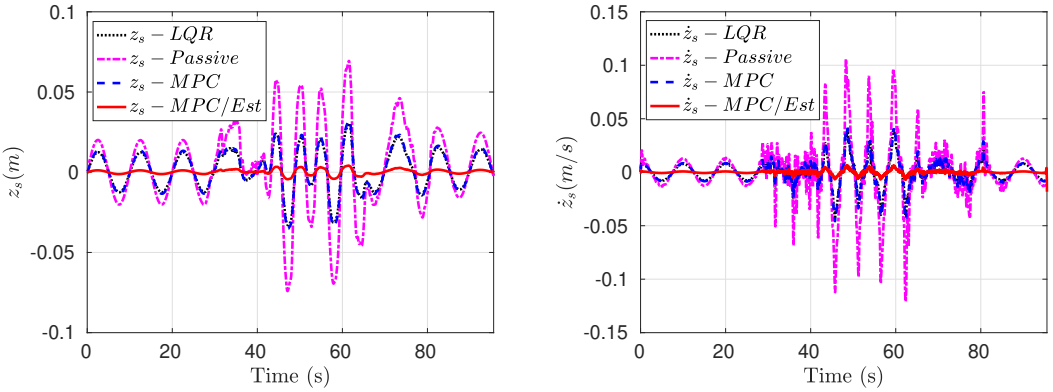

(a) z_s response with four closed loop systems to compare passive, LQR and MPC.

(b) $\dot{z}_s$ response with four closed loop systems to compare passive, LQR and MPC.

Figure 7.7 – Vehicles for different purposes: Competition and daily life

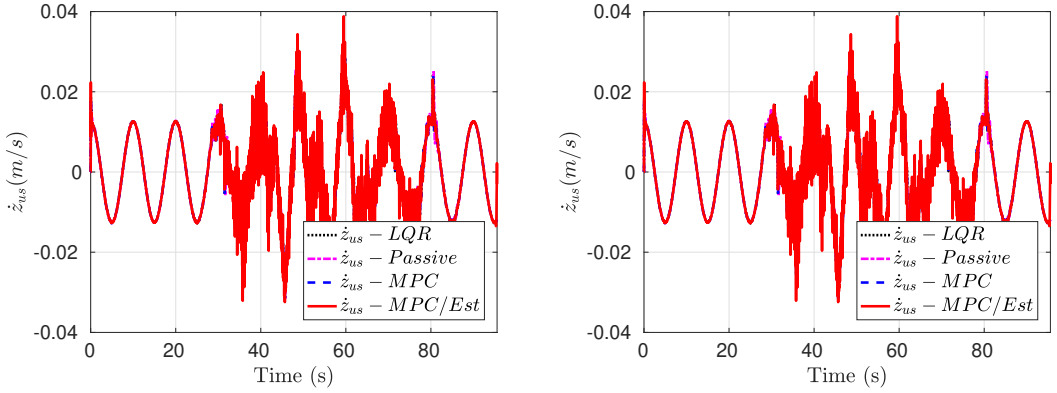

(a) z_{us} response with four closed loop systems to compare passive, LQR and MPC.

(b) $\dot{z}_{us}$ response with four closed loop systems to compare passive, LQR and MPC..

Figure 7.8 – Vehicles for different purposes: Competition and daily life

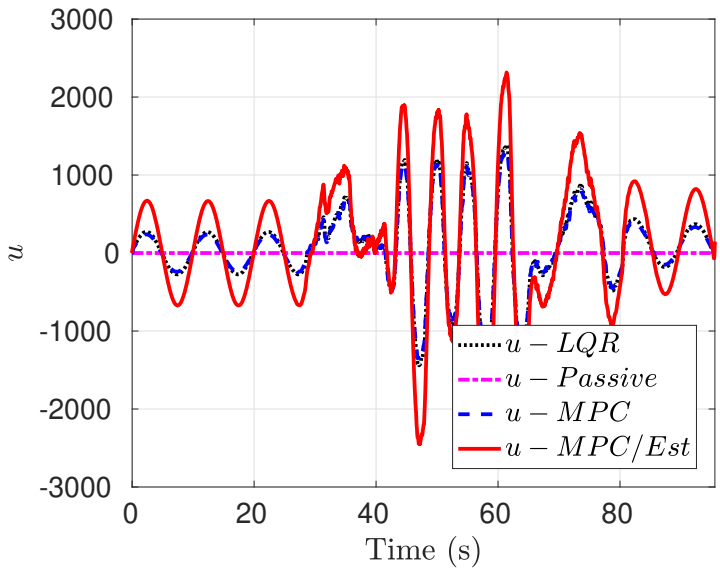

Figure 7.9 – Control input comparison between the four closed loop systems

comfort criteria J_R; thus, the controllers applied are trying to minimize the comfort cost function by reducing the controllable state z_s. This section compares an LQR controller, MPC with and without knowledge of the disturbance, and a passive suspension system with no actuators.

Therefore, on the one hand in Figure 7.7(a), the chassis displacement is depicted, on black-solid line, the closed-loop system with an LQR controller is presented, in pink-dashed line, the passive system response is portrayed, in blue-dotted-dashed line, the closed-loop system with an MPC design without prior knowledge on disturbances. Finally, in red -dotted line, the closed-loop implementation using MPC is displayed. Observe that in Figures 7.7(a) and 7.7(b), the improvement of closed-loop performance with the proposed controller is easily noticeable, also while the transfer load affects the system from seconds 25 to 80, the performance is greatly improved compared with all other formulations.

On the other hand, in Figure 7.8(a) and 7.8(b), the unsprung mass displacement and its derivate responses are presented; observe here a similar behavior between the four controllers; this could be predicted in advance since the controllers are configured to optimize the road comfort criterion, ignoring this way the road holding criterion. Here is shown that the road-holding performance would be at least as good as with a passive suspension system.

Finally, in Figure 7.9, the controller's response is portrayed; in the red-dotted line, the controller proposed uses more energy to overcome the road disturbances z_r, because they are included on the control design. The LQR controller and MPC designs react to the disruption and could not achieve a better response.

7.4 Conclusions and perspectives

A vehicle dynamics control methodology is presented to optimize the ride characteristics of automobiles equipped with active suspension. The method is based on the MPC algorithm designed, taking into account the road profile. The sensors used to perform such estimations are longitudinal, lateral accelerometers, and suspension deflection sensors available in most recent vehicle models. The proposal is validated through emulating real experimental data into simulations with a comparison between different control schemes. Future work will address the prediction of the load transfer by including the gas and steering vehicle inputs and the actuator dynamic model's inclusion. The main goal of this research is the real-time implementation of an experimental testbed.

Conclusions and Perspectives

Conclusions

This thesis presents a series of strategies to estimate vehicle dynamics. The goal of this work is to develop an observation strategy that can be applied to mass-produced vehicles. The idea of having an algorithm in a mass-produced car comes up with a large number of challenges; the ones that we consider in this work are robustness and cost.

We have proposed models and observer strategies that can cope with high and low excitation levels to tackle robustness. We have validated the algorithm robustness with many tests, from small tracks at low speed to ISO double lane-change maneuvers. Our algorithms have been re-worked several times to achieve a degree of accuracy that can be useful for integrating into ADAS.

We have also proposed observer strategies that allow this degree of robustness while maintaining a low-cost sensor grid. The future work will have to address eliminating the use of deflection sensors and still maintaining a closed-loop observer strategy to compute the vehicle's mass and the COG—the integration of environmental sensing devices as the camera to improve state variables and parameters estimation.

Chapter 3 deals with the estimation of the lateral and longitudinal speed; these variables are essential for good feedback for stabilization and cruise speed controllers. Our proposal uses as base a kinematic model to avoid using parameters related to mass into our model; this is possible since our sensor grid includes accelerometers and gyroscopes. One of the main contributions in this section is compensating the gravity; a quaternion differential equation defines our system's attitude. More than 100 tests validate the algorithm's robustness, and we obtain consistent results in all of them.

Chapter 4 tackles the estimation of the normal tire-ground force estimation. This variable is, in our opinion, the most difficult one to estimate since the sensor grid of mass-produced vehicles does not contain many sensors that measure vertical

dynamics. In this section, we have to scope our solution to mass-produced vehicles with improved suspension systems, including deflection sensors. With those sensors in place, we can estimate the mass, the mass distribution, and the center of gravity and forward the normal tire-ground force estimation.

Chapter 5 and 6 presents our estimation strategies for the longitudinal and lateral tire-ground forces. The first method uses the known single-track and hoverboard models and Kalman filters to estimate the TGFs, and further models are introduced to split such forces to the adequate tire. This method has to deal with tire saturation, to separate the virtual TGFs properly. The second method uses the Newton laws of motion; here, we compute the local accelerations using a rigid body's acceleration and rotations. Considering that we already know the normal TGFs at each tire, we can calculate the lateral and longitudinal TGFs with great accuracy. The latter method is more accurate and robust than the first method, and further research should be directed towards improving the mass estimation using gravity.

Chapter 7 shows a small result that uses the estimated state to improve on first hand the road profile estimation and later the comfort and road holding of an automobile with active suspension.

Experimental Vehicle Infraestructure

Figure A.1 – Experimental testbed: Dyna

Our experimental vehicle known as DYNA is instrumented by the laboratory HEUDIASYC UMR 7253 CNRS at Compiègne, France, see Figure A.1. The baseline vehicle is a Peugeot 308sw, this car is additionally instrumented with transducers to measure vehicle dynamic states and perform tests.

A.1 Embedded sensors

The sensor used in our vehicle are classified as validation sensors, input sensors, and exteroceptive sensors.

A.1.1 Validation sensors

- CORREVIT S-400: Its a non-contact optical sensor that measures the transversal dynamics at large operating ranges. The sensor is installed at the place of the spare wheel under the car it returns the measurement of transversal speed, $v_g = \sqrt{v_x^2 + v_y^2}$, and sideslip angle, β (see Figure A.2(a)).

(a) Correvit Sensor (b) Kysler Sensor

Figure A.2 – Validation sensors

- Kistler RoaDyn S625 wheel force transducers: four wheel force sensors for passenger cars RoaDyn (Kistler) are fixed at each wheel, see Figure A.2(b). They measure all the forces and wheel torques for the three three axes (x, y, z), it also offers an accurate measurement of the rotation angle. The cost a single Kysler sensor is around 120, 000 €.
- GPS receiver operating in RTK mode locates the vehicle with a centimeters accuracy.

A.1.2 Sensors used as input in our algorithms

- CROSSBOW VG700AB: An inertial measurement unit designed specifically for automotive test applications. It combines MEMSIC's high performance fiber optic gyros with silicon micro-machined (MEMS) accelerometer technology, in order to provide a highly accurate Vertical Gyro (VG) and Inertial Measurement Unit.
- CORRSYS-DATRON HT500: This transducer is an optical device who measures the distance between chassis and ground. They are installed respectively at each vehicle corner, see Figure A.3(a).
- Sensor WAYCON SX50: These sensors are installed at the suspension, see Figure A.3(b), these sensors are able to measure the deflection of the suspension, emulating the distance between the sprung and unsprung mass.
- Available data on CAN bus: wheel rotation velocity, engine speed, yaw rate, brake pressure, lateral acceleration from the ESP, steering wheel angle.

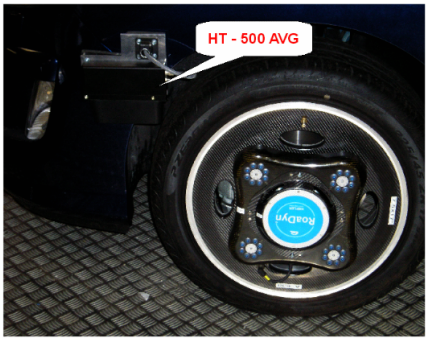

(a) Laser Sensor

(b) Deflection Sensor

(c) Front laser

(d) Computer

Figure A.3 – Validation sensors

A.1.3 Exteroceptive sensors

- A scenario record camera is used to register the vehicle trajectory.
- Mobileye system: it is able to provide a list of detected obstacles (pedestrians, vehicles, ...) and the position of the vehicle relative to the ground side markings on the vehicle CAN bus in real-time.
- Ibeo Standard (8L) Eight Layer/Multi-Echo LUX Sensor (Ibeo LUX 8L): the sensor is installed at front bumper to track the object on top 4 layers and raw data ground scanning/profiling (see Figure A.3(c)).
- All the electronics systems and PC are located in the trunk ,see Figure A.3(d).

The variables obtained from our experimental testbed are displayed in Table A.1.

Table A.1 – Variables available at Dyna

T	Timestamps (s)	PC
H_{ij}	Distance berween chassis and the ground at each corner (m)	HT500
β_m	Sideslip angle (deg)	S-400
V_m	Vehicle speed (m/s)	S-400
$F_{x,i,j}$	Longitudinal TGFs (N)	S625
$F_{y,i,j}$	Lateral TGFs (N)	S625
$F_{z,i,j}$	Normal TGFs (N)	S625
$M_{x,i,j}$	Longitudinal Moments (N m)	S625
$M_{y,i,j}$	Lateral Moments (N m)	S625
$M_{z,i,j}$	Vertical Moments (N m)	S625
θ_{ij}	Wheel angles (deg)	S625
ω_{ij}	Wheel angular velocity	S625
a_x	Longitudinal acceleration (g)	VG700AB
a_y	Lateral acceleration (g)	VG700AB
a_z	Vertical acceleration (g)	VG700AB
$\dot{\phi}$	Roll rate (deg/s)	VG700AB
$\dot{\theta}$	Pitch rate (deg/s)	VG700AB
$\dot{\psi}$	Yaw rate (deg/s)	VG700AB
ϕ	Roll angle (deg)	VG700AB
$\dot{\psi}_c$	Yaw rate (deg/s)	CAN bus
a_{y_c}	Lateral acceleration (m/s^2)	CAN bus
P_b	Brake pressure (bar)	CAN bus
V_s	Vehicle speed (km/h)	CAN bus
S	Traveled distance (m)	CAN bus
a_{x_c}	Longitudinal acceleration (m/s^2)	CAN bus
δ	Steering wheel angle (deg)	CAN bus
$\dot{\delta}$	Rotation rate of the steering wheel (deg/s)	CAN bus
$\dot{\delta_{opt}}$	Optimized rotation rate of the steering wheel (deg/s)	CAN bus
ω_F	Mean speed of the front wheels	CAN bus
ω_{RL}	speed of the rear left wheel	CAN bus
ω_{RR}	speed of the rear right wheel	CAN bus
λ	Longitude (rad)	GPS
γ	Latitude (rad)	GPS

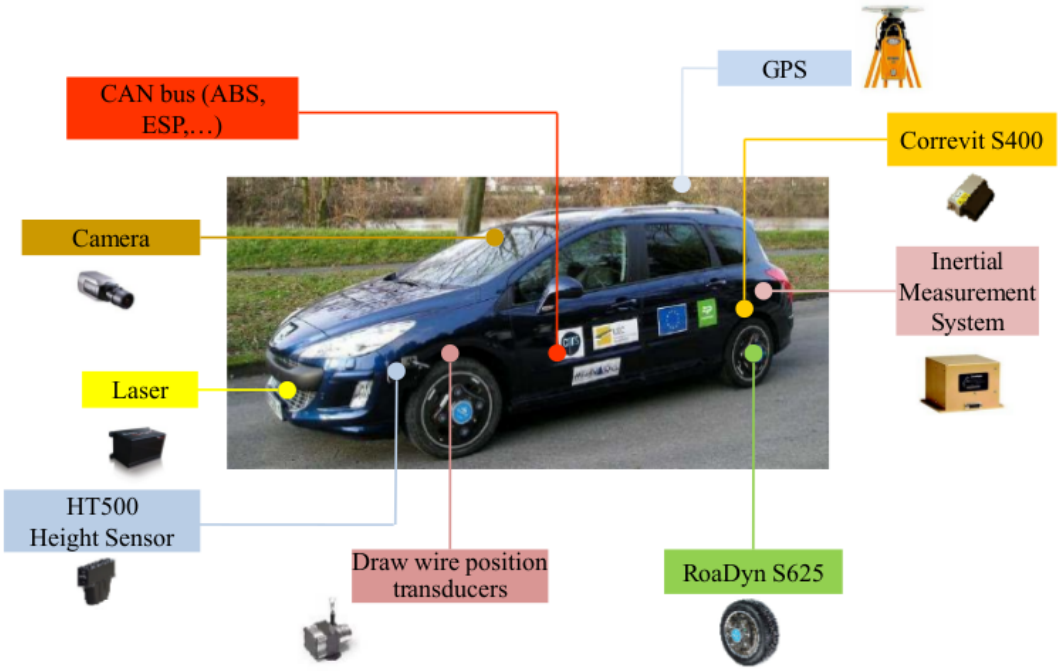

Figure A.4 – Dyna Onboard Sensors

A.2 Software modules

A.2.1 Architecture of the acquisition system

We have developed an system capable of acquiring 16, 32 or 48 analog channels using a 24-bit converter. It consists of a computer UEI powered by a 200 MHz PowerPC processor running a real-time operating system Xenomai. The UEILogger is a powerful standalone data logger based on the UEI PowerDNA Ethernet DAQ Cube. The Cube is based on the framework of Xenomai with 48 acquisition inputs. The Xenomai is a real-time development framework cooperating with the Linux kernel. It is used to provide a pervasive, interface-diagnostic, real-time support to user-space applications. Some tasks are executed in the framework of Xenomai:

- Task of acquiring the highest priority, periodic frequency and frequency acquisition.
- Task of digital filters function that can be applied to all channels. The software provides data acquisition by using the analog cards AI-217. The DNA-AI-217 Analog Input Board is compatible with cube chassis. The DNA version is a kind of analog input module for using with the PowerDNA Cube.

A.2.2 Communication Protocol

Cube runs with the software that can constitute a system of acquisition network incorporating digital filters with different cutoff frequencies. Cube returns as UDP frame according to the request from PC. The packet is sent back on a low frequency. In our embedded data acquisition system, the acquisition frequency is 4kHz, however the data packet is sent back with 200Hz.

A.2.3 Digital filter

In order to deal with the signals, a 5^{th} order Chebyshev filter applied has a cutoff frequency of 35Hz, no aliasing and loss of information allows it up to 20Hz.

A.2.4 Implementation

The stability of acquisition system is guaranteed with Xenomai, the sub-kernel real-time Linux framework. The tasks are distributed as follows:

- An acquisition task maximum up to 4kHz.
- A filtering task using a 5^{th} order Chebyshev filter.
- A surveillance task for each request to be served. A FIR filter is employed for a specified sample channel. This process will cost more computation power, hence, its used it has to be commanded.
- A duty that awaits for client requests. Otherwise, the vehicle CAN bus is available in the acquisition system of the host PC. The GPS and camera are directly connected to the computer. All the devices are located in the trunk of the car with the electric circuit system as shown in Figure A.3(d). The monitoring equipment is located on the back left seat. The operator can manipulate the configuration of the system with a monitor and keyboard.

A.2.5 Software architecture

A.2.6 Rapid prototyping environment: the framework PAPCUS

Heudiasyc laboratory has developed a rapid prototyping environment for designing software modules and testing them in real time with the vehicle architecture. The framework PACPUS is available as an open source with free license CeCILL-C. The framework PACPUS was developed following the principle of component-oriented design to provide users more versatility in their developments. The rapid

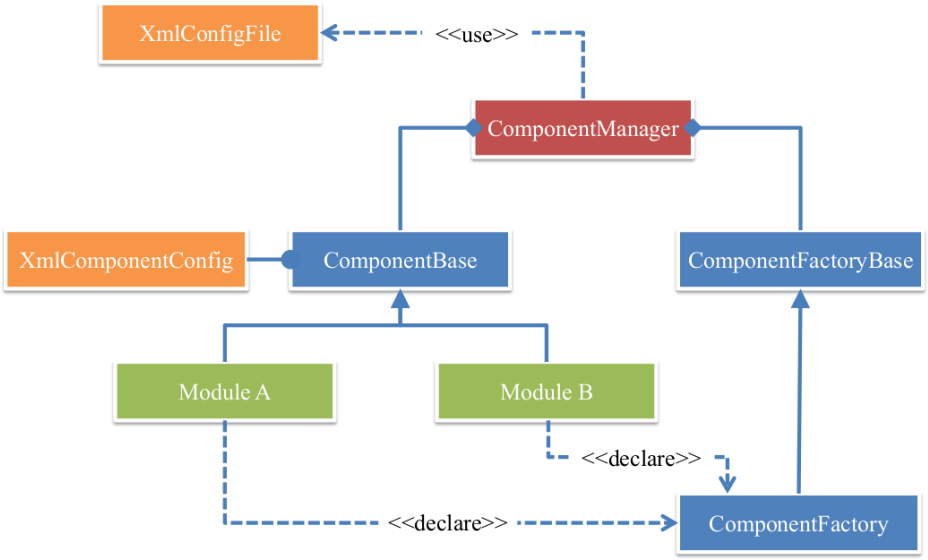

Figure A.5 – Pacpus Framework

prototyping environment PACPUS is developed in C++ with multiple operating systems (Windows, Linux, Mac) in order to:

- keep a close compatibility with C and thus facilitate the development of lower layers (drivers, sensor interfaces, system calls, ...).
- able to use the mechanisms of object-oriented programming, meet the requirement for modularity.
- obtain a code compiled with higher execution speeds which are much closer to real-time constraint.

The framework PACPUS employs the Qt API for graphical interfaces and can be integrated with other development environment for multi-sensor fusion. The class diagram in Figure A.5 presents the typical architecture of an application using the framework PACPUS.

This car is equipped with an industrial PC in the trunk. Particular software is developed for the acquisition system in C/C++. In the data structure, the data read by the acquisition task is stored in a circular buffer. The buffer is large enough to prevent the risk of exceeding. The cube sends the packet by Ethernet to the PC. The signal sequence after the filter FIR is 100Hz. On the PC, the application "CubeClient" is created to maintain communication between the cube and the PC. After this, the data is sent to the application which includes the user application written in C++. The schema shown in Figure A.6 illustrate the just mentioned. Other components which are designed for the management of different equipments

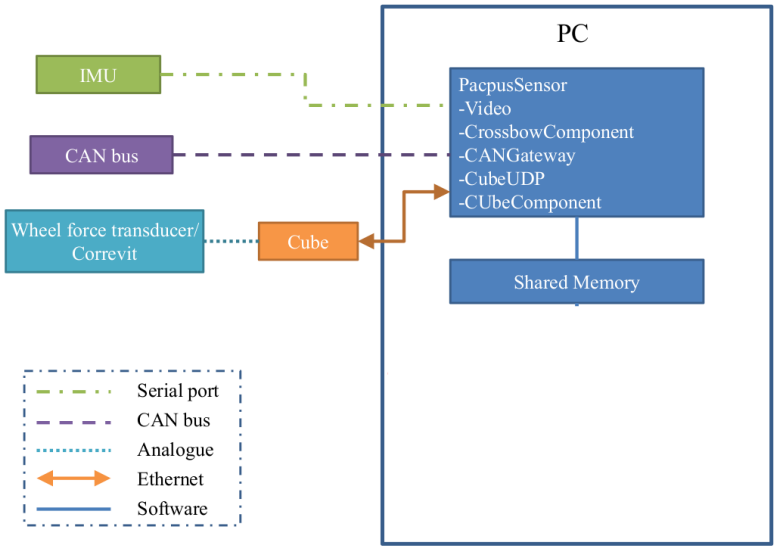

Figure A.6

were constructed as well. In the system of the estimation process, the observer is developed in .DLL library form as a real-time application operating at 200Hz.

ISO Double lane change

Originally known as the "moose test" the lane change maneuver was transferred to the International Standard ISO 3888-2 after a revision by the Association of the German Automotive Industry (VDA). The ISO and VDA lane-change test is used to evaluate the handling performance of a vehicle and is an integral part of the vehicle design procedures and vehicle assessment. Based on 3 cone lanes with a total length of 61 meters a double lane change is defined, which must be completed with maximum speed.

The ISO double lane change test consists of an entry and an exit lane and with a length of 12m and a side lane with a length of 11m. The width of the entry and side lane are dependent on the width of the vehicle, the width of the exit lane is constantly 3m wide. The lateral offset between entry and side lane is 1 m and the longitudinal offset is 13.5 m. For the same lateral offset the side and exit lane has a slightly shorter longitudinal displacement of 12.5m. 2m after the start of the entry lane the throttle is released so that the entire maneuver is completed in the overrun mode with the top gear and an engine speed of at least 2000 rev/min. At the end of the entry and exit lane the velocity is measured. The entry velocity is increased gradually. If no cones are overturned, the test is passed.

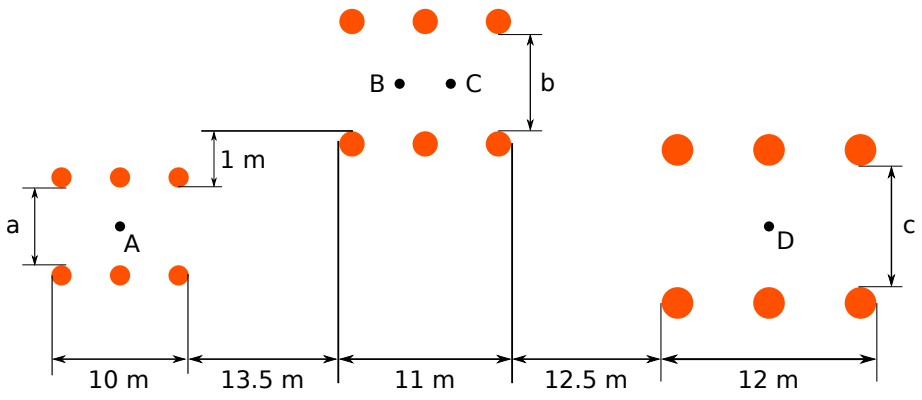

Figure B.1 – ISO double lane change

Quaternion Background

C.1 Quaternion operations and properties

Let $\mathbf{p}$,$\mathbf{q} \in \mathbb{H}$ be a couple of quaternions in a Hamiltonian space, then the following operations are defined as:

C.1.1 Hamilton product

$$\mathbf{p} \otimes \mathbf{q} = [p_0 * q_0 - \bar{\mathbf{p}}\bar{\mathbf{q}},\ p_0 * \bar{\mathbf{q}} + q_0 * \bar{\mathbf{p}} + \bar{\mathbf{p}} \times \bar{\mathbf{q}}]$$

where $*$ defines the scalar multiplication, and the operators $\cdot$ and $\times$ stands for the dot and cross products respectively.

C.1.2 Quaternion inner product

$$\mathbf{p} \cdot \mathbf{q} = p_0 * q_0 + \bar{\mathbf{p}} \cdot \bar{\mathbf{q}}$$

C.1.3 Conjugation Rule

$$\mathbf{q}^* = [q_0, -\bar{\mathbf{q}}]; \quad \tilde{\mathbf{q}} \in \mathbb{H}$$

such that satisfies the following

$$\mathbf{q} \otimes \mathbf{q}^* = [\mathbf{q} \cdot \mathbf{q}, \bar{\mathbf{0}}]$$

C.1.4 Quaternion inverse

The use of quaternions in this work is restricted to unitary quaternions, therefore $\mathbf{q} \cdot \mathbf{q} = 1$, thus, the inverse of a given quaternion obeying the unit length constrain is given by

$$\mathbf{q} \otimes \mathbf{q}^* = [1, \bar{\mathbf{0}}]$$

C.1.5 Unit Quaternion Rotation Matrix

A unit quaternion can be used to describe the attitude of a body. Let be $\bar{\mathbf{v}} \in \mathbb{R}^3$ a vector in fixed coordinate system and be $\bar{\mathbf{v}}' \in \mathbb{R}^3$ the same vector in a body coordinated frame. The following relations are satisfied

$$\begin{bmatrix} 0 \\ \bar{\mathbf{v}}' \end{bmatrix} = \quad \mathbf{q} \otimes \begin{bmatrix} 0 \\ \bar{\mathbf{v}} \end{bmatrix} \otimes \mathbf{q}^*$$

C.1.6 Quaternion time derivative

The time derivative of the unit quaternion is the vector of quaternion rates, $\dot{\mathbf{q}}$. This vector is related to the angular velocities $\dot{\bar{\omega}}$. Then,

$$\dot{\mathbf{q}} = \frac{1}{2}\mathbf{q} \otimes \begin{bmatrix} 0 \\ \bar{\omega} \end{bmatrix}$$

C.1.7 Quaternion axis angle representation

One of the most common and advantageous form to represent a quaternion is the axis-angle representation, defined as

$$\begin{aligned} q_0 &= \cos(\eta/2) \\ q_1 &= n_1 * \sin(\eta/2) \\ q_2 &= n_2 * \sin(\eta/2) \\ q_3 &= n_3 * \sin(\eta/2) \end{aligned}$$

where $\bar{\mathbf{n}} = (\cos\alpha \sin\beta, \sin\alpha \sin\beta, \cos\beta) = (n_1, n_2, n_3)$ and η is the rotation angle.

Least Squares

D.1 Least Squares

Least squares (LS) is the most applied and studied regression estimator. Its popularity is due to two facts: First, when invented (around 1800) there were no computers, and the LS estimator could be computed explicitly from data. Second, in the one-dimensional case the LS tends toward the arithmetical mean of the observations; after, when Gauss introduced the Gaussian distribution the LS found its optimal solution.

Lets consider the following system

$$\mathbf{AX} \approx \mathbf{B} \tag{D.1}$$

where $\mathbf{A} \in \mathbb{R}^{m \times n}$ is the measured input, $\mathbf{X} \in \mathbb{R}^{n \times d}$ are the unknown parameters and $\bar{\mathbf{B}} \in \mathbb{R}^{m \times d}$ is the measured output. Gauss also defined the LS cost function as:

$$\min_{X} \sum_{i=1}^{m} (\mathbf{B}_i - \mathbf{A}_i \mathbf{X})^2 \tag{D.2}$$

it follows that LS solution is optimal for a Gaussian distribution of the output ($\mathbf{B}$). Nevertheless, if the assumption Gaussian distribution does not hold, outliers could lead to poorly estimated parameters.

Outliers could appear in the measured input ($\mathbf{A}$) or in the measured output ($\mathbf{B}$). Figure D.1 shows the difference between an outlier in $\mathbf{A}$ or $\mathbf{B}$. Notice that the response is more prone to error if the outlier is found at the input. Figure D.2 displays the error response for a percentage of outliers within the measurement at the input or output. Notice that with poor sets of data, such that, 50 % of the measurement are considered outlilers, the outlier at the output is prone to produce the bigger error index, nonetheless, from 33 % to zero outliers, in nominal conditions, the outlier at the input impact more on the LS method response.

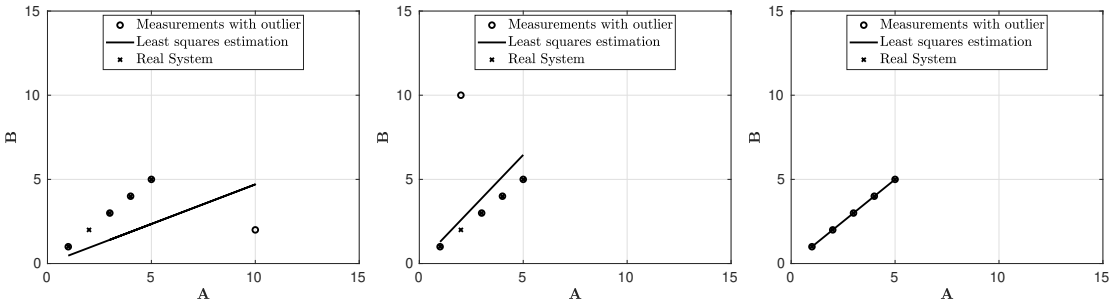

(a) Outlier in A (b) Outlier in B (c) Without Outlier

Figure D.1 – LS response to data with outliers in the input, in the output and without.

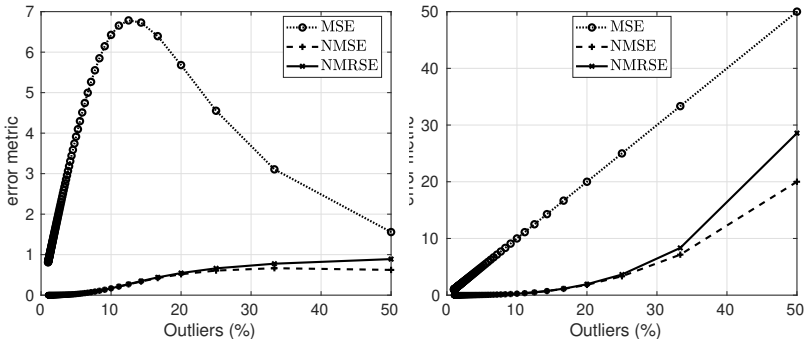

(a) Breaking point for outlier in the input (b) Breaking point for outlier in the output

Figure D.2 – LS response to a different percentage of outliers within the input and the output

The LS closed form solution for (D.1) is:

$$\mathbf{X} = \left(\mathbf{A}^T\mathbf{A}\right)^{-1}\mathbf{A}^T\mathbf{B}$$

Proof. From the LS cost function defined in eq. (D.2), then,

$$|| \mathbf{B} - \mathbf{AX} ||_2^2 = \mathbf{B}^T\mathbf{B} - \mathbf{B}^T\mathbf{AX} - \mathbf{X}^T\mathbf{A}^T\mathbf{B} + \mathbf{X}^T\mathbf{A}^T\mathbf{AX} \tag{D.3}$$

the derivative of the cost function respect to the parameters $(\mathbf{X})$ gives

$$\frac{d\left(|| \mathbf{B} - \mathbf{AX} ||_2^2\right)}{d\mathbf{X}} = -2\mathbf{A}^T\mathbf{B} + 2\mathbf{A}^T\mathbf{AX} \tag{D.4}$$

setting this derivate to zero, gives

$$\mathbf{X} = \left(\mathbf{A}^T\mathbf{A}\right)^{-1}\mathbf{A}^T\mathbf{B}$$

□

Particle Swarm Optimization

Particle swarm optimization (PSO) is a computational method that optimizes a problem by iteratively trying to improve a candidate solution with regard to a given measure of quality. It solves a problem by having a population of candidate solutions, here dubbed particles, and moving these particles around in the search-space according to simple mathematical formulae over the particle's position and velocity. Each particle's movement is influenced by its local best known position, but is also guided toward the best known positions in the search-space, which are updated as better positions are found by other particles. This is expected to move the swarm toward the best solutions.

PSO is a metaheuristic as it makes few or no assumptions about the problem being optimized and can search very large spaces of candidate solutions. However, metaheuristics such as PSO do not guarantee an optimal solution is ever found. Also, PSO does not use the gradient of the problem being optimized, which means PSO does not require that the optimization problem be differentiable as is required by classic optimization methods such as gradient descent and quasi-newton methods.

E.1 Algorithm

A basic variant of the PSO algorithm works by having a population (called a swarm) of candidate solutions (called particles). These particles are moved around in the search-space according to a few simple formulae. The movements of the particles are guided by their own best known position in the search-space as well as the entire swarm's best known position. When improved positions are being discovered these will then come to guide the movements of the swarm. The process is repeated and by doing so it is hoped, but not guaranteed, that a satisfactory solution will eventually be discovered.

Algorithm E.1: Particle swarm optimization

Initialization
for each particle
  Initialize the particle's position with a random vector: $\mathbf{x_i}$
  Initialize the particle's best known position: $\mathbf{p_i} \longleftarrow \mathbf{x_i}$
  if $f(\mathbf{p_i}) < f(\mathbf{g})$
    update the swarm's best known position:$\mathbf{g} \longleftarrow \mathbf{p_i}$
  Initialize the particle's velocity: $\mathbf{v_i}$
end
while a criterion is not met
  for each particle
    Pick randon numbers: $\mathbf{r_p}$, $\mathbf{r_g}$
    Update velocity: $\mathbf{v_i} \longleftarrow \mathbf{w v_i} + \boldsymbol{\phi}_\mathbf{p}\mathbf{r_p}(\mathbf{p_i} - \mathbf{x_i}) + \boldsymbol{\phi}_\mathbf{g}\mathbf{r_g}(\mathbf{g} - \mathbf{x_i})$
  Update particle's position: $\mathbf{x_i} \longleftarrow \mathbf{x_i} + \mathbf{v_i}$
  if $f(\mathbf{x_i}) < f(\mathbf{p_i})$
    Update particle best known position: $\mathbf{p_i} \longleftarrow \mathbf{x_i}$
    if $f(\mathbf{p_i}) < f(\mathbf{g})$
      Update the swarm's best known position: $\mathbf{g} \longleftarrow \mathbf{p_i}$

References

[ONI, 2018] (2018). La sécurité routière en france: Bilan de l'accidentalité de l'année 2018. techreport, Observatoire national interministériel de la sécurité routière, Paris, France. url: https://www.onisr.securite-routiere.interieur.gouv.fr/.

[Abe et al., 2001] Abe, M., Kano, Y., Suzuki, K., Shibahata, Y., and Furukawa, Y. (2001). Side-slip control to stabilize vehicle lateral motion by direct yaw moment. *JSAE Review*, 22(4):413 – 419, doi: http://dx.doi.org/https://doi.org/10.1016/S0389-4304(01)00124-2.

[Acosta et al., 2017] Acosta, M., Alatorre, A., Kanarachos, S., Victorino, A., and Charara, A. (2017). Estimation of tire forces, road grade, and road bank angle using tire model-less approaches and fuzzy logic. *IFAC-PapersOnLine*, 50(1):14836 – 14842, doi: http://dx.doi.org/https://doi.org/10.1016/j.ifacol.2017.08.2583. 20th IFAC World Congress.

[Alatorre et al., 2017] Alatorre, A. G., Victorino, A., and Charara, A. (2017). Robust multi-model longitudinal tire-force estimation scheme: Experimental data validation. In *2017 IEEE 20th International Conference on Intelligent Transportation Systems (ITSC)*.

[Antonov et al., 2011] Antonov, S., Fehn, A., and Kugi, A. (2011). Unscented kalman filter for vehicle state estimation. *Vehicle System Dynamics*, 49:1497–1520, doi: http://dx.doi.org/10.1080/00423114.2010.527994.

[Bae et al., 2001] Bae, H., Ryu, J., and Gerdes, J. (2001). oad grade and vehicle parameter estimation for longitudinal control using gps. In *ITSC 2001. 2001 IEEE Intelligent Transportation Systems. Proceedings (Cat. No.01TH8585)*, pages 166–171.

[Bakker et al., 1987] Bakker, E., Nyborg, L., and Pacejka, H. B. (1987). Tyre modelling for use in vehicle dynamics studies. *SAE Transactions*, pages 190–204.

[Bakker et al., 1989] Bakker, E., Pacejka, H. B., and Lidner, L. (1989). A new tire model with an application in vehicle dynamics studies. *SAE transactions*, pages 101–113.

[Bastow et al., 2004] Bastow, D., Howard, G., and Whitehead, J. P. (2004). *Car Suspension and Handling*. Wiley.

[Bemporad and Morari, 1999] Bemporad, A. and Morari, M. (1999). Robust model predictive control: A survey. In *Robustness in identification and control*, pages 207–226. Springer.

[Bevly et al., 2006] Bevly, D. M., Ryu, J., and Gerdes, J. C. (2006). Integrating ins sensors with gps measurements for continuous estimation of vehicle sideslip, roll, and tire cornering stiffness. *IEEE Transactions on Intelligent Transportation Systems*, 7(4):483–493, doi: http://dx.doi.org/10.1109/TITS.2006.883110.

[Bevly et al., 2001] Bevly, D. M., Sheridan, R., and Gerdes, J. C. (2001). Integrating ins sensors with gps velocity measurements for continuous estimation of vehicle sideslip and tire cornering stiffness. In *Proceedings of the 2001 American Control Conference. (Cat. No.01CH37148)*, volume 1, pages 25–30 vol.1.

[Boyden and Velinsky, 1994] Boyden, F. D. and Velinsky, S. A. (1994). Dynamic modeling of wheeled mobile robots for high load applications. In *Proceedings of the 1994 IEEE International Conference on Robotics and Automation*, pages 3071–3078. IEEE.

[Brunner et al., 2015] Brunner, T., Lauffenburger, J.-P., Changey, S., and Basset, M. (2015). Quaternion-based imu and stochastic error modeling for intelligent vehicles.

[Brunner et al., 2017] Brunner, T., Ledy, J., Lauffenburger, J.-P., Manzano, M. J. R. S. Q., Changey, S., Lambert, J., and Basset, M. (2017). Road vehicle relative motion estimation using gyro-free imus and system independent observers. *IFAC-PapersOnLine*, 50(1):14824 – 14829, doi: http://dx.doi.org/https://doi.org/10.1016/j.ifacol.2017.08.2580. 20th IFAC World Congress.

[Busnelli et al., 2017] Busnelli, F., Panzani, G., Corno, M., and Savaresi, S. M. (2017). Two-wheeled vehicles black-box sideslip angle estimation. In *2017 IEEE 56th Annual Conference on Decision and Control (CDC)*, pages 351–356. IEEE.

[Chen et al., 2018] Chen, T., Chen, L., Cai, Y., and Xu, X. (2018). Robust sideslip angle observer with regional stability constraint for an uncertain singular intelligent vehicle system. *IET Control Theory and Applications*, 12(13):1802–1811.

[Chen et al., 2014] Chen, Y., Ji, Y., and Guo, K. (2014). A reduced-order nonlinear sliding mode observer for vehicle slip angle and tyre forces. *Vehicle System Dynamics*, 52(12):1716–1728, doi: http://dx.doi.org/10.1080/00423114.2014.960430.

[Chokor et al., 2016] Chokor, A., Talj, R., Charara, A., Shraim, H., and Francis, C. (2016). Active suspension control to improve passengers comfort and vehicle's stability. In *2016 IEEE 19th International Conference on Intelligent Transportation Systems (ITSC)*, pages 296–301.

[Dakhlallah et al., 2008] Dakhlallah, J., Glaser, S., Mammar, S., and Sebsadji, Y. (2008). Tire-road forces estimation using extended kalman filter and sideslip angle evaluation. In *2008 American Control Conference*, pages 4597–4602.

[De Martino et al., 2017] De Martino, M., Farroni, F., Pasquino, N., Sakhnevych, A., and Timpone, F. (2017). Real-time estimation of the vehicle sideslip angle through regression based on principal component analysis and neural networks. In *2017 IEEE International Systems Engineering Symposium (ISSE)*, pages 1–6. IEEE.

[Ding and Taheri, 2010] Ding, N. and Taheri, S. (2010). A modified dugoff tire model for combined-slip forces. *Tire Science and Technology*, 38(3):228–244.

[Doumiati et al., 2012] Doumiati, M., Charara, A., Victorino, A., and Lechner, D. (2012). *Vehicle Dynamics Estimation using Kalman Filtering: Experimental Validation*. WILEY.

[Doumiati et al., 2017] Doumiati, M., Martinez, J., Sename, O., Dugard, L., and Lechner, D. (2017). Road profile estimation using an adaptive youla–kučera parametric observer: Comparison to real profilers. *Control Engineering Practice*, 61:270 – 278.

[Doumiati et al., 2011] Doumiati, M., Victorino, A., Charara, A., and Lechner, D. (2011). Estimation of road profile for vehicle dynamics motion: Experimental validation. In *Proceedings of the 2011 American Control Conference*, pages 5237–5242.

[Dugoff, 1969] Dugoff, H. (1969). Affecting vehicle response to steering and braking control inputs. Report, The University of Michigan, Highway Safety Research Institute, Institute of Science and Technology.

[Eckermann, 2001] Eckermann, E. (2001). *World history of the automobile*. SAE.

[ElMadany and Abduljabbar, 1999] ElMadany, M. M. and Abduljabbar, Z. S. (1999). Linear quadratic gaussian control of a quarter-car suspension. *Vehicle System Dynamics*, 32(6):479–497.

[Fathy et al., 2008] Fathy, H. K., Kang, D., and Stein, J. L. (2008). Online vehicle mass estimation using recursive least squares and supervisory data extraction. In *2008 American Control Conference*, pages 1842–1848.

[Fremd, 1987] Fremd, R. (1987). Apparatus for measuring the mass of a motor vehicle. Technical report, U.S. Patent No. 4656876.

[Gadola et al., 2014] Gadola, M., Chindamo, D., Romano, M., and Padula, F. (2014). Development and validation of a kalman filter-based model for vehicle slip angle estimation. *Vehicle System Dynamics*, 52(1):68–84, doi: http://dx.doi.org/10.1080/00423114.2013.859281.

[Ganji et al., 2011] Ganji, B., Kouzani, A. Z., and Khayyam, H. (2011). Look-ahead intelligent energy management of a parallel hybrid electric vehicle. In *2011 IEEE International Conference on Fuzzy Systems (FUZZ-IEEE 2011)*, pages 2335–2341.

[Garcia et al., 1989] Garcia, C. E., Prett, D. M., and Morari, M. (1989). Model predictive control: theory and practice—a survey. *Automatica*, 25(3):335–348.

[Genise, 1996] Genise, T. (1996). Control method/system including determination of an updated value indicate of gross combination weight of vehicles. Technical report, U.S. Patent No. 5490063.

[Gillespie, 1992] Gillespie, T. D. (1992). *Fundamentals of Vehicle Dynamics*. SAE International.

[Grip et al., 2009] Grip, H. F., Imsland, L., Johansen, T. A., Kalkkuhl, J. C., and Suissa, A. (2009). Estimation of road inclination and bank angle in automotive vehicles. In *2009 American Control Conference*, pages 426–432.

[Grip et al., 2009] Grip, H. F., Imsland, L., Johansen, T. A., Kalkkuhl, J. C., and Suissa, A. (2009). Vehicle sideslip estimation. *IEEE Control Systems Magazine*, 29(5):36–52, doi: http://dx.doi.org/10.1109/MCS.2009.934083.

[Han et al., 2009] Han, K.-J., Kim, I.-K., and H Y Jo, K.-S. H. (2009). Development and experimental evaluation of an online estimation system for vehicle mass. *Proceedings of the Institution of Mechanical Engineers, Part D: Journal of Automobile Engineering*, 223(2):167–177, doi: http://dx.doi.org/10.1243/09544070JAUTO99.

[Harrison, 1999] Harrison, H. (1999). Quaternions and rotation sequences: a primer with applications to orbits, aerospace and virtual reality, jb kuipers, princeton university press, 41 william street, princeton, nj 08540, usa. 1999. 372pp. illustrated.£ 35.00. isbn 0-691-05872-5. *The Aeronautical Journal*, 103(1021):175–175.

[Hellström et al., 2009] Hellström, E., Ivarsson, M., Åslund, J., and Nielsen, L. (2009). Look-ahead control for heavy trucks to minimize trip time and fuel consumption. *Control Engineering Practice*, 17(2):245–254.

[Hong et al., 2015] Hong, S., Lee, C., Borrelli, F., and Hedrick, J. K. (2015). A novel approach for vehicle inertial parameter identification using a dual kalman filter. *IEEE Transactions on Intelligent Transportation Systems*, 16(1):151–161, doi: http://dx.doi.org/10.1109/TITS.2014.2329305.

[Imine et al., 2005] Imine, H., Delanne, Y., and M'sirdi, N. (2005). Road profile inputs for evaluation of the loads on the wheels. *Vehicle System Dynamics*, 43(sup1):359–369.

[ISO21994, 2006] ISO21994 (2006). Passenger cars – braking in a turn – open-loop test method. techreport, International Organization for Standardization, Geneva, Switzerland.

[ISO21994, 2007] ISO21994 (2007). Straight-ahead braking on surfaces with split coefficient of friction– open-loop test procedure. techreport, International Organization for Standardization, Geneva, Switzerland.

[ISO3888-1, 1999] ISO3888-1 (1999). Passenger cars – test track for a severe lane-change manoeuvre – part 1: Double lane-change. techreport, International Organization for Standardization, Geneva, Switzerland.

[ISO4138, 2012] ISO4138 (2012). Passenger cars - steady-state circular driving behaviour - open-loop test methods. techreport, International Organization for Standardization, Geneva, Switzerland.

[ISO7401, 2011] ISO7401 (2011). Passenger cars – test track for a severe lane-change manoeuvre – part 1: Double lane-change. techreport, International Organization for Standardization, Geneva, Switzerland.

[Jacobs, 1994] Jacobs, H. R. (1994). *Mathematics: A human endeavor*. Macmillan.

[Jiang et al., 2014] Jiang, K., Pavelescu, A., Victorino, A., and Charara, A. (2014). Estimation of vehicle's vertical and lateral tire forces considering road angle and road irregularity. In *17th International IEEE Conference on Intelligent Transportation Systems (ITSC)*, pages 342–347. IEEE.

[Jiang et al., 2016] Jiang, K., Victorino, A., and Charara, A. (2016). Robust estimation of vehicle's dynamics states employing a parameter-variable ekf observer. In *2016 IEEE 19th International Conference on Intelligent Transportation Systems (ITSC)*, pages 2219–2224.

[Katriniok and Abel, 2016] Katriniok, A. and Abel, D. (2016). Adaptive ekf-based vehicle state estimation with online assessment of local observability. *IEEE Transactions on Control Systems Technology*, 24(4):1368–1381, doi: http://dx.doi.org/10.1109/TCST.2015.2488597.

[Katz, 1997] Katz, A. (1997). *Computational rigid vehicle dynamics*. Krieger Publishing Co., Inc.

[Kawashima et al., 2010] Kawashima, K., Hori, Y., Uchida, T., and Oh, S. (2010). Robust bank angle estimation for rolling stability control on electric vehicle. In *2010 11th IEEE International Workshop on Advanced Motion Control (AMC)*, pages 448–453. IEEE.

[Kawashima et al., 2010] Kawashima, K., Hori, Y., Uchida, T., and Oh, S. (2010). Robust bank angle estimation for rolling stability control on electric vehicle. In *2010 11th IEEE International Workshop on Advanced Motion Control (AMC)*, pages 448–453.

[Khayyam et al., 2011] Khayyam, H., Nahavandi, S., Hu, E., Kouzani, A., Chonka, A., Abawajy, J., Marano, V., and Davis, S. (2011). Intelligent energy management control of vehicle air conditioning via look-ahead system. *Applied Thermal Engineering*, 31(16):3147 – 3160, doi: http://dx.doi.org/https://doi.org/10.1016/j.applthermaleng.2011.05.023.

[Kiencke and Nielsen, 2005] Kiencke, U. and Nielsen, L. (2005). *Automotive Control Systems - For Engine, Driveline, and Vehicle*. Springer-Verlag Berlin Heidelberg.

[Kim and Ro, 2000] Kim, C. and Ro, P. I. (2000). Reduced-order modelling and parameter estimation for a quarter-car suspension system. *Proceedings of the Institution of Mechanical Engineers, Part D: Journal of Automobile Engineering Institution of Mechanical Engineers*, 214(8):851 – 864.

[Kim et al., 2002] Kim, H.-J., Yang, H. S., and Park, Y.-P. (2002). Improving the vehicle performance with active suspension using road-sensing algorithm. *Computers and Structures*, 80(18):1569 – 1577.

[Klomp et al., 2014] Klomp, M., Gao, Y., and Bruzelius, F. (2014). Longitudinal velocity and road slope estimation in hybrid electric vehicles employing early detection of excessive wheel slip. *Vehicle System Dynamics*, 52(sup1):172–188, doi: http://dx.doi.org/10.1080/00423114.2014.887737.

[Kunze and Schaeben, 2004] Kunze, K. and Schaeben, H. (2004). The bingham distribution of quaternions and its spherical radon transform in texture analysis. *Mathematical Geology*, 36(8):917–943.

[Lipschutz and Lipson, 2001] Lipschutz, S. and Lipson, M. (2001). *Schaum's outline of theory and problems of linear algebra*. Erlangga.

[Liu and Ye, 2011] Liu, C. and Ye, T. J. (2011). Run-off-road crashes: An on-scene perspective. Report, Mathematical Analysis Division, National Center for Statistics and Analysis, National Highway Traffic Safety Administration 1200 New Jersey Avenue SE., Washington, DC 20590.

[Madhusudhanan et al., 2016] Madhusudhanan, A. K., Corno, M., and Holweg, E. (2016). Vehicle sideslip estimator using load sensing bearings. *Control Engineering Practice*, 54:46 – 57, doi: http://dx.doi.org/https://doi.org/10.1016/j.conengprac.2016.05.008.

[McCarthy, 1990] McCarthy, J. M. (1990). *Introduction to theoretical kinematics*. MIT press.

[McIntyre et al., 2009] McIntyre, M. L., Ghotikar, T. J., Vahidi, A., Song, X., and Dawson, D. M. (2009). A two-stage lyapunov-based estimator for estimation of vehicle mass and road grade. *IEEE Transactions on Vehicular Technology*, 58(7):3177–3185, doi: http://dx.doi.org/10.1109/TVT.2009.2014385.

[Naets et al., 2017] Naets, F., van Aalst, S., Boulkroune, B., Ghouti, N. E., and Desmet, W. (2017). Design and experimental validation of a stable two-stage estimator for automotive sideslip angle and tire parameters. *IEEE Transactions on Vehicular Technology*, 66(11):9727–9742, doi: http://dx.doi.org/10.1109/TVT.2017.2742665.

[Nguyen et al., 2012] Nguyen, B., Wang, Y., Fujimoto, H., and Hori, Y. (2012). Sideslip angle estimation using gps and disturbance accommodating multi-rate kalman filter for electric vehicle stability control. In *2012 IEEE Vehicle Power and Propulsion Conference*, pages 1323–1328.

[Nilsson and Lingefelt, 2011] Nilsson, A. and Lingefelt, H. (2011). Estimation of vehicle roll angle. *CODEN: LUTEDX/TEIE*.

[Pacejka and Bakker, 1993] Pacejka, H. and Bakker, E. (1993). The magic formula tyre model. *Vehicle Systems Dynamics*, 21:1–18.

[Pacejka and Besselink, 1997a] Pacejka, H. and Besselink, I. (1997a). Magic formula tyre model with transient properties. *Vehicle system dynamics*, 27(S1):234–249.

[Pacejka and Besselink, 1997b] Pacejka, H. B. and Besselink, I. J. M. (1997b). Magic formula tyre model with transient properties. *Vehicle System Dynamics*, 27(sup001):234–249, doi: http://dx.doi.org/10.1080/00423119708969658.

[Pai, 2017] Pai, J. (2017). Trends and rollover-reduction effectiveness of static stability factor in passenger vehicles. Report, Mathematical Analysis Division, National Center for Statistics and Analysis, National Highway Traffic Safety Administration, Washington, DC 20509, NHTSA Technical Report: DOT HS 182 444.

[Piyabongkarn et al., 2008] Piyabongkarn, D., Rajamani, R., Grogg, J. A., and Lew, J. Y. (2008). Development and experimental evaluation of a slip angle estimator for vehicle stability control. *IEEE Transactions on control systems technology*, 17(1):78–88.

[Pletschen and Badur, 2014] Pletschen, N. and Badur, P. (2014). Nonlinear state estimation in suspension control based on takagi-sugeno model. *IFAC Proceedings Volumes*, 47(3):11231 – 11237. 19th IFAC World Congress.

[Qin and Badgwell, 2003] Qin, S. J. and Badgwell, T. A. (2003). A survey of industrial model predictive control technology. *Control engineering practice*, 11(7):733–764.

[Rajamani and Hedrick, 1995] Rajamani, R. and Hedrick, J. K. (1995). Adaptive observers for active automotive suspensions: theory and experiment. *IEEE Transactions on Control Systems Technology*, 3(1):86–93, doi: http://dx.doi.org/10.1109/87.370713.

[Ray, 1995] Ray, L. R. (1995). Nonlinear state and tire force estimation for advanced vehicle control. *IEEE Transactions on Control Systems Technology*, 3(1):117–124.

[Regolin et al., 2017] Regolin, E., Incremona, G. P., and Ferrara, A. (2017). *Sliding mode control of vehicle dynamics*, chapter Longitudinal Vehicle Dynamics Control via Sliding Modes Generation, pages 33–76. IET, London.

[Reif, 2014] Reif, K. (2014). *Fundamentals of Automotive and Engine Technology*. Springer Vieweg.

[Rezaeian et al., 2015] Rezaeian, A., Zarringhalam, R., Fallah, S., Melek, W., Khajepour, A., Chen, S. K., Moshchuck, N., and Litkouhi, B. (2015). Novel tire force estimation strategy for real-time implementation on vehicle applications. *IEEE Transactions on Vehicular Technology*, 64(6):2231–2241, doi: http://dx.doi.org/10.1109/TVT.2014.2345695.

[Rhode et al., 2016] Rhode, S., Hong, S., Hedrick, J. K., and Gauterin, F. (2016). Vehicle tractive force prediction with robust and windup-stable kalman filters. *Control Engineering Practice*, 46:37 – 50, doi: http://dx.doi.org/https://doi.org/10.1016/j.conengprac.2015.10.002.

[Ryu and Gerdes, 2004] Ryu, J. and Gerdes, J. C. (2004). Estimation of vehicle roll and road bank angle. In *Proceedings of the 2004 American Control Conference*, volume 3, pages 2110–2115 vol.3.

[Savaresi et al., 2010a] Savaresi, S., Poussot-Vassal, C., Spelta, C., Sename, O., and Dugard, L. (2010a). *Semi-Active Suspension Control Design for Vehicles*. Butterworth-Heinemann.

[Savaresi et al., 2010b] Savaresi, S. M., Poussot-Vassal, C., Spelta, C., Sename, O., and Dugard, L. (2010b). *Semi-active suspension control design for vehicles*. Elsevier.

[Sayers and Karamihas, 1998] Sayers, M. W. and Karamihas, S. M. (1998). *The Little Book of Profiling*. The Regent of the University of Michigan.

[Sebsadji et al., 2008] Sebsadji, Y., Glaser, S., Mammar, S., and Netto, M. (2008). Vehicle roll and road bank angles estimation. *IFAC Proceedings Volumes*, 41(2):7091 – 7097, doi: http://dx.doi.org/https://doi.org/10.3182/20080706-5-KR-1001.01202. 17th IFAC World Congress.

[Selmanaj et al., 2017a] Selmanaj, D., Corno, M., Panzani, G., and Savaresi, S. M. (2017a). Vehicle sideslip estimation: A kinematic based approach. *Control Engineering Practice*, 67:1 – 12, doi: http://dx.doi.org/https://doi.org/10.1016/j.conengprac.2017.06.013.

[Selmanaj et al., 2017b] Selmanaj, D., Corno, M., Panzani, G., and Savaresi, S. M. (2017b). Vehicle sideslip estimation: A kinematic based approach. *Control Engineering Practice*, 67:1 – 12, doi: http://dx.doi.org/https://doi.org/10.1016/j.conengprac.2017.06.013.

[Sename et al., 2013] Sename, O., Gaspar, P., and Bokor, J. (2013). *Robust control and linear parameter varying approaches: application to vehicle dynamics*, volume 437. Springer.

[Shakouri and Ordys, 2014] Shakouri, P. and Ordys, A. (2014). Nonlinear model predictive control approach in design of adaptive cruise control with automated switching to cruise control. *Control Engineering Practice*, 26:160 – 177, doi: http://dx.doi.org/https://doi.org/10.1016/j.conengprac.2014.01.016.

[Shin et al., 2014] Shin, D., Seo, J., Lee, G., and Yi, K. (2014). Mode control of motorized active suspension damper for ride quality and energy efficiency. In *17th International IEEE Conference on Intelligent Transportation Systems (ITSC)*, pages 1335–1340.

[Shoemake, 1985] Shoemake, K. (1985). Animating rotation with quaternion curves. In *Proceedings of the 12th annual conference on Computer graphics and interactive techniques*, pages 245–254.

[Smith and Starkey, 1995] Smith, D. E. and Starkey, J. M. (1995). Effects of model complexity on the performance of automated vehicle steering controllers: Model development, validation and comparison. *Vehicle System Dynamics*, 24(2):163–181.

[Sontag, 1998] Sontag, E. D. (1998). *Mathematical Control Theory: Deterministic Finite Dimensional Systems*. Springer.

[Stéphant et al., 2007] Stéphant, J., Charara, A., and Meizel, D. (2007). Evaluation of a sliding mode observer for vehicle sideslip angle. *Control Engineering Practice*, 15(7):803 – 812, doi: http://dx.doi.org/https://doi.org/10.1016/j.conengprac.2006.04.002. Special Issue on Award Winning Applications.

[Tchamna and Youn, 2013] Tchamna, R. and Youn, I. (2013). Yaw rate and side-slip control considering vehicle longitudinal dynamics. *International Journal of Automotive Technology*, 14(1):53–60, doi: http://dx.doi.org/10.1007/s12239-013-0007-1.

[Tseng, 2001] Tseng, E. (2001). Dynamic estimation of road bank angle. *Vehicle System Dynamics - VEH SYST DYN*, 36:307–328, doi: http://dx.doi.org/10.1076/vesd.36.4.307.3547.

[Vahidi et al., 2005] Vahidi, A., Stefanopoulou, A., and Peng, H. (2005). Recursive least squares with forgetting for online estimation of vehicle mass and road grade: Theory and experiments. *Vehicle System Dynamics*, 43(1):31–55, doi: http://dx.doi.org/10.1080/00423110412331290446.

[Wang et al., 2017] Wang, Z., Dong, M., Qin, Y., Du, Y., Zhao, F., and Gu, L. (2017). Suspension system state estimation using adaptive kalman filtering based on road classification. *Vehicle System Dynamics*, 55(3):371–398.

[Wilkin et al., 2006] Wilkin, M. A., Manning, W. J., Crolla, D. A., and Levesley, M. C. (2006). Use of an extended kalman filter as a robust tyre force estimator. *Vehicle System Dynamics*, 44(sup1):50–59, doi: http://dx.doi.org/10.1080/00423110600867325.

[Winstead and Kolmanovsky, 2005] Winstead, V. and Kolmanovsky, I. V. (2005). Estimation of road grade and vehicle mass via model predictive control. In *Proceedings of 2005 IEEE Conference on Control Applications, 2005. CCA 2005.*, pages 1588–1593.

[Yoon and Peng, 2013] Yoon, J.-H. and Peng, H. (2013). Robust vehicle sideslip angle estimation through a disturbance rejection filter that integrates a magnetometer with gps. *IEEE Transactions on Intelligent Transportation Systems*, 15, doi: http://dx.doi.org/10.1109/TITS.2013.2275173.

[You et al., 2009] You, S.-H., Hahn, J.-O., and Lee, H. (2009). New adaptive approaches to real-time estimation of vehicle sideslip angle. *Control Engineering Practice*, 17(12):1367 – 1379, doi: http://dx.doi.org/https://doi.org/10.1016/j.conengprac.2009.07.002. Special Section: The 2007 IFAC Symposium on Advances in Automotive Control.

[Zhang et al., 2016a] Zhang, B., Du, H., Lam, J., Zhang, N., and Li, W. (2016a). A novel observer design for simultaneous estimation of vehicle steering angle and sideslip angle. *IEEE Transactions on Industrial Electronics*, 63(7):4357–4366, doi: http://dx.doi.org/10.1109/TIE.2016.2544244.

[Zhang et al., 2016b] Zhang, H., Zhang, G., and Wang, J. (2016b). Sideslip angle estimation of an electric ground vehicle via finite-frequency$\mathcal{H}_\infty$approach. *IEEE Transactions on Transportation Electrification*, 2(2):200–209, doi: http://dx.doi.org/10.1109/TTE.2015.2511659.

[Zhang et al., 1998] Zhang, Y., Hong, D., Chung, J. H., and Velinsky, S. A. (1998). Dynamic model based robust tracking control of a differentially steered wheeled mobile robot. In *Proceedings of the 1998 American Control Conference. ACC (IEEE Cat. No. 98CH36207)*, volume 2, pages 850–855. IEEE.

[Zhao et al., 2011] Zhao, L., Liu, Z., and Chen, H. (2011). Design of a nonlinear observer for vehicle velocity estimation and experiments. *IEEE Transactions on Control Systems Technology*, 19(3):664–672, doi: http://dx.doi.org/10.1109/TCST.2010.2043104.

[Zhu et al., 2013] Zhu, H., Li, L., Jin, M., Li, H., and Song, J. (2013). Real-time yaw rate prediction based on a non-linear model and feedback compensation for vehicle dynamics control. *Proceedings of the Institution of Mechanical Engineers, Part D: Journal of Automobile Engineering*, 227(10):1431–1445, doi: http://dx.doi.org/10.1177/0954407013482070.